Genetic Risk Factors and Disease Mechanisms in Mitochondrial Optic Neuropathy

Wellcome Centre for Mitochondrial Research
Institute of Genetic Medicine, Faculty of Medical Sciences
Newcastle University

Sarah Elizabeth Nesbitt

Thesis submitted for the degree of Doctorate of Philosophy

July, 2020

Supervisors

Doctor Gavin Hudson

Doctor Angela Pyle

Doctor Joanna Elson

Honorary Supervisors

Doctor Patrick Yu-Wai-Man

Professor Michael Coleman

Abstract

Mitochondrial vitality is dependent upon continued cooperation between nuclear (nDNA) and mitochondrial genomes (mtDNA) and defects in either genome can result in a broad spectrum of human disease.

Leber's Hereditary Optic Neuropathy (LHON) is an inherited blindness caused by the selective loss of retinal ganglion cells (RGCs) which predominantly affects young males. In 90% of LHON, cases harbour one of three primary mutations, m.11778G>A, m.3460G>A and m.14484T>C, which affect Complex I subunits of the electron transport chain. mtDNA mutations alone cannot explain the characteristic reduced penetrance, gender bias and secondary phenotypes of LHON. Recent work on LHON has often, unsuccessfully, focused on the identification of a nuclear-encoded modifying gene which would explain these characteristics.

Thus, the aims of this PhD were, i) to improve our estimates of disease penetrance and investigate other potential disease modifiers, ii) to use LHON patient cell lines to investigate the effect of mtDNA mutations on cellular processes which may contribute to LHON and iii) to evaluate retinal degeneration in a mtDNA mutation animal model. By investigating these key components of LHON we hope to improve our understanding of the disease process.

Using a large familial cohort, we were able to update and improve current LHON penetrance estimates, with our analysis indicating that the penetrance in females is much higher than previous estimates. In addition, we were able to show that LHON cases have differential genetic variants and methylation patterns, identifying ~45 nDNA modifier genes that may explain the variable penetrance and gender bias in LHON. Primary LHON fibroblasts were further characterised across a range of biochemical mechanisms.

Analysis of an mtDNA mutation mouse has improved our understanding of the effect of mtDNA mutation on RGC loss. Work in this PhD has identified a technical framework that could be applied to other models with optic neuropathy.

Acknowledgements

A PhD is often seen to be undertaken as a monumental, individual task; however, in my experience that has absolutely not been the case and I have an abundance of people that I would like to thank for their assistance throughout the course of my project.

I would like to thank the Ferguson family for creating the Joan Margaret Ferguson Studentship and my supervisor, Patrick Yu-Wai-Man, for offering me the opportunity to do this project and continuing to offer and support me through exciting new opportunities, both technical and professional. I am genuinely thankful for the experience.

I would also like to thank my supervisor Gavin Hudson for massively stepping up to become my primary supervisor and Angela Pyle and Joanna Elson for volunteering to adopt another PhD student as my secondary supervisors. Your generosity and support has been invaluable.

Many thanks to Florence Burté for inspiring me with her passion towards protein work - even when I'm forever skewed towards genetics - and extended lab supervision. I learnt so much from you.

Thanks to my supervisory team, John Sayer and Robert Lightowlers, for offering availability in case of issues and passing me through annual exams; I enjoyed our chats.

Further, I would like to thank Michael Coleman and Patrick Chinnery for allowing me to join the Brain Repair Centre and Mitochondrial Biology Unit respectively at the University of Cambridge. This was an unmissable experience.

I would like to give particular thanks to Michal Minczuk and Keith Martin for welcoming me into their research groups whilst I was in Cambridge and making me feel welcome. This open acceptance meant so much to me and I wouldn't have been able to do a lot of my work without your support.

I need to thank Andrew Osborne and Cristiane Benincá for their efforts to help me with the whole tissue collection and processing. I would be missing a chapter without their specialist knowledge and assistance.

Further thanks to Mike Cheetham for allowing me to visit his lab in University College London and to Dimitra Athanasiou for her additional training in whole tissue work. I really enjoyed visiting and seeing how methodologies vary between labs.

Thanks to Valerio Carelli for the collaboration and data exchange regarding the disease penetrance work. I hope that it was as useful to you as it was to me.

I would also like to thank Joanna Howson for taking the time to meet up with me and talking both genetics, statistics, programming and careers. This was eye opening and most helpful to me.

Many thanks to all of the staff and students at Newcastle's Institute of Genetic Medicine, and Cambridge's Brain Repair Centre and Mitochondrial Biology Unit for your support and presence throughout the course of my degree.

Finally, I would like to thank my friends and family for not only tolerating me throughout, but cheering me on and always believing in me. For my parents, who have always been my first supporters and proof-readers, this should be the last tome! I wouldn't have made it without you.

Contents

List of Figures

List of Tables

List of Abbreviations and Nomenclature

Abbreviations

5hmC 5-Hydroxymethylcytosine

5mC 5-Methylcytosine

acetyl-CoA acetyl coenzyme A

AOO Age of Onset

APAF1 Apoptotic Protease-Activating Factor 1

ATF Activating Transcription Factor

ATP Adenosine Triphosphate

BC Bipolar Cell

BH BCL-2 Homology

BNIP3 BCL2 Interacting Protein 3

cAMP Cyclic Adenosine Monophosphate

CARD Caspase Recruitment Domain

CHOP C/EBP Homologous Protein

CoQ10 Ubiquinone

COX Complex IV (Cytochrome Oxidase)

CRISPR Clustered Regularly Interspaced Short Palindromic Repeats

CTPR Computerised Tomography

Cytc Cytochrome c

DMEM Dulbecco's Modified Eagle Medium

DMSO Dimethyl Sulfoxide

DNMT1 Deoxyribonucleic Acid Methyltransferase 1

DNMT3 Deoxyribonucleic Acid Methyltransferase 3

Drp1 Dynamin-Related Protein 1

eIF2 Eukaryotic Initiation Factor 2

ER Endoplasmic Reticulum

ERA Estrogen Receptor α

ERB Estrogen Receptor β

ERG Electroretinography

ETC Electron Tansport Chain

FAD Flavin Adenine Dinucleotide

$FADH_2$ Dihydroflavine-Adenine Dinucleotide

FasL Fas Ligand

FBS Fetal Bovine Serum

FCCP Carbonyl Cyanide 4-(Trifluoromethoxy)phenylhydrazone

FDR False Discovery Rate

GADD34 Growth Arrest And DNA-Damage-Inducible 34

GCL Ganglion Cell Layer

GDP Guanosine Diphosphate

GFP Green Fluorescent Protein

GMEM Growth Medium

GO Gene Ontology

GPCR G-Protein-Coupled Receptor

GRP75 Chaperone Glucose-Regulated Protein 75

GSEA Gene Set Enrichment Analysis

GSK3-β Glycogen Synthase Kinase 3-Beta

GTP Guanosine Triphosphate

HEPES 4-(2-hydroxyethyl)-1-Piperazineethanesulfonic Acid

IAP Inhibitor of Apoptosis Protein

IDT Integrated DNA Technologies Inc.

IMS Intermembrane Space

INL Inner Nuclear Layer

IP_3 Inositol 1,4,5-Trisphosphate

IP_3R Inositol 1,4,5-Trisphosphate Receptor

IPL Inner Plexiform Layer

ipRGC Intrinsically Photosensitive Retinal Ganglion Cell

iPSC Induced Pluripotent Stem Cell

IRE1 Inositol-Requiring Protein-1

LGN Lateral Geniculate Nucleus

LHON Leber Hereditary Optic Neuropathy

lncRNA Long Noncoding Ribonucleic Acid

MAM Mitochondria-Associated Membrane

MAPK Mitogen-Activated Protein Kinase

MELAS Mitochondrial Encephalomyopathy, Lactic Acidosis, and Stroke-like episodes

MEM Minimum Essential Media

Mfn1 Mitofusin 1

Mfn2 Mitofusin 2

MIM Mitochondrial Inner Membrane

miRNA Micro-Ribonucleic Acid

$\Delta\Psi$**m** Mitochondrial Membrane Potential

MnSOD Mitochondrial Antioxidant Manganese Superoxide Dismutase

MOM Mitochondrial Outer Membrane

MOMP Mitochondrial Outer Membrane Permeabilization

mPTP Mitochondrial Permeability Transition Pore

MRI Magnetic Resonance Imaging

MSigDB Molecular Signatures Database

mtDNA Mitochondrial DNA

NAD^+ Nicotinamide Adenine Dinucleotide

NADH NAD + Hydrogen

ND1 Mitochondrially Encoded NADH:Ubiquinone (Coenzyme Q; CoQ) Oxidoreductase Core Subunit 1

ND2 Mitochondrially Encoded NADH Dehydrogenase 2

ND3 Mitochondrially Encoded NADH Dehydrogenase 3

ND4 Mitochondrially Encoded NADH:CoQ10 Oxidoreductase Core Subunit 4

ND4L Mitochondrially Encoded NADH:CoQ10 Oxidoreductase Core Subunit 4L

ND5 Mitochondrially Encoded NADH:CoQ10 Oxidoreductase Core Subunit 5

ND6 Mitochondrially Encoded NADH:CoQ10 Oxidoreductase Core Subunit 6

nDNA Nuclear DNA

NGSeq Next-Generation Sequencing

NRF Nuclear Respiratory Factors

OCR Oxygen Consumption Rate

ONL Outer Nuclear Layer

Opa1 Optic Atrophy Protein 1

OPL Outer Plexiform Layer

OXPHOS Oxidative Phosphorylation

PARK2 Parkin RBR E3 Ubiquitin Protein Ligase

PBS Phosphate Buffered Saline (Dulbecco A)

PCR Polymerase Chain Reaction

PERK Protein Kinase Ribonucleic Acid-like Endoplasmic Reticulum Kinase

PFA Paraformaldehyde

PGC-1 Peroxisome Proliferator-Activated Receptor Gamma Coactivator 1

PINK1 PTEN-Induced Kinase 1

PLC Phospholipase C

PR Photoreceptor

QC Quality Control

qPCR Quantitative Polymerase Chain Reaction

rAAV2 Recombinant Adeno-Associated Virus 2

RFU Relative Fluorescence Units

RGC Retinal Ganglion Cell

RITOLS Ribonucleotide Incorporation Throughout the Lagging Strand

ROS Reactive Oxygen Species

SERCA Sarcoendoplasmic Reticulum Ca^{2+}-ATPase

Smac/DIABLO Second Mitochondria-derived Activator of Caspases/Direct IAP-Binding protein with Low PI

SNP Single Nucleotide Polymorphism

TALEN Transcription Activator-Like Effector Nuclease

TFAM Mitochondrial Transcription Factor A

TGF-β Transforming Growth Factor-β

TM C-Terminal Trans-Membrane Domain

TMRM Tetramethylrhodamine Methyl Ester

TNF Tumor Necrosis Factor

TSPO Translocator Protein

UPR^{ER} ER-Unfolded Protein Response

VDAC Voltage-Dependent Anion Channel (VDAC) (Mitochondrial Porin)

XBP1 X-box Binding Protein 1

ZFN Zinc-Finger Nuclease

NOMENCLATURE

~ Approximately

ΔG Gibbs free energy change

bp Base pairs

Kb Kilo base pairs; thousand base pairs; 10^3 base pairs

Da Dalton; $1.992646547 \times 10^{-23}$ grams

KDa Kilodalton; $1.992646547 \times 10^{-20}$ grams

ml Mlilitre; cubic millimetre; 10^{-3} litres

µl Microlitre; cubic micrometre; 10^{-6} litres

µm Micrometre; micron; 10^{-6} metres

nm Nanometre; 10^{-9} metres

mM Milimole; 10^{-3} moles; $6.02214179 \times 10^{20}$ atoms

µM Micromole; 10^{-6} moles; $6.02214179 \times 10^{17}$ atoms

nM Nanomole; 10^{-9} moles; $6.02214179 \times 10^{14}$ atoms

RCF Relative Centrifugal Force; G-Force

ms Millisecond; 10^{-3} seconds

V Volt; unit of electric potential difference

mV Millivolt; 10^{-3} volts

Chapter 1 | Introduction

1.1 Mitochondria

Mitochondria are complex cellular organelles, responsible for a number of biological processes and cellular control. Often named, 'the powerhouse of the cell', they produce more than 90% of the cells' energy in mammalian systems by oxidative phosphorylation (Chance et al., 1979). In addition to providing the vast majority of energy for many species, they also have a role in many other cellular processes, including, Ca^{2+} regulation, fatty acid synthesis, haem and iron-sulphur cluster biogenesis, and cell signalling, particularly within the intrinsic pathway of apoptosis.

In healthy individuals, mitochondria are able to respond appropriately to energy demands, such as upregulating mitochondrial biogenesis and Adenosine Triphosphate (ATP) production via the Electron Tansport Chain (ETC) in individuals who regularly exercise (Menshikova et al., 2006).

Mitochondria have a key role in managing healthy states, however, in cases of mitochondrial dysfunction, it often results in debilitating disease, respiratory defects and death. Different tissue types have differing numbers of mitochondria to handle varying metabolic demands (Cole, 2016; Okie et al., 2016); with high energy demands, muscle and neurological tissue are often most severely affected (De Vivo and DiMauro, 1990; Pacheu-Grau et al., 2018; Wang et al., 2010). This project focuses on mitochondrial dysfunction which leads to retinal and visual defects, predominantly, Leber Hereditary Optic Neuropathy (LHON).

1.1.1 Mitochondrial Structure

Mitochondria are double membrane bound organelles, evolutionary derived from α-proteobacteria which developed a symbiotic relationship with eukaryotic cells (Wallace and Fan, 2010). Singular mitochondria are small, oval shaped organelles, typically 1–2 µm by 0.5–1 µm (Tzagoloff, 1982). Mitochondrial morphology does show distinct specialisation between different tissue types and metabolic demands with most mitochondria being either 'mitos' (thread) or 'chondros' (grain) shaped (Damirchi, 2012; Youle and Karbowski, 2005; Youle and van der Bliek, 2012). They exist in a complex mitochondrial network which is further described in Section 1.3.1.

Mitochondria are highly compartmentalised, with different regions of the mitochondria specialising in specific roles. The mitochondria are separated from the cell's

cytoplasm by the outer membrane and within the mitochondria, an inner membrane, comprised of tightly folded, pleomorphic, cristae separates the central matrix from the Intermembrane Space (IMS). The mitochondrial matrix is the site of the citric acid cycle and also contains nucleoids of mitochondrial DNA (mtDNA), ribosomes and granules containing ions, lipids, and other molecules (Jacob et al., 1994; Mannella, 2006; Pasquali-Ronchetti et al., 1969).

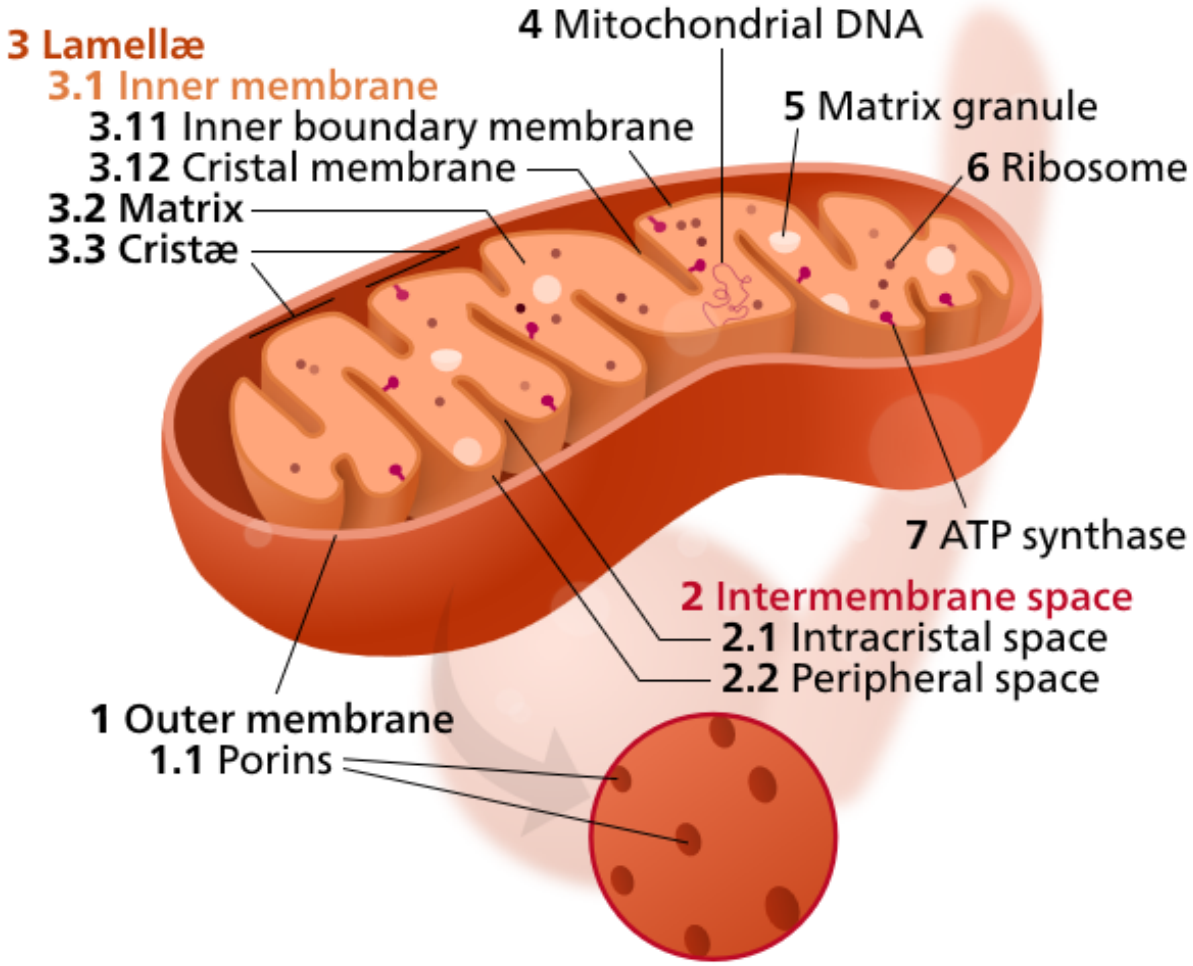

Figure 1.1: *Illustration of a mitochondrion, showing the baffle-shape folded, double membrane bound structure and internal attributes as labelled. Figure from Song (2013), available under Creative Commons CC0 1.0 Universal Public Domain Dedication Licensing.*

The Mitochondrial Outer Membrane (MOM) is highly porous to molecules below 3,000 Da due to the great expression of Voltage-Dependent Anion Channel (VDAC) (Mitochondrial Porin) (Bayrhuber et al., 2008; Benz, 1990). For larger molecules, specialised mitochondrial translocases are used (Sokol et al., 2014). In contrast, the Mitochondrial Inner Membrane (MIM) is highly selective, with many membrane-associated proteins embedded in the MIM, particularly the Oxidative Phosphorylation (OXPHOS) machinery (Schenkel and Bakovic, 2014). This selectivity results in an electrochemical Mitochondrial Membrane Potential ($\Delta\Psi m$) of -180 mV between the matrix and IMS (Kühlbrandt, 2015).

While mitochondria are dynamic structures, often undergoing fusion and fission with other mitochondria in response to biochemical triggers, such as restructuring the mitochondria between condensed and orthodox (respectively, matrix contracted and expanded) topologies as required (Mannella et al., 2001), and as further described in Section 1.3.1, their internal structure is very specific. The matrix contains independent mtDNA, MIM-bound ribosomes (Pfeffer et al., 2015), tRNAs and associated protein factors, responsible for synthesising both their own DNA and proteins (Kühlbrandt, 2015), and the outlying IMS has a role in signalling pathways and protein transport (Herrmann and Riemer, 2010).

1.1.2 mtDNA

More than 99% of the DNA used in mitochondrially associated actions is located within the nuclear DNA (nDNA), however, mitochondria still maintain their own individual genome (Kühlbrandt, 2015).

mtDNA, shown in Figure 1.2, is a 16,569 bp circular genome encoding 37 overlapping genes, 2 RNAs, 22 tRNA and 13 polypeptides (Taanman, 1999) organised into ~100 nm spherical nucleoids with Mitochondrial Transcription Factor A (TFAM) coating a singular mtDNA (Bogenhagen, 2012; Kühlbrandt, 2015; Wang et al., 2013). Alongside structuring the nucleoids, TFAM is also responsible for supercoiling, transcription initiation, and mtDNA copy number (Campbell et al., 2012).

mtDNA is extremely gene dense, with overlapping genes and few non-coding regions. mtDNA has both a heavy (H-strand, outer, guanosine rich) and light (L-strand, inner, cytosine-rich) strand with different origins of replication. There is also a non-coding region called the D-loop, where the H-strand origin of replication (O_H) sits (Gammage and Frezza, 2019). In some mtDNA molecules, the DNA exists in a triple helix structure due to the incorporation of 7S DNA, a ~680 bp DNA strand (Anderson et al., 1981; Nicholls and Minczuk, 2014). ~10% of mtDNA contains the 7S triple strand in cultured human cells but the proportion varies (Nicholls and Minczuk, 2014).

There are three proposed methods for mtDNA replication: strand displacement, strand-synchronous and Ribonucleotide Incorporation Throughout the Lagging Strand (RITOLS), but at present, strand displacement is the favoured methodology for replication (Anderson et al., 1981; Falkenberg, 2018; Holt et al., 2000; Nicholls and Minczuk, 2014; Yasukawa et al., 2006).

Strand displacement theorises that replication begins at O_H (Anderson et al., 1981; Clayton, 2000) where the H-strand is replicated for ~2/3 of the genome in an anti-clockwise direction whereafter the L-strand origin (O_L) is exposed. The L-strand synthesis then begins and takes place in a clockwise direction whilst the H-strand replication continues (Anderson et al., 1981; Falkenberg, 2018).

The number of mitochondria present in each cell and their respective quantity of mtDNA varies between 10^2 and 10^4 between cells (Ye et al., 2014); variation in mtDNA

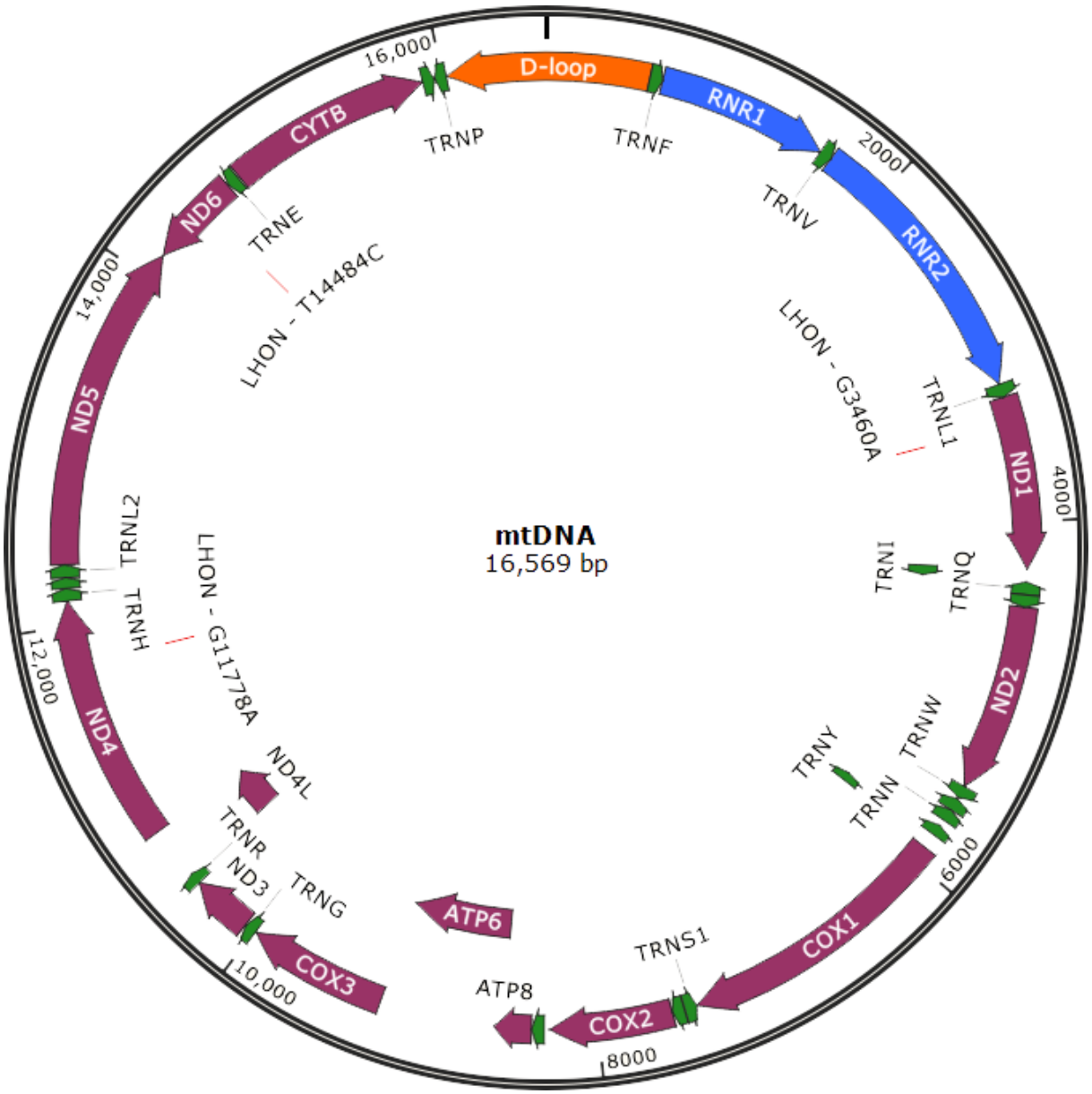

Figure 1.2: *mtDNA showing mitochondrial coding regions in purple, tRNA in green, ribosomal RNA in blue and the D-loop in orange. Three primary LHON mutations which account for the majority of LHON cases are shown in red.*

copy number has been linked with a variety of diseases, including neurodegeneration (Rooney et al., 2015).

As all cells contain multiple mitochondria and each mitochondrion contains multiple copies of mtDNA, this can result in heteroplasmy, whereby some of the cellular mitochondria carry a variant which the others do not, or homoplasmy, where all of the mtDNA is homologous. In clinical settings, heteroplasmy and homoplasmy typically refer to the presence of a pathogenic mutation and how the patient can be affected as a carrier. Whilst some mitochondrial mutations commonly exist as homoplasmic mutations (Yu-Wai-Man et al., 2002), it is common for mitochondrial disease to occur in heteroplasmic states when the mutant mitochondrial burden exceeds a 'threshold' whereby the organisms' ability to compensate for defective mitochondria is exceeded

and disease onset occurs (Rossignol et al., 2003; Ye et al., 2014).

During cell division, mitochondria are split between the two daughter cells and this can result in one cell carrying a disproportionately high number of mutant mtDNA molecules compared to the other. Heteroplasmic mothers can produce egg cells with differing levels of heteroplasmy (Wallace and Chalkia, 2013), resulting in subsequent difficulties in prediction of disease transmission.

mtDNA inheritance is matrilineal, and as such, it does not undergo recombination and can be prone to transmission of pathogenic mutations. Whilst it is believed that there have been exceptions to the matrilineal inheritance (Luo et al., 2018), this is likely a result of technical error identifying nuclear mtDNA concatamers as mtDNA (Balciuniene and Balciunas, 2019). Next-Generation Sequencing (NGSeq) screening by Professor Patrick Chinnery (University of Cambridge) (manuscript in preparation) further disproves this inheritance mechanism.

mtDNA has a mutational rate 10x that of nDNA as it is arranged in nucleoids, without histone protection, and has a close proximity to the genotoxic mitochondrial chain (Pinto and Moraes, 2014). In addition to this, mtDNA does not have nucleotide excision repair pathways; instead, only base excision repair, mismatch repair, direct reversal and single strand break repair have been confirmed to occur (Jeppesen et al., 2011). It was believed that mtDNA damage could further induce mitochondrial dysfunction, leading to a self-amplifying, 'vicious' cycle which produces more Reactive Oxygen Species (ROS) which further damages mtDNA (Jeppesen et al., 2011), however, recent studies have indicated that ROS is a poor effector of mtDNA damage and that the mutations actually arise from the mode of mtDNA replication rather than oxidative stress (Gammage and Frezza, 2019). The 'vicious cycle' model would indicate many *de novo* mutations arising throughout life when mutant mtDNA tends to instead undergo clonal expansion (De Grey, 2005; Kowald and Kirkwood, 2013).

mtDNA instability leads to point mutations, insertions or deletions. It is particularly prone to mtDNA deletions between 8,469-13,447 bp (Fukui and Moraes, 2009; Phillips et al., 2014) which spans the major arc of the mtDNA at 10,912-10,994 bp rather than the minor arc, positioned at 16,528-43 bp (Phillips et al., 2014). This deletion spans several genes, including *MT-ND3* and *MT-ND4*.

1.2 RESPIRATION

Respiration is the cellular process whereby glucose is converted to energy. In humans, there are four stages: glycolysis, the link reaction, the citric acid cycle and the ETC. Respiration occurs under both aerobic and anaerobic conditions which respectively produce a net of 26 and 2 ATP molecules from each molecule of glucose.

Glycolysis occurs in the cytoplasm and 2 molecules of pyruvate are produced from each glucose molecule. In anaerobic conditions, pyruvate undergoes conversion into lactic acid - in a reversible reaction - or in aerobic conditions, pyruvate goes into the

link reaction, whereby it is imported into the mitochondrial matrix by carrier-mediated proteins and oxidised to acetyl coenzyme A (acetyl-CoA), losing CO_2 as a product (McCommis and Finck, 2015).

Next, acetyl-CoA joins the citric acid cycle which joins with oxaloacetate and goes through a cycle of reactions to produce one molecule of Guanosine Triphosphate (GTP) from Guanosine Diphosphate (GDP) and reduce both Flavin Adenine Dinucleotide (FAD) to Dihydroflavine-Adenine Dinucleotide ($FADH_2$) and 3 molecules of Nicotinamide Adenine Dinucleotide (NAD^+) to NAD + Hydrogen (NADH). CO_2 is produced as waste and a molecule of water is also used in the cycle, which is required to recreate the oxaloacetate used at the start of the cycle.

The $FADH_2$ and NADH created in the citric acid cycle then move to the MIM where the complexes of the ETC are located.

1.2.1 Oxidative Phosphorylation

The mitochondrial respiratory chain is comprised of five complexes, NADH:CoQ10 oxidoreductase, succinate dehydrogenase, CoQ10-cytochrome c reductase, cytochrome c oxidase and ATP synthase, also named Complex I:V respectively, amongst other names. Embedded within the MIM, they are the site of OXPHOS and responsible for the majority of energy production for the cell. $FADH_2$ and NADH from the citric acid cycle are oxidised and the H^+ ions (protons) are pumped out of the mitochondrial matrix by complexes I, III and IV into the IMS, with Complex IV creating water as a byproduct, and setting up a proton motive force across the MIM (Jastroch et al., 2010).

As protons return into the cell through Complex V, these are used to synthesise ATP from ADP and one Inorganic Phosphate group, (P_i).

The complexes all work together to produce energy, sometimes directly; with Complexes I, III and IV capable of integrating to form respirasomes or respiratory supercomplexes (Signes and Fernandez-Vizarra, 2018).

Complex I

Complex I, as shown in Figure 1.4, is the largest enzyme of the mitochondrial respiratory chain at ~980 KDa (Brandt and Zickermann, 2013; Mimaki et al., 2012); as such, it is vulnerable to sequence mutations and assembly error. It is the first enzyme of the mitochondrial ETC and comprised of 45 subunits, of which Mitochondrially Encoded NADH:CoQ10 Oxidoreductase Core Subunit 1 (ND1), Mitochondrially Encoded NADH Dehydrogenase 2 (ND2), Mitochondrially Encoded NADH Dehydrogenase 3 (ND3), Mitochondrially Encoded NADH:CoQ10 Oxidoreductase Core Subunit 4L (ND4L), Mitochondrially Encoded NADH:CoQ10 Oxidoreductase Core Subunit 4 (ND4), Mitochondrially Encoded NADH:CoQ10 Oxidoreductase Core Subunit 5 (ND5) and Mitochondrially Encoded NADH:CoQ10 Oxidoreductase Core Subunit 6 (ND6) are mitochondrially encoded (Dieteren et al., 2008; Mimaki et al., 2012) and the remaining

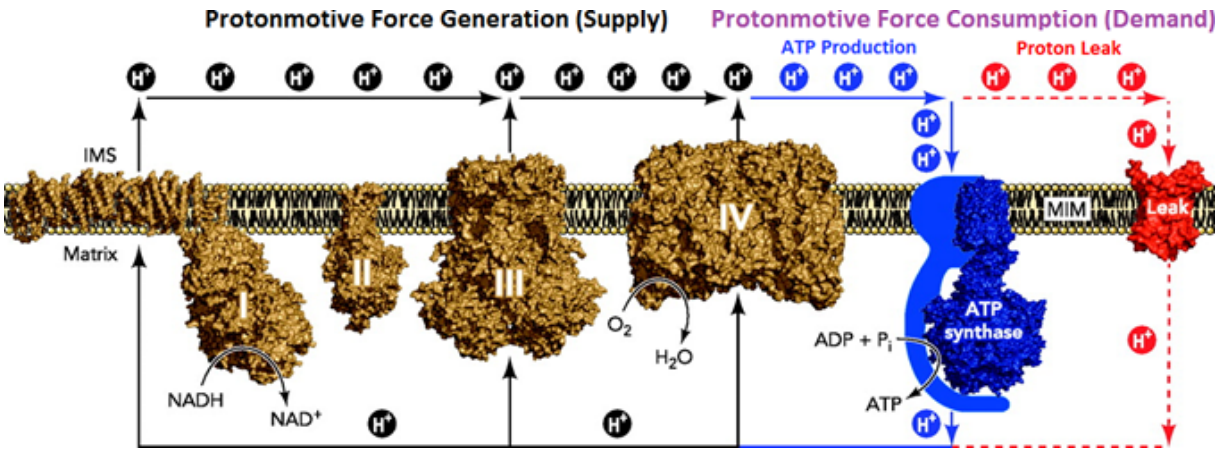

Figure 1.3: *MIM, showing the matrix and IMS with complexes I-V of the mitochondrial respiratory chain embedded into the MIM. The mitochondrial respiratory chain is used to transport electrons to generate ATP by usage of an unequal electrical charge on each side of the membrane in a process called oxidative phosphorylation. Electrons are passed along the respiratory chain from Complex I-IV to Complex V, which is used to produce ATP from ADP + P_i. Electrons are also lost via proton leak pathways, which are used to protect from oxidative damage. Figure adapted from Divakaruni and Brand (2011).*

38 are nuclear-encoded.

Three of the proton transfer units in Complex I are comprised of ND4, ND2 and ND5 with the latter unit comprised of ND1, ND6 and ND4L (Hirst and Roessler, 2015) which transfer the protons across the MIM (Hirst, 2013). ND3 is also a component of Complex I, which supports ND1 in the 'L' shaped structure of the complex (Hirst, 2013).

NADH from the citric acid cycle is oxidised by flavin mononucleotide and a seven-chain of iron-sulphur clusters transfers electrons from flavin to the quinone binding site (as seen in Figure 1.4) (Hirst and Roessler, 2015). This reduces CoQ10 to ubiquinol, producing electrons for the reduction of O_2 to water by the rest of the ETC (Hirst, 2013). This action results in the concurrent translocation of four protons through Complex I from the matrix to the IMS (Giachin et al., 2016).

During the electron transport, Complex I produces ROS, including superoxide ($O_2^{\bullet}$), hydrogen peroxide (H_2O_2) and hydroxyl radical ($^{\bullet}OH$). These are then either used by the cell or deactivated by antioxidants (Jeppesen et al., 2011) but they may cause oxidative damage when the mitochondrial NADH/NAD^+ ratio rises due to Complex I catalytic inhibition (Hirst, 2013; Jeppesen et al., 2011).

Complex I exists in two conformational shapes; A-form (active) and D-form (de-active). D-formation has been used to prevent oxidative damage to the cell and it can transform back to A-formation with increased energy demand (Wirth et al., 2016). Complex I is particularly important in cellular respiration, producing ~40% of the proton motive force used in ATP synthesis (Giachin et al., 2016). It can be inhibited by treatments, such as rotenone, and mutations in Complex I. This can decrease ATP synthesis and oxidative phosphorylation which limits the cell's respiratory capacity (Haroon et al., 2007). Complex I mutations are known to arise in a number of diseases

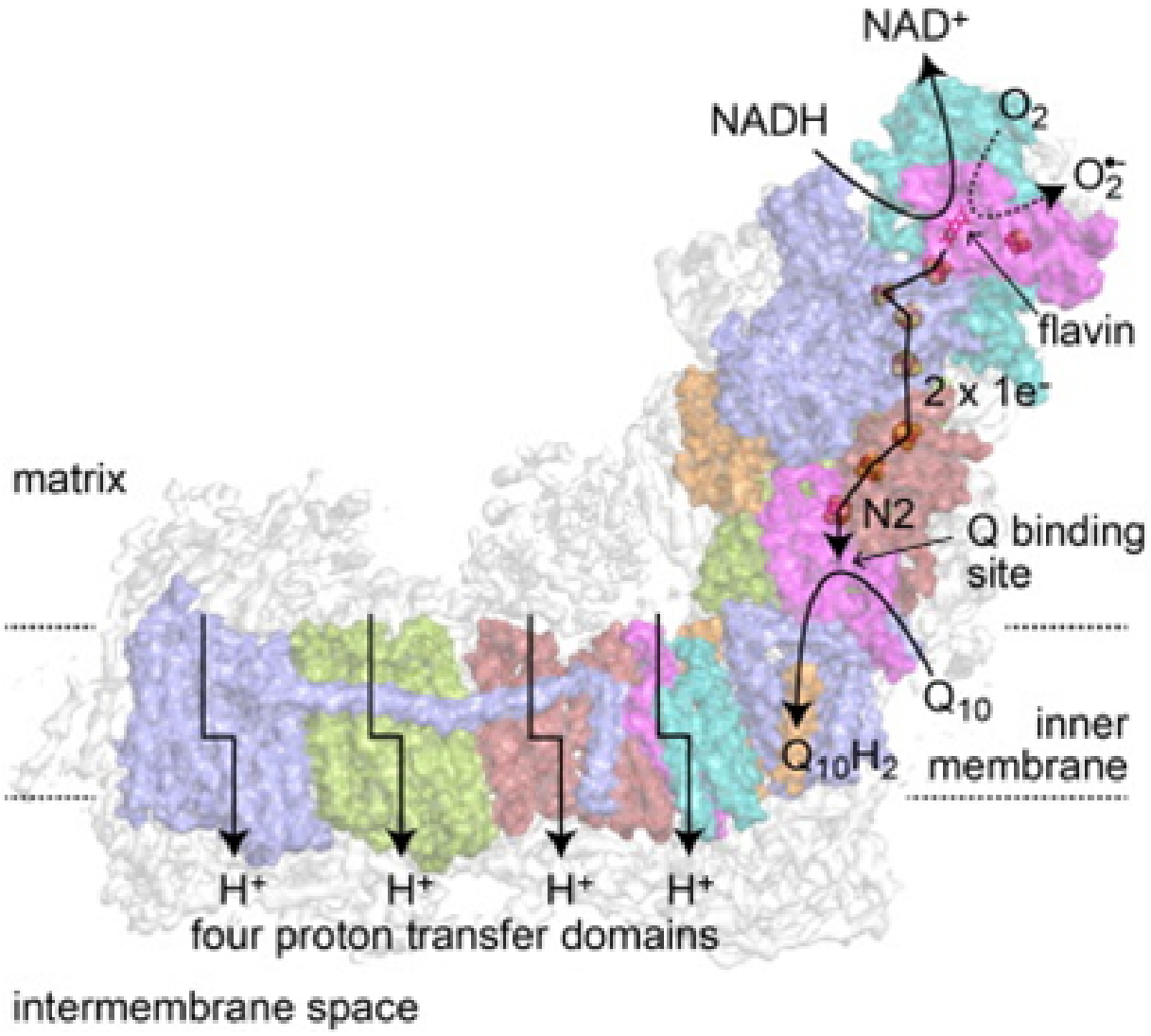

Figure 1.4: *Cryo-electron microscopy of mitochondrial Complex I showing the complete enzyme with the fourteen core subunits of the enzyme in colour. Electron flow is indicated by arrows which directs electrons from the top of the iron-sulphur clusters to the quinone binding site, generating electrons which are then transferred into the IMS via four proton transfer domains. Figure from Hirst and Roessler (2015).*

including LHON, Mitochondrial Encephalomyopathy, Lactic Acidosis, and Stroke-like episodes (MELAS) and Alzheimer's (Giachin et al., 2016).

Complex II

The four components of Complex II are nuclear encoded and targeted to the mitochondria (Spinazzola and Zeviani, 2009), with subunits A and B forming the succinate dehydrogenase activity and subunits C and D anchoring it to the MIM.

Complex II catalyses oxidation of succinate to fumarate and transfers electrons to the respiratory chain CoQ10 pool. Many molecules ROS species are produced through reverse electron transfer (Bezawork-Geleta et al., 2017).

Much like Complex I, Complex II is also required for Ca^{2+} homeostasis, which is

independent of the $\Delta\Psi m$ (Jaña et al., 2019).

Complex III

Complex III is predominantly nuclear encoded with only one of the eleven subunits mitochondrially encoded. It oxidises ubiquinol to transfer electrons and oxidise Cytochrome c (Cytc) and transfers electrons across MIM in the Q-cycle mechanism (Fernández-Vizarra and Zeviani, 2015).

The MIM anionic phospholipid, cardiolipin, stabilises Complexes III and IV (Schenkel and Bakovic, 2014). Cardiolipin binds the highly basic Cytc by electrostatic and hydrophobic bonds (Kalkavan and Green, 2017).

Complex III activity can be inhibited by Antimycin A treatment.

Complex IV

Complex IV is comprised of ten nuclear encoded subunits and three mitochondrially encoded subunits (Fernández-Vizarra and Zeviani, 2015; Spinazzola and Zeviani, 2009). It works with Complex III, sometimes within a respirasome, to catalyse the oxidation of Cytc and reduce oxygen to water through proton translocation (Signes and Fernandez-Vizarra, 2018).

Complex IV is the last electron acceptor of the respiratory chain and also indirectly regulates the stability and activity of Complex I within mammalian and invertebrate systems (Li et al., 2007; Suthammarak et al., 2009).

Complex V

Complex V is the final complex in the oxidative phosphorylation process which is comprised of 14 nuclear and 2 mitochondrially encoded subunits (Fernández-Vizarra and Zeviani, 2015; Spinazzola and Zeviani, 2009).

As eponymously named (ATP Synthase), Complex V uses the CI, CIII and CIV generated proton motive force to synthesise ATP from ADP $+P_i$ by allowing proton flux to pass through the central channel back into the mitochondrial matrix (Fernández-Vizarra and Zeviani, 2015).

Complex V activity can be inhibited by oligomycin A.

1.3 MITOCHONDRIAL INTERACTIONS

Whilst widely known for their role in ATP production, mitochondria are extensively involved in multiple complex pathways. They are capable of initiating the intrinsic cell death pathway for apoptosis. Further, crosstalk to the Endoplasmic Reticulum (ER) regulates calcium homeostasis (Marchi et al., 2014), which in turn acts as a secondary messenger in many signalling processes. Mitochondria are also involved in β-oxidation of fatty acids and iron-sulphur cluster biogenesis (Benard and Karbowski, 2009).

These products and signals are then propagated downstream into further biological processes, resulting in an intricate web of mitochondrial mechanistic action.

Figure 1.5 shows a representation of the typical structure of a mammalian cell, note the ER position between the nucleus and mitochondria.

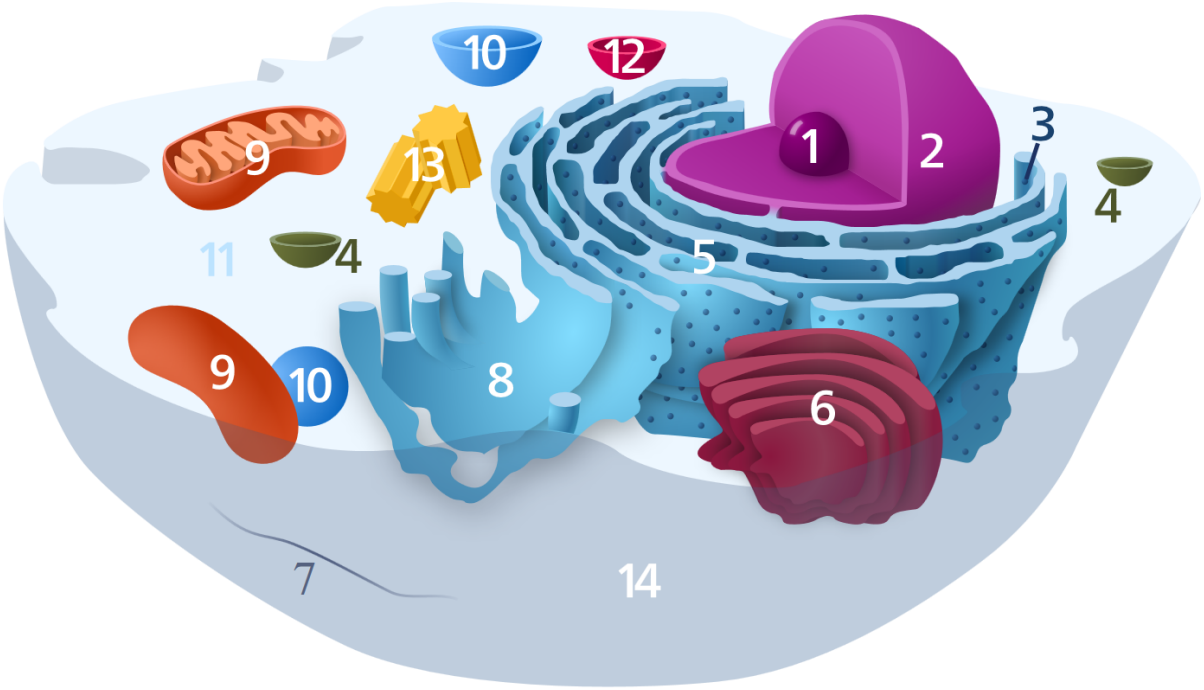

Figure 1.5: *Diagram of typical mammalian cell structure. Labels numerically represent organelles as follows: 1 - Nucleolus, 2 - Nucleus, 3 - Ribosomes (dots), 4 - Vesicle, 5 - Rough ER, 6 - Golgi apparatus, 7 - Cytoskeleton, 8 - Smooth ER, 9 - Mitochondrion, 10 - Vacuole, 11 - Cytosol, - 12 Lysosome, 13 - Centriole, 14 - Cell membrane. Figure from Song (2012), available under Creative Commons CC0 1.0 Universal Public Domain Dedication Licensing.*

1.3.1 Fusion and Fission

Whilst mitochondria are semiautonomous organelles which are able to exist as independent, singular units and function as usual without the mitochondrial network, it is common for mitochondria to regularly migrate along cytoskeletal tracks and undergo a process of fusion or fission of approximately 5 events hourly (Alexandre et al., 1978; Twig et al., 2008b; van der Bliek et al., 2013).

Fusion refers to the amalgamation of two distinct mitochondria into one singular mitochondrion, joining both their MIM and MOM. Fission is the opposite, with a single mitochondrion separating both membranes and forming two individual mitochondria which continue to function as distinct entities.

In healthy states, mitochondrial fusion and fission exist in a state of dynamic equilibrium to allow the exchange of mitochondrial proteins, molecules and mtDNA (Chen and Chan, 2006; Youle and Karbowski, 2005); giving more mitochondria to cells with a higher energy demand, like neurons, which are susceptible during mitochondrial dysfunction and these dynamics could allow for pathogenic mitochondria to be relocated

and recycled in autophagy (Twig et al., 2008a). Equally, fusion and fission are directly involved in apoptosis inhibition and activation respectively (Li et al., 2012b).

The balance between mitochondrial fusion and fission is affected by cellular condition, compartmentalisation and mitochondrial functional state (Benard and Karbowski, 2009).

Fusion

Mitochondrial fusion is regulated by 3 main genes, *MFN1*, *MFN2* and *OPA1*, respectively encoding GTPase dynamin-like proteins Mitofusin 1 (Mfn1), Mitofusin 2 (Mfn2) and Optic Atrophy Protein 1 (Opa1) (Ranieri et al., 2014; van der Bliek et al., 2013).

MOMs and MIMs are highly coordinated (Benard and Karbowski, 2009; van der Bliek et al., 2013), with MOM-bound Mfn1 and Mfn2 initiating tethering between mitochondria, with Mfn1 particularly responsible due to a much higher dimerisation affinity than Mfn2 (Benard and Karbowski, 2009; Ishihara et al., 2004). Following mitochondria:mitochondria binding, Opa1 MIM fusion occurs (Benard and Karbowski, 2009).

Mitochondrial fusion requires a large number of interacting proteins to consolidate the MOM and MIM between mitochondria. Membrane structural components, such as phosphatidylethanolamine, are also required for mitochondrial fusion and phosphatidylethanolamine defects result in mitochondrial fusion defects (Schenkel and Bakovic, 2014).

Problems with mitochondrial fusion have been identified in a number of neurological disorders, including autosomal dominant optic atropy - particularly associated with *OPA1* mutations - and Charcot-Marie-Tooth disease type 2A (Ranieri et al., 2014).

Mfn1 and Mfn2 have been shown to bind multiple other proteins, alongside the Mfn1 and Mfn2 homo/heterotypic complexes (Suen et al., 2008); this includes a number of pro-apoptotic Bcl-2 family members, particularly Bak and Bax (Suen et al., 2008). Mfn2 has been shown to interfere with apoptotic Bax activation and trigger protective mitochondrial fusion (Neuspiel et al., 2005); Bax activation, however, prevents mitochondrial fusion and induces apoptosis (Karbowski et al., 2004)

Fission

Mitochondrial fission is also regulated by another GTPase dynamin-like protein, Dynamin-Related Protein 1 (Drp1). Drp1 is a cytosolic protein and is recruited to the MOM where oligomeric Drp1 complexes wrap and constrict the mitochondria to mediate fission (Losón et al., 2013). An alternate method of mitochondrial fission, focal region vesicle scission, has also been proposed (Fonseca et al., 2019; Youle and Karbowski, 2005).

Mitochondrial fission is known to be difficult to study (van der Bliek et al., 2013) and a number of MOM proteins, Fis1, Mid49, Mid51, and Mff, have been proposed to recruit Drp1, however, there is conflicting evidence in their role and necessity (Losón

et al., 2013; Otera et al., 2010; van der Bliek et al., 2013). While the mechanism is still not well understood, the MOM adaptor proteins are known to be responsible for managing fission and punctate formation (Youle and Karbowski, 2005). Mitochondrial-ER contact points have also been shown to often be trigger points for mitochondrial fission events (Friedman et al., 2011).

Mitochondrial fission can be used to specialise mitochondria for metabolic demands or segregate damaged mitochondria into a consolidated cell which undergoes autophagy to remove the damaged mitochondria from usage (Damirchi, 2012; Karbowski and Youle, 2003; Ranieri et al., 2013; Wright et al., 2007). Mitochondrial fission is seen in the early stages of apoptosis and after onset, invariably results in mitochondrial fragmentation (Suen et al., 2008).

Mitochondrial Outer Membrane Permeabilization (MOMP) is seen in the vast majority of cell death signal-transduction cascades but mitochondrial fission cell death can work both independently or downstream of MOMP (Perfettini et al., 2005).

In many instances, mitochondrial fission is seen in apoptosis, but depending on the upstream signal, mitochondrial fission can prevent cell death; this is specifically seen when disconnected mitochondria are unable to transmit the Ca^{2+} wave to propagate the pro-apoptotic signal (Perfettini et al., 2005).

Whilst associated with apoptosis, a key role of mitochondrial fission is actually mitochondrial biogenesis. Mitochondria are not independently synthesised, but rather, inherited from the maternal line and as metabolic demands increase, the mitochondrial mass increases before undergoing fission and creating new daughter mitochondria (Wright et al., 2007). This is a natural process during growth, improving metabolic fitness levels, and following the destruction of unhealthy mitochondria to replace and restore mitochondria to the cell.

Healthy and diseased states between fusion and fission are not governed by one particular mechanism, but rather the balance of the two and their ability to respond appropriately to metabolic demands.

1.3.2 Endoplasmic Reticulum-Mitochondrial Interactions

Mitochondria interact with a number of other cellular components, particularly, the ER. The ER form a number of contact points of ~10-50 nm gap, namely, Mitochondria-Associated Membranes (MAMs) (Giacomello and Pellegrini, 2016). These contact points are used to transfer molecules which interact in a number of biological signalling processes.

MAMs have been shown to have a role in cell fate, immune response, glucose homeostasis, mitochondrial fission and mitophagy, amongst other processes (Friedman et al., 2011; McLelland et al., 2018; Rieusset, 2018; Tubbs and Rieusset, 2017).

Many proteins are involved in mitochondria-ER tethering; much like mitochondrial fusion (as described in Section 1.3.1), Mfn1 and Mfn2 are used to tether the two

organelles (Basso et al., 2018; de Brito and Scorrano, 2008).

MAMs also have a role in mitochondrial biogenesis by ER mediated mitochondrial constriction for fission; tubules of the ER have been seen to constrict the mother mitochondrion to allow for distribution of nucleoids to daughter mitochondria (Rieusset, 2018).

ER dysfunction has been shown to cause a broad range of disease states, particularly neurodegenerative conditions (Roussel et al., 2013).

Calcium Regulation

Many cellular processes use Ca^{2+} ions to signal. Cells generally maintain a cellular Ca^{2+} concentration of ~100 nM compared to the much stronger concentration (~2mM) in the extracellular space (Clapham, 2007). To maintain this concentration gradient, plasma membrane Ca^{2+} pumps remove Ca^{2+} from the cell and Sarcoendoplasmic Reticulum Ca^{2+}-ATPase (SERCA) sequesters Ca^{2+} into the ER where it is stored (Clapham, 2007).

Like the ER, the mitochondrial Ca^{2+} concentration normally exists in the mM range (Britti et al., 2018) but when this exceeds physiological norm it triggers Mitochondrial Permeability Transition Pore (mPTP) opening and subsequent cell death.

Due to the abundance of VDAC on the MOM, Ca^{2+}, an ion much smaller than the 3,000 Da limit (Bayrhuber et al., 2008; Benz, 1990), is capable of freely moving into the mitochondria via VDAC. VDAC exists in both an open and closed state, the latter of which is a partial close and still allows some molecules to travel into the mitochondria (Britti et al., 2018; Martel et al., 2014). Ca^{2+} is particularly favoured in the VDAC closed state, increasing mitochondrial Ca^{2+} concentrations relative to other metabolites and triggering cell death (Tan and Colombini, 2007).

Phospholipase C (PLC) agonist activation is capable of producing three distinct downstream signals, notably Inositol 1,4,5-Trisphosphate (IP_3) (Putney and Tomita, 2012). Cytosolic IP_3 can then bind IP_3 Receptor (IP_3R), located on the ER cytosolic face, triggering IP_3 Receptor opening and Ca^{2+} release via the transmembrane domain (Rizzuto et al., 2009).

Mitochondrially connected ER then transmit Ca^{2+} through the MOM. Ca^{2+} then travels through the mitochondrial calcium uniporter into the matrix (Marchi et al., 2014) where it can then act as a secondary messenger in a number of roles including hormone secretion, neuronal signalling, gene expression and apoptosis (Rimessi et al., 2008).

Over-excitation can cause cytoplasmic calcium overload which may enhance oxidative stress, increasing the likelihood of a mPTP opening (Haroon et al., 2007), an ER-Unfolded Protein Response (UPR^{ER}), or an intrinsic apoptotic event taking place, as reviewed in Sections 1.3.2 and 1.3.3. The mPTP is located in the MIM and both causes the mitochondrion to swell and uncouples the ETC (Halestrap, 2006). There has been debate regarding the mPTP role in cell death but it now seems to be associated

with necrotic, rather than apoptotic, pathways (Halestrap, 2006; Kinnally et al., 2011). Despite this, mPTP can still trigger release of apoptotic factors, including Cytc and Second Mitochondria-derived Activator of Caspases/Direct IAP-Binding protein with Low PI (Smac/DIABLO) depending upon the initiation method (Ding and Yin, 2012).

VDAC itself plays a role in cell death (Keinan et al., 2010; McCommis and Baines, 2012) and phosphorylation of different isoforms can affect mitochondrial calcium permeability and apoptosis susceptibility by triggering anti- or pro-apoptotic pathways. Phosphorylation by Glycogen Synthase Kinase 3-Beta (GSK3-β) stimulates VDAC/Bcl-X_L binding which makes the cell both less permeable and prevents VDAC from interacting in pro-apoptotic pathways (Beurel and Jope, 2006; Martel et al., 2014). VDAC phosphorylation also causes Translocator Protein (TSPO) to deregulate mitochondrial Ca^{2+} signalling which subsequently increases cytosolic Ca^{2+} pools (Gatliff et al., 2017)

VDAC also directly interacts with the ER Ca^{2+} transmission mechanism via Chaperone Glucose-Regulated Protein 75 (GRP75) which directly binds IP_3 Receptor and crosslinks the pathways (Szabadkai et al., 2006).

ER-Mitochondrial interaction has been seen to be disrupted in neurological disease, particularly Wolfram Syndrome, another mitochondrial disorder which causes visual degeneration (Angebault et al., 2018; Lee et al., 2018).

Unfolded Protein Response

The UPR^{ER} occurs following ER stress, caused by the burden of unfolded proteins in the ER lumen. Improperly folded proteins are displayed on the ER surface for proteasome degradation as part of healthy cell homeostasis and protein Quality Control (QC), however, displaying misfolded proteins for extended time periods can trigger apoptosis (Tabas and Ron, 2011; Walter and Ron, 2011). There are three branches which work in unison to perform the UPR^{ER}.

Inositol-Requiring Protein-1 (IRE1) exists as α and β isoforms, with IRE1-α ubiquitously expressed and IRE1-β in the gastrointestinal and respiratory tracts. IRE1 is activated by imbalance of ER-displayed unfolded proteins to chaperones which subsequently splices X-box Binding Protein 1 (XBP1) mRNA (Tabas and Ron, 2011). XBP1 is a transcription factor and the IRE1-cleaved isoform then promotes expression of many UPR^{ER} genes (Acosta-Alvear et al., 2007; Lee et al., 2003; Tabas and Ron, 2011).

Protein Kinase RNA-like ER Kinase (PERK) phosphorylates Eukaryotic Initiation Factor 2 (eIF2) which initially upregulates selective translation of Activating Transcription Factor (ATF)-4 by limiting the pool of inhibitive unphosphorylated eIF2. ATF-4 then targets C/EBP Homologous Protein (CHOP) which interacts with transcriptional regulators to induce the pro-adaptive, ER-stress-corrective signalling pathway, particularly through Growth Arrest And DNA-Damage-Inducible 34 (GADD34) (Rozpedek et al., 2016; Tabas and Ron, 2011). GADD34 dephosphorylates phosphorylated eIF2 to continue the cycle and constant activation results in a change in cellular response to

trigger the apoptotic branch of the UPR^{ER} instead (Bravo et al., 2013; Rozpedek et al., 2016; Tabas and Ron, 2011; Thuerauf et al., 2007).

ATF-6 is transported to the Golgi apparatus following unfolded protein exposure where it is cleaved to a short-form which translocates to the nucleus and binds ER stress promoter regions which signal cell stress and induce apoptotic triggers, such as promoting CHOP expression (Bravo et al., 2013; Tabas and Ron, 2011; Yoshida et al., 2000; Yu et al., 2017).

Chronic ER-stress has been shown to induce apoptosis (Szegezdi et al., 2006), potentially through direct interaction, such as pro-apoptotic proteins, Bak and Bax, directly interacting with IRE1 (Hetz et al., 2006).

1.3.3 Intrinsic Apoptosis

There are three known pathways which induce cellular apoptosis: Intrinsic (mitochondrial), extrinsic (death cell receptor) and the perforin/granzyme (cytotoxic T-cell) pathways (Elmore, 2007). Intrinsic and extrinsic lead to the majority of apoptotic events with the perforin/granzyme pathway less frequently causative (Elmore, 2007; Voskoboinik et al., 2015).

As implied, the extrinsic pathway is induced through an extracellular signalling process, namely, ligands binding to the cell death receptor, such as Fas Ligand (FasL) and Tumor Necrosis Factor (TNF)-α (Elzey et al., 2001; Furuichi et al., 2012). The intrinsic pathway, however, is triggered directly through the mitochondria, although there is some evidence suggesting that the two pathways can interact with each other, particularly through Caspase-8/tBid interactions (Dewson and Kluck, 2009; Igney and Krammer, 2002).

The intrinsic pathway is predominantly triggered through intracellular stimuli from many subcellular compartments, withdrawal of growth factors, or DNA damage from ROS or radiation (Galluzzi et al., 2014; Hekimi et al., 2016; Wu and Bratton, 2013). Additionally, it is primarily regulated by members of the Bcl-2 protein family (Shamas-Din et al., 2013; Westphal et al., 2011).

Bcl-2 class family proteins contain a combination of BCL-2 Homology (BH)1-4 domains alongside a C-Terminal Trans-Membrane Domain (TM) (Lomonosova and Chinnadurai, 2008). Depending on their sharing of Bcl-2 homologous domains, Bcl-2 class family proteins can be split into three broad categories: BH1-3 + TM, which form pores to permeabilise the MOM, BH3-only + TM proteins which activate the pore-forming proteins and BH1-4 + TM anti-apoptitic proteins which inhibit the former two groups (Lomonosova and Chinnadurai, 2008; Shamas-Din et al., 2013).

To initiate apoptosis, there are three models of activation: BH1-3 protein displacement from BH1-4 protein complexes, conformational activation of BH1-3 proteins and membrane remodelling/insertion (Lomonosova and Chinnadurai, 2008). All models start with BH1-3 proteins, such as Bad, Bid, NOXA, etc. responding to intracellular

stress by binding anti-apoptotic BH1-4 proteins' (e.g. Bcl-2, Bcl-X_L, MCL-1, etc.) regulatory sites and inhibiting them (Kögel and Prehn, 2013; Lomonosova and Chinnadurai, 2008; Shamas-Din et al., 2013; Sinicrope et al., 2008).

Location of BH3-only and BH1-3 proteins depends upon cellular apoptotic state. For example, BH3-only protein NOXA is in a stable, cytosolic multiprotein complex prior to apoptotic activation (Matsuura et al., 2016) alongside pro-apoptotic BH1-3 protein Bax, whereas Bak, another pro-apoptotic BH1-3 protein, resides in the mitochondria. Following apoptotic activation, many BH3-only and BH1-3 proteins migrate to the MOM (Gross et al., 1999; Nechushtan et al., 2001; Popgeorgiev et al., 2018; Shamas-Din et al., 2011; Wolter et al., 1997).

At the MOM, activated pro-apoptotic proteins undergo a conformational change from their passive α-helical globular structure to oligomerise into higher order structures (Westphal et al., 2011). These highly oligomerised structures create pores which cause MOMP (Dewson and Kluck, 2009; Gavathiotis et al., 2010; Lovell et al., 2008).

While there are exceptions, the vast majority of MOMP instances lead to irrevocable apoptosis (Kalkavan and Green, 2017) by releasing intermembrane space molecules, such as Cytc and Smac/DIABLO (Muñoz-Pinedo et al., 2006).

Cytc normally acts as a ROS scavenger within the ETC process, between complexes III and IV (Hüttemann et al., 2011; Kalkavan and Green, 2017), but after exiting the mitochondria it binds Apoptotic Protease-Activating Factor 1 (APAF1), revealing the N-terminal Caspase Recruitment Domains (CARDs) (Kalkavan and Green, 2017; Li et al., 1997; Tait and Green, 2010). This structure, the apoptosome, cleaves procaspase-9, leading to the initiator caspase-9 form cleaving the executioner caspases-3 and -7, causing apoptosis (Kalkavan and Green, 2017; Malladi et al., 2009; Roberts et al., 2001; Tait and Green, 2010).

Smac/DIABLO binds Inhibitor of Apoptosis Proteins (IAPs) (including X-linked-IAP, c-IAP1, c-IAP2, and ML-IAP), preventing them from their inhibitory role on caspases (Fu et al., 2003). X-linked-IAP, for example, binds executioner caspases-3 and -7, and alongside c-IAP-1, and c-IAP-2, has been identified to bind procaspase-9 (Deveraux et al., 1998). Following release of the the executioner caspases, apoptosis then proceeds.

Caspases are proteolytic proteins which work to efficiently and neatly break down the cell and contents (Youle and Karbowski, 2005).

1.3.4 Autophagy

Autophagy is the process whereby the body 'self-eats' to degrade unwanted intracellular components. These can include proteins, foreign bodies, or whole organelles (Yu et al., 2018b). It can occur in both selective and non-selective states depending upon the upstream stimuli (Ding and Yin, 2012).

It can be broken out into further pathways, including, macroautophagy, microau-

tophagy, chaperone-mediated autophagy and mitophagy, amongst others (Ding and Yin, 2012), depending on the substrate and mechanism involved.

This process is useful to destroy unhealthy or pathogenic cellular components, alongside recycling their materials for further usage.

Autophagy works by surrounding the substrate in a double-membrane autophagosome vesicle in the cytoplasm, before fusing with lysosomes for degradation (Glick et al., 2010; Mizushima et al., 2008; Yang and Klionsky, 2009; Yu et al., 2018b).

Autophagy can be triggered by ER stress (reviewed in Section 1.3.2) and dysregulation of autophagy renders cells particularly susceptible to ER stress, favouring downstream cell death rather than homeostatically recovering (Liu et al., 2015; Ogata et al., 2006; Yorimitsu et al., 2006).

Mitophagy

Focusing on the mitophagy pathway, mitochondria are particularly susceptible to organelle damage due to the proximity to the ETC, ROS exposure and limited DNA repair methods (Jeppesen et al., 2011; Pinto and Moraes, 2014). Neurons' mitochondria are particularly susceptible to mitophagy when deprived of nerve growth factor (Xue et al., 1999).

There are two stages to mitophagy: macroautophagy initiation and subsequent mitochondrial ubiquitination by PTEN-Induced Kinase 1 (PINK1)-PARK2 (Parkin RBR E3 Ubiquitin Protein Ligase) or BCL2 Interacting Protein 3 (BNIP3) pathways for selective autophagic recognition (Ding and Yin, 2012; Gatliff et al., 2017).

TSPO is capable of inhibiting mitophagy by accumulating ROS to prevent PARK2-mediated mitochondrial ubiquitination (Gatliff and Campanella, 2015; Gatliff et al., 2017).

1.3.5 Nuclear-Mitochondrial Interactions

As described in Section 1.1.2, mitochondrial proteins are encoded both by the nuclear and mitochondrial genome. Whilst mtDNA remains within the mitochondria, nDNA proteins which are relevant to the mitochondria are co- or post-translationally transported to the mitochondria. Nuclear genetic background has also been seen to alter expression of primary mitochondrial disease (Cock et al., 1998; Mossman et al., 2019; Wei et al., 2017).

Interaction between the two organelles occurs in both anterograde (nuclear to mitochondrial) and retrograde (mitochondrial to nuclear) directions. Anterograde is often a stimulator of mitochondrial biogenesis, with factors such as Nuclear Respiratory Factors (NRF)-1 and -2 and Peroxisome Proliferator-Activated Receptor Gamma Coactivator 1 (PGC-1)-α, -β and -γ (Guha and Avadhani, 2013; Matilainen et al., 2017; Whelan and Zuckerbraun, 2013; Xia et al., 2019), whereas retrograde signalling works with other pathways, such as acmTOR pathways and ER-Ca^{2+} signalling (Guha and Avadhani,

2013; Matilainen et al., 2017; Whelan and Zuckerbraun, 2013; Xia et al., 2019).

While the anterograde pathway is often used to co-ordinate biogenesis of the mtDNA, the retrograde pathway can be used to cause epigenetic modification of the nDNA mitochondrial genes (Guha and Avadhani, 2013; Matilainen et al., 2017; Whelan and Zuckerbraun, 2013; Xia et al., 2019) with different mitochondrial haplotypes capable of altering nDNA methylation patterns by S-adenosyl methionine regulation (Vivian et al., 2017).

Long Noncoding RNAs (lncRNAs) and Micro RNAs (miRNAs) have also been seen to have a role in signalling between the nucleus and mitochondria (Carden et al., 2017; Dong et al., 2017) with miRNAs also found to affect expression of mtDNA (Sadakierska-Chudy et al., 2014).

The role, mechanism and result of epigenetic modifications within neurological norm and neurodegenerative disease has been relatively well characterised (Berson et al., 2018; Ma et al., 2010; Riccio, 2010; van Heesbeen and Smidt, 2019), however mitochondrial epigenetic modification, or 'mitoepigenetics', has been less characterised.

Initially, it was believed that there was no epigenetic modification of mtDNA due to lack of histone structure (Ghosh et al., 2015; Iacobazzi et al., 2013), with mitochondrial CpG sites identified, but the role and possibility of mitochondrial methylation has been debated (Castegna et al., 2015; Manev et al., 2012; Matilainen et al., 2017; Sanchez et al., 2006; van der Wijst and Rots, 2015). TFAM, rather than histones, has since been shown to also have differential methylation patterns (Rebelo et al., 2009).

ROS modulation of mtDNA methylation has been shown to affect mtDNA expression and that oxidative stress increases the TFAM:mtDNA ratio, triggering nucleoids to a more compact state to prevent further mtDNA damage (Noack et al., 2006; Rebelo et al., 2009; Sadakierska-Chudy et al., 2014), but likely downregulating mtDNA expression.

Shock et al. (2011) identified that DNA Methyltransferase 1 (DNMT1) translocates to the mitochondria using an upstream start site of DNMT1 to allow for mitochondrial targeting; mtDNMT1 plays a regulatory role during oxidative stress (van der Wijst and Rots, 2015). Additionally, Chestnut et al. (2011) found DNA Methyltransferase 3 (DNMT3)-α in human brain and spinal cord and that enforced expression of DNMT3-α, but not DNMT1 induced apoptosis in motor neurons. Methylation patterns of mtDNA have been shown to be conserved between tissue types (Ghosh et al., 2014).

It has been suggested that mtDNA methylation is overestimated at CpG sites (Liu et al., 2016), however, mitochondria are of α-proteobacteria origin as opposed to the mammalian origin (Wallace and Fan, 2010); exclusively looking at CpG sites overlooks the presence of non-CpG methylation within the mitochondrial genome (Bellizzi et al., 2013).

Further, 5-Hydroxymethylcytosine (5hmC) 5-Methylcytosine (5mC) was found to affect nucleoid structure in mammalian mtDNA (Kukat et al., 2011) and H1, H2A, H2B,

H3 and H4 histone family members are found as integral mitochondrial membrane proteins which may form complex 'viaprotein-protein' interactions as they bind the D-loop (Choi et al., 2011).

More recently, Ghosh et al. (2014, 2015) identified variable methylation density in a region which encodes *MT-ND6*. In LHON, *MT-ND6* m.14484T>C mutations account for ~14% of patients and mitoepigenetics have now been reviewed for neurodegenerative disease, particularly for D-loop region methylation impairment (Coppedè and Stoccoro, 2019).

1.4 Visual Pathways

The retina (Figure 1.6) is a complex structure derived from the embryonic forebrain. It is capable of transmitting information about photons of light to the brain via the optic nerve where it may then be integrated and visually reconstructed as an image.

Light passes to the outer segment layer at the back of the eye where photosensitive rod and cone cells are located. The rod and cone cells are bordered by pigmented epithelia which contain melanosomes that also absorb photons to prevent light reflection back into the retina and supplement the rods and cones with nutrients (Nickla and Wallman, 2010; Strauss, 2005). Rod cells have a low resolution, however, they are capable of generating electrical impulses from a single photon of light. Cone cells are less sensitive but have a higher resolution and different forms of cone cells differentiate between photons of different electromagnetic wavelengths due to the variation in the photosensitive pigment between the cells - allowing for colour perception (Berg et al., 2002; Purves et al., 2001). The electrical impulses are then transmitted through the Outer Nuclear Layer (ONL) and into the Outer Plexiform Layer (OPL) where the rod and cone cells' synaptic terminal connects to horizontal or Bipolar Cells (BCs). Horizontal cells may connect to the BCs' dendrites or directly to the BCs in the Inner Nuclear Layer (INL), which are then responsible for transmission directly to Retinal Ganglion Cells (RGCs) in the Inner Plexiform Layer (IPL) or via INL amacrine cells.

In summary, to reach the RGCs, electrical signals from the Photoreceptors (PRs) are transmitted down the vertical (via BCs) or lateral (via horizontal cells to BCs then amacrine cells) pathways.

The RGCs are located in the Ganglion Cell Layer (GCL) but their dendrites extend into the IPL. Both the RGCs and BCs can be classified as either ON-centre or OFF-centre cells (Neumann et al., 2016; Pavlidis et al., 2006; Pickard and Sollars, 2012) with BCs also being organised by their level of stratification (as reviewed by Euler et al., 2014), where typically, the ON-centre stratify to the retina's distal IPL or OFF-centre if the dendrites extend only to the proximal IPL. ON-centre bipolar cells become more depolarised when PRs in the centre of the receptive field (as shown in Figure 1.7) are stimulated with light whereas this has the inverse response in OFF-centre cells; similarly in darkness OFF-centre cells are more depolarised whereas ON-centre hyperpolarise

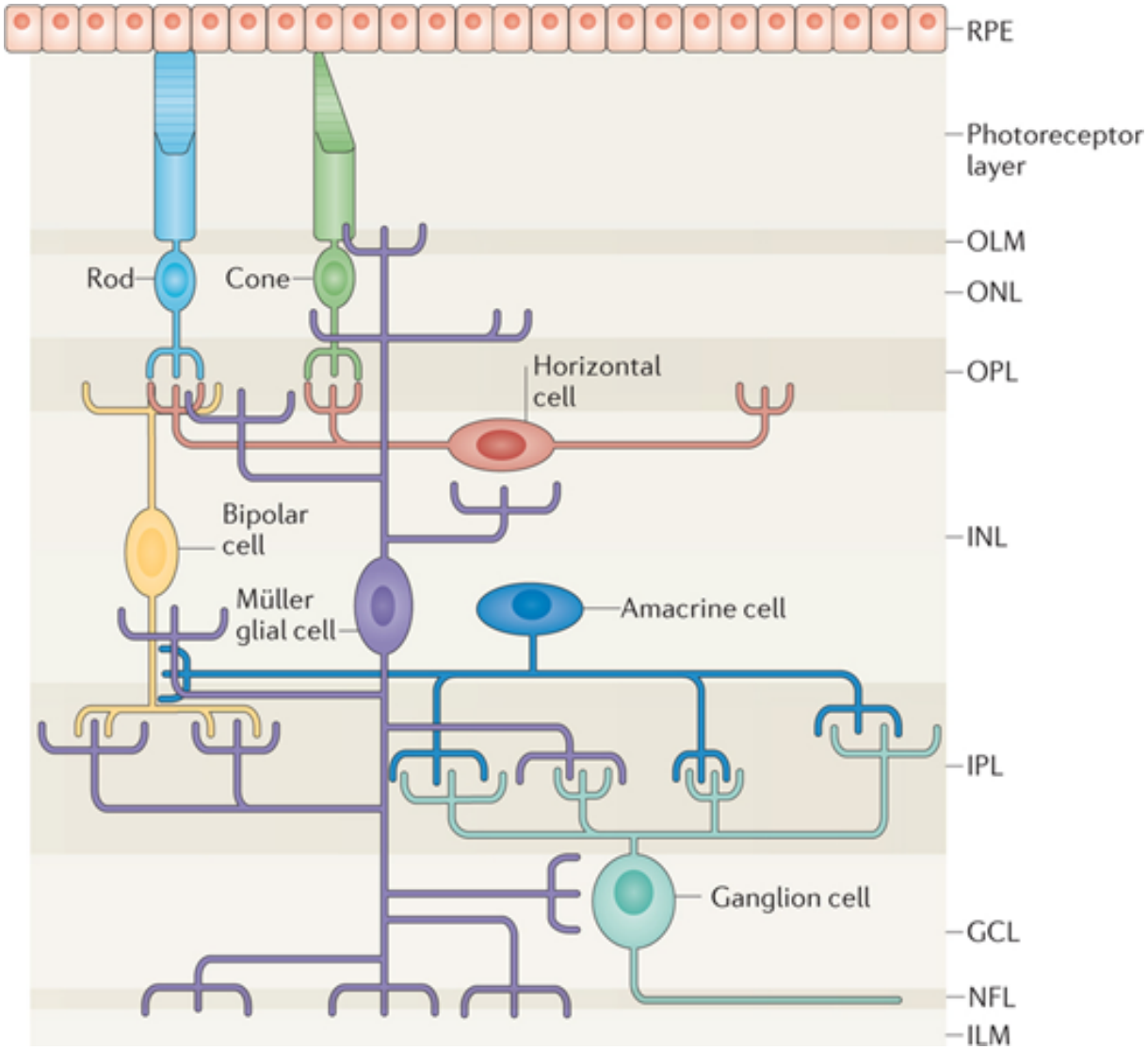

Figure 1.6: *Illustration of retinal organisation, showing RPE, the PR layer, the OLM, ONL, OPL, INL, IPL, GCL, NFL and ILM. Light approaches towards the bottom of the diagram, passing the cell layers until it reaches the photoreceptive layer where rod and cone cells detect it and initiate signal transduction towards the RGCs. Figure from Goldman (2014).*

(Neumann et al., 2016).

ON-centre BCs signal to ON-centre RGCs and OFF-centre BCs signal OFF-centre RGCs (Kolb and Marshak, 2003) with stimulated ON-centre RGCs increasing firing rate, however, OFF-centre cells work in the opposite way, as hyperpolarised BCs trigger fewer action potentials from OFF-centre RGCs. Both ON- and OFF-centre RGCs send more action potentials from greater graded potential signals from the bipolar cells. RGCs (and some amacrine cells) are the first retinal neurons to initiate action potentials rather than graded potentials (Field and Chichilnisky, 2007).

LHON arises from loss of RGCs - primarily those in the papillomacular bundle (Yu-Wai-Man et al., 2009). The papillomacular bundle is comprised of a range of different types of RGCs, namely: parasol RGCs (M-cells, Type A cells), midget RGCs (P-cells, Type B cells), small bistratified cells (Pavlidis et al., 2006), Intrinsically Photosensitive Retinal

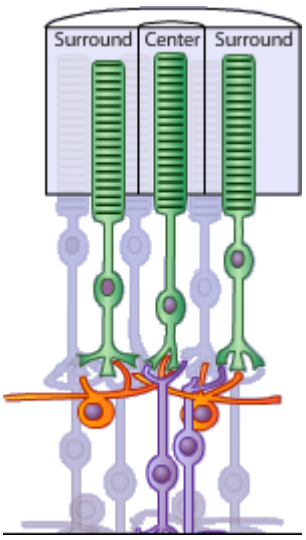

Figure 1.7: *Illustration of retinal cells, indicating ON- and OFF-centre BC cell types in green; ON-centre BCs are stimulated when light is detected by central PRs and inhibited when light is detected by the surrounding PRs. OFF-centre BCs work in the opposite way, where central light is inhibitory and surrounding light stimulatory. Figure from Watson and Breedlove (2012).*

Ganglion Cells (ipRGCs) and Melanopsin-containing RGCs (Pickard and Sollars, 2012) as shown in Figure 1.8.

RGCs cells are highly varied from species to species (Kolb et al., 1981; Masland, 2001), however, it is estimated that 10-20 morphologically different cell subtypes exist in humans.

The combination of phototransduction signalling between the photoreceptive cells to the RGCs allows for complex parallel processing of information which permits for the complex image of the visual field to be generated through the differing informational inputs from different points of the retina with the variation across the retina being considered a 'mosaic' due to the complex networking interactions and preferential relay of different information via particular cellular pathways (Rossi et al., 2011; Wassle, 2004). For example, an OFF-centre midget BC innervates a singular OFF-centre midget RGC - which are used to relay action potentials - whereas ON-centre midget RGCs are innervated by multiple ON-centre BCs, with an input of 9-12 photoreceptive cells being relayed to the ON-centre RGC (Kolb and Marshak, 2003).

The RGCs then extend to form the optic nerve, resulting in the 'blind spot' where it leaves the eye, and continues to the brain. Different RGC types innervate different regions of the brain with ipRGCs innervating a large range (Do and Yau, 2010). Parasol ganglion cells - which transmit non-opponent light responses - project to the parvocellular layers of the Lateral Geniculate Nucleus (LGN) and midget ganglion cells - which transmit colour and fine detail perception – project to the parvocellular layers of the LGN (Kolb and Marshak, 2003; Pavlidis et al., 2006).

The LGN receives information from both eyes as shown in Figure 1.9 with information in G1, G4 and G6 being contralateral and layers G2, G3 and G5 ipsilateral. Small

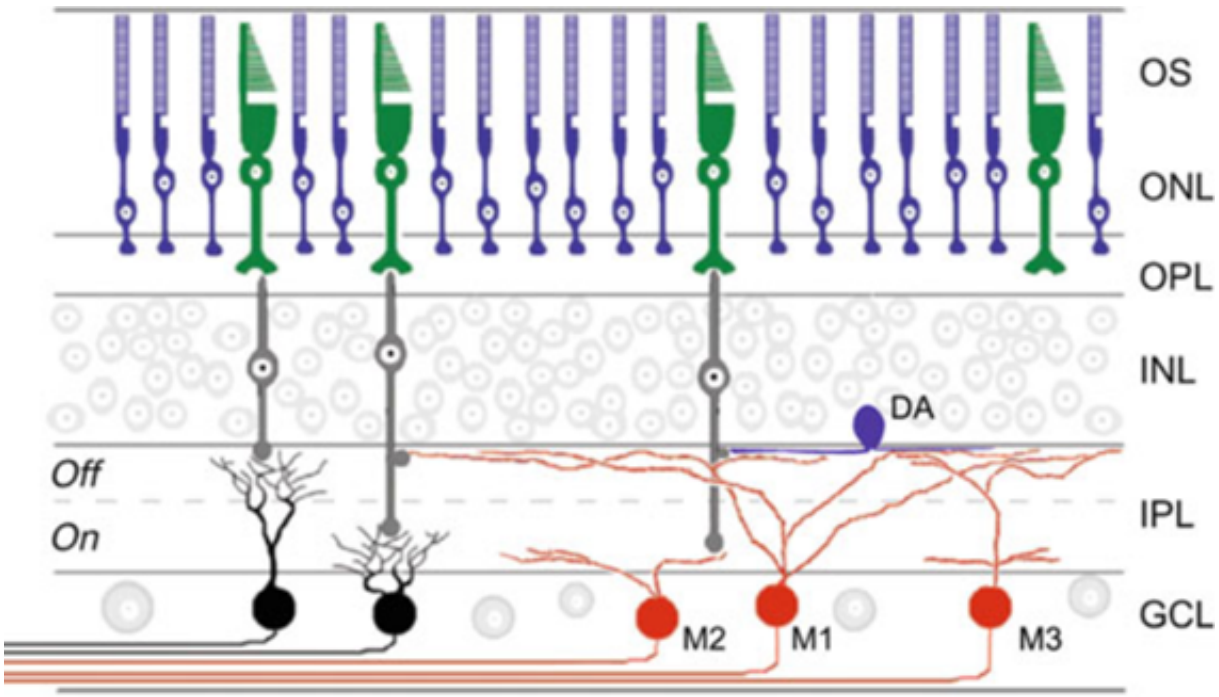

Figure 1.8: *Illustration of retina structure showing PRs in the outer segment layer (OS), and outer nuclear layer (ONL) with innervations to BCs in the outer plexiform layer (OPL). The BCs stretch across the INL where dopaminergic amacrine cells (DA) also receive bipolar input from the "off" IPL sublamina. Similarly, OFF-centre RGCs traditionally synapse in the "off" sublamina and ON-centre in the "on" sublamina with RGCs located in the ganglion cell layer (GCL) with variations of RGC species. BC innervation of RGCs is shown with black cells representing parasol, midget and small bistratisfied cells with three forms of ipRGCs shown in orange. Figure from Pickard and Sollars (2012).*

bistratified RGCs project to the koniocellular layers, in between the parvo- and magnocellular layers of the LGN (Kolb and Marshak, 2003; Pavlidis et al., 2006); collectively, the layers allow for parallel processing (Wassle, 2004) and most RGCs synapse with the parvocellular, magnocellular and koniocellular cells in the LGN (Xu et al., 2001).

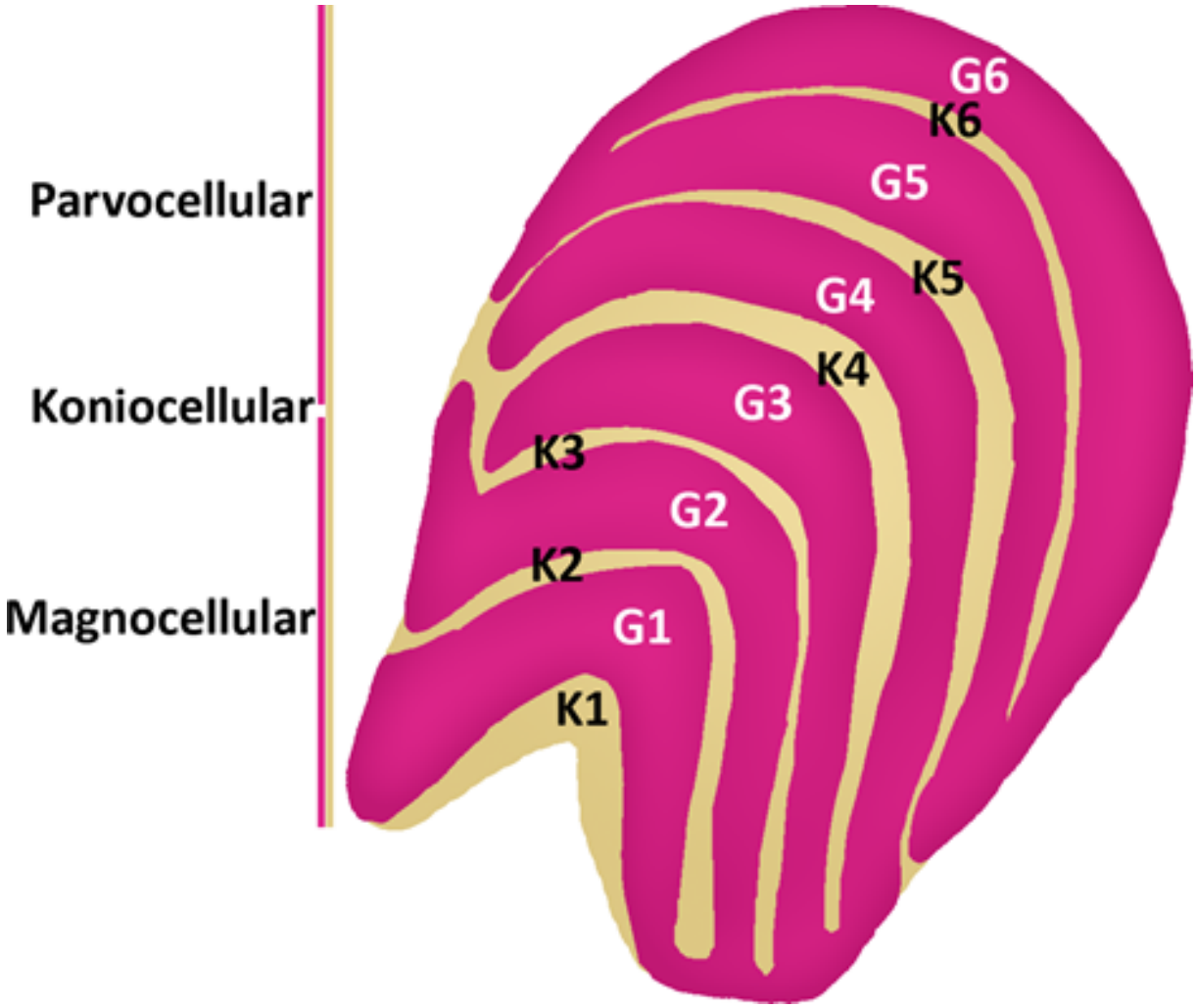

Figure 1.9: *Illustration of LGN, showing parvocellular, koniocellular and magnocellular layers. Layers K1-K6 are koniocellular which receive information from small bistratified RGCs. The G1 layer receives information from the contralateral eye and G2 ipsilateral with both in the magnocellular region, innervated by parasol cells. Layers G3, G4, G5 and G6 are parvocellular, innervated by parasol cells and alternate eye input with G3 and G5 ipsilateral but G4 and G6 contralateral.*

1.5 Leber Hereditary Optic Neuropathy

1.5.1 Phenotype

LHON is a rare genetic disorder which results in severe loss of visual acuity via unilateral degeneration of the optic nerve with bilateral degeneration occurring simultaneously or within 6-8 weeks in 75% of cases (Yu-Wai-Man et al., 2009).

Following from the first clinical report of a patient suffering LHON, by von Graefe (1858), the disease was then further characterised by its namesake, Theodore Leber, a German ophthalmologist who identified LHON in 16 families in 1871 (Leber, 1871).

Clinical Phenotype

Patients first experience painless visual clouding, and sometimes impaired colour perception, before the characteristic development of a central scotoma (defect of central fixation) or centrocaecal scotoma (defect of central fixation and area between the blind spot to fixation point) by loss of predominantly RGCs, as shown in Figure 1.10. This causes loss of central vision, with 25% of cases presenting simultaneous bilateral visual loss (Yu-Wai-Man et al., 2009) but 75% sequential with onset in a singular eye first before bilateral involvement, typically 1.8 months after the initial singular eye onset (Sadun and Kim, 2010). Visual acuity deteriorates within 4-6 weeks with vision typically settling at or below 20/200 (Sadun and Kim, 2010; Yu-Wai-Man et al., 2009) before full optic atrophy at six months (Sadun and Kim, 2010; Yu-Wai-Man et al., 2009).

Compared to other mitochondrial disorders, LHON is generally considered to have a very mild phenotype. Typical other mitochondrial diseases include MELAS and Leigh Syndrome, both of which are severe and the latter of which usually results in childhood death. In LHON, life quality rather than expectancy is generally more greatly affected, however, LHON has been seen to double mortality risk ratio through strokes and quadruple dementia risk alongside other conditions (Orssaud, 2018; Riordan-Eva et al., 1995). Rare cases of visual recovery have been reported, particularly associated with m.14484T>C mutations but most cases do not recover after visual loss (Oostra et al., 1994; Riordan-Eva et al., 1995).

Visual Pathophysiology

The complex mosaicism of the eye is necessary for colour and edge perception, however, in LHON, the loss of RGCs of the papillomacular bundle results in preferential removal of visual circuitry which is more common within the predominantly affected region, but other regions are less affected, and hence, different cell populations. This can account for why central vision and red-green colour perception are primarily affected (Yu-Wai-Man et al., 2009).

Red and green light is initially detected by M-cone and L-cone, respectively, which are named in accordance with their ability to detect medium (green) and long (red) wavelengths of light. Similarly, S-cones detect short wavelength blue light, however,

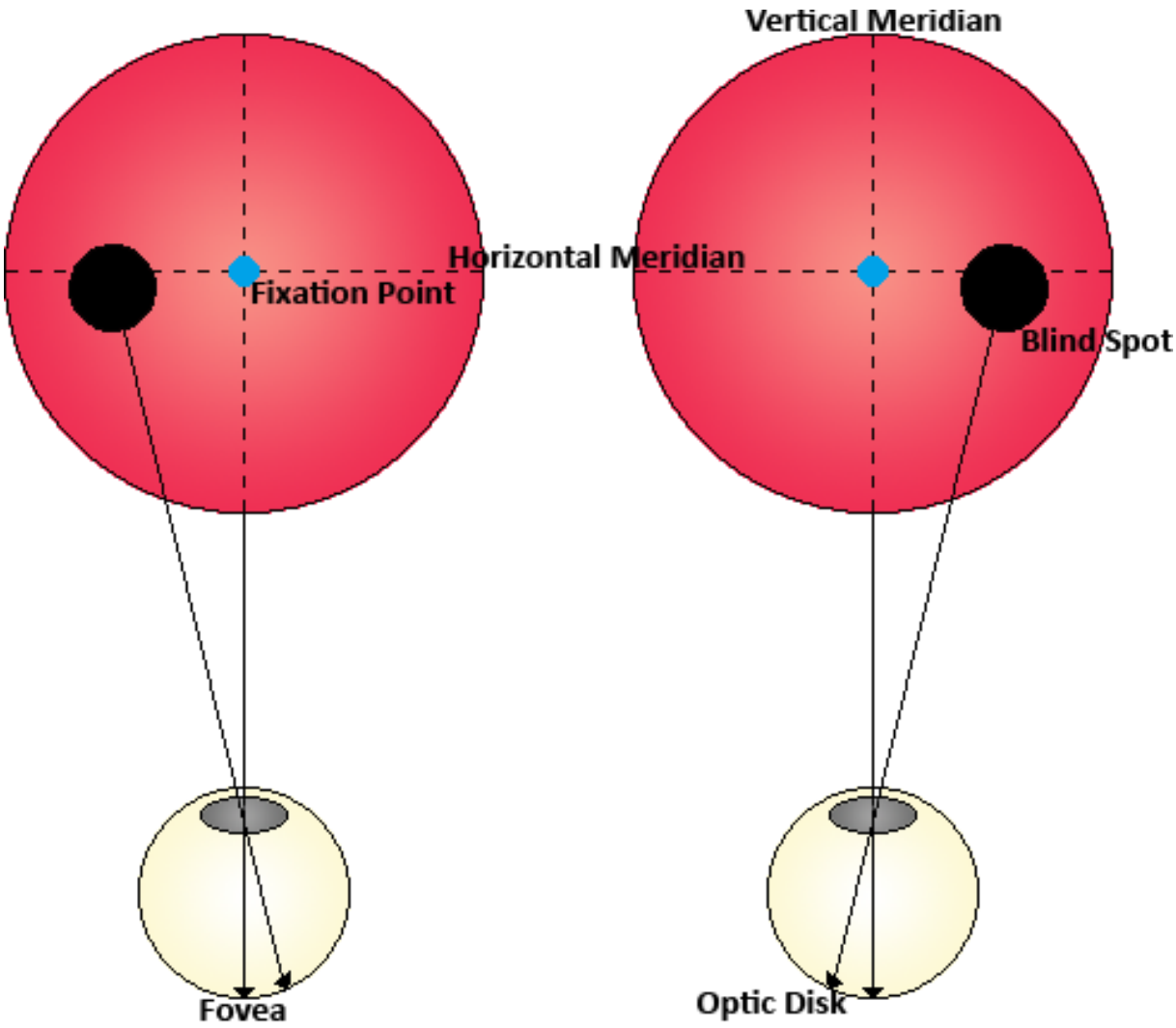

Figure 1.10: *llustration of retinal light input showing eyes' respective vision. In LHON, visual defects cause central scotomas where the vision of the fixation point deteriorates or centrocaecal scotoma where vision deteriorates from the fixation spot to the blind spot.*

the S-cone phototransduction pathway is lower resolution with few S-cones present in the foveal pit and unlike the midget pathways of M- and L-cones, it uses non-midget BCs connecting to a small bistratified blue/yellow RGC (Kolb and Marshak, 2003). In LHON, the S-cone pathway is normally unaffected by the disease (Sadun et al., 2000; Ventura et al., 2005).

Studies in the optic nerve have shown the depletion of the central optic nerve, where axons of midget RGCs are located (Sadun et al., 2000), which is in concordance with the loss of cells from the papillomacular bundle where midget cells are, again, primarily located (Pavlidis et al., 2006; Sadun et al., 2000). Midget RGCs vastly outnumber parasol RGCs within the central retina, with a 20-30 times prevalence (Dacey and Petersen, 1992; Pavlidis et al., 2006) and small bistratified cells and ipRGCs account for significantly less of the cell types in the whole of the GCL (Pavlidis et al., 2006; Pickard and Sollars, 2012). In LHON, midget cells are primarily affected, however, the direct mechanism which causes this is not yet determined.

RGCs are particularly susceptible to mitochondrial dysfunction due to their high metabolic demand (Ito and Di Polo, 2017) and as comparatively small cells, midget cells may be less capable of surviving metabolic distress with lower energy reserves. This smaller size also creates difficulty in mitochondrial transport and mitochondria are normally strategically distributed along the long axons in unmyelinated gap junctions (Carelli et al., 2004). Yang et al. (2020) found an increase of retrograde mitochondria and decrease of stationary mitochondria in affected axons alongside an increase of ROS in human Induced Pluripotent Stem Cells (iPSCs).

RGC cell lines have also been shown to produce superoxides at a rate of one fifth of brain mitochondria (Levin, 2007). This tighter control could indicate that they are particularly susceptible to oxidative stress which results in RGC death through apoptosis given the increased ROS production in LHON (Lin et al., 2012; Yang et al., 2020; Zhuo et al., 2012).

Variation of LHON Phenotype

There are some incidents of 'LHON Plus', or Harding's Disease, which is LHON with further multiple sclerosis-like comorbidity, including demyelination, tremors, epilepsy and dementia, amongst others (Carelli et al., 2001; Joshi and Kermode, 2019; Nikoskelainen et al., 1995). LHON Plus occurs more commonly in female LHON patients than male (2.1:1) and often presents with a longer interval time (1.66 years) from unilateral to bilateral onset (Pfeffer et al., 2013). Co-occurrence of multiple sclerosis and LHON mutations are likely by chance but the co-occurrence results in a phenotype which is painless but also more aggressive and irreversible (Pfeffer et al., 2013).

Another variant is 'Childhood LHON' where the patient typically develops LHON before age 12, which is half the median Age of Onset (AOO) (Chinnery, 2000; Majander et al., 2017). Childhood LHON disease development is quite different to classical LHON and is seen to have a better prognosis, however, sample size is limited and 1/5 patients remain legally blind (Barboni et al., 2006; Majander et al., 2017).

There are few cases of Childhood LHON' but some evidence has suggested that the more severe m.3460G>A mutation is more common (18%) within a cohort of hypothetical Childhood LHON cases (Barboni et al., 2006). Childhood LHON exhibits diffuse optic disc atrophy without microangiopathy in acute bilateral LHON but a variable degree of atrophy and microangiopathy in acute unilateral LHON (Barboni et al., 2006). Childhood LHON which exhibited a slowly progressive course had limited bilateral optic atrophy within the temporal sector of the optic disc and variable degree of microangiopathy (Barboni et al., 2006).

There are a few cases of concurrent LHON mutation inheritance (Cruz-Bermúdez et al., 2016; Howell et al., 2002; Kerrison et al., 1995; Mimaki et al., 2003), across a range of mtDNA mutations, including concurrent LHON associated mutations with another mtDNA mutation and multiple LHON associated mutations - both primary, and primary and rare variant combinations.

Case numbers are limited, and whilst phenotype has been seen to vary (Kerrison et al., 1995; Mimaki et al., 2003), this could arise concomitantly, given the variation in the mutations, rather than synergistically as a triple concomitant LHON mutation case showed no evidence of mutation synergistic effect on mitochondrial activity (Cruz-Bermúdez et al., 2016). It is possible for some mutations that LHON is an isolated disease and the LHON plus phenotype arises from inheritance of additional mutations which modify the phenotype into a compounded form of dual disease expression (Morgia et al., 2008; Pfeffer et al., 2013).

1.5.2 Epidemiology

LHON is the most common primary mitochondrial disorder (Chinnery and Turnbull, 2001), harbouring mutations in the mtDNA with prevalence depending upon region and haplogroup background, such as 3.22 per 100,000 in the North East of England (Yu-Wai-Man et al., 2003) and 2.06 per 100,000 in Finland (Puomila et al., 2007) with founder mutations contributing to population frequency of disease and disease causing variant (Macmillan et al., 2000a).

LHON is complicated by incomplete penetrance and a marked sex bias, with 50% of males harbouring a primary LHON mutation developing the disease but only 10% of females (Yu-Wai-Man et al., 2003). Median onset age is 24 years old (Chinnery, 2000), however, the age can vary greatly and carriers are generally considered at risk of developing LHON until over 50.

Globally, three primary mutations account for ~90% of LHON cases (Brown et al., 1997; Jurkute et al., 2019; Taylor et al., 2003; Yu-Wai-Man et al., 2003, 2014), namely m.11778G>A, m.3460G>A and m.14484T>C which respectively cause point mutations in *MT-ND4*, *MT-ND1* and *MT-ND6* genes (Gorman and Taylor, 2011; Yu-Wai-Man et al., 2003), all of which encode subunits of Complex I of the mitochondrial respiratory chain. These mutations may be found both in heteroplasmy and homoplasmy (Yu-Wai-Man et al., 2003).

Further mutations, such as m.10663T>C, which is associated with mitochondrial haplogroup J (Brown et al., 2002), can also cause LHON alongside the three more common variants. m.3460G>A is a phylogenetically older mutation, randomly distributed within haplogroups (Torroni et al., 1997). To date, as seen in Figure 1.1, MITOMAP lists 19 primary LHON mutations (Lott et al., 2013). This indicates that the mutations have been confirmed to be inherited in pedigrees of families, with multiple cases of LHON patients with the same mtDNA background.

While the majority of LHON mutations affect Complex I subunits, other genes affecting other molecules have also been implicated, such as *MT-CYB*, *MT-CO3*, and *MT-ATP6* (Yu-Wai-Man and Chinnery, 2000).

Table 1.1: *Top 19 LHON primary mutations, as according to MITOMAP (Lott et al., 2013).*

Mutation	Affected Subunit	AA Δ	AA Conservation	% Patients	Relatives' Penetrance %
m.11778G>A	ND4	R340H	100%	69%	33-60%
m.3460G>A	ND1	A52T	91%	13%	14-75%
m.14484T>C	ND6	M64V	31%	14%	27-80%
m.3376G>A	ND1	E24K	98%	Rare	NA
m.3635G>A	ND1	S110N	93%	Rare	29%
m.3697G>A	ND1	G131S	100%	Rare	NA
m.3700G>A	ND1	A112T	93%	Rare	NA
m.3733G>A	ND1	E143K	100%	Rare	24-30%
m.4171C>A	ND1	L289M	93%	Rare	46%
m.10197G>A	ND3	A47T	96%	Rare	NA
m.10663T>C	ND4L	V65A	89%	Rare	56%
m.13051G>A	ND5	G239S	98%	Rare	56%
m.13094T>C	ND5	V253A	100%	Rare	NA
m.14459G>A	ND6	A72V	89%	Rare	NA
m.14482C>A	ND6	M64I	31%	Rare	NA
m.14482C>G	ND6	M64I	31%	Rare	NA
m.14495A>G	ND6	L60S	100%	Rare	NA
m.14502T>C	ND6	I58V	78%	Rare	10%
m.14568C>T	ND6	G36S	87%	Rare	NA

1.5.3 Diagnosis

As a rare disease, LHON is often initially difficult to diagnose without known familial history, and a number of initial neuroimaging tests are frequently used to characterise the phenotype before specific genetic testing. This may include optic disc examination, visual field testing, an Electroretinography (ERG), or Magnetic Resonance Imaging (MRI) or Computerised Tomography (CTPR) scans (LHON Society, 2020; Traboulsi, 2012). An ERG measures retinal electrical responses and a CTPR scan can typically exclude other mechanisms of optic neuritis or optic nerve inflammation but an MRI can provide additional information (LHON Society, 2020; Traboulsi, 2012). In some cases, lumbar punctures or steroids may be ordered in cases of suspected central nervous system infection or optic neuritis respectively (LHON Society, 2020).

Following from suspected LHON diagnosis, a blood sample is usually collected and a targeted genetic test is typically performed. The Genetic Testing Registry presently lists 57 clinical tests for LHON at labs across the world (National Institutes of Health (NIH), 2020), however, more perform this test than those registered on this list. The majority of tests are either targeted variant analysis or coding region sequence analysis. The targeted analyses often only check for m.11778G>A, m.3460G>A and m.14484T>C mutations resulting in ~10% of LHON cases failing to be diagnosed through this method and requiring further diagnoses.

1.5.4 Susceptibility Factors and Disease Triggers

A broad range of susceptibility factors and disease triggers have been studied in LHON, however, cause of disease onset is still widely unknown.

Susceptibility factors relate to features which increase risk of disease onset in a susceptible person whilst disease triggers are features which directly cause disease (Yeatts et al., 2006). For example, a range of mutations and environmental factors have been investigated in LHON, this includes smoking, alcohol consumption and many others (Kirkman et al., 2009; Newman, 2009; Sadun et al., 2003) to account for variable penetrance, but these do not directly cause LHON. A LHON mutation makes a person greatly susceptible to LHON but it does not trigger disease onset, again, environmental influences affect the likelihood that a person with a genetic background for LHON will develop the disease, but they do not directly cause LHON. The susceptibility factors may indirectly trigger LHON disease onset by a presently unconfirmed trigger mechanism, such as oxidative stress, which results in the LHON phenotype of RGC cell death.

Genetics

As a primary mitochondrial disease, mitochondrial mutations are an obvious factor. Many investigations have also sought to find nDNA factors which affect LHON development as the majority of mitochondrial genes are located in the nucleus.

Alongside the 19 primary LHON mutations shown in Table 1.1, MITOMAP presently also recognises a further 18 secondary LHON mutations (Lott et al., 2013). Secondary mutations occur in individual patients within a LHON family with one of the primary mutations and they are hypothesised to be a causative factor in the likelihood for developing the disease. Secondary variants are defined as further genetic variants which affect genes encoding neither function nor production of the OXPHOS proteins or environmental factors (Niyazov et al., 2016); they can also be acquired instead of inherited (Niyazov et al., 2016) and are often mutations which affect mtDNA outside of the primary 19 LHON mutations.

There is some debate over whether secondary variants are pathogenic or not as further rare mutations have also been identified (Chalmers and Schapira, 1999; Chinnery et al., 2001; Fauser et al., 2002a; Howell et al., 1993; Johns and Berman, 1991) and additional testing is necessary to determine whether they are pathogenic or harmless polymorphisms which are observed by chance.

Extensive in-house studies have sought to identify novel LHON genetic variants which could predict disease onset or identify a causative pathway which is directly responsible, but both these and published data have yet to pinpoint a root genetic cause for why some carriers develop and others do not (Fauser et al., 2002b; Phasukkijwatana et al., 2010; Rosenberg et al., 2016; Vilkki et al., 1991).

Mitochondrial haplogroup is one factor which is capable of further modulating ex-

pression of disease. This results in further difficulty to discern the underlying genetic cause of LHON. Some 'pathogenic' variants only cause disease within certain mitochondrial genetic backgrounds, making it harder to attain sample numbers and power within the same haplogroups to identify why those variants act as modifiers (Ji et al., 2012; Strauss et al., 2013). B5a1, J1b and J2c haplogroup backgrounds have been shown to increase penetrance of the m.11778G>A and m.14484T>C LHON mutations (Carelli et al., 2006; Hudson et al., 2007; Kaewsutthi et al., 2011).

As stated in Section 1.1.2, mtDNA does not undergo recombination, and haplogroup refers to the clonal manner of mitochondrial inheritance. Rather than tracking recombination between generations, haplogroups describe the accumulation of various mutations through the matrilineal inheritance across populations (Elson et al., 2001; Soares et al., 2011). It has been suggested that non-pathogenic missense mtDNA polymorphisms can result in an accumulation of mutations which accumulate to create a sufficient mutational burden which triggers LHON (Caporali et al., 2018). Wei et al. (2017) hypothesise that older mtDNA haplogroups have naturally selected against these mutations, leading to different disease penetrances by haplogroup - or ethnogeographics - as these mutations are not necessarily non-pathogenic, as originally believed, and could directly accumulate to cause disease or interfere with mitochondrial-nuclear crosstalk (Chinnery and Gomez-Duran, 2018).

With the crosstalk between the nuclear and mitochondrial genome, it is possible that any modifier genes could occur on either nuclear or mitochondrial genome and these could directly affect the system, or act as a trans-acting variant which modifies a distant gene. Further, with environmental factors known to affect LHON onset, epigenetic modification of either genome could be causative in disease onset.

Mitochondrial copy number has also been identified as neuroprotective in LHON carriers, with LHON patients unable to implement the same neuroprotective mitochondrial biogenesis (Bianco et al., 2017, 2015, 2018), however, Finsterer and Zarrouk-Mahjoub (2018) challenged the study design and belief that mtDNA biogenesis is protective, rather than a result of the condition, alongside other points. Within LHON, no other research group has presently, independently proven that mitochondrial copy number is protective rather than as a result of LHON mutations. In broader mitochondrial defects, mtDNA copy number has further been shown to ameliorate pathogenic burden of mtDNA defects, such as Filograna et al. (2019), who found that elevated mtDNA copy number partially rescues cardiomyopathy and Complex IV (Cytochrome Oxidase) (COX) deficiency within a m.5024C>T + m.13715C>T heteroplasmic mouse.

Sex-Bias

As mentioned in Section 1.5.2, LHON predominantly affects males, with ~5x incidence rate when compared to the female disease incidence.

This has resulted in a number of theories for the bias, however, at present it is not

fully understood. Two main theories presently lead to explain this aspect to disease progression: X-linked modifier genes and hormonal disease suppression.

Many different X-linked genes have been identified and presented as a causative factor in disease onset, however, often a subsequent paper refutes the accuracy of the named variant (Chen and Denton, 1991; Hudson et al., 2005; Phasukkijwatana et al., 2010; Qu et al., 2010; Shankar et al., 2008; Vilkki et al., 1991).

It is possible that within alternate studies, their hypothetical gene is causative but that it is only relevant within the specific haplogroup backgrounds captured within that study and that it does not influence penetrance in other haplogroup backgrounds (Ji et al., 2012; Strauss et al., 2013).

The alternate theory is that oestrogen plays a neuroprotective role in LHON disease onset by doubling Mitochondrial Antioxidant Manganese Superoxide Dismutase (MnSOD) efficacy and as a result, minimising ROS activity (Pedram et al., 2006).

Estrogen Receptor β (ERB) is now being targeted for LHON treatment as it has been shown to increase mitochondrial copy number, prevent ROS production and improve cell viability (Pisano et al., 2015), therapy for this pathway is further reviewed in Section 1.5.5.

ROS has been shown to be a poor mediator of DNA damage, however, so it is possible that oestrogen is protective by other means (Brawn and Fridovich, 1981; Gammage and Frezza, 2019; Halliwell and Aruoma, 1991).

Age

Few LHON patients develop disease in childhood. When they do, this tends to be the childhood LHON form, with a different clinical progression (Barboni et al., 2006; Majander et al., 2017). The likelihood of developing LHON continues to increase with a median age onset of 24 (Chinnery, 2000), whereafter the odds ratio of development eventually reduces and plateaus around age 50 with 95% of those affected developing disease before this point (Yu-Wai-Man and Chinnery, 2000).

The body undergoes multiple different hormonal changes throughout life. In addition to this, genes are regularly switched on and off throughout different sections of life to adjust to demands of growth, systems repair and eventual senescence. There is a broad range of years whereby LHON onset is likely to occur, however, so it is difficult to associate it with any particular biological age response.

Smoking

Smoking has been seen to have a direct impact on LHON onset; Kirkman et al. (2009) found a penetrance of 93% in male smokers compared to male non-smokers' 66% penetrance; female smokers, however, were only affected with 33% penetrance (Kirkman et al., 2009). Further, visual acuity has been seen to decrease with smoking (Karanjia et al., 2014).

It has also been shown that smoking is a causative factor in LHON by depressing mtDNA copy number and oxidative phosphorylation, only compensated by efficient ROS detoxification (Giordano et al., 2015; Tsao et al., 1999). Further, smoking has been shown to induce epigenetic modifications (Breitling et al., 2011; Monick et al., 2012) which could be a further influence in disease development by nuclear-mitochondrial interactions, as described in Section 1.3.5.

Cigarette smoke is highly poisonous and genotoxic (DeMarini, 2004; Talhout et al., 2011). Some chemical compounds within it only affect local tissue, however, some, like nicotine, are absorbed where they can then be transmitted around the body and cause effects elsewhere.

Nicotine has been found to act both in a neuroprotective and neurotoxic manner, depending on the situation (Ferrea and Winterer, 2009; Ma et al., 2017). While isolated nicotine can be neuroprotective, there are hundreds of chemicals which could be concurrently absorbed and which could be responsible for the detrimental effect of smoking on LHON onset.

Alcohol Consumption

Alcohol is believed to possibly affect LHON disease onset, however, this trend was only seen with heavy alcohol intake (Kirkman et al., 2009). Morris and Votruba (2012) also reported a case where a male recovered 5 months after disease onset following lifestyle change where he quartered smoking intake and ceased alcohol intake from 60 weekly units.

While alcohol has been seen to increase likelihood of disease onset, it has also been associated with better visual acuity following disease onset (Karanjia et al., 2014).

1.5.5 Treatment Strategies

At present, there is no cure nor guaranteed prevention strategy for LHON and treatment options are both very limited and often expensive. Additionally, as time progresses from AOO, the potential for visual recovery becomes increasingly less viable. In England, treatments are limited to clinical trials and lack of options results in some patients choosing to self medicate through Internet purchases, based on experimental research.

These strategies are not always confirmed to be beneficial and could cause a number of complications; whilst one of the supplements, Idebenone, has shown improvements in patients (Klopstock et al., 2011), it does not guarantee that online purchases are of medical grade.

A number of different treatment options are in consideration, as well as lifestyle aids which help LHON patients manage their illness. As summarised in Table 1.2, ClinicalTrials.gov (National Institutes of Health, 2020) lists 19 interventional studies for LHON, of which 8 are complete, 3 are recruiting and 4 are presently active but not recruiting. The remaining 4 have been terminated, withdrawn or are of unknown

status. Presently ongoing clinical trials have also been described by Jurkute et al. (2019).

Table 1.2: *Summary table of active or complete interventional clinical trials on LHON from ClinicalTrials.gov (National Institutes of Health, 2020).*

Status	**Study**	**Treatment**
Completed	Safety and Efficacy Study of rAAV2-ND4 Treatment of Leber Hereditary Optic Neuropathy (LHON)	Drug: rAAV2-ND4
Active, not recruiting	Safety and Efficacy Study of Gene Therapy for The Treatment of Leber's Hereditary Optic Neuropathy	Drug: rAAV2-ND4
Completed	A Study Investigating the Safety, Tolerability, and Efficacy of Elamipretide (MTP-131) Topical Ophthalmic Solution for the Treatment of Leber's Hereditary Optic Neuropathy	Drug: Elamipretide (MTP-131) 1% topical ophthalmic solution
Recruiting	Safety Study of an Adeno-associated Virus Vector for Gene Therapy of Leber's Hereditary Optic Neuropathy	Drug: Injection of scAAV2-P1ND4v2
Active, not recruiting	Safety Evaluation of Gene Therapy in Leber Hereditary Optic Neuropathy (LHON) Patients	Genetic: GS010
Completed	Study to Assess Efficacy, Safety and Tolerability of Idebenone in the Treatment of Leber's Hereditary Optic Neuropathy (RHODOS)	Drug: Idebenone
Active, not recruiting	Efficacy & Safety Study of Bilateral IVT Injection of GS010 in LHON Subjects Due to the ND4 Mutation for up to 1 Year	Genetic: GS010
Active, not recruiting	Study to Assess the Efficacy and Safety of Raxone in LHON Patients	Drug: Idebenone
Completed	A Randomized, Double-blind, Placebo-controlled Trial of Curcumin in Leber's Hereditary Optic Neuropathy (LHON)	Drug: Curcumin
Recruiting	New Non-invasive Modalities for Assessing Retinal Structure and Function	Device: LSFG-NAVI
Recruiting	Stem Cell Ophthalmology Treatment Study II	Procedure: Arm
Completed	Efficacy Study of GS010 for Treatment of Vision Loss From 7 Months to 1 Year From Onset in LHON Due to the ND4 Mutation (REVERSE)	Biological: GS010
Completed	Efficacy Study of GS010 for the Treatment of Vision Loss up to 6 Months From Onset in LHON Due to the ND4 Mutation	Biological: GS010
Completed	Safety Study of a Single IVT Injection of QPI-1007 in Chronic Optic Nerve Atrophy and Recent Onset NAION Patients	Drug: QPI-1007 at various doses
Completed	Open-Label, Dose-Escalating Study Assessing Safety, Tolerability, Efficacy, of RP103 in Mitochondrial Disease	Drug: Cysteamine Bitartrate

Antioxidants

Idebenone (Raxone/Catena) is an antioxidant which inhibits lipid peroxidation and facilitates electron flux to bypass Complex I (Klopstock et al., 2011). It is a short-chain analogue of CoQ10 which works in the same manner but is more bioavailable in neurological tissue and mitochondria due to the structural modification (Jurkute et al., 2019). It has been used in a number of trials (Cortelli et al., 1997; Klopstock et al., 2011; Yu-Wai-Man et al., 2013) and does appear to improve visual acuity, however, application is limited and it is possible that it ameliorates Complex I dysfunction in some RGC species but the midget cells do not recover (Klopstock et al., 2011). Some RGCs could potentially be functionally suppressed but respond favourably to treatment if treated quickly (Jurkute et al., 2019).

Idebenone has been approved in the European Union under "exceptional circumstances" under "orphan designation" from Santhera Pharmaceuticals GmbH (Deutschland) (European Medicines Agency, 2015) and it is available in Scotland to LHON patients who do not yet meet the UK criteria to be registered as severely sight impaired (Scottish Medicines Consortium, 2017).

While the response to Idebenone has been variable, such as only specific cell lines responding to treatments (Yu-Wai-Man et al., 2017), and NHS England not offering Idebenone as a treatment to LHON, Idebenone is safe and well tolerated with original treatments of 270 mg·day^{-1} (Carelli et al., 2011) and rising up to 900 mg·day-1 in later studies which indicate that Idebenone has a favourable clinical outcome in LHON treatment (Llòria et al., 2017; Lyseng-Williamson, 2016; Zhao et al., 2020). The RHODOS clinical trial did not find an improvement in visual acuity recovery (Klopstock et al., 2011) but *post hoc* and follow up analysis found an improvement in best visual acuity (Klopstock et al., 2013, 2011). Further studies also found an improvement in visual acuity, field and evoked potential (Lyseng-Williamson, 2016; Pemp et al., 2019; Zhao et al., 2020) alongside increased clinically relevant recovery in both recent and chronic LHON (Carelli et al., 2011; Lyseng-Williamson, 2016; Pemp et al., 2019).

In addition to this, EPI-743, a para-benzoquinone therapeutic related to Vitamin E, has been shown to have a clinically favourable response (Sadun et al., 2012).

Minocycline has been used as a neuroprotective agent which blocks mPTP formation and acts as an antioxidant (Haroon et al., 2007). MTP-131 increases OXPHOS efficiency and reduces ROS generation (Koopman et al., 2016) and it is presently undergoing phase 2 clinical trials as Ocuvia™ (Stealth BioTherapeutics Inc., 2019); it has also been seen to associate with cardiolipin, a molecule known for stabilising Complexes III and IV, and binding Cytc (Kalkavan and Green, 2017; Sabbah et al., 2016; Schenkel and Bakovic, 2014).

Hormonal Treatments

Recent treatments have looked at targeting ERB to reduce apoptosis, induce mitochondrial biogenesis and reduce ROS in LHON (Giordano et al., 2011; Pisano et al., 2015). They suggest that the hormonal dimorphism between sexes could factor into the reduced penetrance in females, further implicating ERB as a beneficial target.

No present clinical trials involve treating with oestrogen to target the ERB, however, it is being considered as a mechanism in preventing onset (Giordano et al., 2011; Pisano et al., 2015). There are concerns in treating with oestrogen given the number of side effects of hormonal treatments, however, both oestrogens and androgens have been investigated in therapy across a range of mitochondrial diseases (Mohajeri et al., 2019).

G protein-coupled oestrogen receptor has also been seen to act in a neuroprotective manner against Complex I neuronal insult (Yuan et al., 2019) and crosstalk between both G protein-coupled estrogen receptors and ERB and Estrogen Receptor α (ERA) has been observed (Romano and Gorelick, 2018). This research is still at an early stage but could lead to a promising treatment.

Mitochondrial Biogenesis

Mitochondrial biogenesis has been implicated with hormonal treatments as the attributing factor for why ERB treatment has been particularly effective (Giordano et al., 2011; Pisano et al., 2015).

In addition to this, cigarette smoke, a known causative factor of LHON onset, discussed in Section 1.5.4, has been shown to depress mtDNA copy number within patient fibroblasts (Giordano et al., 2015), indicating that smoking could increase LHON onset likelihood by reducing mitochondrial biogenesis.

Some contention has been raised towards these studies by Finsterer (2017), with Yen et al. (2002) finding that all LHON carriers' copy number is increased when compared to wild type controls. This contradiction between the results questions whether mitochondrial biogenesis is truly neuroprotective, or rather, a result of LHON development and at best a potential biomarker of disease onset which arises as a result of carrying a LHON mutation.

Improved mitophagy also appears to improve cell survival by reducing mutant mtDNA burden in cybrid cell lines (Sharma et al., 2018). Ketogenic treatment has also been shown to reduce mutant mtDNA burden in cybrid heteroplasmic cell lines whilst upregulating mitochondrial copy level in homoplasmic cell lines (Emperador et al., 2019).

Gene Therapy

Gene therapy by Recombinant Adeno-Associated Virus 2 (rAAV2) allotopic expression of *MT-ND4* has been trialled with LHON patients (Wan et al., 2016), showing some improvement in visual acuity and field but no improvement to the GCL.

GenSight have also performed rAAV2 allotopic expression of *MT-ND4*, called GS010 (GenSight Biologics, 2019). Week 48 of the RESCUE Phase III had no difference compared to the sham placebo in the temporal retinal nerve fiber layer, papillomacular bundle thickness or ganglion cell volume. Week 96 REVERSE Phase III clinical trials similarly show no statistical significance in the effect of GS010 in visual acuity or contrast sensitivity, however, there is a clinically relevant improvement and treatment was well tolerated (Bouquet et al., 2019).

Other studies of rAAV2 allotopic expression have generally found treatment to be safe in humans (Guy et al., 2017; Vignal et al., 2018) but no trial has been marked as statistically successful yet - possibly due to small sample sizes - as clinical improvement has been identified across multiple studies (Zhang et al., 2018).

Stem Cells

Conversion of patients' cells to iPSCs and reprogramming to RGCs before editing the mtDNA and transplanting back to the patient has also been strategised (Kim et al., 2018; Wong et al., 2017). There are a number of difficulties with this method at present, particularly with reprogramming and transplantation, however there has been some success in retinal disease with iPSC treatment. Mandai et al. (2017) used autologous iPSCs to transplant new RPE cells to a neovascular age-related macular degeneration patient and the same team also treated another patient with age-related macular degeneration with cells from an anonymous donor (Cyranoski, 2017). Another Japanese group have also recently announced iPSCs transplant to treat corneal epithelial stem cell deficiency, with the patient showing improvement without problems (The Japan Times, 2019).

There are still concerns on the safety of iPSC treatment (Singh et al., 2019) but despite this, it is seen as a positive development in therapeutic treatments, with a number of studies looking at iPSC treatments across a range of optic neuropathies (Maeda et al., 2019).

Wong et al. (2017) has suggested Clustered Regularly Interspaced Short Palindromic Repeats (CRISPR) reprogramming of iPSCs, however, despite the increasing popularity of the gene editing tool, it is probably not a good strategy for treating LHON. Given the difficulties of targeting CRISPR to mtDNA, treatments should instead focus on Transcription Activator-Like Effector Nucleases (TALENs) and Zinc-Finger Nucleases (ZFNs) (Gammage et al., 2018a).

Mitochondrial Donation

While mitochondrial donation will not cure any LHON patients, it could prevent the transmission of LHON mutations through the maternal lineage.

The UK became the first country in the world to legalise mitochondrial donation/mitochondrial replacement therapy in 2015 (United Kingdom Houses of Parlia-

ment, 2015) with countries, such as Singapore, also looking to legalise this option (Singapore Bioethics Advisory Committee, 2018). The response in some other countries, like the Republic of Ireland, have been less favourable, with the Republic of Ireland proposing a bill to expressly prohibit all forms of mitochondrial replacement (An Roinn Sláinte Department of Health, 2017).

Three methods of mitochondrial donation persently exist: pronuclear transfer, maternal spindle transfer and polar body transfer with the former two methods legalised in the UK (Craven et al., 2010; Tachibana et al., 2009; Wang et al., 2014).

The technique varies but the end effect is that the nDNA comes from two parents whilst the mtDNA comes from a third donor parent who does not carry mtDNA disease.

There have been successes with mitochondrial donation (Zhang et al., 2017), however, as it is a new technique, long-term risk has not been ascertained.

Lifestyle Aids & Assistive Technology

Whilst a cane or Braille has classically been used to support the visually impaired, newer technology aims to specifically support LHON patients.

Specialised computer software, such as JAWS or ZoomText act as screen readers or magnifiers (Freedom Scientific Inc, 2019a,b) which can support LHON patients. Modern mobile features, such as Apple's Voiceover and Android's Talkback allow people to interact with their phones despite being visually impaired.

Both classical magnifying glasses and CCTV magnifiers (CCTV camera recording projecting a magnification onto a new screen) can be beneficial, whilst some specialised assistive eyewear, namely NuEyes and eSight, aim to directly use LHON patients' remaining peripheral vision to see and translate text to speech (eSight Corp, 2019; NuEyes, 2019).

A lot of the specialised technology is extremely expensive, however, and the cost of buying lifestyle aids and assistive technology adds to the cost burden that comes with loss of eyesight and abilities that LHON causes.

1.6 Project Aims

Given the limited success in treatment options with LHON, this project has identified three target investigation routes to develop a greater understanding of LHON genetic risk factors and disease mechanisms in mitochondrial optic neuropathies.

Firstly, this project seeks to improve our estimates of disease penetrance and investigate other novel genetic and epigenetic modifiers which could contribute to disease onset. Chapter 2, 'LHON Disease Penetrance', recalculates disease penetrance in a large, modern cohort and investigates the statistical probability of an X-linked modifier gene being involved in LHON disease onset. It also seeks novel nDNA variants which modulate disease penetrance through both genetic and epigenetic molecular investigation.

Secondly, this project seeks to characterise specific LHON patient fibroblast cell lines of the three most common mtDNA mutations, m.11778G>A, m.14484T>C or m.3460G>A, to directly investigate cellular processes which could act as a LHON trigger mechanism. In addition to this, as retinal tissue is not available from patients, accurate characterisation of cell lines could allow for future work to determine whether affected biological pathways improve as a result to drug treatment. Chapter 3, 'Functional Characterisation of LHON Fibroblasts', evaluates mtDNA copy number, ATP production, cellular oxygen consumption, calcium homeostasis, mitochondrial membrane potential and mitochondrial network structure and interactions with the ER in isolated tests to gauge whether these pathways affect LHON expression and whether fibroblast cell lines exhibit quantifiable differences in cases to controls.

Thirdly, given the limitations of cell work, this project finally seeks to develop a technical framework to evaluate retinal degeneration in a m.5024C>T + m.13715C>T mutation mouse model. This holistic approach will allow for evaluation of retinal degeneration both at a systems level and specifically within the affected tissue type. It opens future options for drug testing and application of the methodology in specific LHON mouse models. Chapter 4, 'Retinal Characterisation of Mitochondrial Disease Mouse', investigates mitochondrial heteroplasmy level across the mouse, and characterises cellular organisation in both sections and whole mounts of retinal tissue.

Overall, we hope to identify genetic variants which influence LHON expression, improve our understanding of the disease process and develop methods which would allow for drug evaluation.

Chapter 2 | LHON Disease Penetrance

2.1 Introduction

As present disease onset is not accurately predictable, this chapter seeks to further characterise disease penetrance to ascertain any predictor variable which could aid in diagnostics. There is a discrepancy between known genetic aetiology and phenotype development. As such, there are likely currently unknown genetic links and disease risk factors which have yet to be characterised.

LHON results in a diminishing life quality and awareness of relative disease risk allows for informed decision processes regarding reproductive choices and life-planning, such as preparing career options which do not require great visual acuity. Additionally, our lack of understanding in disease onset raises difficulties in strategising options for both potential gene therapy treatments and drug design.

As discussed in Section 1.5.4, a number of factors influence disease onset. Whilst ~90% of LHON cases carry m.11778G>A, m.14484T>C or m.3460G>A mutations (Yu-Wai-Man and Chinnery, 2011), this is not a guarantee of disease and a number of other factors influence disease onset but both the factors and the effect size of each is presently undetermined.

As further described in Section 1.5.4, mitochondrial haplogroup, and accumulation of non-pathogenic missense mtDNA mutations which could accumulate to trigger LHON disease onset or interfere with mitochondrial-nuclear crosstalk (Chinnery and Gomez-Duran, 2018), affect LHON penetrance. These known factors contribute to penetrance, but at present, they do not fully explain disease onset and this chapter investigates novel genetic mechanisms which could further influence it.

More than 99% of the mitochondrially associated actions are encoded in the nDNA (Kühlbrandt, 2015), as such, it is likely that nuclear background further modulates any additive model for disease penetrance. In ethnically homogeneous populations, it can be assumed that the nuclear and mitochondrial background evolved together and that they are optimised to work most efficiently in conjunction; in cases of admixture, the mtDNA background will only match the nDNA background from one parent and will not have evolved to work so efficiently with the nuclear background of the other parent. The impact of this mismatch depends on several factors: the distance between the co-evolution and whether the mtDNA is aligned with the dominant nDNA alleles which the mtDNA co-evolved with, if genetically distant alleles are dominant in nDNA

encoding, and whether the proteins of the nuclear-encoded mitochondrial respiratory chain work effectively with the mitochondrially-encoded proteins. Nuclear-mtDNA mismatch has been confirmed to increase disease risk (Crawford et al., 2018; Gaweda-Walerych and Zekanowski, 2013; Rishishwar and Jordan, 2017; Zaidi and Makova, 2019) with nuclear-mtDNA background matching considered as a factor in mitochondrial replacement therapy (Rishishwar and Jordan, 2017).

This further indicates that nuclear variants can alter disease expression in primary mitochondrial disease. As such, bioinformatics tools are used to evaluate potential candidate nuclear variants which influence LHON penetrance, both within families to ascertain whether nuclear background affects penetrance and for the statistical probability that an X-linked modifier gene can affect LHON expression.

Additionally, nuclear genes are investigated for differences between LHON patients and unaffected carriers for both sequence-level and also epigenetic modifications, given that age, sex, and environmental factors influence LHON expression, as described in Section 1.5.4. Cases of LHON without an obvious primary mitochondrial disease have also been discovered, questioning whether LHON can also arise solely from a nuclear disease background (Abu-Amero et al., 2005).

At present, there has been limited success in identifying nuclear modifier genes in LHON and whilst epigenetic modifications are known to have a causative role in complex mitochondrial disease (Wallace and Fan, 2010), there has been no systematic study of the role of epigenetics in LHON. Epigenetic factors have been identified and investigated in patients, however, sequence methylation and nuclear epigenetic modifications have not been directly investigated within LHON. This chapter seeks to determine further genetic modifiers to explain some of the missing heritability of LHON. This includes exome analysis and nuclear methylation investigation. Given the disease penetrance differences between male and female LHON primary mutation carriers and also genome-wide variation between male and female methylation values (Singmann et al., 2015), methylation patterns were to be specifically investigated as a potential cause of disease onset. In addition, this chapter aims to calculate statistical probabilities for a modifier gene being X-linked and to also update penetrance measurements in a large, modern cohort LHON for differences in penetrance by primary mutation or country of origin.

2.2 METHODOLOGY

2.2.1 Familial Disease Penetrance

Multiple generations of family pedigrees were collected from 82 families as shown in Table 2.1. Pedigrees ranged from 1-5 generations with 1-34 mothers within the full pedigree. All offspring below the age of 30 (6 years after median AOO (Chinnery, 2000)) were excluded to minimise likelihood of misassignment of disease status by asymptomatic carriers developing at a later age. Within another dataset consisting of 133 Italian and 111 British affected LHON patients, 73.77% of affected LHON patients develop by age 30; counts are shown in Figure S1. Whilst thresholding later would prevent erroneous LHON disease status classification, the majority of LHON cases have developed by age 30 and raising the threshold further would remove many pedigrees from the study.

Disease penetrance was then calculated for male and female offspring, after stratifying the mothers as affected or unaffected (asymptomatic) carriers. This project was undertaken in collaboration with Professor Valerio Carelli (University of Bologna) who previously identified that disease penetrance in offspring is greater in children of affected mothers than unaffected mothers (data unpublished).

This was further segmented by LHON causative mutation and the country in which the family resided.

Table 2.1: *Table of the cohort analysed for differential offspring penetrance, showing the 1001 offspring from all mothers then stratifying by mother's disease status.*

	Offspring	**Male**	**Female**
All Mothers	Affected	219	103
	Unaffected	266	413
Affected Mothers	Affected	65	30
	Unaffected	43	52
Unaffected Mothers	Affected	154	73
	Unaffected	223	361

2.2.2 X-Linked Modifier Gene

Following from the pedigrees collected to measure LHON disease penetrance in Section 2.2.1, statistical analyses were replicated based on the work by Bu and Rotter (1991) to determine the validity of a two locus causative model and feasibility of an X-linked modifier gene accounting for part of the variability in disease penetrance.

The dataset is limited to the maternal line as offspring will share mtDNA lineage and the disease penetrance reflects segregation of nDNA locus, reducing dimension of the model from two loci (nDNA + mtDNA) down to one (nDNA).

The Bu and Rotter (1991) methodology has two hypotheses: the X-linked hypothesis and the X-inactivated hypothesis. A Haldane correction was not applied as Burton et al. (2000) found that ascertainment bias adjustments with heterogeneity often results in biased parameter estimates which do not match those in the sample or original population. Due to the advances of computational power, exact p-values were calculated and Fisher's exact test was replaced by ANOVA analysis of deviance for evaluation of heterogeneity.

The X-linked hypothesis restricts mothers in the pedigrees to those which are obligate heterozygotes and calculates an X-linked goodness-of-fit test for male offspring and assumes a binomial distribution of inheritance for the affected X chromosome from the mother to her son, giving a segregation ratio, T, of 0.5. This is then tested in pooled sibships through Chi-Squared testing and individual male sibships through the expected offspring formula, Equation 2.1.

$$E_s(x) = \sum_{r=1}^{s} \frac{r(\frac{s}{r})(\frac{1}{2})^s}{1-(\frac{1}{2})^s} \tag{2.1}$$

The X-Inactivation hypothesis also limits the pedigrees to obligate heterozygous mothers and calculates T, the segregation ratio; q, the population frequency of an allele and K, the probability of a heterozygous female being affected (penetrance). It then calculates the proportion of affected, female LHON patients who develop LHON due to X-inactivation and those who are homozygous for the mutant allele on both X chromosomes.

2.2.3 Nuclear DNA Variants

A cohort of 30 patients were chosen for nDNA methylation analysis, as shown in Table 2.2. The nDNA methylation cohort covered 4 families and a total of 30 LHON family members. 16 carried m.11778G>A mutations, 3 m.14484T>C and 11 m.3460G>A. 9 of the 30 members were unaffected carriers.

Whole blood was collected and DNA was extracted and bisulphite converted by Doctor Hannah Elliot (University of Bristol, formerly, Newcastle University), who sent samples to Illumina (Illumina, Inc., San Diego), where samples were loaded onto an Illumina Infinium HumanMethylation27 BeadChip microplate for amplification, fragmentation, precipitation and resuspension. Samples were then transferred to an array for hybridisation and Xstaining before loading into an Illumina scanner and imaging.

Data was returned as .idat files and decrypted in Illumina® GenomeStudio 2011 + v1.9.0 Methylation module before exporting to R version 3.3.2 (2016-10-31), Platform: x86_64-w64-mingw32/x64 (64-bit), Running under: Windows 7 x64 (build 7601) via methylumi_2.20.0.

Two samples which failed on the chip (F1B_3460_M_U_38 and F1C_3460_M_A_38) were excluded. A detection threshold of p=0.01 and a minimum of 3 beads per probe

were then set to remove low quality probes and poorly covered genes before quantile normalisation (rescales distribution of pooled intensities of methylated and unmethylated probes to be identical). Normalised methylation beta methylated and unmethylated values were then used to calculate methylation M-values (log2 ratio of methylated and unmethylated probe intensity), indicating whether or not a gene was methylated at the probe position. Beta-values are prone to severe heteroscedasticity in the high and low methylation range making it inappropriate for statistical analysis; the M-value is more homoscedastic and thus suitable for subsequent analysis (Du et al., 2010).

limma_3.30.2 (Ritchie et al., 2015) performed 80 combinations of covariates (Status + Gender + Age + Mutation + Batch + Never Smoked + CPD) in a linear regression across the full data set - using 20/28 samples which contained metadata for Never Smoked and CPD (this excludes all children who are legally too young to smoke). Data was then stratified into females and affected patients only and running 32 combinations on the females then another 40 combinations (Gender + Age + Mutation + Batch + Never Smoked + CPD) on the affected patients.

Significant genes were grouped from the full data set and females with a non-adjusted p-value <0.05 which occur in >95% of tests to identify hyper- and hypomethylated genes.

Genes were further cross-matched against in-house exome sequencing data. 25 affected patients and 3 unaffected carriers described in Table 2.3 had whole blood samples taken and DNA extracted. Exome data was captured using Nextera Rapid Exome Capture 37Mb and Illumina TruSeq 62Mb. 17,403 genes 62Mb were captured by probes and samples were sequenced on an Illumina HiSeq2000. BWA (v0.7.10) (Li and Durbin, 2009) aligned paired-end reads to Human Reference Genome, GRCh38 (Schneider et al., 2016) with Ensembl gene annotations. Samtools (v.01.18) (Li et al., 2009) compressed and generated indexes for the alignments and Picard (v1.85) (Broad Institute, 2016) removed duplicate reads. Variants were detected by Varscan (v2.3.8) (Koboldt et al., 2012) and annotated by ANNOVAR (v529) (Li and Wang, 2017).

Exome data was cleaned by removal of probes which failed exome sequencing and given the number of variants across any site, dominant and recessive models were performed against the exome dataset to identify differential variants between LHON patients and carriers. These were then cross-matched against the list of hyper- and hypomethylated genes to identify genes which contained both differential methylation and exome variants.

Genes were analysed through Gene Set Enrichment Analysis (GSEA) with cross-matched genes against Molecular Signatures Database (MSigDB) gene sets (Mootha et al., 2003; Subramanian et al., 2005) to calculate overlap against MSigDB's C2 curated gene sets of chemical and genetic perturbations and MSigDB's C5 GO gene sets of biological processes; gene sets larger than 500 and smaller than 15 were excluded.

The full cross-matched gene list of exome variants and LHON hyper- and hy-

pomethylated genes then underwent PANTHER 14.1 Overrepresentation Test (Released 20190711) (Mi et al., 2018; Mi and Thomas, 2009) against GO gene sets of biological processes by Fisher's Exact Test, restricting to False Discovery Rate (FDR) $p < 0.05$.

Table 2.2: *Samples in nDNA methylation arrays; gender indicating if male (M) or female (F), status indicating whether they are affected (A) or unaffected carriers (U (C)). CPD indicates Cigarettes Per Day, current.*

Sample	UNIQUE_ID	ARRAY_ID	Age	Gender	Family	LHON Mutation	Status	Current Smoker	Never Smoked	Age Started	CPD	AOO	Smoker Before AOO
1	F1A_3460_F_A_38	A38_A	61	F	1	m.3460G>A	A	NA	NA	NA	NA	12	NA
2	F1B_3460_M_U_38	A38_B	42	M	1	m.3460G>A	U (C)	NA	NA	NA	NA	NA	NA
3	F1C_3460_M_A_38	A38_C	39	M	1	m.3460G>A	A	Yes	No	16	35	6	No
4	F1D_3460_F_A_38	A38_D	37	F	1	m.3460G>A	A	Yes	No	14	40	20	Yes
5	F1E_3460_F_A_38	A38_E	40	F	1	m.3460G>A	A	Yes	No	14	20	7	No
6	F1F_3460_M_A_38	A38_F	19	M	1	m.3460G>A	A	NA	NA	NA	NA	13	NA
7	F1G_3460_F_A_38	A38_G	15	F	1	m.3460G>A	A	NA	NA	NA	NA	11	NA
8	F1H_3460_F_U_38	A38_H	20	F	1	m.3460G>A	U (C)	NA	NA	NA	NA	NA	NA
9	F1I_3460_F_A_38	A38_I	15	F	1	m.3460G>A	A	NA	NA	NA	NA	7	NA
10	F1J_3460_F_A_38	A38_J	12	F	1	m.3460G>A	A	NA	NA	NA	NA	3	NA
11	F1K_3460_F_A_38	A38_K	16	F	1	m.3460G>A	A	NA	NA	NA	NA	6	NA
12	F2A_11778_M_A_38	A38_L	72	M	2	m.11778G>A	A	No	No	17	7.143	16	No
13	F2B_11778_M_A_40	A40_A	79	M	2	m.11778G>A	A	No	No	15	30	57	Yes
14	F2C_11778_M_A_40	A40_B	80	M	2	m.11778G>A	A	No	No	20	7.143	22	Yes
15	F2D_11778_F_U_40	A40_C	76	F	2	m.11778G>A	U (C)	No	Yes	NA	0	NA	NA
16	F2E_11778_F_U_40	A40_D	48	F	2	m.11778G>A	U (C)	No	Yes	NA	0	NA	NA
17	F2F_11778_M_A_40	A40_E	46	M	2	m.11778G>A	A	No	No	15	30	16	No
18	F2G_11778_M_A_40	A40_F	39	M	2	m.11778G>A	A	Yes	No	15	10	17	No
19	F3A_14484_F_U_40	A40_G	58	F	3	m.14484T>C	U (C)	No	Yes	NA	0	NA	NA
20	F3B_14484_M_A_40	A40_H	31	M	3	m.14484T>C	A	No	No	15	10	20	Yes
21	F3C_14484_M_U_40	A40_I	30	M	3	m.14484T>C	U (C)	No	No	13	5	NA	NA
22	F4A_11778_M_A_40	A40_J	54	M	4	m.11778G>A	A	No	No	18	20	18	No
23	F4B_11778_F_U_40	A40_K	64	F	4	m.11778G>A	U (C)	No	Yes	NA	0	NA	NA
24	F4C_11778_F_A_40	A40_L	71	F	4	m.11778G>A	A	Yes	No	15	20	NA	No
25	F4D_11778_F_A_41	A41_A	71	F	4	m.11778G>A	A	No	Yes	NA	0	54	NA
26	F4E_11778_M_A_41	A41_B	40	M	4	m.11778G>A	A	No	Yes	NA	0	22	NA
27	F4F_11778_F_U_41	A41_C	38	F	4	m.11778G>A	U (C)	NA	NA	NA	NA	NA	NA
28	F4G_11778_M_A_41	A41_D	49	M	4	m.11778G>A	A	No	Yes	NA	0	5	NA
29	F4H_11778_M_A_41	A41_E	48	M	4	m.11778G>A	A	Yes	No	14	40	NA	Yes
30	F4I_11778_F_U_41	A41_F	42	F	4	m.11778G>A	U (C)	Yes	No	15	20	NA	NA

Table 2.3: *Samples in nDNA exome sequencing; gender indicating if male (M) or female (F), status indicating whether they are affected (A) or unaffected (U (C)).*

Sample	UNIQUE_ID	Gender	Family	LHON Mutation	Status
1	F1B_3460_M_U_38	M	1	m.3460G>A	U (C)
2	F1C_3460_M_A_38	M	1	m.3460G>A	A
3	F1F_3460_M_A_38	M	1	m.3460G>A	A
4	F1F_3460_M_A_38	M	1	m.3460G>A	A
5	F1I_3460_F_A_38	F	1	m.3460G>A	A
6	F1L_3460_M_A	M	1	m.3460G>A	A
7	F1M_3460_M_A	M	1	m.3460G>A	A
8	F1N_3460_F_A	F	1	m.3460G>A	A
9	F1O_3460_F_A	F	1	m.3460G>A	A
10	F1P_3460_M_A	M	1	m.3460G>A	A
11	F2A_11778_M_A_38	M	2	m.11778G>A	A
12	F2B_11778_M_A_40	M	2	m.11778G>A	A
13	F2E_11778_F_U_40	F	2	m.11778G>A	U (C)
14	F2G_11778_M_A_40	M	2	m.11778G>A	A
15	F3B_14484_M_A_40	M	3	m.14484T>C	A
16	F3D_14484_M_U	M	3	m.14484T>C	U (C)
17	F3E_14484_M_A	M	3	m.14484T>C	A
18	F3F_14484_M_A	M	3	m.14484T>C	A
19	F4E_11778_M_A_41	M	4	m.11778G>A	A
20	F4J_11778_M_A	M	4	m.11778G>A	A
21	F5A_3460_M_A	M	5	m.3460G>A	A
22	F5B_3460_M_A	M	5	m.3460G>A	A
23	F6A_11778_M_A	M	6	m.11778G>A	A
24	F6B_11778_M_A	M	6	m.11778G>A	A
25	F7A_14495_M_A	M	7	m.14495A>G	A
26	F7B_14495_M_A	M	7	m.14495A>G	A
27	F8A_11778_M_A	M	8	m.11778G>A	A
28	F8B_11778_M_A	M	8	m.11778G>A	A

2.3 RESULTS

2.3.1 Familial Disease Penetrance

Pedigrees of 82 families were collected and analysed for differential penetrance in offspring between affected and unaffected mothers. Data set is summarised in Figure 2.1; this clearly shows that the majority of LHON pedigrees only had a single mother and most data came from unrelated pedigrees. However, some were large multi-generational pedigrees, of up to 34 mothers passing QC across their generational pedigree. The majority of captured offspring are female and a greater proportion of the male offspring are affected than female. The majority of mothers captured are asymptomatic, from the UK cohort, and m.11778G>A carriers. Within the total cohort, haplogroup H is most common, however, the majority of families have not had their haplogroup determined.

Figure 2.2 further segments the samples, by familial mutation and cohort, looking at the percentage affected in offspring; sons and daughters.

Table 2.4 shows differences in the mother's disease status and how this affects their children's likelihood of developing LHON. This looks at the entire cohort then segments by LHON causative mutation and the country that the recruited family lived in. Offspring age was thresholded at 30 years old, so this assumes that the majority of offspring have developed LHON by this point if they are to develop, however, this is likely a slight under-representation of the lifetime LHON penetrance as some who are older than 30 could still develop beyond the date of this study.

Cohorts were further described in Figure 2.3, which shows the breakdown of mutation in offspring by the cohort. m.11778G>A was the most prevalent mutation in all countries with the Finnish cohort only containing m.11778G>A and m.3460G>A, and the Tasmanian cohort only containing m.11778G>A and m.14484T>C. The Tasmanian cohort seems to have a lower percentage of offspring affected, as seen in Figure 2.2 B; stringent thresholding was applied on the pedigrees to improve sample quality, however, the pedigrees did appear to be biased to recording female offspring and male offspring had not been included in some of the generations which were excluded. Female offspring were recorded for all generations and given the lower rate of affected females, it is possible that the lower male affected rate is also an accurate representation of the dataset. The Tasmanian cohort has a greater proportion of m.14484T>C which is the most mild LHON mutation and could be the reason for the lower penetrance.

m.14495A>G and m.12719T>A are single family mutations which only appear in the UK population and metadata describing the pathogenic LHON mutation was missing for some samples in the UK cohort. m.12719T>A is also a single family mutation, not presently recognised in MITOMAP (Lott et al., 2013) and needs validation as causative for LHON.

Whilst all countries have a large proportion of m.11778G>A offspring, the differences

seen between penetrance in the Finnish and Tasmanian cohort (Figure 2.4) could be due to the difference in mutation burden rather than nuclear background. Table S1 does show that the penetrance in m.3460G>A and m.14484T>C is significantly different (sons p = 5.05e-03; daughters p = 3.66e-04) whilst testing for all mutations, a significant difference is found (sons p = 2.599e-12; daughters p = 1.82e-04). In the cohorts, no significant difference is found between sons' penetrance (p = 0.092) whilst daughters' has some significance (p = 1.051e-05).

There are significant differences in the penetrance of LHON in offspring between affected and unaffected mothers. As shown in Table S1, total offspring significance is p = 8.43e-09, with female offspring more affected by mothers' status (p = 7.62e-05) than male offspring (p = 5.60e-04).

This continues to be true in m.11778G>A carriers with affected mothers more likely to have affected daughters and offspring in general (p = 0.008 and p = 0.001 respectively). m.3460G>A carriers are more affected by mothers' disease status with offspring 28.6% more likely to be affected if their mother is affected (p = 0.001) and both sons and daughters are affected by mothers' status (p = 0.025 and p = 0.046 respectively).

Both UK and Finnish offspring are more likely to be affected by mothers' status (p = 0.002 and p = 5.43E-05), however, this is predominantly for sons in the UK (p = 0.014) whilst both sons and daughters are affected in Finland (p = 0.041 and p = 0.001), with daughters more influenced than sons.

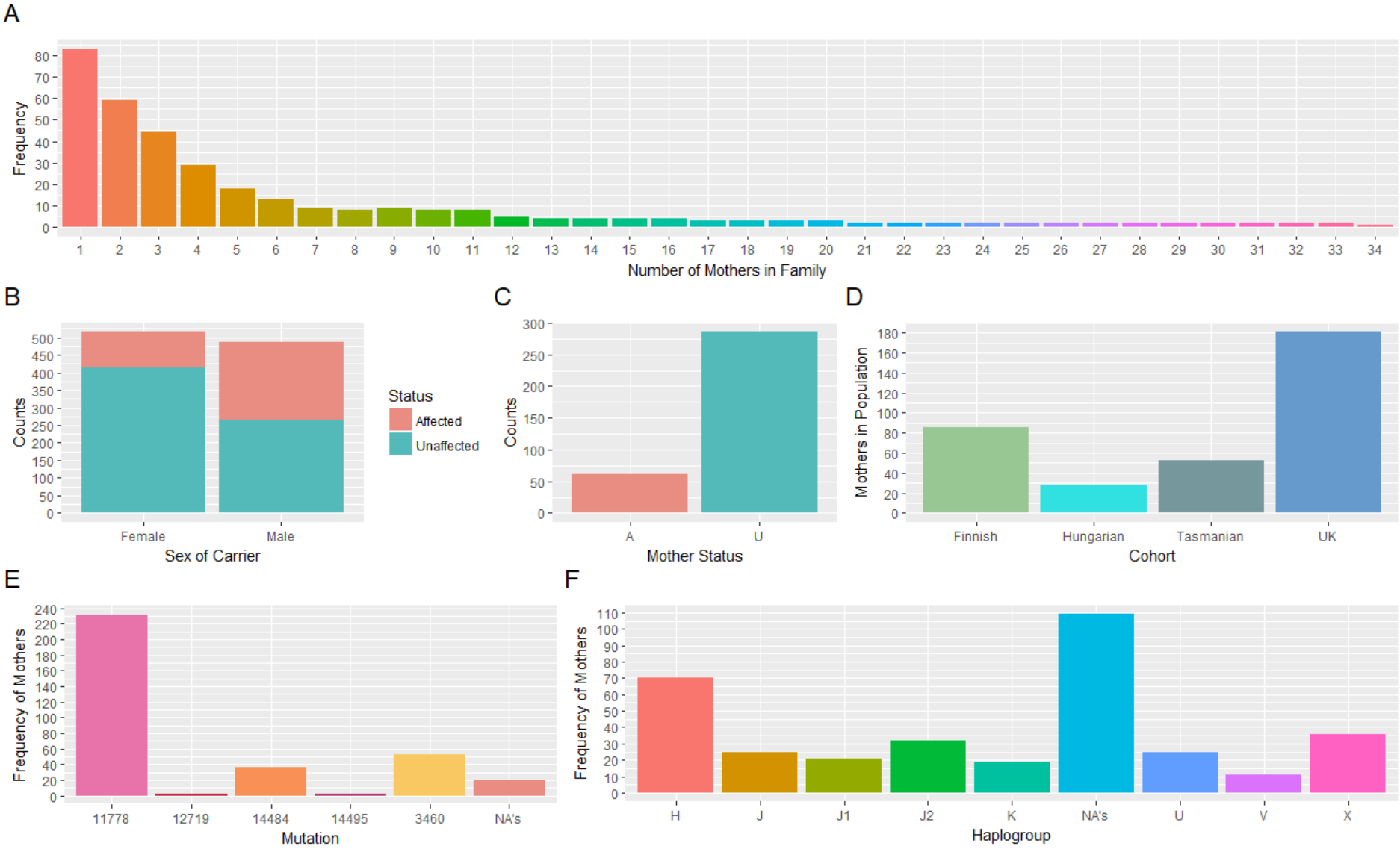

Figure 2.1: *The characterised cohort of LHON families. Number of mothers within each family (A), total number of offspring by gender and disease status (B), number of mothers by disease status (C), total number of generations by country (D), number of mothers within the cohort by LHON mutation (E) and total number of generations by haplogroup (F).*

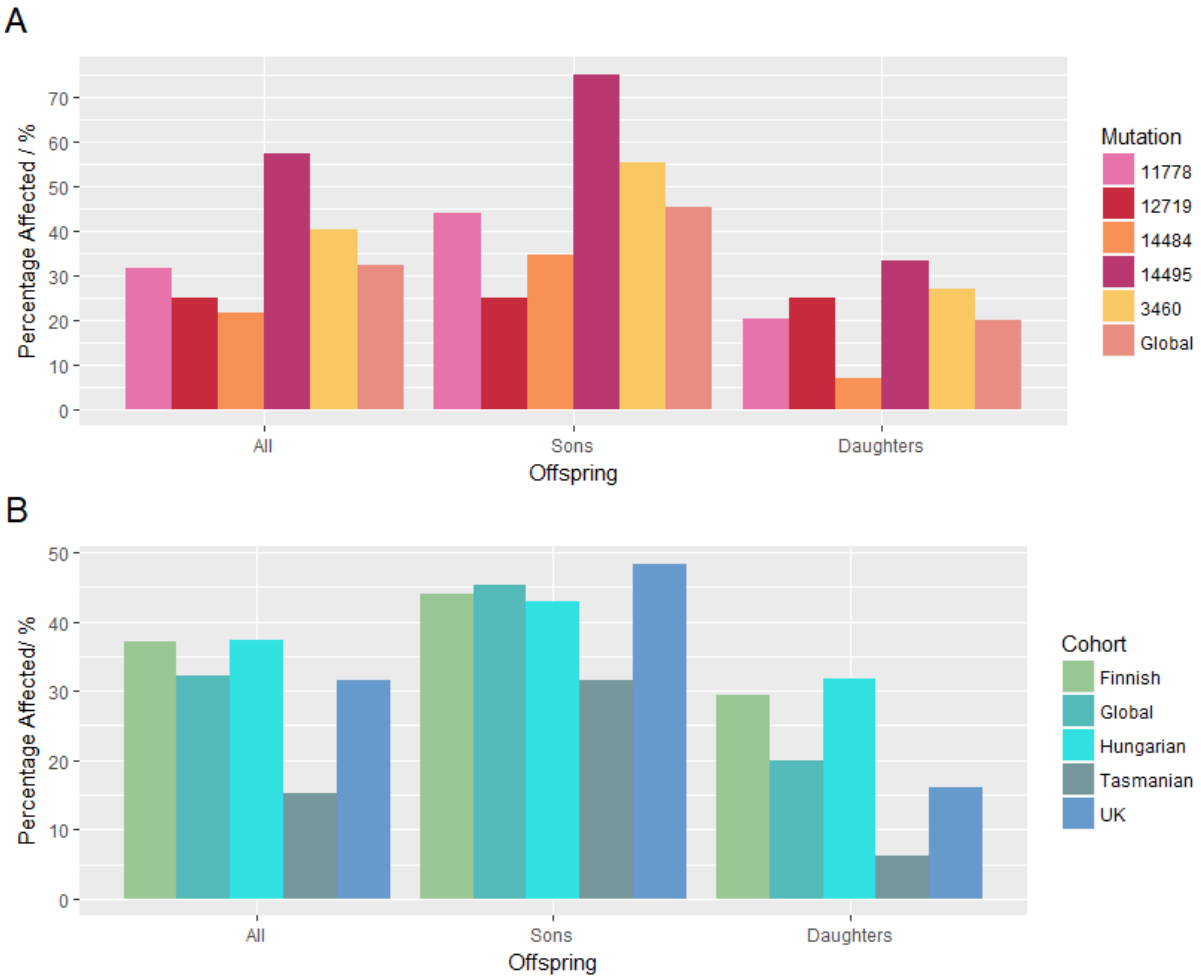

Figure 2.2: *The characterised cohort of LHON families showing penetrance in all offspring, sons and daughters, stratifying by familial mutation (A) and country of collection (B).*

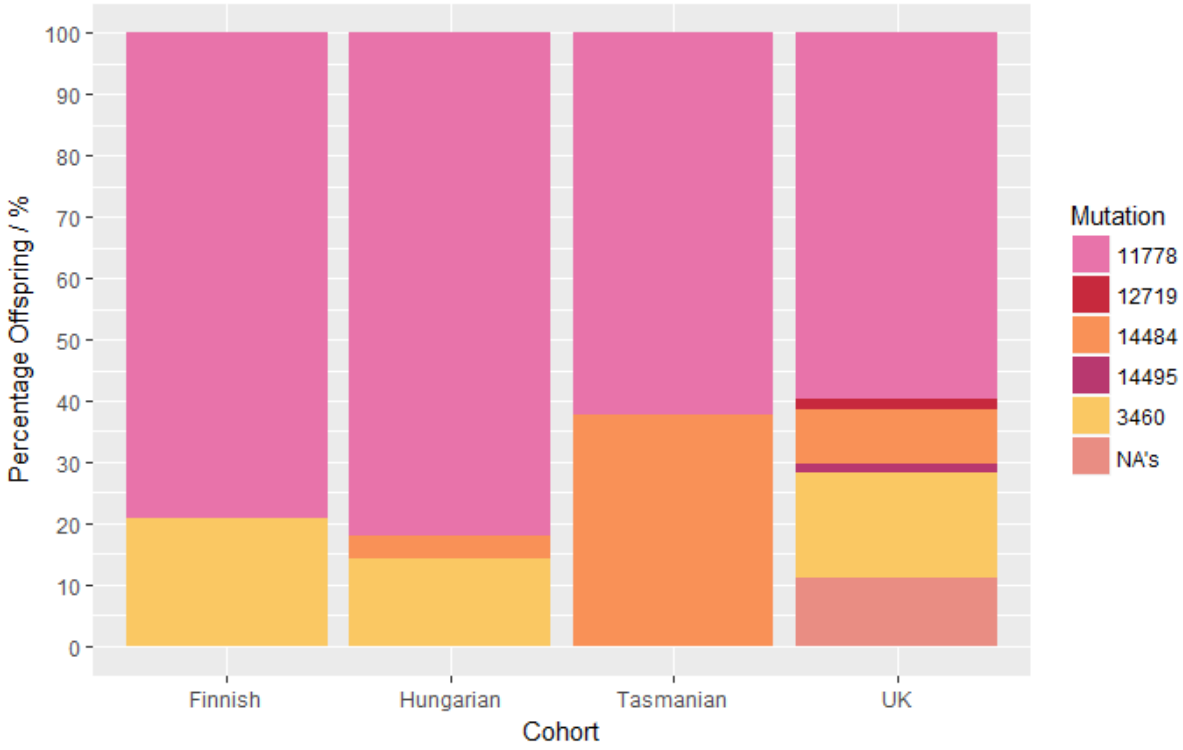

Figure 2.3: *The characterised cohort of LHON families showing the proportions of each mutation within the sampled cohort.*

Table 2.4: *Pedigrees of 82 families with a LHON mutation; 348 generations of mothers penetrance in offspring, stratifying by offspring sex, mother's disease status and familial LHON mutation or cohort. n = number of offspring analysed.*

	Mother's Disease Status	**Offspring Penetrance**	**Son's Penetrance**	**Daughter's Penetrance**
Total (n = 1001)	Total	32.17%	45.15%	19.96%
	Affected	50%	60.19%	36.59%
	Unaffected	27.99%	40.84%	16.82%
m.11778G>A (n = 656)	Total	31.71%	43.95%	20.47%
	Affected	44.63%	53.03%	34.55%
	Unaffected	28.79%	41.53%	17.77%
m.3460G>A (n = 176)	Total	40.34%	55.42%	26.88%
	Affected	60.00%	73.33%	44.00%
	Unaffected	31.40%	45.28%	20.59%
m.14484T>C (n = 92)	Total	21.74%	34.69%	6.98%
	Affected	25.00%	25.00%	-
	Unaffected	21.59%	35.56%	6.98%
m.14495A>G (n = 7)	Total	57.14%	75.00%	33.33%
	Affected	100%	100%	-
	Unaffected	25.00%	0.00%	33.33%
m.12719T>A (n = 8)	Total	25.00%	25.00%	25.00%
	Affected	-	-	-
	Unaffected	25.00%	25.00%	25.00%
UK (n = 501)	Total	31.54%	48.33%	16.09%
	Affected	47.44%	66.67%	25.00%
	Unaffected	28.61%	44.44%	14.67%
Finnish (n = 326)	Total	37.11%	44.05%	29.33%
	Affected	55.95%	56.86%	54.55%
	Unaffected	30.34%	38.46%	22.22%
Hungarian (n = 83)	Total	37.35%	42.86%	31.71%
	Affected	47.83%	57.14%	33.33%
	Unaffected	33.33%	35.71%	31.25%
Tasmanian (n = 99)	Total	15.15%	31.43%	6.25%
	Affected	0.00%	0.00%	0.00%
	Unaffected	15.96%	32.35%	6.67%

Table 2.5: *Pedigrees of 56 families with a m.11778G>A LHON mutation; 312 generations of mothers penetrance in 656 offspring, stratifying by offspring sex, mother's disease status and cohort. n = number of offspring analysed.*

	Mother's Disease Status	**Offspring Penetrance**	**Son's Penetrance**	**Daughter's Penetrance**
Total (n = 345)	Total	29.57%	42.07%	18.23%
	Affected	43.04%	48.84%	36.11%
	Unaffected	25.56%	39.67%	13.79%
UK (n = 276)	Total	31.16%	48.84%	15.65%
	Affected	37.93%	64.29%	13.33%
	Unaffected	30.36%	46.96%	15.91%
Finnish (n = 247)	Total	35.22%	41.86%	27.97%
	Affected	50.75%	50.00%	51.85%
	Unaffected	29.44%	38.20%	20.88%
Hungarian (n = 72)	Total	37.50%	42.86%	32.43%
	Affected	45.00%	54.55%	33.33%
	Unaffected	34.62%	37.50%	32.14%
Tasmanian (n = 61)	Total	13.11%	28.57%	5.00%
	Affected	-	-	-
	Unaffected	14.29%	30.00%	5.56%

Table 2.6: *Pedigrees of 46 British families with a LHON mutation; 224 generations of mothers penetrance in offspring, stratifying by offspring sex, mother's disease status and familial LHON mutation. n = number of offspring analysed.*

	Mother's Disease Status	**Offspring Penetrance**	**Son's Penetrance**	**Daughter's Penetrance**
Total (n = 1001)	Total	32.17%	45.15%	19.96%
	Affected	50%	60.19%	36.59%
	Unaffected	27.13%	39.73%	16.37%
m.11778G>A (n = 357)	Total	28.85%	41.67%	17.46%
	Affected	42.50%	54.55%	27.78%
	Unaffected	28.79%	41.53%	17.77%
m.3460G>A (n = 99)	Total	48.48%	63.04%	35.85%
	Affected	61.22%	76.00%	45.83%
	Unaffected	36.00%	47.62%	27.59%
m.14484T>C (n = 73)	Total	21.92%	33.33%	8.82%
	Affected	0.00%	0.00%	-
	Unaffected	22.86%	36.11%	8.82%
m.14495A>G (n = 7)	Total	57.14%	75.00%	33.33%
	Affected	100%	100%	-
	Unaffected	25.00%	0.00%	33.33%
m.12719T>A (n = 8)	Total	25.00%	25.00%	25.00%
	Affected	-	-	-
	Unaffected	25.00%	25.00%	25.00%

2.3.2 X-Linked Modifier Gene

Following from pedigree collection in Section 2.3.1, to measure LHON disease penetrance, statistical analyses, based upon the work of Bu and Rotter (1991), were replicated to determine the validity of a two locus causative model and feasibility of an X-linked modifier accounting for part of the variability in LHON disease penetrance.

X-Linked Hypothesis

Data was restricted to obligate heterozygotes and the new dataset is summarised in Figures 2.4 and 2.5. Compared to Figures 2.1 and 2.2, limiting to obligate heterozygotes has clearly limited the number of mothers within each pedigree (Figure 2.5 A). Fewer female offspring are included and a larger proportion of male offspring are affected. Whilst there are fewer mothers, the ratio of affected to unaffected does not significantly change and nor do the cohort or mutation proportions. There are fewer mothers of haplogroup H, however, the relative proportions do not shift greatly. The percentage affected in the m.12719T>A mutation has greatly increased while the m.14495A>G mutation has been removed; these mutations occurred in single families so penetrance proportions are readily influenced by sample removal. Aside from this, the mutation percentage affected did not greatly change, with the largest change seen within the Tasmanian families (Figure 2.5).

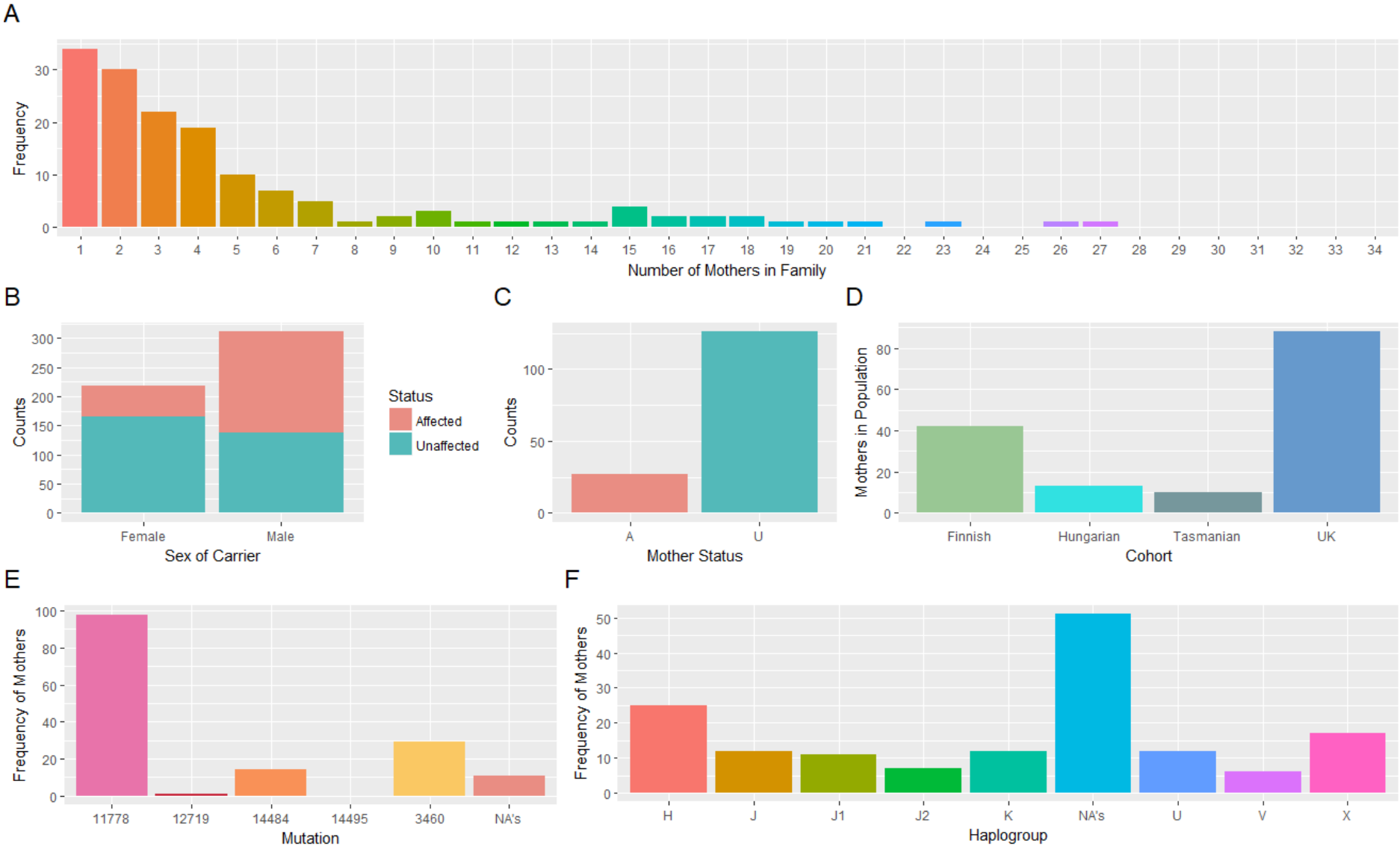

Figure 2.4: *The characterised cohort of LHON obligate heterozygote mothers' families. Number of mothers within each family (A), total number of offspring by gender and disease status (B), number of mothers by disease status (C), total number of generations by country (D), number of mothers within the cohort by LHON mutation (E) and total number of generations by haplogroup (F).*

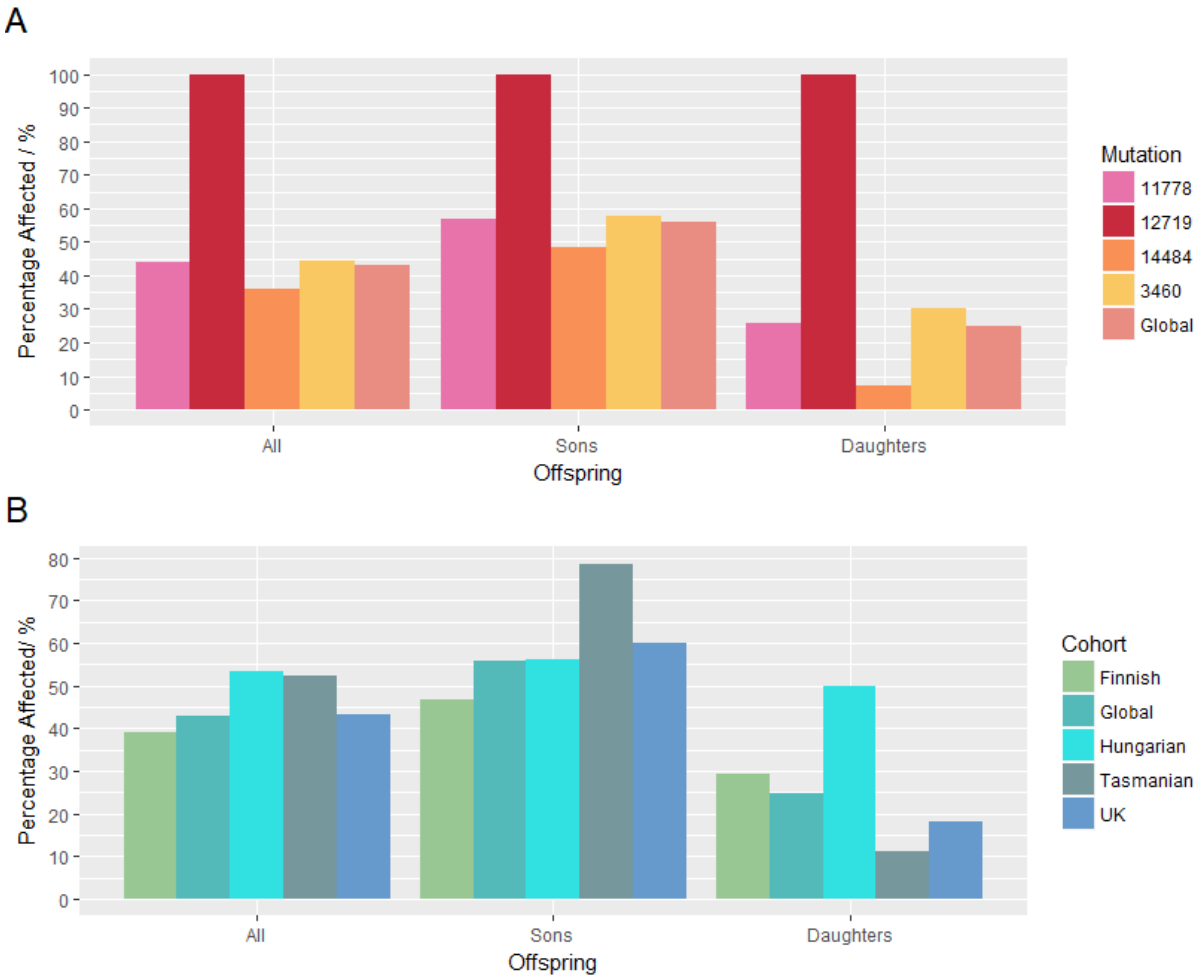

Figure 2.5: *The characterised cohort of LHON obligate heterozygote mothers' families showing penetrance in all offspring, sons and daughters, stratifying by familial mutation (A) and country of collection (B).*

The X-linked goodness-of-fit test for males was first calculated in the pooled and individual sibships (the former split by cohort and latter by cohort and sibship size), as shown in Tables 2.7 and 2.8 respectively. Given that H_0 = Male offspring develop LHON depending upon their inheritance of the wildtype or mutant X-linked allele and H_1 = Male offspring LHON penetrance is not caused by their equal likelihood inheritance of the wildtype or mutant X-linked allele, it appears that the null hypothesis must be rejected in some populations, including the entire dataset as a whole ($p = 0.036$). In the pooled male groups, the null hypothesis must also be rejected for Tasmania and the UK ($p = 0.033$ and $p = 0.010$) respectively. After splitting by sibship size and calculating individual expected affected sample frequencies, the Finnish population must also reject the null hypothesis ($p = 0.041$), but the other countries pass using this methodology.

As the null hypothesis was rejected, it must be assumed that male offspring LHON penetrance is not caused by the equal likelihood inheritance of the wildtype or mutant X-linked allele.

Despite the Bu and Rotter (1991) methodology stating that their male goodness-of-

fit test used obligate heterozygote mothers, a further filtration was carried out given the appearance of their data in comparison to ours, whereby only unaffected mothers with one or more affected sons was considered, as shown in Table 2.9. In this dataset, the p-value does not reach significance and as such, it can instead be said that male offspring develop LHON depending upon their inheritance of the wildtype or mutant X-linked allele.

Table 2.7: *Values and significance of pooled goodness-of-fit test for males.*

Cohort	**Observed**	**Expected**	χ^2	***P***
All	174	155.5	4.402	0.036
Finnish	50	53.5	0.458	0.499
Hungarian	14	12.5	0.360	0.549
Tasmanian	11	7.0	4.571	0.033
UK	99	82.5	6.600	0.010

Table 2.8: *Values and significance of individual goodness-of-fit test for males. s = sibship size, n_s = number of families.*

	s	n_s	**Observed**	**Expected**	χ^2	P
Finnish	1	12	8	12.000		
	2	17	20	22.667		
	3	3	4	5.143		
	4	5	6	10.667		
	5	2	6	5.161		
	6	1	2	3.048		
	8	2	4	8.031		
Total	29	42	50	66.716	4.188	0.041
Hungarian	1	6	5	6.000		
	2	3	3	4.000		
	3	3	4	5.143		
	4	1	2	2.133		
Total	10	13	14	17.276	10.621	0.431
Tasmanian	1	7	6	7.000		
	2	2	3	2.667		
	3	1	2	1.714		
Total	6	10	11	11.381	0.013	0.910
UK	1	37	36	37.000		
	2	34	37	45.333		
	3	12	17	20.571		
	4	3	5	6.400		
	5	1	1	2.581		
	7	1	3	3.528		
Total	22	88	99	115.413	2.334	0.127

Table 2.9: *Values and significance of individual goodness-of-fit test for males whilst limiting to unaffected mothers with one or more affected sons. s = sibship size, n_s = number of families.*

	s	n_s	**Observed**	**Expected**	χ^2	P
Finnish	1	8	8	8.000		
	2	13	18	17.333		
	3	2	2	3.429		
	4	4	6	8.533		
	5	2	6	5.161		
	6	1	2	3.048		
	8	1	3	4.016		
Total	29	31	45	49.520	0.413	0.521
Hungarian	1	5	5	5.000		
	3	2	3	3.429		
	4	1	2	2.133		
Total	8	8	10	10.562	0.030	0.863
Tasmanian	1	6	6	6.000		
	2	2	3	2.667		
	3	1	2	1.714		
Total	6	9	11	10.381	0.037	0.848
UK	1	36	36	36.000		
	2	30	35	40.000		
	3	8	11	13.714		
	4	2	2	4.267		
	5	1	1	2.581		
	7	1	3	3.528		
Total	22	78	88	100.089	1.460	0.227

X-Inactivation Hypothesis

Data was further restricted to unaffected mothers with one or more affected sons and the new dataset is summarised in Figures 2.6 and 2.7. Compared to Figures 2.4 and 2.5, again, limiting sample size further clearly limits the number of mothers within each pedigree (Figure 2.6 (A)). All affected mothers are excluding by this filtration (Figure 2.6 (C)) but the general proportions do not seem to have been largely affected. There has been little change in percentage affected by mutation or cohort, although the Hungarian penetrance does slightly decrease (Figure 2.7).

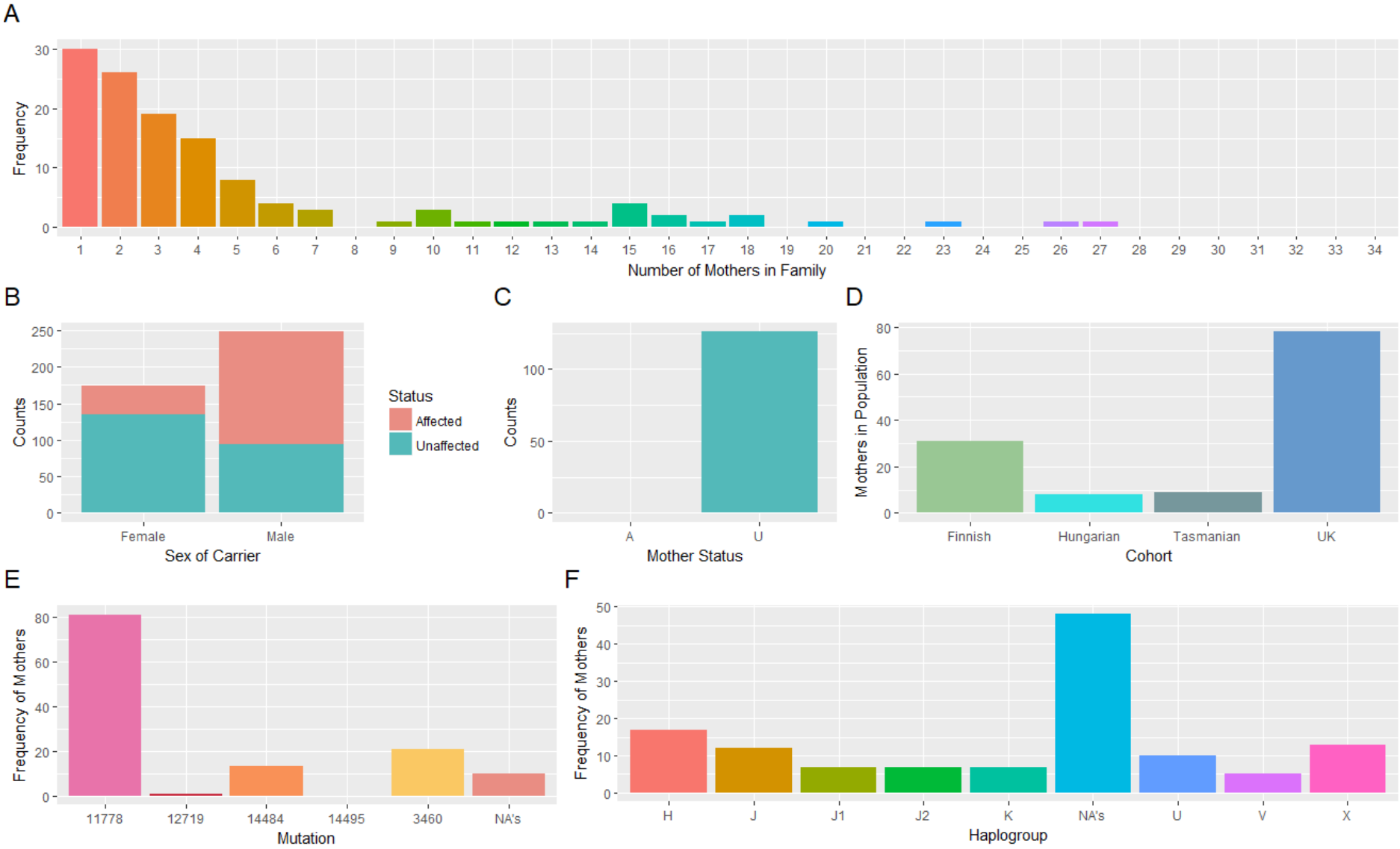

Figure 2.6: *The characterised cohort of LHON unaffected mothers, with one or more affected sons, families. Number of mothers within each family (A), total number of offspring by gender and disease status (B), number of mothers by disease status (C), total number of generations by country (D), number of mothers within the cohort by LHON mutation (E), total number of generations by haplogroup (F).*

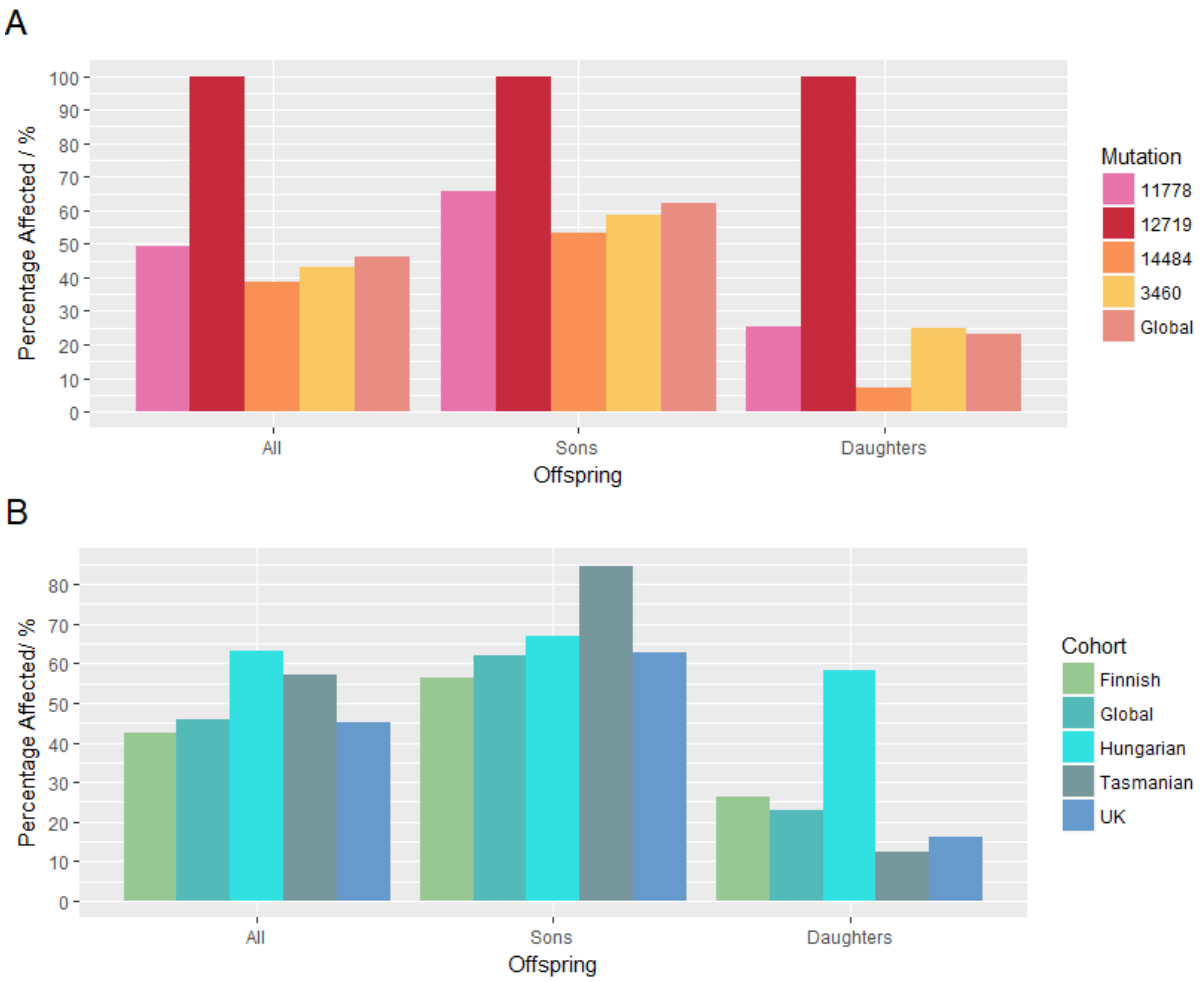

Figure 2.7: *The characterised cohort of LHON unaffected mothers, with one or more affected sons, families showing penetrance in all offspring, sons and daughters, stratifying by familial mutation (A) and country of collection (B).*

T, the segregation ratio, was calculated, as shown in Table 2.10, and cohorts were tested for heterogeneity by Analysis of Deviance ($p = 0.960$) by comparing each country T to the global measurement, indicating that there is not heterogeneity between the cohorts.

K, the probability that a heterozygous female will be affected (penetrance), was then calculated using the global T value (as there were no significant differences in cohort heterogeneity). This used the obligate heterozygote mothers described in Figures 2.4 and 2.5. Analysis of deviance was performed ($p = 0.9877$) and no significant difference was found in the measurements of K, as shown in Table 2.11.

q, the frequency of the abnormal X-linked gene, was finally calculated to be $q = 0.283$, using the global T and K values. Affected LHON females were then calculated to be homozygous carriers of the X-linked gene in 61.62% instances whilst the other 38.38% of LHON affected females are heterozygotes who develop the disease by X-inactivation.

Table 2.10: *T, the segregation ratio, for total dataset and stratified by country.*

Cohort	**T**
Global	0.230
Finnish	0.265
Hungarian	0.583
Tasmanian	0.125
UK	0.163

Table 2.11: *K, the probability that a heterozygous female will be affected (penetrance), total dataset and stratified by country.*

Cohort	**K**
Global	0.176
Finnish	0.114
Hungarian	0.385
Tasmanian	0.100
UK	0.262

2.3.3 Nuclear DNA Variants

Figure 2.8 shows the abnormal grouping of two samples by PCA, phylogenetic distance, M-Value intensity and Log2-Intensity of CPG sites, indicating their outlier status. Review of control probes shows that these samples had poor specificity and failed both bisulphite conversion and negative control checks. Samples F1B_3460_M_U_38 and F1C_3460_M_A_38 were removed and individual probe quality was then assessed as in Figure S2. A quality threshold of p = 0.01 was then set as shown with low confidence probes excluded. A minimum of 3 beads per probe was also set, with final probe counts per chromosome described in Table S2. 27,220 probes remained of the original 27,578.

Final sample detection P-value confidence is shown in Figure S4. Sample F2A_11778_M_A_38 does appear to be increased compared to other samples, however, this is still below acceptable levels for sample P-value quality.

Samples underwent quantile normalisation at a probe level to standardise the methylated and unmethylated probes intensity between different samples. Colour density distribution of the two channels are shown in Figure S5 and phylogenetic trees of methylation status are in Figure 2.9.

Linear regressions of all permutations of $y \sim Status + Gender + Age + Mutation + Family + Batch + NeverSmoked + CPD$ were analysed. To choose variables, linear regressions were performed with all available metadata variables, and those which significantly affected the output gene list results were incorporated into the model; mutation + family + batch were all included as the sample loading pattern does not allow for differentiation between these variables. Regressions were performed on the full dataset where metadata was available, and split into further segmentations with limited input variables depending upon metadata availability. Males and females were analysed separately as differences were seen between male and female methylation patterns (Figure S6), with females having a greater proportion of methylated sites than males. Whilst standard practice often disregards the 23rd chromosome, this would not be effective for LHON given the potential for an X-linked modifier gene. Comparisons of gene matches are shown in Figure 2.10, indicating that gender and smoking variables influence methylation patterns most significantly.

Hyper- and hypomethylated genes identified by linear regression are then shown in Tables S3 and S4 respectively.

Figures S7 and S8 respectively show matches of the hyper- and hypomethylated genes against MSigDB's C2 curated gene sets of chemical and genetic perturbations, and MSigDB's C5 GO gene sets of biological processes.

Exome analysis of dominant and recessive models was undertaken and 3,833 genes were identified which contain variants which exclusively occur within affected or unaffected LHON carriers in either dominant or recessive models. Models were defined as variants which existed exclusively within affected or asymptomatic carriers which were not present within the reciprocal group with dominant models being a single

allele and recessive models as combinations of homozygous alleles or heterozygous combinations of minor alleles in case of compound heterozygosity. This resulting gene list was cross-matched against the LHON hyper- and hypomethylated genes. Results are shown in Tables 2.12 and 2.13 respectively.

Figures 2.11 and 2.12 respectively show matches of the cross-matched genes against LHON hyper- and hypomethylated genes against MSigDB's C2 curated gene sets of chemical and genetic perturbations, and MSigDB's C5 GO gene sets of biological processes. All of the listed gene sets have a minimum FDR q-value of 0.05; full significance shown in Tables S5 and S6 respectively.

PANTHER14.1 Overrepresentation Test of the 45 cross-matched genes showed that pathways for generation of neurons and neurogenesis were overrepresented at an FDR-q = 0.027 and p = 0.020 respectively. No other pathways reached significance for over-representation after FDR correction. Genes which contributed to these pathways are described in Table S7.

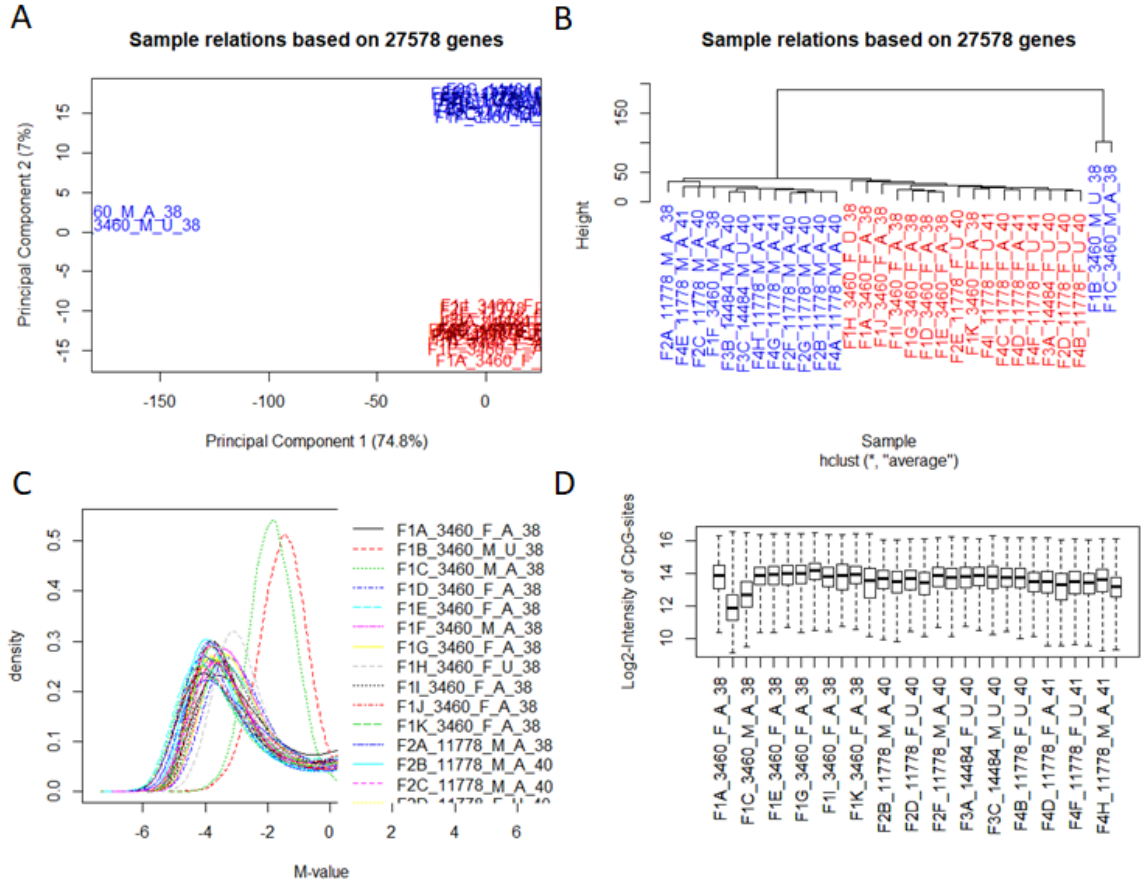

Figure 2.8: *Reviewing raw dataset sample quality by PCA clustering (A), phylogenetic clustering (B), probe density across M-value (C) and CpG site Log2 Intensity (D).*

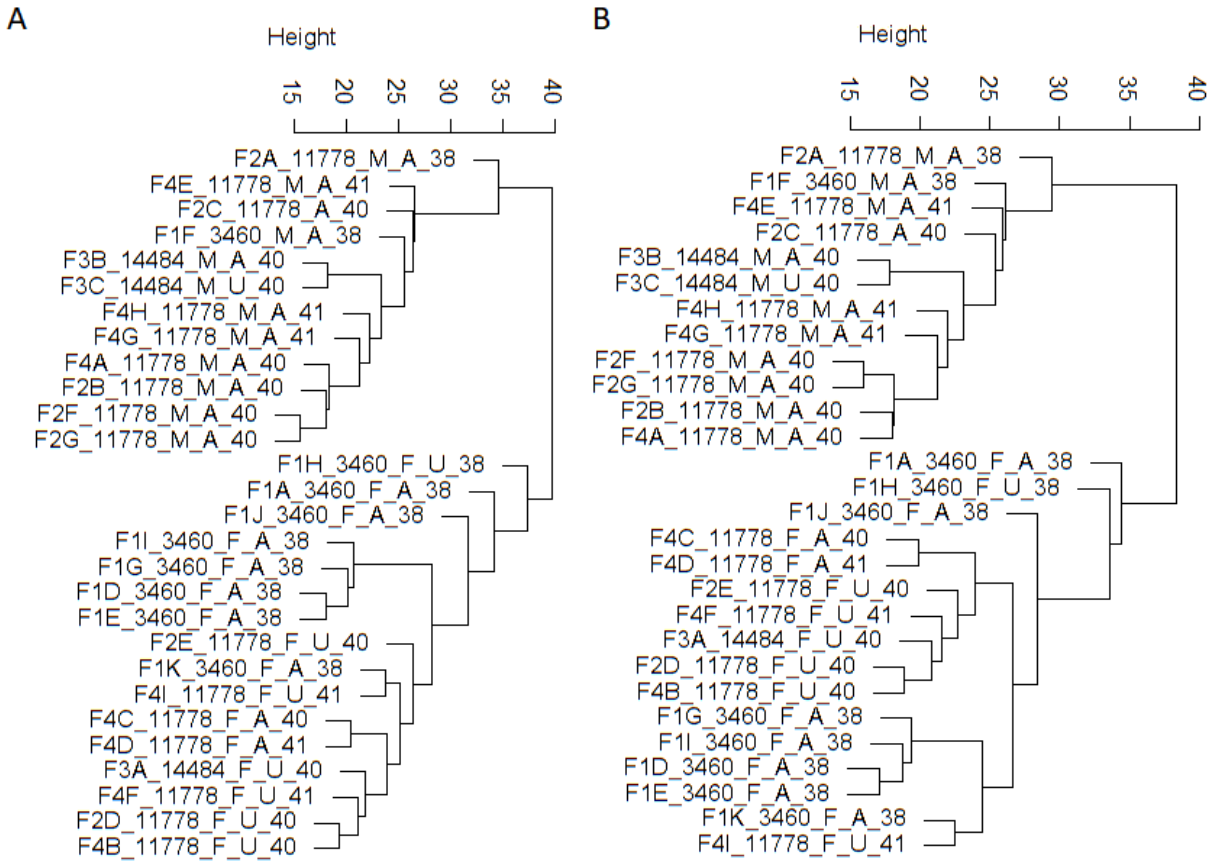

Figure 2.9: *Phylogenetic tree of sample nuclear methylatio relations based on 27,220 probes; before (A) and after (B) quantile normalisation.*

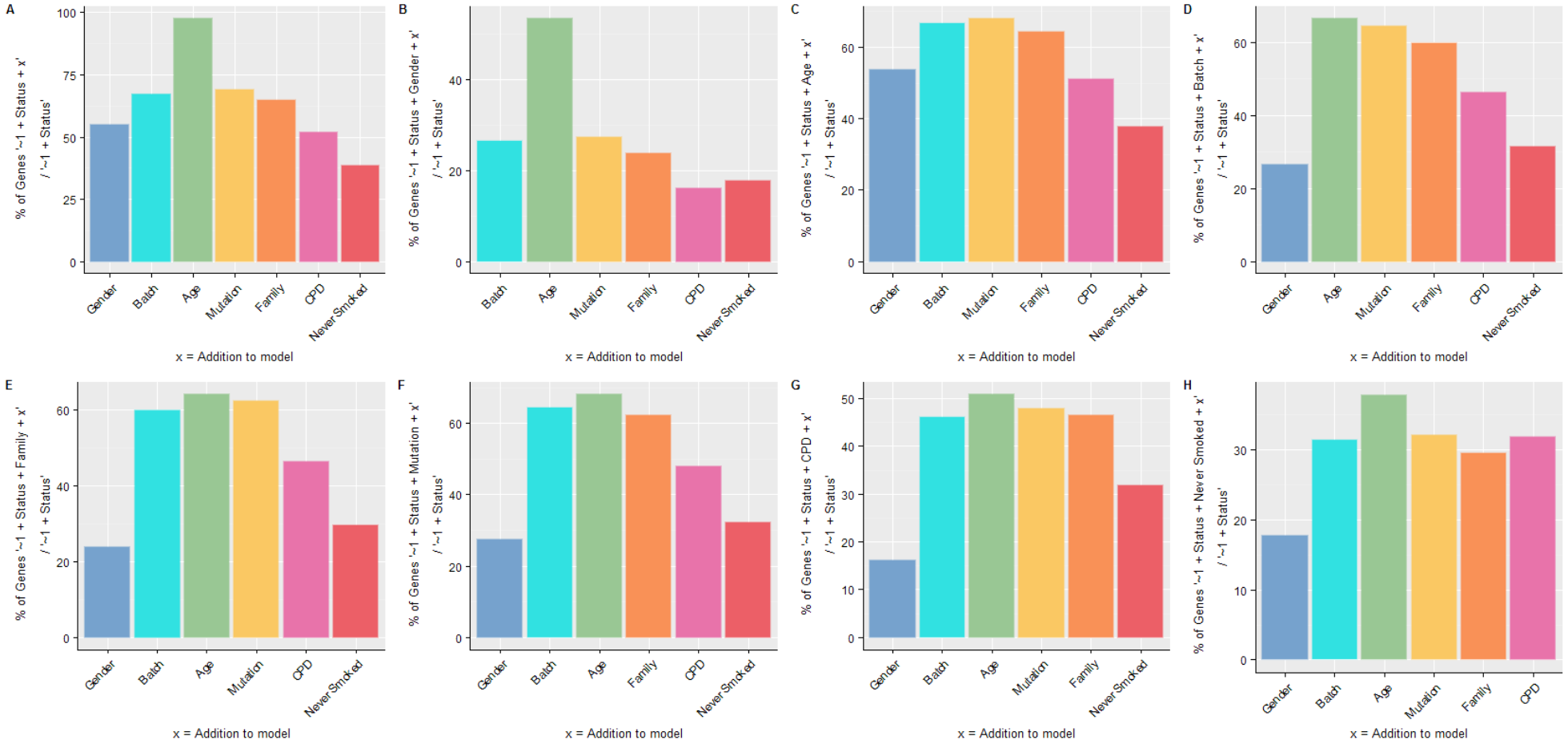

Figure 2.10: *Comparisons of different genes included in different linear model combinations; comparing % match between y 1 + Status to y 1 + Status + Variable on X axis (A), then y 1 + Status to y 1 + Status + Variable on X axis +, Gender (B), Age (C), Batch (D), Family (E), Mutation (F), CPD (G) and Never Smoked (H), indicating the difference which incorporating an additional variable has on the gene list compared to the gene list prior to inclusion.*

Table 2.12: *Differentially hypermethylated genes in LHON patients compared to unaffected carriers, which also contain genetic variants that are unique to either patients or carriers in either dominant or recessive models of alleles captured in exome sequencing. Mitochondrial genes identified from MitoCarta 2.0 (Calvo et al., 2016; Pagliarini et al., 2008) and retinal genes identified from TIGEM (Pinelli et al., 2016).*

Gene	Dominant Model	Recessive Model	Mitochondrial	Retinal
ADCY2	YES	YES	NA	YES
AIRE	YES	YES	NA	NA
BMP8A	YES	YES	NA	NA
CMTM6	NO	YES	NA	YES
ECT2	NO	YES	NA	YES
FGF20	YES	YES	NA	NA
FZD1	YES	YES	NA	NA
GNAI1	NO	YES	NA	YES
GPM6A	NO	YES	NA	YES
GPR157	YES	YES	NA	NA
GRB10	NO	YES	NA	YES
HGF	NO	YES	NA	YES
IPO9	NO	YES	NA	YES
IRF6	NO	YES	NA	YES
ITGA1	YES	YES	NA	YES
LAMC2	YES	YES	NA	NA
MEGF10	YES	YES	NA	YES
NETO1	NO	YES	NA	YES
NIPA1	YES	YES	NA	YES
PCDHGC4	NO	YES	NA	YES
RAB32	NO	YES	YES	YES
RBP4	NO	YES	NA	NA
SCN4B	YES	YES	NA	YES
SCUBE3	NO	YES	NA	NA
SLC25A36	NO	YES	YES	YES
THRB	NO	YES	NA	YES
TLX2	NO	YES	NA	YES
TSPAN32	YES	YES	NA	NA
ZNF273	NO	YES	NA	YES

Table 2.13: *Differentially hypomethylated genes in LHON patients compared to unaffected carriers, which also contain genetic variants that are unique to either patients or carriers in either dominant or recessive models of alleles captured in exome sequencing. Mitochondrial genes identified from MitoCarta 2.0 (Calvo et al., 2016; Pagliarini et al., 2008) and retinal genes identified from TIGEM (Pinelli et al., 2016).*

Gene	Dominant Model	Recessive Model	Mitochondrial	Retinal
COPB2	NO	YES	NA	NA
DNAJB13	YES	YES	NA	NA
DNASE1L1	YES	YES	NA	NA
EFNB1	NO	YES	NA	NA
EVL	NO	YES	NA	NA
GPR37L1	NO	YES	NA	NA
IDH3G	YES	YES	YES	YES
IGSF8	NO	YES	NA	NA
IQSEC1	NO	YES	NA	NA
LINS1	YES	YES	NA	NA
NANP	NO	YES	NA	NA
PHYH	YES	YES	YES	YES
RAB32	NO	YES	YES	YES
RUNX3	YES	YES	NA	NA
SLC6A18	YES	YES	NA	NA
TFAP4	NO	YES	NA	NA
TNS3	YES	YES	NA	NA

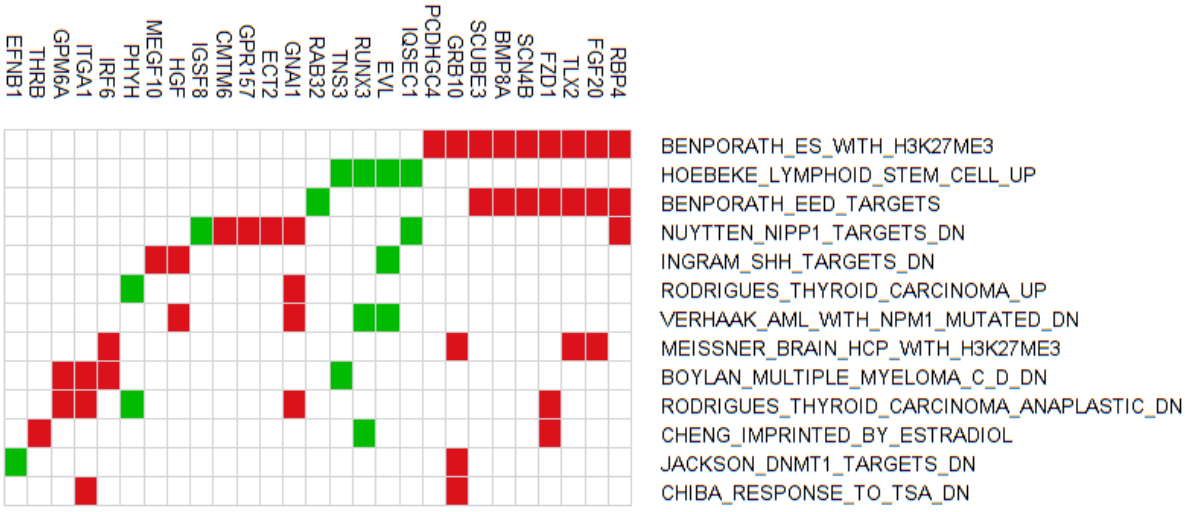

Figure 2.11: *Matches of exome cross-matched LHON hypermethylated (red) and hypomethylated (genes) in MSigDB's C2 curated gene sets of chemical and genetic perturbations (3302 gene sets).*

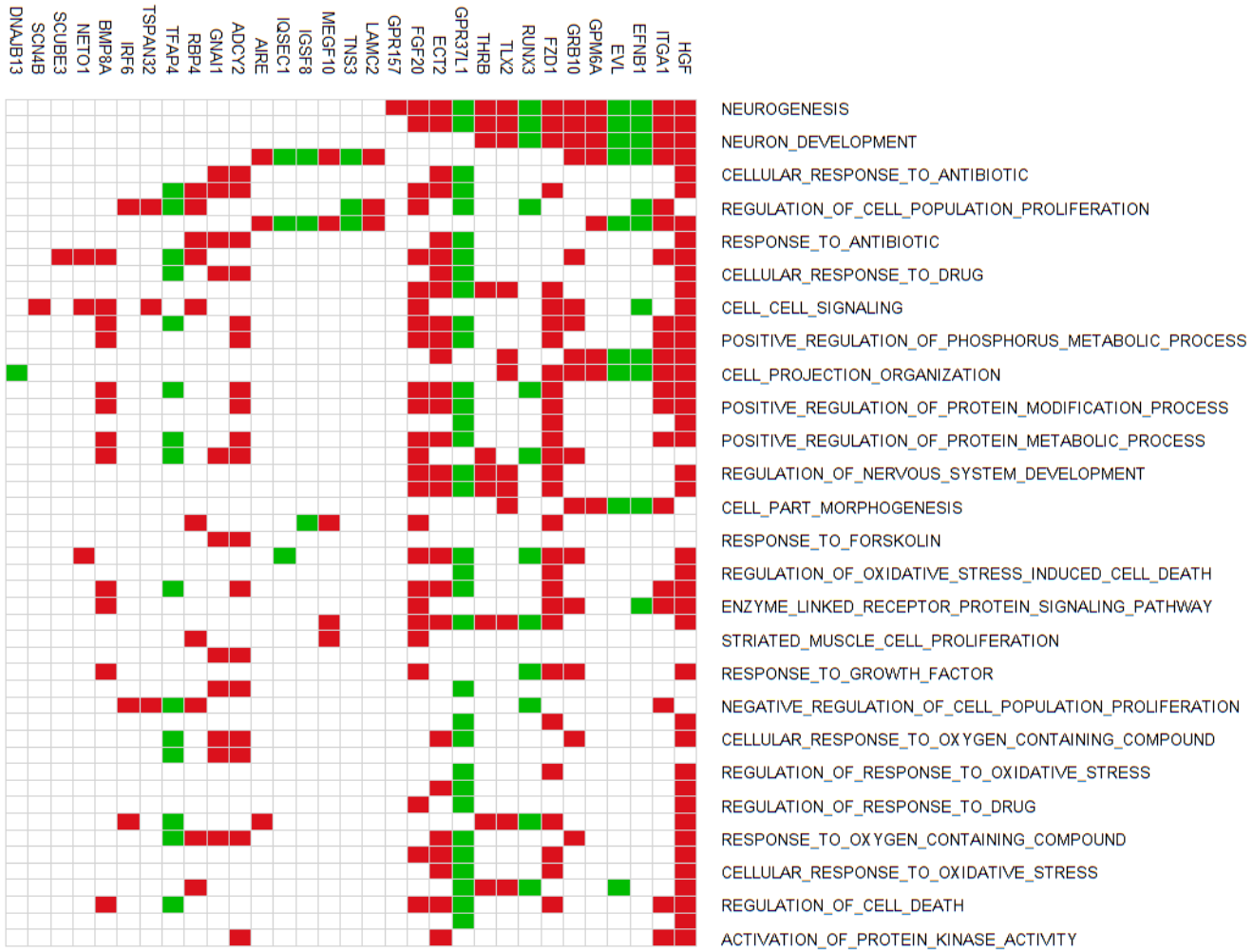

Figure 2.12: *Matches of exome cross-matched LHON hypermethylated (red) and hypomethylated (genes) in MSigDB's C5 GO gene sets of biological processes (7350 gene sets).*

Table 2.14: *Pathways in GO C5 Biological Process Complete overrepresented by gene list identified as cross-matched between exome analysis and differentially methylated between LHON patients and carriers.*

GO C5 Biological Process	**Observed**	**Expected**	**Fold Enrichment**	**+/-**	**Raw P-value**	**FDR**
Generation of Neurons	14	3.38	4.15	+	3.45E-06	0.027
Neurogenesis	15	3.59	4.17	+	1.26E-06	0.020

2.4 Discussion

2.4.1 Familial Disease Penetrance

The familial disease penetrance was an expansion of previous calculations of penetrance in LHON families looking at male and female offspring, then stratifying by mothers' disease status, LHON mtDNA mutation and country of collection.

As seen in Table 2.4, penetrance estimates in our sampled cohort are higher than those which were seen previously, particularly in females, where it was estimated to have a penetrance of 10% (Yu-Wai-Man et al., 2003, 2009), whilst our cohort shows a penetrance of 19.96% in all female offspring. The male penetrance is 45.15% which is not a significant deviation of the 50% previously described (Yu-Wai-Man et al., 2003, 2009). Our cohort contains all pedigrees previously identified by Yu-Wai-Man et al. (2009) with additional generations and families. Given that families require an affected family member to be diagnosed, penetrance values are likely artificially inflated by ascertainment bias and smaller families skew towards penetrance inflation whilst our expanded cohort is more representative of true penetrance. Counteracting this inflation, 26.23% of LHON cases develop after age 30, indicating that a number of our 'unaffected' carriers would develop LHON at a later age. As seen in Figure 2.1, the majority of our cohort are multigenerational pedigrees meaning that the true percentile which go on to develop LHON at a later date would actually be much lower than this percentile. As a whole, the biases in ascertainment and late onset disease onset act in opposite directions and our penetrance estimates are likely an improvement from previous measures.

The increase of penetrance seen in females could be attributed to improved genetic diagnostics within the last decade; while males were classically diagnosed with LHON, given the lower likelihood of being affected, females could have previously had lower positive diagnoses.

We segmented the data further into m.11778G>A mutations by country of collection in Table 2.5 and British families by mutation in Table 2.6. We found it is probable that mutation has a greater influence on offspring's penetrance than country of origin, particularly in males (sons p = 2.60e-12; daughters p = 1.82e-04). Country of origin does seem to influence penetrance in females (p = 1.051e-05) but not males (p = 0.092), however, this could be indirectly measuring the differences in LHON causative mutation pathogenicity as the sampled mutant variant proportions differ by country of collection (Figure 2.3).

Phylogenetically speaking, the Finnish and Hungarian cohorts are likely to be most related, with the UK also quite closely related (Duda and Jan Zrzavý, 2016). Whilst only tracking the maternal line, Finnish pedigrees contained members of haplogroups H, J1, X, J2 and V while Hungarian pedigrees contained members of H, J1, X, K and U. Many of the UK cohort did not have haplogroup data, however, those covered were of

H, J, K and U haplogroups.

Tasmanian pedigrees are expected to have the most divergent nDNA background (whilst haplogroup directly assesses mtDNA ancestry, it indirectly also covers the maternal nDNA lineage to a less accurate degree), however, most of the country are not indigenous (Australian Bureau of Statistics, 2016) and it is likely that this cohort is comprised of some European ancestry family members, although this would still likely be most divergent. Given that the haplogroups of the Tasmanian families are H and J2, European ancestry is likely. H is extremely common in Europe while J2 is more commonly found within Near Eastern (Arabic and North Eastern Africa) regions and some European subclades (Pala et al., 2012; Roostalu et al., 2006).

In addition to haplogroup data and ethnogeographic data, indicating that our pedigrees are likely all of European descent (Richards et al., 2002), clinical notes indicate that the Tasmanian pedigrees were from families who emigrated from Britain and are related to the UK cohort. No data showing direct pedigree relation was available, however.

Finland and Hungary have the most similar LHON penetrance measurements (least squares), however, they also have the most similar proportions of LHON primary mutations (Figure 2.3) and it is likely that this effect is greater than the nDNA background effect.

This is further compounded by restricting data to the m.11778G>A mutation (Table 2.5); there is no difference in proportions of penetrance by country of collection in male offspring ($p = 0.057$), however, females are more affected ($p = 7.055e\text{-}06$), indicating that there is an effect of country of origin, albeit, not as significant as the mutation specific penetrance. Restricting data to the UK cohort (largest dataset, with all greatest range of LHON causative mutations), as seen in Table 2.6, further shows that mutation has a significant impact (sons $p = 2.616e\text{-}14$; daughters $p = 1.627e\text{-}05$).

The data also shows that the mothers' disease status greatly affects penetrance in offspring. This was extremely significant (total $p = 9.43e\text{-}09$) in the total population, particularly as the 2-sample test used Yates Correction, which is extremely stringent and has been argued that it is so stringent that it should not be used regardless of data normality (Hitchcock, 2009; Thompson, 1988). With our data, it was determined that Yates Correction should be used as the sample size was not extremely small and data was heteroskedastic. The sample size was, however, not so large that all populations and mutation groups could be tested. Only stratifications of m.11778G>A and m.3460G>A could be tested, alongside the UK and Finnish country groups. All tested measurements were significant, with the exception of UK daughters and m.11778G>A sons, indicating that these two groups were not affected by mothers' disease status, or more likely given the other results, were inadequately powered to detect significance at that sample stratification.

As such, we can confidently state that mothers' disease status greatly affects LHON

penetrance in offspring. This could be due to the environment in which the children are raised, as LHON is known to have an environmental influence to onset (a number of which are discussed in Section 1.5.4), or a secondary genetic loci which could be passed from mother to child (as discussed in Section 2.4.2 for X-linked loci).

If a secondary genetic loci exists on any autosomal chromosome, in a recessive model, an affected homozygous mother would have a 100% likelihood of passing this onto the child, alongside the mtDNA mutation, whilst a heterozygous mother would have a 50% chance of transmitting the mutant secondary loci allele. In a dominant model, an affected mother could be homozygous or heterozygous, each which would again be transmitting the mutant allele at 100% and 50% likelihood.

In terms of the 23rd chromosome, male children would receive a mutant allele from a heterozygous mother at 50% likelihood or 100% from a homozygous mother. When assuming the father does not carry the mutant allele on his X-chromosome, the odds of developing LHON by inheriting a mutant allele from a carrier mother are reduced as she could be affected by X-inactivation of the healthy allele within retinal tissue. If the father does carry the mutant allele on his X-chromosome, female offspring will receive this X chromosome from the father, which may or may not be inactivated in optic tissue, leaving the mother's X chromosome active in the eye.

This is greatly influenced by the prevalence of any abnormal allele at a secondary loci within the population.

2.4.2 X-Linked Modifier Gene

Following from the work by Bu and Rotter (1991), this project sought to test the X-linked hypothesis and the X-inactivated hypothesis in a newer data set and determine whether the results which Bu and Rotter (1991) found hold true nearly three decades later. The overarching hypothesis is that a hypothetical X-linked gene could be responsible for the difference in penetrance seen between male and female LHON carriers and this is further broken down into the X-linked hypothesis and the X-inactivation hypothesis. Males only have one X chromosome which they inherited off their mother, whereas females have two X chromosomes, one off each parent, and one of which undergoes X-inactivation for gene dosage purposes (Panning, 2008).

As such, males can be more susceptible to X-linked disease onset as they only have one X chromosome whereas females have two. All females are chimeras, being that X-inactivation does not occur at a single cell level but rather approximately at the 8 cell stage (Shvetsova et al., 2019), leading to some tissues having the X chromosome from one parent inactivated whilst other tissues can inactivate the X chromosome from the other parent. X-chromosome inactivation is not equally balanced, with skewed X-inactivation common in the general population (Shvetsova et al., 2019). Given the penetrance dimorphism between males and females, specific X-linked models were investigated rather than autosomal models which were more likely to be directly captured

by investigating nuclear DNA variants, as discussed in Section 2.4.3.

Unlike Bu and Rotter (1991), who found that the p-value was > 0.05 in all samples, which supported their H_0 theory that the X-linked and mitochondrial model was accurate, as seen in Tables 2.7 and 2.8, some of the χ^2 measurements in our cohort were large leading to a p-value below 0.05 and the rejection of the null hypothesis. Unusually, in this instance Bu and Rotter (1991) described a "straightforward χ^2 test", however, they use Equation 2.2.

$$\chi^2 = 2\Big(\sum \frac{(O_i - E_i)^2}{E_i} \Big) \tag{2.2}$$

This is double the standard Chi-Squared equation for the pooled goodness-of-fit test for males, Table 2.7. There is no indication why this is performed and χ^2 is inherently a two-tailed test which tests in both directions for differences between the observed and expected; doubling the classical χ^2 test does would create a four-tailed test while only a single dimensionality is tested. In practical terms, it increases the χ^2 value and increases the chances that the H_0 should be rejected, as happened in the total dataset and both the Tasmanian and UK Cohorts. If using a classical χ^2 formula, no probabilities are significant.

Despite this, Table 2.8, which does use a classical χ^2 formula, does have significant measurements for the Finnish population - which was not significant in the pooled cohort.

Bu and Rotter (1991) define an obligate heterozygote to be an unaffected mother with one or more affected sons, or an affected mother with one or more unaffected sons but as seen in Table 2 of their paper, where $s = 1$, all pedigrees show an observed value equal to n_s, indicating that all obligate heterozygous mothers within their study of $s = 1$ must have been an unaffected mother with one affected son rather than any affected mothers with one or more unaffected sons. As such, the dataset was further limited to unaffected mothers with one or more affected sons as seen in Table 2.9.

Limiting to unaffected mothers with affected sons removes the bias in the expected offspring formula (Equation 2.1) which demands that when $s = 1$, that the number of expected affected offspring = 1. It is further skewed towards smaller family sizes expecting to have a higher penetrance than larger ones, with a penetrance of 67.7% when $s = 2$ and 57.1% when $s = 3$. This approaches 50% penetrance When $s = 10$, where penetrance becomes 50.0%. In Table 2.9 the χ^2 test never returns a significant p-value and this is likely a more accurate test given the manner of deriving the expected number of male offspring.

As such, significance in Table 2.9 are the recommended measurements for the individual goodness-of-fit test, despite the apparent stated methodology, given the reparations to the bias in the lower sibship size families. In this model the male offspring develop LHON depending upon their inheritance of the wildtype or mutant X-linked allele.

This reduction of sample size lowers the χ^2 test's power to detect significant differences, however, only 20 of 174 mothers are excluded by this limitation. Further, whilst using a standard χ^2 test rather than the Bu and Rotter (1991) equation, described in Equation 2.2 for pooled cohorts, there is no significance of the χ^2 measurement either. This supports the statement that male offspring develop LHON depending upon their inheritance of the wildtype or mutant X-linked allele.

Where affected males = 0, it is a truncated distribution which was not corrected for as with cohorts containing unmodelled heterogeneity, Burton et al. (2000) found that ascertainment bias adjustments results in biased parameter estimates which do not match those in the sample or original population. As such, whilst these calculations are not true to the global population, they remain correct for our sampled participants. Bu and Rotter (1991) did not explicitly state their mechanism of ascertainment bias correction beyond "the Haldane method" which has a number of different implementations, so this methodology could not be directly replicated.

The X-Inactivation Hypothesis states that an affected female must be homozygous mutant or a heterozygous mutant with the healthy allele having undergone X-inactivation of the healthy allele in optic tissue.

To calculate T, the segregation ratio, data was restricted to unaffected mothers who have one or more affected sons. These are obligate heterozygotes and a larger cohort than affected mothers with one or more unaffected sons. This removes families with no male affected offspring, however, as T looks at the female offspring, the T ratio will be unaffected by this selection method.

T is shown in Table 2.10 with a range of 0.125-0.583 and a global value of 0.230. No significance was found by analysis of deviance or equality of proportions so the global value is an accurate representation of the full dataset. T = 0.230 is different from the value found by Bu and Rotter (1991) (T = 0.093), indicating that our cohort had a higher proportion of affected females.

K, the probability that a heterozygous female will be affected (penetrance; a higher K indicates a lower disease threshold) was then calculated as the ratio of affected mothers in the obligate heterozygote population (Table 2.11). It ranged from 0.100-0.385 with a global measurement of K = 0.176. The global measurement was used as analysis of deviance and equality of proportion tests found no significant differences between the cohorts. Bu and Rotter (1991) found K = 0.111 which was similar to our measurement.

Using global T and K values, q, the frequency of the affected X-linked allele, was then calculated. Bu and Rotter (1991) found q = 0.076 whilst our cohort found q = 0.283. This indicates that the our cohort either has a greater proportion of mutant X-linked modifier alleles in the population by chance, or that the prevalence of q in the population has shifted to favour the abnormal X-linked modifier allele. Calculations for q assume that q is a singular loci on the X-linked allele, however, it could also be a combination of multiple loci on the X chromosome which are inherited together

through linkage disequilibrium.

Given that only one human generation has passed since Bu and Rotter (1991), it is more likely that this is by chance or that our cohorts have different nuclear backgrounds to the samples captured by Bu and Rotter (1991), or that clinical diagnostics have improved. Improved true positive diagnoses of female LHON patients would alter K, the probability that a heterozygous female will be affected. As shown in Section 2.4.1, we did find a much higher penetrance in females which subsequently affects the calculation of q, the X-linked affected allele.

This methodology indirectly looks at the effect of nuclear background to a limited degree. By splitting by cohort and assuming that families within the same country have a closer nuclear background than those in different countries we did calculate individual measurements for T and K but found no significant difference between cohorts. It does not take into account that mutation specific burden could have a greater impact on penetrance and instead equates all 5 individual LHON mutations as the same loci with equal effects. It also assumes that X-inactivation is random, however, this has been shown to not be true, with preferential silencing of abnormal X chromosomes (Shvetsova et al., 2019). Additionally, as discussed in Section 2.4.1, our pedigrees are all European and some are related to each other, indicating that nuclear variation within cohorts could be greater than variation between select cohorts, e.g. Tasmanian and UK.

As q = 0.283 (affected X-linked allele frequency), this is comparatively higher than the q calculated by Bu and Rotter (1991) (q = 0.076). This methodology is based on the assumption that the mutant X allele comes from the maternal line and when q = 0.283, a high proportion of the population would carry the allele by chance, including the father - who was assumed to be a wildtype, selected by chance and not a carrier.

Following from the calculation of q, the proportion of affected females heterozygous at X-linked locus was 38.38% whilst the other 61.62% are assumed to be homozygous mutant. This proportion is close to the inverse of the 60% and 40% respectively found by Bu and Rotter (1991). This is likely a result of the greatly increased q value, indicating that any abnormal X-linked gene is common, rather than rare, within the population.

Following from work by Bu and Rotter (1991), we found that within our cohort, it does statistically indicate that penetrance could occur as a result of an X-linked modifier gene. Unlike their indication that it is rare in the population (q = 0.076) we found the allele to be common in the population (q = 0.283), which could explain why it has been undetected at present. With rare population variants, it can be assumed that carriers would also be LHON affected, however, with it common in the population, it could be inherited from the paternal, rather than just the maternal, line to affect daughters. Further, common alleles require more samples to create a statistical test strong enough to identify the mutant allele within the population. With rare disease, studies often struggle to capture sufficient sample numbers and hence study power to prove common

variants as pathogenic.

This higher penetrance is more explanatory towards the disease patterns seen in the large multi-generational LHON families, however. If q is small, it would be expected that LHON onset would cease within a few generations of the maternal lineage progression as each generation brings a new X chromosome from each father - who could be assumed to not carry the abnormal X-linked gene at q = 0.076. At q = 0.283 there is a larger chance that the X-linked abnormal allele could be inherited from either the mother or father and disease transmission would continue down the pedigree - as is often seen.

2.4.3 Nuclear DNA Variants

Data from Illumina Infinium HumanMethylation27 BeadChips were first analysed to identify differential methylation between LHON affected patients and carriers. The HumanMethylation27 BeadChip is an older array which has been followed by the Infinium HumanMethylation450 BeadChip and Infinium MethylationEPIC BeadChip more recently. The difference between chips relates to the number of probes on the chip (~27,000, ~450,000 and ~850,000, respectively) and the type of chemistry involved on the probes. The HumanMethylation27 BeadChip only contains Type I probes whilst the HumanMethylation450 and MethylationEPIC BeadChips also contain Type II probes - thus the chemistry, and analysis, of arrays differs.

The programming language R was chosen to analyse the BeadChips, as present gold standard analysis pipelines predominantly use packages available through R and Bioconductor (Huber et al., 2015; Morris and Beck, 2015; Wang et al., 2018).

BeadChip analysis pipelines have extensive QC processing to ensure that technical error is minimised throughout the analysis process. Processing standards have changed since the release of the HumanMethylation27 BeadChip and some of the recommended pipeline processes are built to directly handle the HumanMethylation450 BeadChip and later (Morris and Beck, 2015; Touleimat and Tost, 2012; Wang et al., 2018). As such, while some packages do directly handle the data (Davis et al., 2017; Du et al., 2008), they do not have all of the recommended procedures, such as removal of low quality and poorly sampled probes, so these were specifically written into R to implement a more robust analysis than using a historic package and pipeline.

There is a significant effect of batch effect on microarray data (Price and Robinson, 2018), and this effect is directly visible within control probes (Figure S3). When samples were prepared, they were loaded into the BeadChip by family groupings and not randomised which led to difficulty in differentiating between familial, batch and mutation effects. Further variance is seen when assays are performed on different days, however, our samples were performed on the same day with only one additional array between our samples. Had sample order been randomised during loading of the arrays, this batch effect could have been controlled for, but due to the ordered nature

of the samples, any normalisation of the batch effect would also normalise methylation patterns between LHON mutation and familial patterns. This sample arrangement had a detrimental result on our confidence of the analysis but despite this, while noticeable, the batch effect has not prevented identification of candidate differentially methylated genes.

Genotype is also known to affect methylation patterns (Gertz et al., 2011; Grimm et al., 2019) and as genotype runs in families, methylation patterns are affected. Similarly, whilst debated, it is believed that transgenerational epigenetic modifications further occur within families, either as marks which are directly inherited from parents, or as a result of being brought up in a similar environment (Horsthemke, 2018; Kaati et al., 2007; Nilsson et al., 2018).

Samples initially appeared to be grouping by mutation status (Figure 2.9), however, quantile normalisation will have reduced the batch effect and possibly removed any familial/causative mutation methylation significance during this process as quantile normalisation is very stringent.

As metadata regarding smoking status was missing from several samples, different groupings of linear regressions were performed to optimise the available data. For those which contained smoking metadata, cigarettes per day and having ever smoked did greatly impact methylation status, alongside gender. Of the independent variables tested, age had the least impact on methylation status as incorporating it into the regression had minimal impact.

During the QC process, the two samples which failed to pass QC were a male unaffected carrier and his affected brother. This resulted in only 1 of the remaining 8 unaffected carriers being male and the other 7 all female; there are significant methylation differences between males and females (Hall et al., 2014; Nino et al., 2018), particularly on the X-chromosome to account for gene dosage. Due to this, it is common for X-chromosome probes to be fully removed from methylation analysis; given that there is a difference between male and female methylation patterns and that only 1 male unaffected carrier passed QC and that it is predicted that LHON could be affected by an X-Linked gene (Bu and Rotter, 1991; Chen and Denton, 1991; Hudson et al., 2005; Phasukkijwatana et al., 2010; Qu et al., 2010; Shankar et al., 2008; Vilkki et al., 1991), data was split into male and female cohorts and analysed separately rather than excluding the X-chromosome or comparing male autosomal chromosomes to unaffected autosomal chromosomes which are heavily skewed towards female methylation patterns.

44 genes were found to be hypermethylated and 23 hypomethylated in LHON patients when compared to controls, with some sex differences between males and females (Tables S3 and S4).

Exome analysis identified 3,833 genes which exclusively occurred in either LHON patients or carriers in both dominant and recessive models. The exome array captured information on 17,403 genes indicating that 22.02% of the genes had unique variants

and this was too large to accurately identify any novel LHON disease causing variants.

These unique exome variants were then cross-matched against the list of differentially methylated genes, resulting in 29 hypermethylated and 17 hypomethylated genes which contained unique variants between the LHON patients and carriers - that could be either causative or protective.

They then underwent pathway analysis to identify gene sets which could indicate novel pathways which affect LHON expression. Most of the chemical and genetic perturbations gene sets were from cancer data sets, relating to cell survival. Interestingly, they mapped to the gene set which is identified to become hypermethylated in breast progenitor cells pre-exposed to estradiol (Cheng et al., 2008), which is a sex hormone that targets ERA and ERB, the latter of which has been investigated for a target in LHON treatment (Giordano et al., 2011; Pisano et al., 2015).

The most significant matches within the C5 Biological Process Complete gene set list are from pathways involved in neurogenesis, neuron differentiation and development. LHON results in RGC cell death, a type of neuronal cell (Kirches, 2011; Maresca, 2011; Wong et al., 2002; Yu-Wai-Man and Chinnery, 2000; Yu-Wai-Man et al., 2009) and of our identified list of 45 candidate genes, these were over-represented in neuronal gene sets, indicating that these variants and methylation patterns could implicate novel genes as modifier genes which are either causative or protective towards LHON. Whilst methylation can occur as a result of LHON onset, the genotype is upstream, meaning that these genes are more likely to be causative rather than develop changes as a result of LHON onset. The identification of neuronal gene sets as significant was further confirmed by the more stringent Fisher's Exact Test used by PANTHER's Overrepresentation Test.

Additional neuronal gene sets were also identified within the C5 Biological Process Complete gene set database, significantly, gene sets relating to regulation of oxidative stress induced cell death, cell death in response to oxidative stress, and further cell death and oxidative stress pathways. Oxidative stress triggers nucleoids to fold to a more compact state (Noack et al., 2006; Rebelo et al., 2009; Sadakierska-Chudy et al., 2014) and could down-regulate mitochondrially encoded genes which are required for OXPHOS. LHON cells are particularly susceptible to oxidative stress (Battisti et al., 2004; Meyerson et al., 2015), which also increases free radical production, and this can directly result in cell death (Ott et al., 2007; Ryter et al., 2006; Zhuo et al., 2012).

This work seems to identify novel genes which interact in pathways which realistically could be related to the LHON phenotype, and potentially, these genes could act as modifiers to explain some of the variable expression and unpredictable disease onset of LHON.

Directly reviewing specific gene function, a number of genes seem to directly relate to mitochondrial, neuronal or retinal function, including *FGF20*, *FZD1*, *GPM6A*, *GPR157*, *GPR37L1*, *GRB10*, *IDH3G*, *LAMC2*, *MEGF10*, *NIPA1*, *PCDHGC4*, *PHYH*, *RAB32*, *RBP4*, *SLC25A36* and *SLC6A18*.

All gene functions are reviewed within Section 5.4 and some genes present functional features which are particularly relevant to LHON.

FZD1, which is associated with exudative vitreoretinopathy (Kaykas et al., 2004), a condition which prevents peripheral retinal angiogenesis and causes a diverse range of phenotypes within a familial lineage, with some patients asymptomatic carriers (National Library of Medicine (US), 2019). Additionally, *PHYH* mutations are found within 90% of patients clinically diagnosed with Refsum disease, another retinal disorder which causes retinitis pigmentosa (Patterson and Percy, 2015). Severe autosomal recessive retinitis pigmentosa has also been found to be caused by *RBP4* mutations (Cukras et al., 2012).

MEGF10 also has a role in retinal neuron mosaic distribution, particularly for starburst amacrine cells and horizontal cells (Kay et al., 2012). Interruptions in supporting neuronal cell types could induce cell death in dependent cells.

IDH3G encodes isocitrate dehydrogenase, a mitochondrial matrix protein which catalyses oxidative decarboxylation of isocitrate into α-ketoglutarate within the citric acid cycle (Smolková and Ježek, 2012). *SLC25A36* has an essential role in mtDNA and mtRNA synthesis and breakdown through pyrimidine transport (Di Noia et al., 2014) and *RAB32* has a role in both autophagy (Wang et al., 2012) and apoptosis via mitochondrial fission control (Bui et al., 2010). Rab32 is upregulated throughout multiple sclerosis disease progression and causes ER stress with mitochondrial cell death in primary neurons (Haile et al., 2017). Multiple sclerosis-like symptoms are often seen in Harding's disease (LHON-plus) (Carelli et al., 2001; Joshi and Kermode, 2019; Nikoskelainen et al., 1995). Of note, *RAB32* is significantly methylated in different regions of the 6:146905888-146907189 locus, with opposing methylation patterns between affected LHON patients and asymptomatic carriers, with one region hypermethylated in patients when compared to carriers, whilst another region is hypomethylated when compared to carriers across multiple probes.

Both results from pathway analysis and individual gene investigation look promising for LHON novel candidate genes. Three of the identified 45 genes directly relate to retinal disease, a further 3 affect mitochondrial function and many affect neurogenesis, as identified through over-representation of genes within gene set pathway analysis. Given the thousands of genes investigated and functional results, our candidate gene list warrants further investigation.

Chapter 3 | Functional Characterisation of LHON Fibroblasts

3.1 Introduction

LHON is a disease that predominantly affects RGCs, however, they exist within the eye's retina and their axons extend to form the optic nerve. As such, this tissue is not readily available for study from live patients and another model must be used. Bahr et al. (2020); Jankauskaitė et al. (2017) reviewed cellular and animal models of LHON and after consideration of resources and the ability of the model to accurately represent LHON, a primary fibroblast model was selected.

Primary fibroblasts have long been used in a broad range of scientific studies (Li et al., 2013; Marthandan et al., 2016; Rohde et al., 2014), particularly within mitochondrial disease (Distelmaier et al., 2015; Millis and Pious, 1973; Woś et al., 2016).

Fibroblasts are easily attainable from a skin biopsy and readily established (Villegas and McPhaul, 2001). With proper preparation, the minimally invasive method can allow for a high cell yield, with minimal contamination from morphologically different keratinocytes (Takashima, 2001). Studies involving other cell types, such as myoblasts, often struggle with fibroblast contamination (Chowdhury et al., 2015; Froehlich et al., 2014) which can affect study results when samples are each comprised of differing proportions of cell types. Despite the many advances in iPSCs models with three LHON specific models developed (Bahr et al., 2020), in-house work has seen difficulty in reprogramming iPSCs, with variable differentiation success. Given the breadth of other work throughout this project, iPSCs were not chosen as a model due to time and availability constraints.

Most importantly, fibroblasts have been previously identified and used as a model for LHON in a range of experiments (Angebault et al., 2011; Jankauskaitė et al., 2017; Pisano et al., 2015; Yu-Wai-Man et al., 2017), with fibroblasts behaving as expected for a Complex I disorder. They have not previously been modelled in LHON against the extensive range of biological mechanisms that this project seeks to investigate.

This chapter seeks to further establish specific patient-derived LHON fibroblast cell lines and comprehensively characterise them with the goal of identifying biological pathways which could have a role in disease onset and suitability for that cell line within drug testing. Cells must be characterised to confirm that they are behaving as expected for a LHON model before interrogation of further biochemical pathways. Ac-

curate characterisation of disease mechanisms will allow for identification of involved pathways which may allow for novel treatment strategies which minimise, or ideally prevent, disease progression. Furthermore, functional analysis in cell models could confirm hypothetical genes identified in the genetic studies discussed in Chapter 2.

Characterisation covers a number of interrelated systems to identify pathological mechanisms which may precipitate visual loss in LHON patients including: mitochondrial copy number, ATP production, cellular oxygen consumption, calcium homeostasis, mitochondrial membrane potential, the mitochondrial network and ER-mitochondrial interactions. These mechanisms are implicated in mitochondrial biogenesis, energy metabolism, calcium signalling, and cell death pathways.

3.2 METHODOLOGY

3.2.1 Patient Cohort

Skin biopsies were collected from the forearm of LHON patients and healthy control volunteers by Doctors Patrick Yu-Wai-Man (University of Cambridge) and Hannah Steele (Newcastle University); many thanks to those involved in both sample collection and donation. Samples were transferred to Newcastle Biobank where primary fibroblast cell lines were established. The patient cohort was composed of three unrelated, healthy controls and five unrelated cases with both a clinical diagnosis of LHON and confirmed homoplasmic, pathogenic primary mutations in mtDNA Complex I subunits. They carried one of the three primary LHON mutations which account for the majority of LHON cases (Yu-Wai-Man and Chinnery, 2000); three patients are affected by the m.11778G>A mutation, A1-11778, A3-11778 and A4-11778, and the remaining two patients, A2-14484 and A5-3460, are affected by the m.14484T>C and m.3460G>A mutations respectively, as indicated in Table 3.1. An unaffected carrier was also investigated in preliminary work, U1-11778, who was the mother to A1-11778.

Table 3.1: *Details of primary fibroblast cell lines functionally characterised.*

Cell Line	Status	Gender	Age
C1	Control	Female	45
C2	Control	Female	26
C3	Control	Female	34
U1-11778	m.11778G>A carrier	Female	53
A1-11778	m.11778G>A mutant	Male	20
A2-14484	m.14484T>C mutant	Male	33
A3-11778	m.11778G>A mutant	Male	42
A4-11778	m.11778G>A mutant	Male	45
A5-3460	m.3460G>A mutant	Male	36

3.2.2 Cell Culture

To establish cell lines, cryovials acquired from Newcastle Biobank were quickly thawed in a 37°C water bath until samples approached phase transition from solid to liquid. These were then removed and transferred into a T25 CELLSTAR Filter Cap Cell Culture Flask (690175; Greiner Bio-One) with Growth Medium (GMEM), comprised of Minimum Essential Media (21090-055; GIBCO) (MEM) supplemented with 10% (v/v) Fetal Bovine Serum (F7524; Sigma-Aldrich) (FBS), 1% (v/v) MEM Vitamins Solution (100x) (11120037; GIBCO), 1% (v/v) L-Glutamine (200 mM) (25030024; GIBCO), 1% (v/v) Penicillin-Streptomycin (10,000 U/mL) (15140122; GIBCO), 1% (v/v) Sodium Pyruvate (100 mM) (11360070; GIBCO) and 1% (v/v) MEM Non-Essential Amino Acids Solution (100X) (11140035; GIBCO).

Cells were given 3-4 hours to adhere before washing in Phosphate Buffered Saline (Dulbecco A) (BR0014G; Oxoid Ltd.) (PBS) and replacing the media.

Cell lines were initially cultured in T25 CELLSTAR Filter Cap Cell Culture Flasks and fed every 2-4 days as necessary before transferral to T75 CELLSTAR Filter Cap Cell Culture Flasks (658175; Greiner Bio-One).

Cells were trypsinised for passaging and collection using 10% Trypsin-EDTA (0.5%), no phenol red (15400054; GIBCO) in PBS for 5 minutes at 37°C before inactivation with GMEM.

Cells were pelleted by centrifugation at 1300 RCF for 5 minutes at 24°C for live cells and 4°C for protein and DNA collection.

Pelleted cells were resuspended and frozen in 10% (v/v) Dimethyl Sulfoxide (D8418; Sigma-Aldrich) (DMSO), filter sterilised with Polyethersulfone Syringe Filter (28145-501; VWR), in 90% (v/v) FBS using a Mr. Frosty™ (5100-0001; Thermo Fisher Scientific) for a minimum of 24 hours at -80°C before long-term storage in gas phase liquid nitrogen.

To count cells, cells were resuspended in 1 ml GMEM and a 10% (v/v) cell suspension, (v/v) 40% GMEM and 50% (v/v) Trypan Blue Solution (T8154; Sigma-Aldrich) solution was prepared for cells to be counted as a monolayer on a BS748 Improved Neubauer Cell Counting Chamber (AS1000; Hawksley) before counting and calculating cells·µl^{-1}.

All cell lines were stored at 37°C, 5% CO_2, and routinely screened for mycoplasma. Experiments were performed on cells from passage 5 to passage 15.

3.2.3 DNA Extraction

Following count, cells were seeded at 1x10^6 into a T75 CELLSTAR Filter Cap Cell Culture Flask and incubated at 37°C for 2 days until they reached 70-80% confluency before being pelleted in PBS and frozen at -80°C.

Cells were later resuspended in 200 µl PBS and the DNA was extracted using DNeasy Blood & Tissue Kit (69506; QIAGEN), following the manufacturer's instructions.

3.2.4 mtDNA Copy Number

Quantification of mtDNA copy number has previously been described by our lab (Grady et al., 2014; Pyle et al., 2016), however, the sequence location of the *MT-ND1* forwards Quantitative Polymerase Chain Reaction (qPCR) primer contains the m.3460G>A primary LHON mutation, so this assay would not be appropriate for quantification of copy number in LHON samples and an altered methodology was necessary. Optimisation of *B2M* qPCR primers were also carried out during validation of a new copy number multiplex.

Determination of Novel Multiplex

MT-RNR2 qPCR primers were designed following in-house meta-analysis of public and private data collections to analyse 20,000 human mtDNA sequences for mutations. Primer and probe sequences were identified by screening the mitochondrial genome for regions of genetic stability as characterised by genetic homogeneity and few mutations. The regions were then subsequently screened for ideal primer and probe sites and further checked on EMPOP (The European DNA Profiling Group et al., 2016) for external confirmation of population sequence data.

The region around the previous lab standard *B2M* probe was then screened for suitable primer sites and new primers were identified and screened using NCBI dbSNP (Sherry et al., 2001) to check for variation in the sequence identity.

All primers and probes were tested using Integrated DNA Technologies Inc. (IDT) OligoAnalyzer 3.1 (Integrated DNA Technologies, 2017) for *in silico* predictions for hairpins, self-dimers and hetero-dimers with other components of the *MT-ND4/B2M/RNR-2* triplex, alongside checking for similar melting temperatures and ~50% GC content.

Primers were then synthesised by IDT and checked for an optimum annealing temperature via gradient PCR (Polymerase Chain Reaction), as shown in Tables 3.2 and 3.3. All PCR was carried out using a Veriti™ 96-Well Thermal Cycler (4375786; Applied Biosystems™).

Table 3.2: *qPCR reaction composition where* MT-ND4/B2M/MT-RNR2 *are amplified with their respective forward and reverse primers. Primer sequence identity shown in Appendix Table S8.*

Volume	Component
5 µl	5x MyTaq Reaction Buffer (BIO-37111; Bioline)
0.2 µl	MyTaq HS DNA Polymerase (BIO-21111; Bioline)
1 µl	10 µM Forward qPCR primer (*MT-ND4/B2M/MT-RNR2)*
1 µl	10 µM Reverse qPCR primer (*MT-ND4/B2M/MT-RNR2)*
1 µl	25-50 ng DNA
16.8 µl	dH_2O

Table 3.3: *Thermocycling program with a variable annealing temperature of 49°C - 61°C.*

	Temperature/Capture	Time	
Initial Denaturation	95°C	1 min	
Amplify	95°C	15 s	35 cycles
	49°C - 61°C (Gradient)	15 s	
	72°C	10 s	
Final Extension	72°C	5 min	
Hold	4°C	∞	

Primers and probes were then tested in a singleplex SYBR Green assay as shown in

Tables 3.4 and 3.5. This was followed by singleplex, duplex and triplex TaqMan assays, which were designed as shown in Tables 3.6 and 3.7.

To determine whether Cq values decreased between single-, du- and triplex, 2-sided T-Tests were calculated for homoscedastic data of the Cq values between assays.

Table 3.4: *qPCR reaction composition for each well where matching forward primers were used with their reverse primer and standard DNA in a singleplex. Primer and probe sequence identity shown in Appendix Tables S9 and S10.*

Volume	**Component**
10 µl	1x iTaq Universal SYBR Green Supermix (1725125; Bio-Rad)
0.6 µl	10 µM *MT-ND4*/New *B2M/MT-RNR2* Forward primer
0.6 µl	10 µM *MT-ND4*/New *B2M/MT-RNR2* Reverse primer
1 µl	Standard *MT-ND4*/New *B2M/MT-RNR2* DNA/Blank
7.8 µl	dH_2O

Table 3.5: *SYBR Green qPCR thermocycling program.*

	Temperature/Capture	**Time**	
Initial Denaturation	95°C	3 min	
Amplify	95°C	10 s	39 cycles
	58°C	1 min	
	Image Fluorescence	-	

Table 3.6: *qPCR reaction composition for each well where water produces a reaction volume of 20 µl but varies depending on singleplex (1 primer and probe set + their standard), duplex (2 primer and probe sets + their standard) or triplex (3 primer and probe sets + their standard). Primer and probe sequence identity shown in Appendix Tables S9 and S10.*

Volume	**Component**
10 µl	iTaq Universal Probes Supermix (1725135; Bio-Rad)
0.4 µl	10 µM *MT-RNR2* Probe
0.14 µl	10 µM *MT-RNR2* Forward primer
0.14 µl	10 µM *MT-RNR2* Reverse primer
0.4 µl	10 µM *B2M* Probe
0.6 µl	10 µM New *B2M* Forward primer
0.6 µl	10 µM New *B2M* Reverse primer
0.4 µl	10 µM *MT-ND4* Probe
0.14 µl	10 µM *MT-ND4* Forward primer
0.14 µl	10 µM *MT-ND4* Reverse primer
1 µl	MT-ND4/New B2M/MT-RNR2 PCR Amplified DNA Standard/Blank
× µl	dH_2O

Table 3.7: *qPCR thermocycling program.*

	Temperature/Capture	**Time**	
Initial Denaturation	95°C	3 min	
Amplify	95°C	10 s	39 cycles
	58°C	1 min	
	Read Plate	-	

Generation of Standards

qPCR standards were amplified using PCR for *MT-ND1*, *MT-ND4*, *B2M* and *MT-RNR2* as shown in Table 3.8 and Table 3.9.

Table 3.8: *PCR reaction composition where* MT-ND1/MT-ND4/B2M/MT-RNR2 *are amplified with their respective forward and reverse primers. Primer sequence identity shown in Appendix Table S8.*

Volume	**Component**
5 µl	5x MyTaq Reaction Buffer
0.2 µl	MyTaq HS DNA Polymerase
1 µl	10 µM Forward primer (MT-ND1/MT-ND4/B2M/MT-RNR2)
1 µl	10 µM Reverse Primer (MT-ND1/MT-ND4/B2M/MT-RNR2)
1 µl	25-50 ng DNA
16.8 µl	dH_2O

Table 3.9: *qPCR standard PCR thermocycling program.*

	Temperature	**Time**	
Initial Denaturation	95°C	1 min	
Amplify	95°C	15 s	35 cycles
	61°C	15 s	
	72°C	10 s	
Final Extension	72°C	5 min	
Hold	4°C	∞	

10 PCR products were pooled and loaded with DNA Gel Loading Dye (6X) (R0611; Thermo Fisher Scientific) then electrophoresed in a large, single well of a 1% agarose gel (BIO-41025; Bioline) + 0.005% SafeView Nucleic Acid Stain (NBS-SV1; NBS Biologicals) in a 1x dilution of Tris-Acetate-EDTA, 50x (129237; QIAGEN) buffer in dH_2O for 90 minutes at 65 V. A GeneRuler 1 Kb Plus DNA Ladder (11511635; Thermo Fisher Scientific) and negative controls were ran in separate wells. Gels were imaged on a GelDoc-It^e (UVP) imaging system with VisionWorks LS (UVP) software for verification

of product size and the PCR product was extracted using a QIAquick Gel Extraction Kit (28706; QIAGEN), as per manufacturer protocol.

DNA concentration of standards and DNA extracted from cell pellet samples (as described in Section 3.2.2) were then measured on an 8-Sample Spectrophotometer NanoDrop (ND-8000-GL; Thermo Fisher Scientific)) and copy number per µl was calculated by:

$$\text{Copy Number}\cdot\mu l^{-1} = [C \div (L \times 2 \times 330)] \times A$$

Where C is DNA concentration x 10^{-9} , L is the amplicon length in bp and A is Avogadro's number.

DNA standards were then rediluted to $1x10^{10}$ copies·µl^{-1} and a range of $1x10^{8}$ copies·µl^{-1} to $1x10^{2}$ copies·µl^{-1} were used to produce standard curves.

qPCR Assay

qPCR was performed as a triplex assay on a CFX96 Touch™ Real-Time PCR Detection System (1855195; Bio-Rad) as shown in Tables 3.10 and Table 3.11; amplification temperature of 58°C used in Table 3.7 was increased to 62°C after trialling the new triplex with the optimum conditions of the old triplex and determining that this was also most efficient for the new triplex. All qPCR assays were analysed in Bio-Rad CFX Manager 3.1.

Table 3.10: *qPCR reaction composition for each well. Primer and probe sequence identity shown in Appendix Tables S9 and S10.*

Volume	Component
10 µl	iTaq Universal Probes Supermix
0.4 µl	10 µM *MT-ND1* Probe
0.14 µl	10 µM *MT-ND1* Forward primer
0.14 µl	10 µM *MT-ND1* Reverse primer
0.4 µl	10 µM *B2M* Probe
0.6 µl	10 µM *B2M* Forward primer
0.6 µl	10 µM *B2M* Reverse primer
0.4 µl	10 µM *MT-ND4* Probe
0.14 µl	10 µM *MT-ND4* Forward primer
0.14 µl	10 µM *MT-ND4* Reverse primer
1 µl	Sample/Standard/Blank
6.04 µl	dH_2O

Results underwent QC to reduce standard deviation of triplicates below 0.3 by removing outlying measurements, and copy number of mtDNA was calculated for LHON patients and controls.

Mitochondrial copy numbers were then calculated using the calculation $2 \times (2^{-\Delta Ct})$ whereby ΔCt represents the change in Ct value (the number of cycles taken to reach the threshold fluorescence and register above background fluorescence) between *MT-*

Table 3.11: *qPCR final thermocycling program.*

	Temperature/Capture	**Time**	
Initial Denaturation	95°C	3 min	
Amplify	95°C	10 s	39 cycles
	62°C	1 min	
	Read Plate	-	

ND1/MT-RNR2 and *B2M* (mitochondrial copy number), and *MT-ND4* and *B2M* (copy number of mitochondria unaffected by deletions).

Direct comparison of the lab standard, original triplex (Grady et al., 2014; Pyle et al., 2016), for blood and fibroblast DNA samples were also measured. Finally, the copy number of all patient fibroblast samples from Table 3.1 were measured across three passages using the new assay.

3.2.5 ATP Production During Metabolic Stress

40,000 cells were seeded in 200 µl of GMEM into 12 wells of a 96 Well Clear Polystyrene TC-Treated Microplate (3599; Corning™) and also a 96 Well Solid White Polystyrene TC-Treated Microplate (3917; Corning™) and incubated overnight at 37°C.

Cells were rinsed in PBS before replacing media with 200 µl ATP Assay Buffer (156mM NaCl (S9888; Sigma-Aldrich), 3mM KCl (746436; Sigma-Aldrich), 2mM $MgSO_4$ (M7506; Sigma-Aldrich), 1.25mM KH_2PO_4, 2mM $CaCl_2$ (C1016; Sigma-Aldrich) and 20mM 4-(2-hydroxyethyl)-1-Piperazineethanesulfonic Acid (H3375; Sigma-Aldrich)) supplemented for one of four conditions: 5mM Glucose (G7021; Sigma-Aldrich), 5mM Deoxyglucose (D8375; Sigma-Aldrich), 5mM Glucose and Oligomycin A (75351; Sigma-Aldrich) 2.5µg·ml^{-1} or 5mM Deoxyglucose and Oligomycin A 2.5µg·ml^{-1}, as biological triplicates and incubated at 37°C for 1.5 hours. Cells under Glucose conditions are capable of undergoing glycolysis whilst Deoxyglucose conditions prevents cells from producing ATP through glycolysis. Oligomycin A inhibits ATP synthase, further limiting cells to rely on the limited ATP production allowed by Complexes I-IV.

90 µl of supplemented ATP Assay Buffer was removed from each well of the white plate and 100 µl CellTiter-Glo Luminescent Reagent (G7570; Promega) (prepared according to manufacturer instructions) was added. The plate was then slowly rocked on a platform shaker (AQS Manufacturing Ltd) for 10 minutes and incubated in the dark for a further 15 minutes. Luminescence was then measured with a 1000 ms integration time on a Luminoskan™ Ascent Microplate Luminometer (5300330; Thermo Fisher Scientific)).

The cells in the 96 Well Solid White Polystyrene TC-Treated Microplate were rinsed with PBS and Protein Assay Dye Reagent Concentrate (5000006; Bio-Rad) was used to perform a Bradford assay in accordance to manufacturer's instructions.

ATP assay measurements were normalised to average mg protein·ml^{-1} across each

cell line.

3.2.6 Cellular Oxygen Consumption

Seahorse XFe96 FluxPaks (102416-100; Agilent Technologies) were used to measure the Oxygen Consumption Rate (OCR). A total of 20,000 cells were seeded into each well of the Seahorse XF96 Cell Culture Microplate in 80 µl GMEM and the Seahorse XF96 Cartridge was rehydrated with 200 µl Seahorse XF Calibrant Solution 24 hours prior to the experiment. Dulbecco's Modified Eagle Medium, no glucose, no glutamine, no phenol red (A1443001; GIBCO) was supplemented with 5.5 mM Glucose, 1 mM Sodium Pyruvate (100 mM) and 2 mM L-Glutamine (200 mM) [pH 7] and cells were incubated in 175 µl of this Seahorse media at 37°C in a non-CO_2 incubator for 1 hour.

OCR was measured on a Seahorse XFe96 Extracellular Flux Analyzer (Agilent Technologies) under basal conditions and following the sequential injection of: A) 1.5 µM Oligomycin A to inhibit ATP synthase, B) 1 µM Carbonyl Cyanide 4-(Trifluoromethoxy)phenylhydrazone (C2920; Sigma-Aldrich) (FCCP) to uncouple the mitochondrial chain, C) 1.5 µM FCCP to ensure full uncoupling and D) 1 µM Rotenone (R8875; Sigma-Aldrich) and 1 µM Antimycin A (A0149; Sigma-Aldrich) to inhibit Complexes I and III respectively, preventing oxidative phosphorylation to measure non-mitochondrial respiration. Protein Assay Dye Reagent Concentrate was used to perform a Bradford assay in accordance to manufacturer's instructions to normalise OCR to mg of protein using Wave Desktop 2.1.2.0 (Agilent Technologies, 2017). Wells with measurements more than 2 standard deviations from the mean of the group were excluded, leaving a minimum of 12 technical replicates of each cell line to calculate basal respiration, ATP production, proton leak, maximal respiration, spare respiratory capacity and non-mitochondrial respiration, with measurements indicated in Figure 3.1.

Statistical analysis was then performed using a two-tailed unpaired t-test for homoscedastic data between patients and controls.

3.2.7 Calcium Homeostasis

Using cells seeded 24 hours previously at 100,000 in a 35 mm Glass Bottom Dish (HBST-3522; WillCo Wells), cells were incubated at room temperature with 0.4% Rhod-2, AM, cell permeant (R1245MP; Life Technologies), reconstituted in DMSO, in 1 ml GMEM for 30 minutes before washing twice in PBS and imaging on a Nikon A1r point-scanning confocal microscope at x60 magnification, using a 1.40 numerical aperture oil objective, in 1 ml Tyrode's solution (136.9 mM NaCl, 2.7 mM KCl, 1.1 mM $MgCl_2$ (M8266; Sigma-Aldrich), 417 µM NaH_2PO_4 (S3264; Sigma-Aldrich), 11.9 mM $NaHCO_3$ (792519; Sigma-Aldrich), 10 mM Glucose and 2 mM $CaCl_2$ [pH 7.4]). 1 minute after Z-project recording, 100 µM Histamine (H7125; Sigma-Aldrich) was applied and cells were recorded for a further 4 minutes.

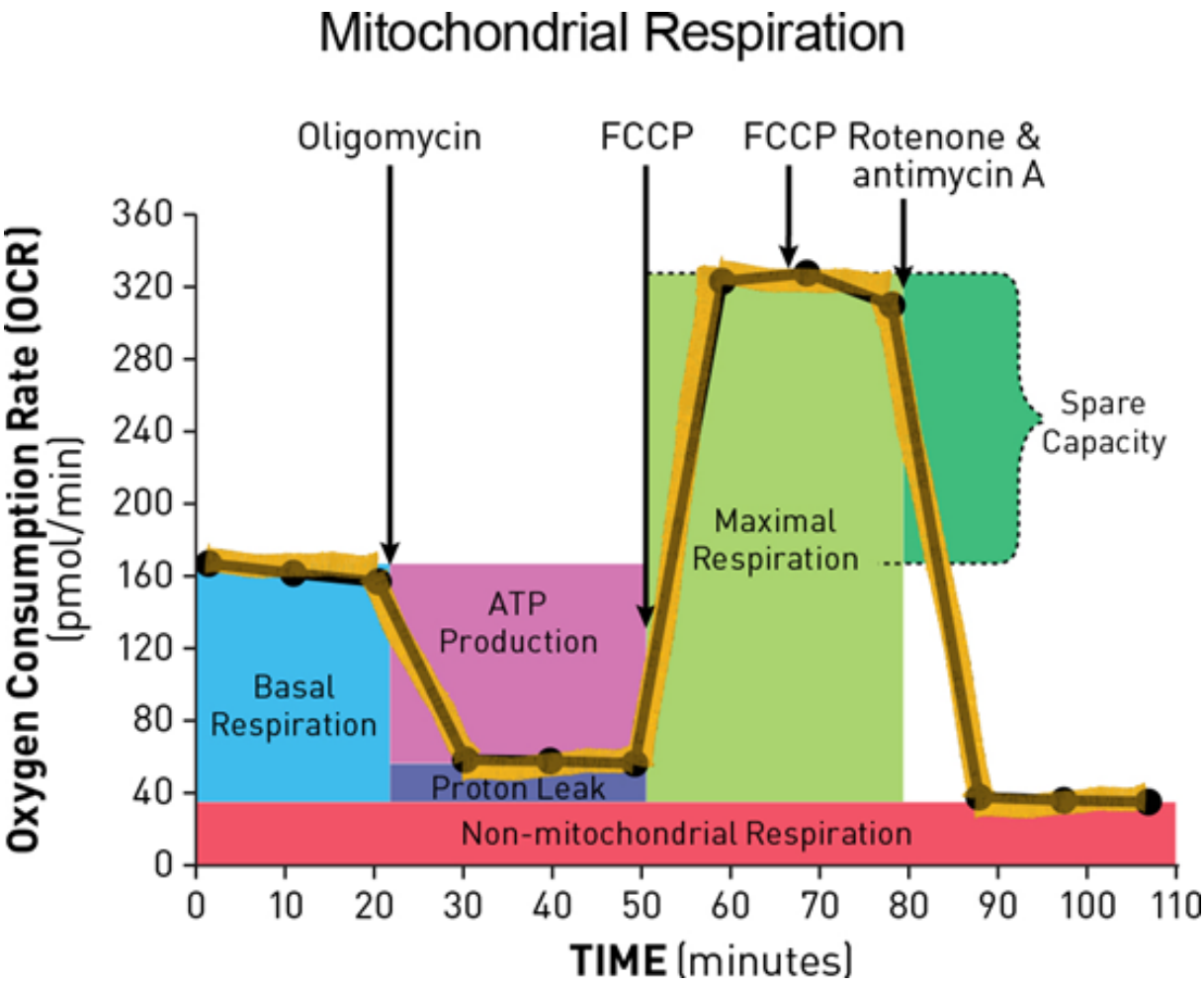

Figure 3.1: *Seahorse XF cell mito stress profile showing proportions of mitochondrial function from assay relating to drug injections. Adapted from Seahorse Bioscience (2015).*

Histamine stimulation triggers PLC to release intracellular Ca^{2+} and induces the influx of extracellular Ca^{2+} (Li et al., 2012a); Rhod-2, AM then binds Ca^{2+} and fluorescence intensity increases more than 100-fold upon binding where it is then sequestered by the mitochondria and a maximal measurement of mitochondrial Ca^{2+} uptake can be measured.

Videos were then analysed using Fiji (ImageJ 1.52i) (Schindelin et al., 2012) by normalising for background intensity and calculating the average intensity and maximum entropy to highlight mitochondria (recognised nuclear elements manually removed) and the pixel units of the particles were analysed to calculate the calcium in the cell of each frame. Relative maximum calcium uptake was then calculated by comparing average fluorescence prior to histamine application when compared to maximal intensity. A two-tailed t-test for heteroscedastic data was then performed.

3.2.8 Mitochondrial Membrane Potential

Using cells seeded 24 hours previously at 100,000 in a 35 mm Glass Bottom Dish, cells were incubated at at 37°C with 10nM Tetramethylrhodamine Methyl Ester (T668;

Thermo Fisher Scientific) (TMRM) in 1 ml GMEM for 40 minutes in the dark before washing twice in PBS and imaging on a Nikon A1r point-scanning confocal microscope at x60 magnification, using a 1.40 numerical aperture oil objective, in 1 ml Tyrode's solution. Cells were imaged for 1 minute before treatment with FCCP and recorded for a further 15 seconds.

Videos were then analysed using Fiji (ImageJ 1.52i) (Schindelin et al., 2012) by isolating a single cell and subtracting background noise. Mitochondria were selected by averaging intensity of time stacks and thresholding automatically on isodata before analysing particles. The multi-measure tool was used to quantify intensity and F was calculated as the mean of TMRM basal intensity (first 10 stacks; 2.404 seconds) and F_0 was calculated as post treatment intensity (last 10 stacks; 2.404 seconds) with measurements presented as F/F_0, $\Delta\Psi m$. Experiment was replicated as biological triplicates.

3.2.9 Mitochondrial Network and ER-Mitochondrial Interactions

Cells were prepared for both mitochondrial network analysis and concurrent visualisation of ER:Mitochondrial network interactions by seeding 100,000 cells in 35 mm Glass Bottom Dishes and transiently transfecting Green Fluorescent Protein (GFP)-Sec61β (Voeltz et al., 2006) 24 hours later.

LB Agar (22700025; Sigma-Aldrich), supplemented with 50 $\mu g \cdot ml^{-1}$ Kanamycin Sulphate (11815-032; Invitrogen) on 90 mm Agar Plates (101IRR; Thermo Fisher Scientific) was prepared aeseptically and air dried before storage at 4°C. Upon use, plates were warmed to 37°C and 25 µl of JM109 Competent Cells (L2001; Promega), previously transformed with GFP-Sec61β (Voeltz et al., 2006) (pAc-GFPC1-Sec61beta was a gift from Tom Rapoport (Addgene plasmid #15108)), were thawed from -80°C and plated before overnight incubation at 37°C.

White colonies were picked and prepared using QIAprep Spin Miniprep Kit (27104; QIAGEN) according to manufacturer instructions before restriction digestion with XBaI (R0145T; New England Biolabs) using CutSmart Buffer (New England Biolabs) conditions for 1 hour.

Digestions were loaded with DNA Gel Loading Dye (6X) then electrophoresed on a 1% agarose gel + 0.005% SafeView Nucleic Acid Stain and plasmids containing GFP-Sec61β were stored at -20°C until use.

To detect ER, the cell lines were transiently transfected ~24 hours prior to imaging, using Opti-MEM (31985062; Thermo Fisher Scientific), GeneJuice Transfection Reagent (70967; Merck Millipore) and 1 µg of plasmid DNA, confirmed for GFP-Sec61β. Mitochondria were detected by loading 75 nM MitoTracker Red FM (M22425; Thermo Fisher Scientific) at 37°C for 30 minutes in the dark before washing twice with PBS and imaged in Tyrode's solution supplemented with 25 mM HEPES.

MitoTracker Red stains mitochondria in live cells and GFP-Sec61β transfection re-

sults in expression of a GFP tagged Sec61 complex within the ER, therefore allowing concurrent visualisation.

Cells were immediately imaged following washing using a Nikon A1r point-scanning confocal microscope at x60 magnification, with a 1.40 numerical aperture oil objective. The high speed Piezo Z Drive took 69 Z-stacks, spanning the full cell depth, at 0.11 µM increments. Number of cells quantified are available in Table S20.

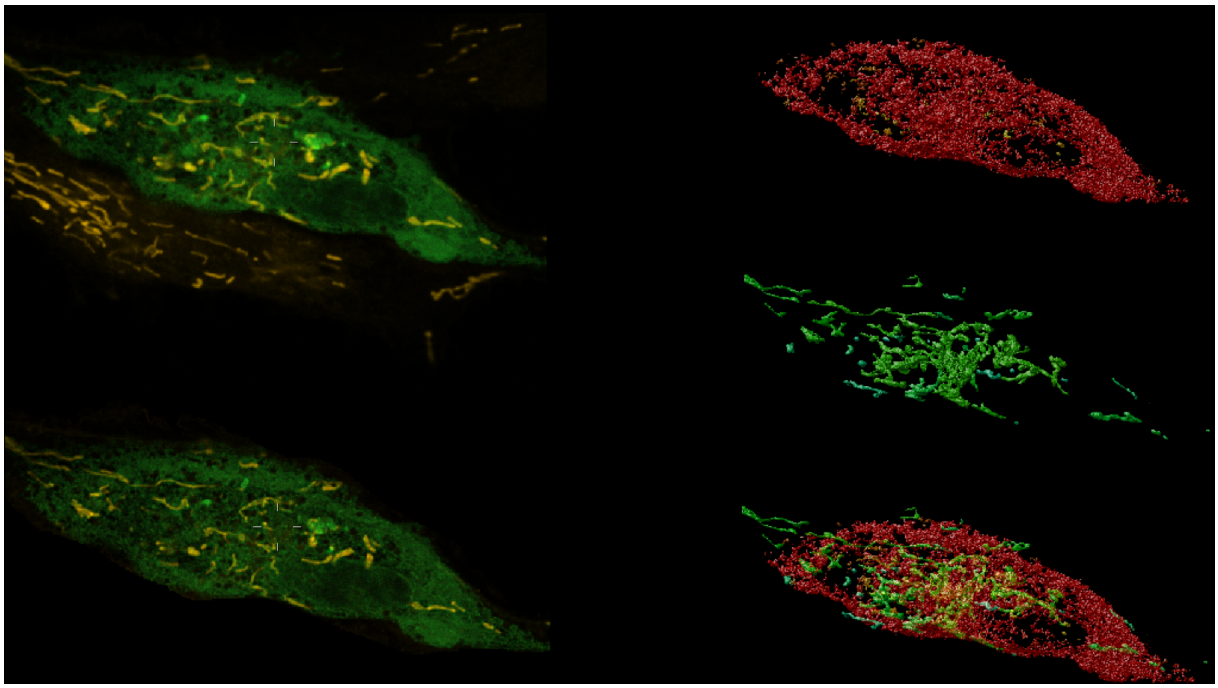

Figure 3.2: *Cell stacks were imaged and adjacent cells were cropped in Huygens Essential Software (SVI). The cleaned image was then deconvolved to separate the red and green channels, ER and mitochondria respectively, before reconstructing the 3D image.*

Huygens Essential Software (SVI) was used to deconvolve both channels of the original figure using an optimised 40 iteration CMLE deconvolution with a signal to noise ratio of 20, thresholding quality at 0.05 and automatic brick layout. Background was automatically estimated to reconstruct the stacks as a 3D image, as demonstrated in Figure 3.2.

Mitochondrial Network

Following collection of data from primary cell lines, prepared as described in Section 3.2.9, and shown in Figure 3.2, the mitochondrial network was further analysed in Huygens Essential Software (SVI).

The Advanced Object Analyzer was used for each deconvolution to segment the objects, thresholding each channel at 10% with a 10% seed and garbage volume of 100. Thresholding and seed values were recorded as detailed in Section 3.2.9 and the objects were then analysed to quantify the mitochondrial network.

ER-Mitochondrial Interactions

Cells were prepared and measured as described in Subsection 3.2.9 before Huygens Essential Software (SVI) was used to calculate the relationship between the ER and mitochondrial network using the Colocalization Analyzer (Bravo et al., 2011).

Using the 10% thresholding values recorded in Section 3.2.9, both the mitochondrial and ER channels were thresholded with a threshold range of 0 and a colocalisation map of the Manders' M1 and M2 coefficients were computed.

3.3 RESULTS

3.3.1 mtDNA Copy Number

Newly designed primers were checked for successful amplification of the target gene and optimum annealing temperature via gradient PCR as seen in Figure 3.3. *B2M* appears to successfully amplify across the whole temperature gradient from 49-61°C whilst *MT-ND4* amplifies more successfully from 53.6-61°C and *MT-RNR2* from 51.3-58.6°C. As such, an annealing temperature of 58°C was chosen to amplify all three genes in triplex.

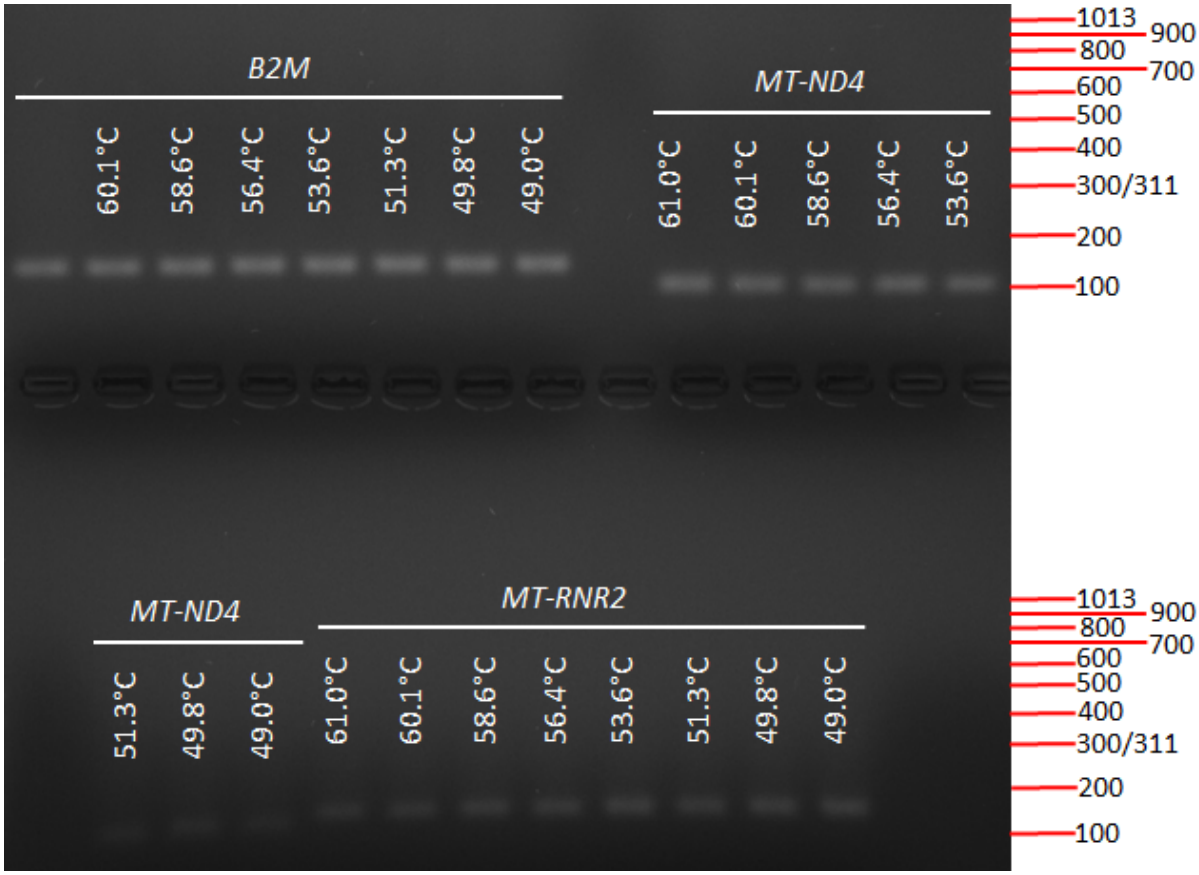

Figure 3.3: *Gradient PCR of B2M, MT-ND4 and MT-RNR2 primers with indicated annealing temperatures to determine optimum triplex assay temperature.* B2M *is expected to amplify a fragment of 141 bp,* MT-ND4 *107 bp and* MT-RNR2 *126 bp.*

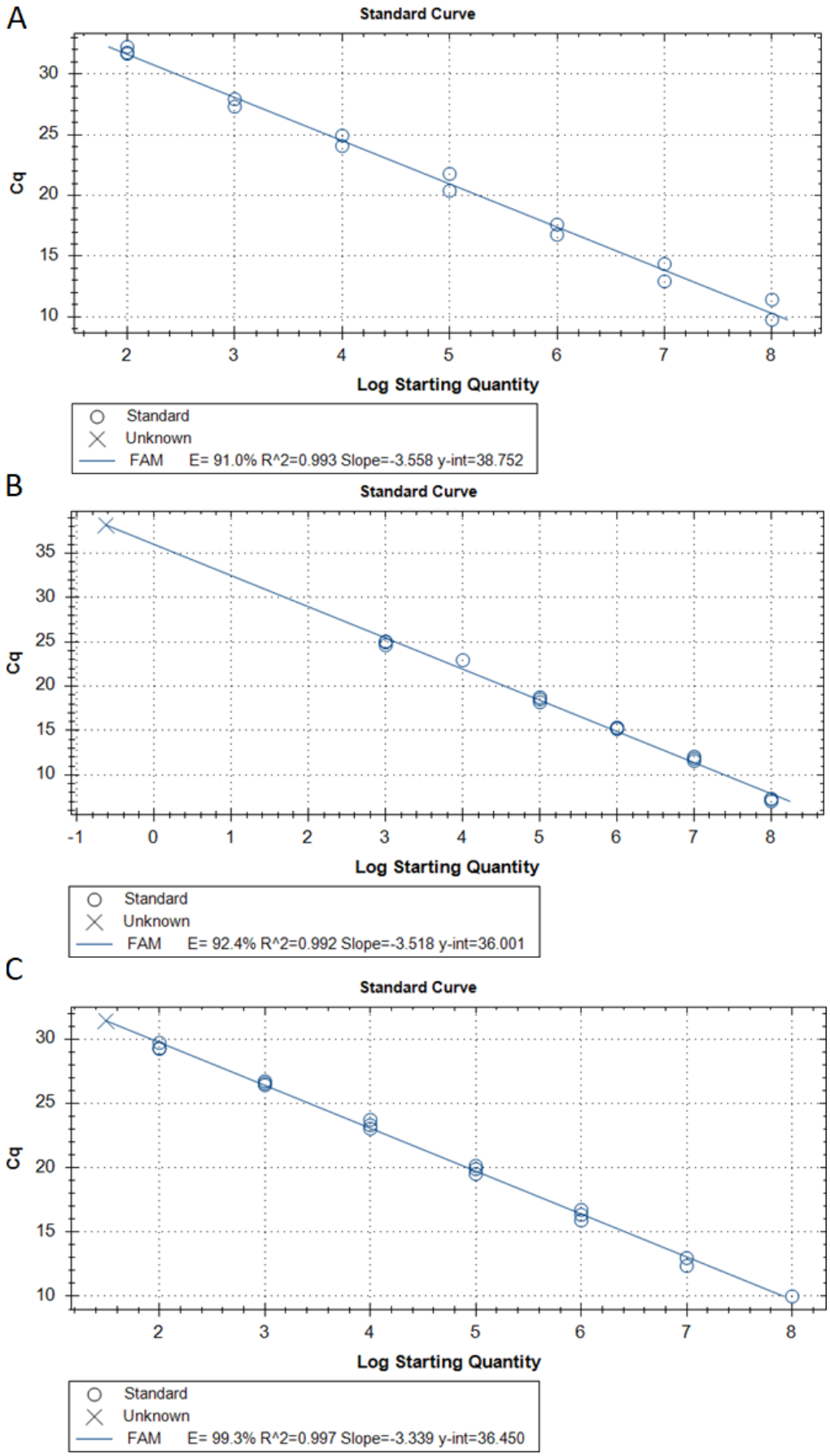

Figure 3.4: *Singleplex standard curves produced using SYBR Green showing* B2M *(A),* ND4 *(B) and* RNR2 *(C) efficiency.*

SYBR Green was used to confirm that all three genes would successfully amplify at 58°C, as confirmed in Figure 3.4.

Given that the primers were redesigned for amplification of B2M, another SYBR Green assay was used to determine whether the new primers increased efficiency of amplification. As shown in Figure 3.5, using the newly designed primers increases efficiency from 87.4% to 90.4% when compared to the original primers. Melt curve analysis was also used in Figure 3.6. The new *B2M* primers melt at a slightly higher temperature and there is a single melting peak, indicating no off-target amplification when compared to the original *B2M* primers.

A singleplex assay of standards was used to ensure successful amplification using the Taqman probe system with good efficiencies of 98.2%, 93.8% and 92.3% of B2M, *MT-RNR2* and *MT-ND4* genes respectively, as shown in Figure 3.7.

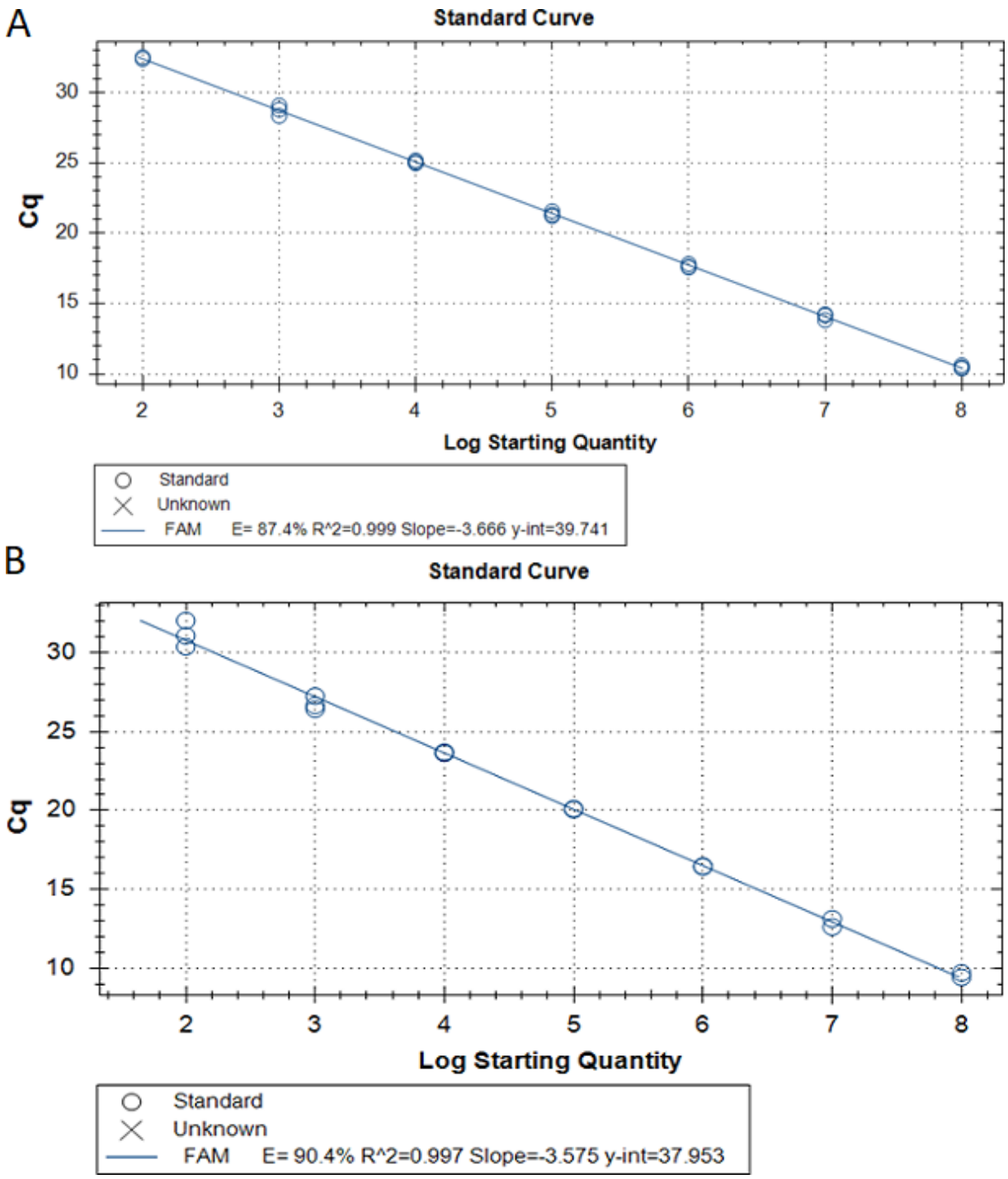

Figure 3.5: *Singleplex standard curves produced using SYBR Green on original (A) and newly designed* B2M *(B) primer sets to determine comparable efficiencies.*

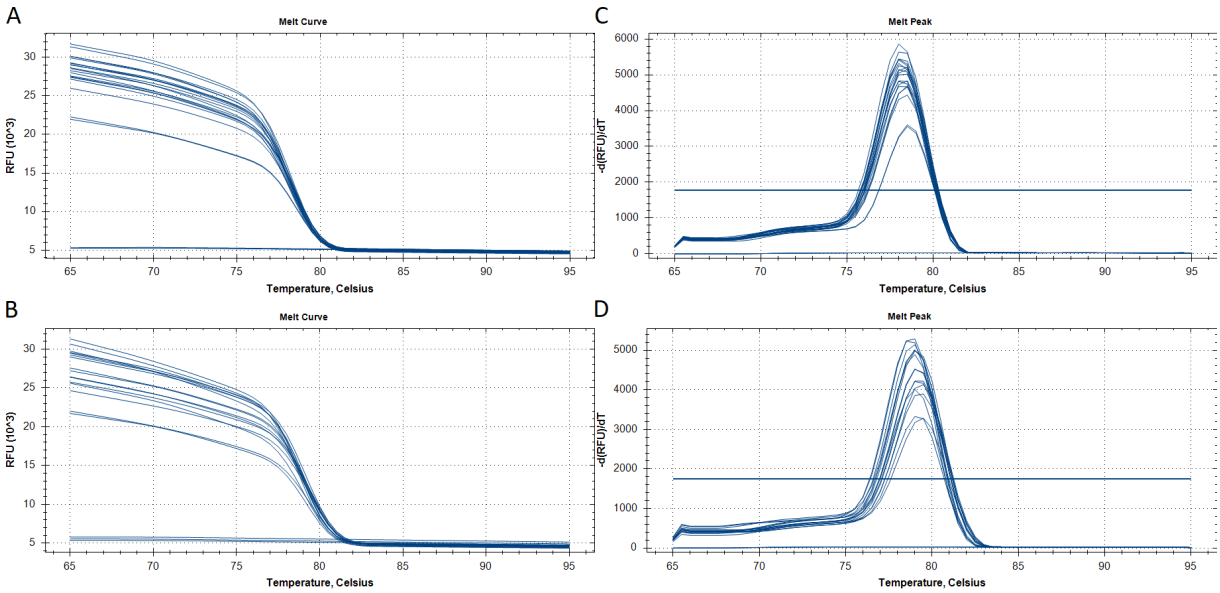

Figure 3.6: *Comparison of SYBR Green melt curves and peaks for the original and new B2M qPCR assays. Original B2M melt curve (A), melt curve for new B2M amplification (B), original B2M melt peak (C) and melt peak for new B2M amplification (D).*

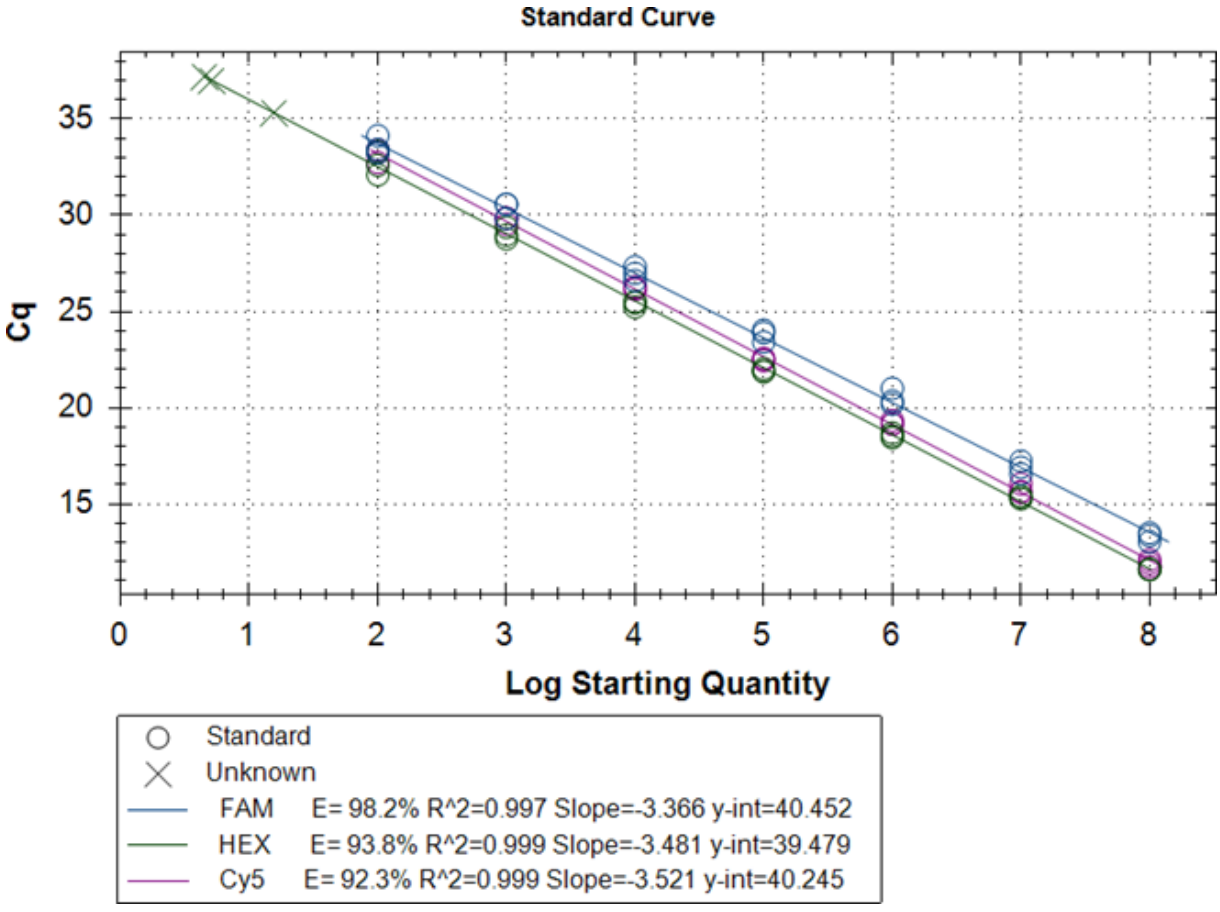

Figure 3.7: *Standard curves produced using Taqman probe system in a singleplex each showing* MT-ND4, B2M *and* MT-RNR2 *on the Cy-5, FAM and HEX channels respectively.*

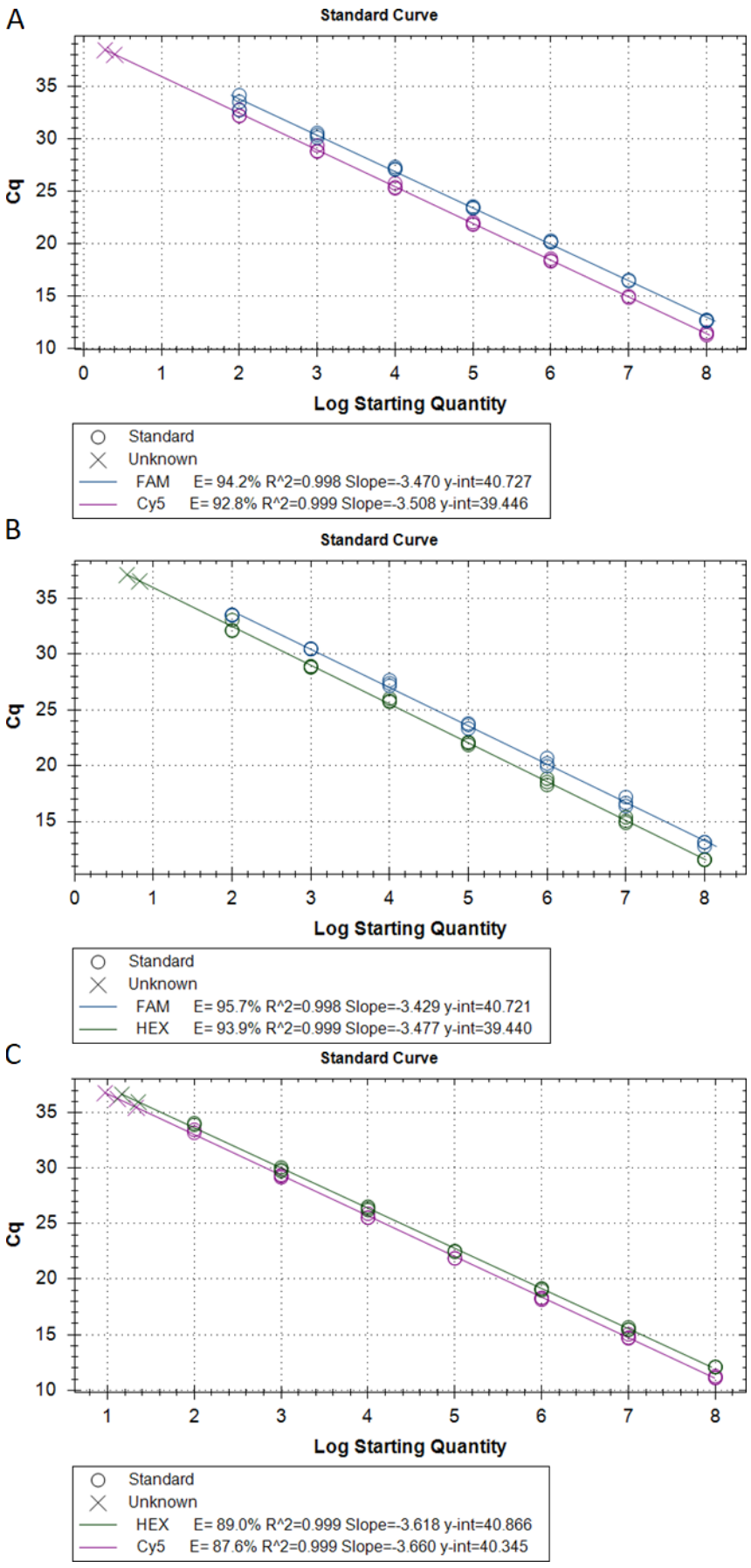

Figure 3.8: *Standard curves produced using Taqman probe system in a duplex of showing* MT-ND4 *and* B2M *on the Cy-5 and FAM channels (A),* B2M *and* MT-RNR2 *on the FAM and HEX channels (B) and* MT-ND4 *and* MT-RNR2 *on the Cy-5 and HEX channels (C).*

A duplex was next set up to determine the efficiency of each gene set when amplified in each possible combination. Figure 3.8 (A) shows good amplification of *B2M* and MT-ND4 in combination and (B) shows good amplification of *B2M* and MT-ND4, however, (C) shows a lowered efficiency of *MT-RNR2* and *MT-ND4* in duplex, possibly due to competition of the primers and probes. This was predicted given that the *MT-ND4* forward and reverse primers were predicted *in silico* to bind the *MT-ND4* probe with a ΔG value of -9.76/-53.42 kcal·mole^{-1} and -8.7/-53.42 kcal·mole^{-1} respectively where the latter figure represents the free energy of the probe binding its perfect complement. Further, the *MT-RNR2* reverse primer was predicted to bind the *MT-ND4* probe with ΔG value of -9.76/-53.42 kcal·mole^{-1} and the combination of these appears to inhibit the efficiency.

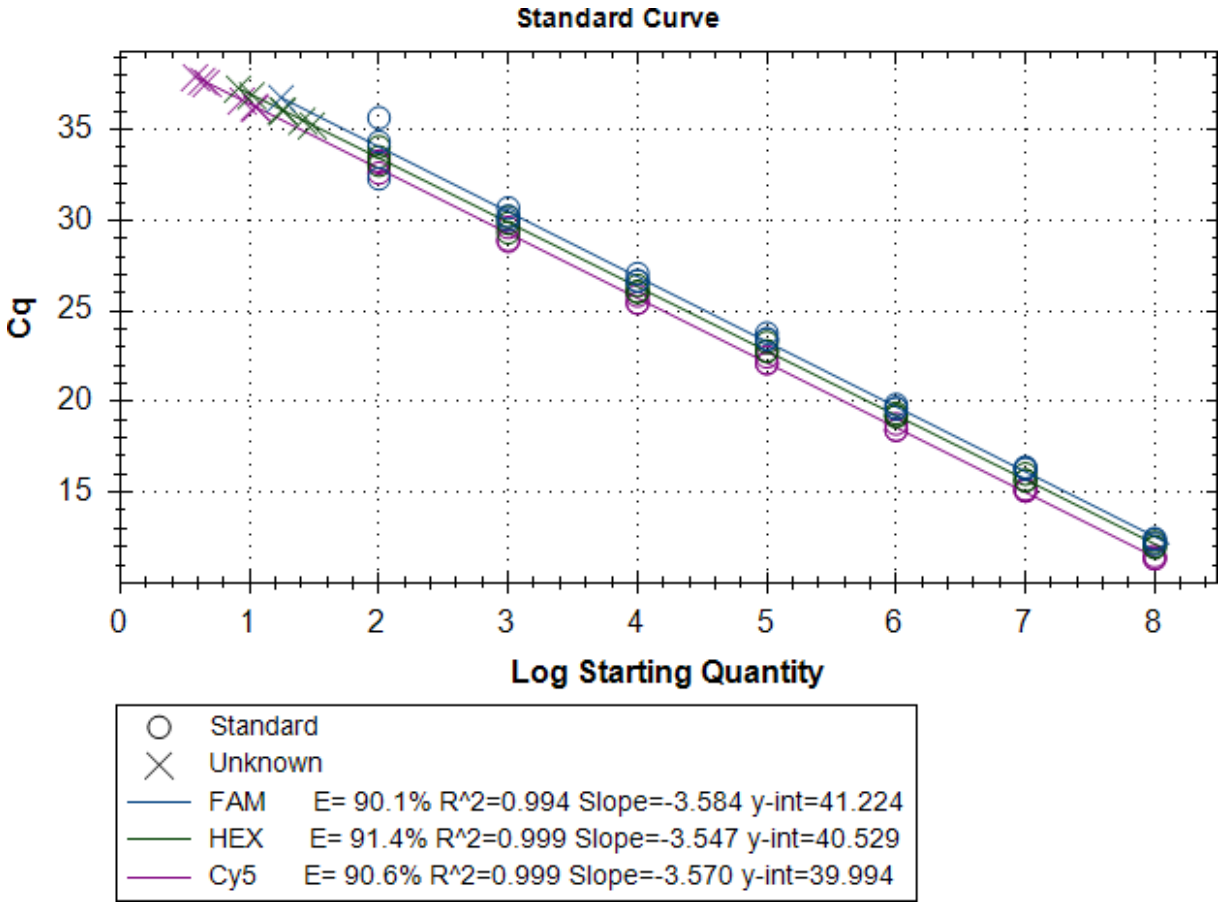

Figure 3.9: *Standard curves produced using Taqman probe system in a triplex, respectively showing* MT-ND4, B2M *and* MT-RNR2 *on the Cy-5, FAM and HEX channels respectively.*

A triplex assay was then set up, as shown in Figure 3.9, to determine that all efficiencies were >90%. The inhibition shown in duplex is less evident in the triplex (Figure 3.9), however, the triplex efficiency was still lower than that of the original triplex.

Tables S11 and S12 show the significance of difference in Ct score between singleplex, duplex and triplex. There is an increase in the number of cycles required to reach the threshold, particularly between *MT-ND4* and *MT-RNR2* (p = 0.015 from singleplex to

duplex of *MT-ND4* and *MT-RNR2* and p = 0.012 for *MT-RNR2* in triplex). Between the duplex to triplex, augmenting with *MT-RNR2* also has a p-value of 0.020, indicating that Ct is affected in triplex settings; however, Ct scores are stable in the other combinations.

Mitochondrial copy number and major arc deletion were measured in triplicate as shown in Figures 3.10 and 3.11. A control deletion sample was included, a transmitochondrial cybrid of ~70% heteroplasmic level, containing a single large-scale mtDNA deletion which spans the major arc from positions m.7,982-15,504 (Diaz et al., 2002).

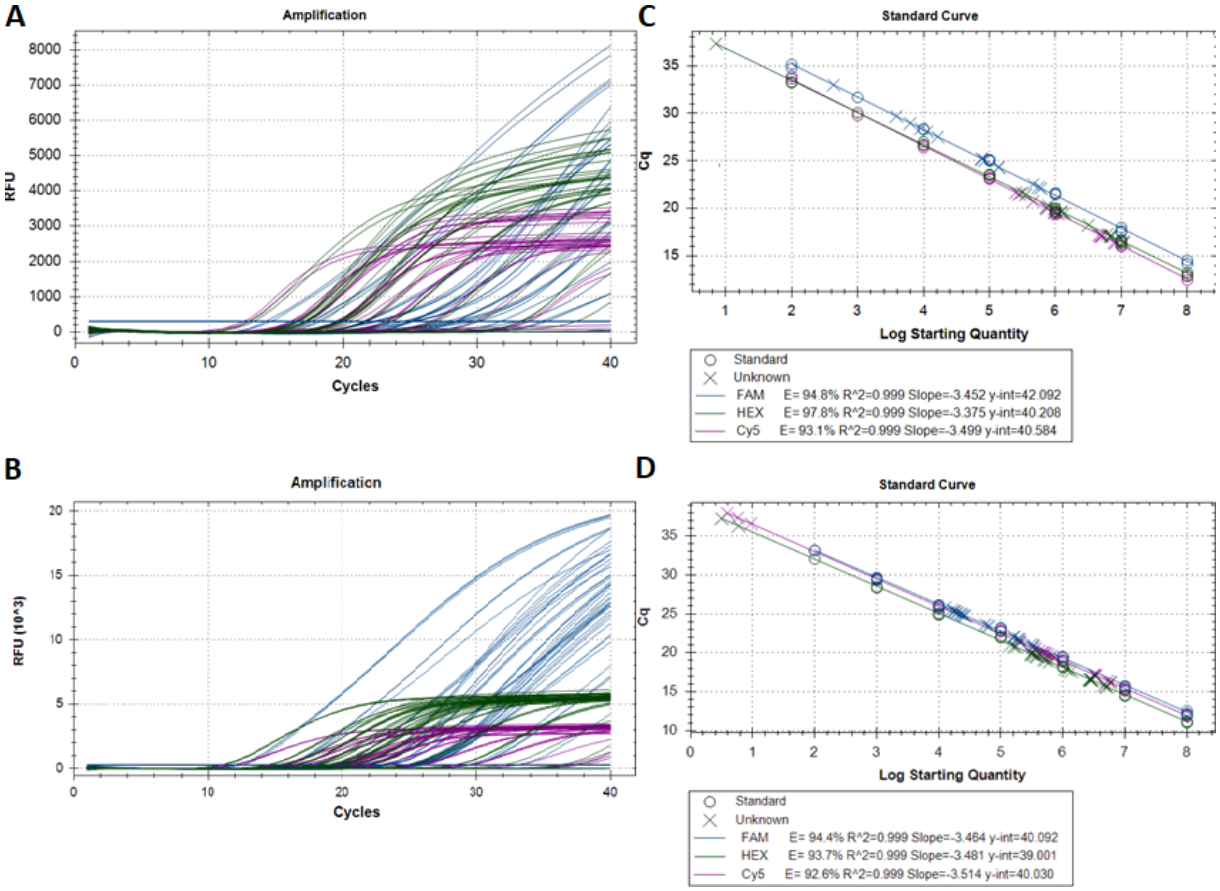

Figure 3.10: *Amplification and standard curves produced using Taqman probe system in a triplex of the original laboratory standard (A) and (C) compared to the new triplex (B) and (D) in blood DNA extractions.* B2M, MT-RNR2 *and* MT-ND4 *on channels FAM, HEX and Cy5 respectively.*

Figure 3.10 shows the comparison of the original laboratory standard assay for mtDNA copy number quantification to the new qPCR assay in blood samples. The annealing temperature was raised to 62°C, which was the previous lab standard optimum temperature, to run the qPCR DNA and deletion controls alongside six control blood samples, with both the original and new qPCR assays on the same plate.

The new *B2M* primers resulted in a great increase of fluorescence for the FAM channel when comparing Figure 3.10 (A) to (B). Switching to *MT-RNR2* also results in a more consistent Relative Fluorescence Units (RFU) for the HEX channel with final amplification cycles plateauing in a narrower range. *MT-ND4* remains consistent between the two qPCR assays. The channels in 3.10 (D) also show a narrower range in

a more consistent efficiency than when compared to 3.10 (C). Increasing the annealing temperature from 58°C to 62°C also results in an overall efficiency increase in Figure 3.10 (D) when compared to Figure 3.9.

The change in Ct across channels between the old and new assays through a range of test samples are summarised in Table 3.12. Overall, it shows that *MT-ND4* amplification was unaffected by the change in assay design, *MT-RNR2* amplifies faster than *MT-ND1* in both blood and fibroblast DNA samples, and that *B2M* amplifies cycles faster in fibroblast and particularly blood DNA samples.

Table 3.12: *Ct scores between original and new qPCR triplex for channels Cy5 (ND4), HEX (ND1/RNR2) and FAM (B2M) in blood and fibroblasts. Channel mean indicates mean of technical replicates after QC; sample mean indicates the mean difference between the original assay and the new one alongside the Ct score percentage change.*

		Cy5 Ct Mean				HEX Ct Mean				FAM Ct Mean			
	DNA Sample	**Original**	**New**	**Diff**	**% Ct Shift**	**Original**	**New**	**Diff**	**% Ct Shift**	**Original**	**New**	**Diff**	**% Ct Shift**
Blood	Ctrl DNA 5	21.60	21.40	-0.20	-1%	21.57	20.88	-0.69	-3%	28.26	25.29	-2.97	-11%
	Ctrl Del	20.01	19.89	-0.12	-1%	18.26	17.81	-0.45	-2%	33.00	25.59	-7.41	-22%
	DNA 1	16.42	16.30	-0.12	-1%	16.46	15.71	-0.75	-5%	24.35	20.99	-3.36	-14%
	DNA 2	20.07	20.14	0.07	0%	20.00	19.66	-0.34	-2%	29.71	25.08	-4.63	-16%
	DNA 3	19.56	19.51	-0.05	0%	19.60	19.03	-0.57	-3%	25.18	23.52	-1.66	-7%
	DNA 4	17.13	17.11	-0.02	0%	17.13	16.55	-0.58	-3%	27.54	22.05	-5.49	-20%
	DNA 5	17.18	17.15	-0.03	0%	17.16	16.57	-0.59	-3%	22.31	21.76	-0.55	-2%
	DNA 6	20.76	20.56	-0.20	-1%	20.33	19.82	-0.51	-3%	28.97	24.83	-4.14	-14%
	Mean			-0.08	0%			-0.56	-3%			-3.78	-13%
Fibro	Ctrl DNA 5	21.91	21.90	-0.01	0%	21.84	21.26	-0.58	-3%	26.74	25.79	-0.95	-4%
	Ctrl Del	19.89	19.81	-0.08	0%	18.29	17.73	-0.56	-3%	27.07	25.28	-1.79	-7%
	C1	21.46	21.52	0.06	0%	21.39	20.97	-0.42	-2%	28.59	27.31	-1.28	-4%
	C2	21.31	21.41	0.10	0%	21.28	20.84	-0.44	-2%	28.37	27.20	-1.17	-4%
	C3	22.71	22.88	0.17	1%	22.63	22.23	-0.40	-2%	28.84	28.26	-0.58	-2%
	A2-14484	21.50	21.43	-0.07	0%	21.42	20.86	-0.56	-3%	29.10	27.46	-1.64	-6%
	A3-11778	23.26	23.21	-0.05	0%	23.15	22.63	-0.52	-2%	32.26	30.05	-2.21	-7%
	A4-11778	22.51	22.32	-0.19	-1%	22.31	21.71	-0.60	-3%	29.50	27.90	-1.60	-5%
	Mean			-0.01	0%			-0.51	-2%			-1.40	-5%

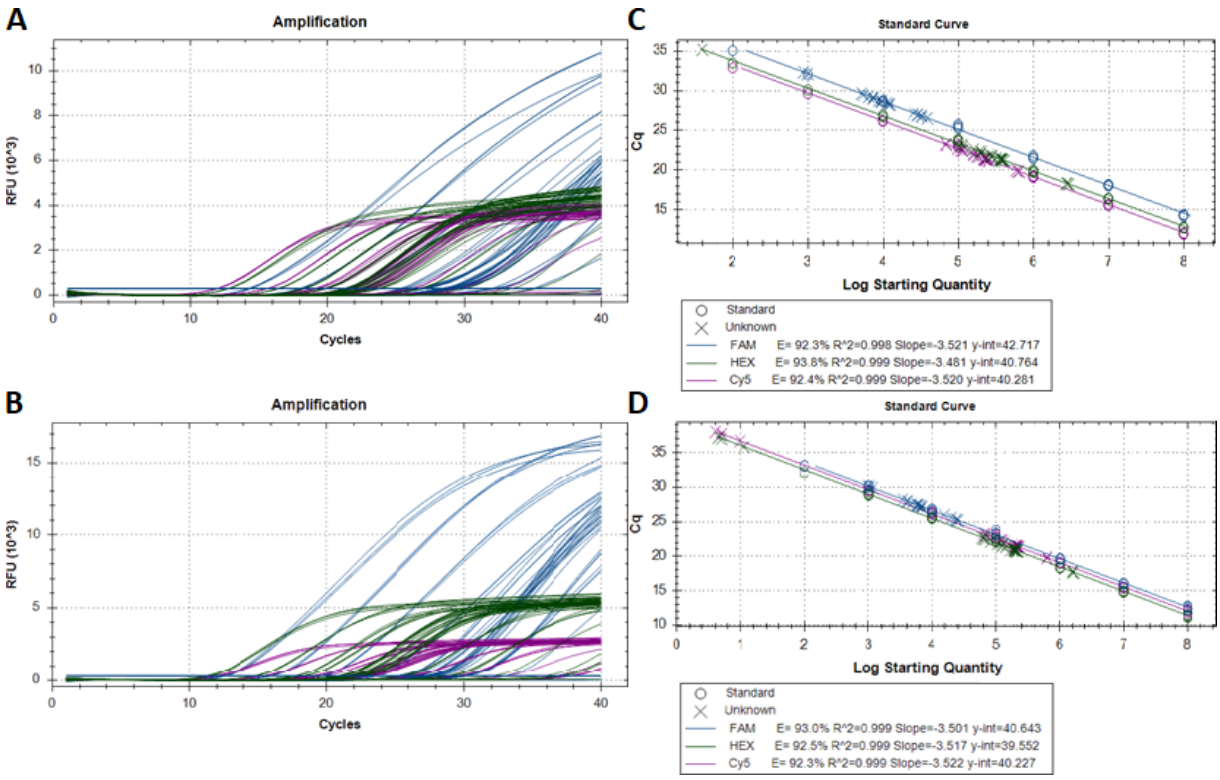

Figure 3.11: *Amplification and standard curves produced using Taqman probe system in a triplex of the original laboratory standard (A) and (C) compared to the new triplex (B) and (D) in fibroblast DNA extractions.* B2M, MT-RNR2 *and* MT-ND4 *on channels FAM, HEX and Cy5 respectively.*

Figure 3.11 shows the comparison of the original laboratory standard assay for mtDNA copy number quantification to the new qPCR assay in fibroblast samples. The annealing temperature was maintained at 62°C to run the qPCR DNA and deletion controls alongside six fibroblast samples, with both the original and new qPCR assays on the same plate.

As with 3.10, the new triplex in Figure 3.11 shows an increase in fluorescence for *B2M* but this is less than the difference in the fibroblast DNA samples. The *MT-RNR2* also results in slightly more consistent RFU for the HEX channel and *MT-ND4* remains consistent between the two qPCR assays again. Finally, the channels in 3.11 (D) also show a more consistent efficiency in the channels when compared to 3.11 (C).

Ct scores for Figures 3.10 and 3.11 are included in Table 3.12. As expected, as the *MT-ND4* primers and probes remained unchanged, there is very little change of Cy5 Ct Score. Switching from *MT-ND1* to *MT-RNR2* improved the assay's ability to detect mtDNA, with the Ct score reaching the detection threshold more than half a cycle earlier. Altering the *B2M* primer positions also greatly improved detection by reducing the qPCR product size from 231 bp to 141 bp; this had a varied response in the difference of detection in blood with a mean detection 3.78 cycles sooner. In fibroblasts, the response was more consistent and it took a mean 1.40 cycles fewer to detect. There is a good correlation between the copy number of samples between the old and new assays, particularly for fibroblasts, as shown in Figure 3.12 and Table S13,

although the correlation is not as strong in blood samples and there is a discrepancy in the ability of the assays to reliably measure copy number in blood compared to fibroblasts.

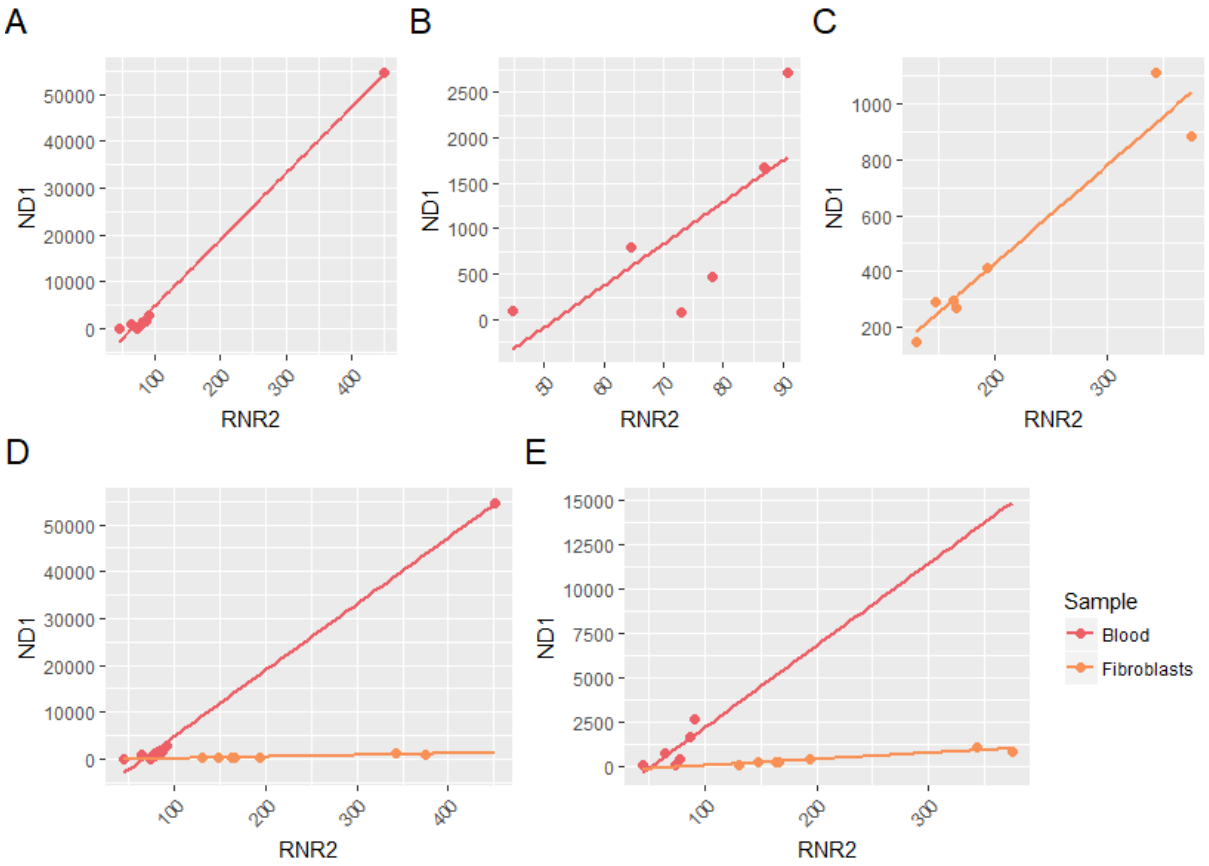

Figure 3.12: *Copy number using Taqman probe system in a triplex of the original laboratory standard,* MT-ND1 *against the new triplex,* MT-RNR2 *in blood (A), blood, excluding high concentration sample (B), fibroblasts (C), all blood and fibroblast samples (D), and blood and fibroblasts, excluding high concentration sample (E).*

Using DNA extracted from primary control and LHON fibroblast cell lines, mitochondrial copy number and major arc deletion were measured in triplicate as indicated previously with a control deletion (Diaz et al., 2002) and control blood DNA sample, with results shown in Figure 3.13. Error bars indicate standard error of mean across biological triplicates of the cell line at three different passages; Figure S10 shows the individual Ct scores for each replicate.

Table S14 shows that there was not a significant deletion of the major arc in any of the samples but the cell line A4-11778 did show a significant reduction of mitochondrial copy number when compared to the controls ($p = 0.036$). This significance was exclusive to this cell line as after grouping by mutation or disease status there was no significant difference from controls.

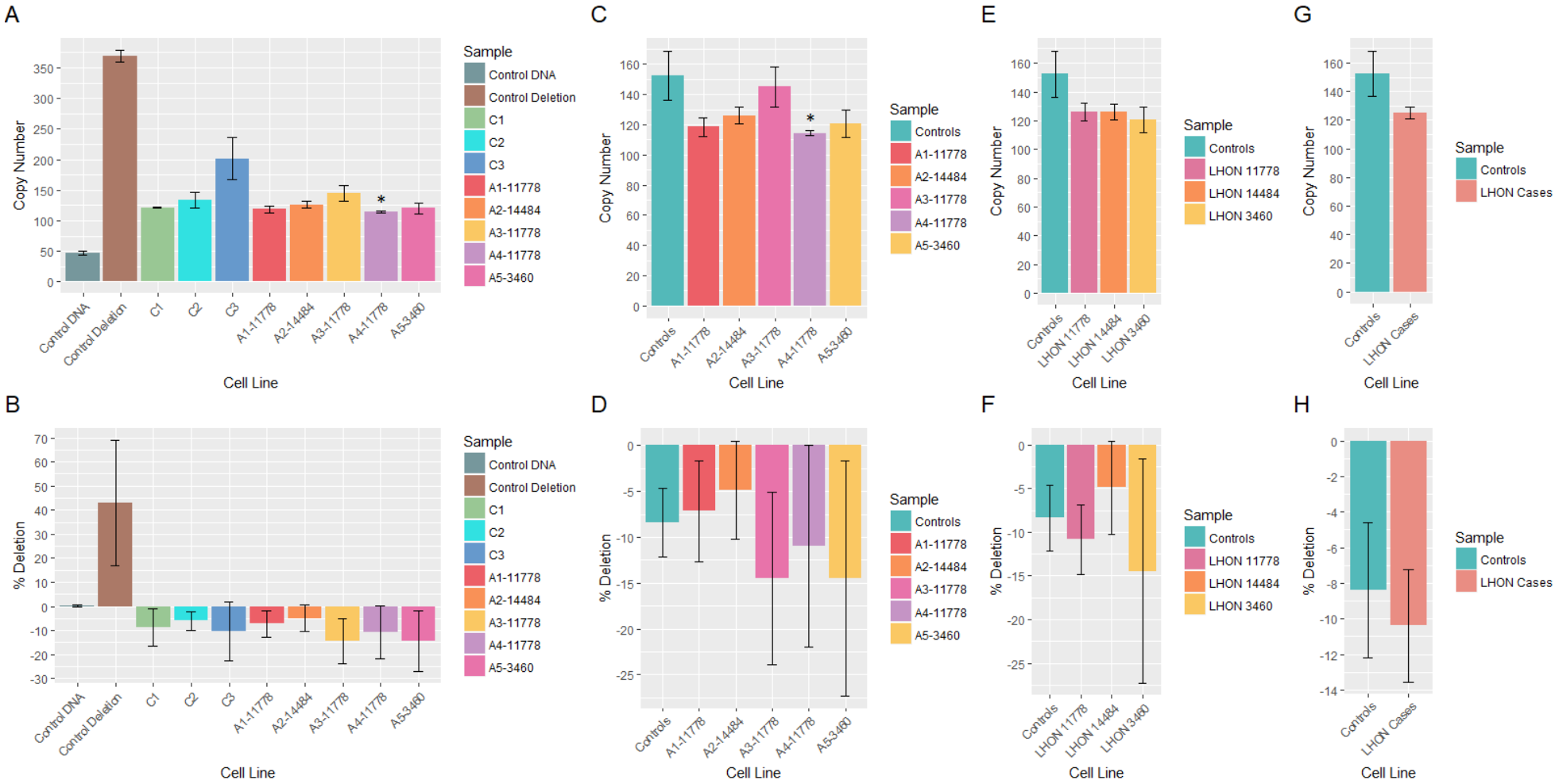

Figure 3.13: *Mitochondrial copy number (A, C, E, G) and respective major arc deletion percentile (B, D, F, H) of LHON fibroblasts. Figures A and B show all individual samples, including control deletion sample. Figures C and D collapse cell lines C1, C2 and C3 as controls, Figures E and F collapse cell lines A1-11778, A3-11778 and A4-11778 as according to LHON primary mutation, and figures G and H collapse all LHON samples against controls. Error bars represent standard error of the mean between three biological replicates collected at different passages. * Indicates $p \leq 0.05$.*

3.3.2 ATP Production During Metabolic Stress

Cells cultured on the 96 Well Solid White Polystyrene TC-Treated Microplate were rinsed with PBS and Protein Assay Dye Reagent Concentrate was used to perform a Bradford assay in accordance to manufacturer's instructions.

CellTiter-Glo Luminescent Reagent was used in a cell viability assay to quantify the ATP produced by cells after treatments with Glucose, Deoxyglucose, Glucose and Oligomycin A, and Deoxyglucose and Oligomycin A in a 96 Well Clear Polystyrene TC-Treated Microplate. Luminescence detection quantifies light produced by a thermostable luciferase which illuminates in the presence of ATP; a greater luminescence is indicative of cells capable of producing more ATP under stress. The concurrent Bradford assay was performed and free ATP was normalised to available protein, the results of which are shown in Figure 3.14.

Table S15 shows that the only significant treatment for reducing ATP production is Deoxyglucose, an inhibitor of glycolysis, in cell line A4-11778 ($p = 0.017$), however, there is no significance once grouping according to the disease causing mutation. Once grouping by disease status, there are no significant differences between cases or controls on any of the measurements.

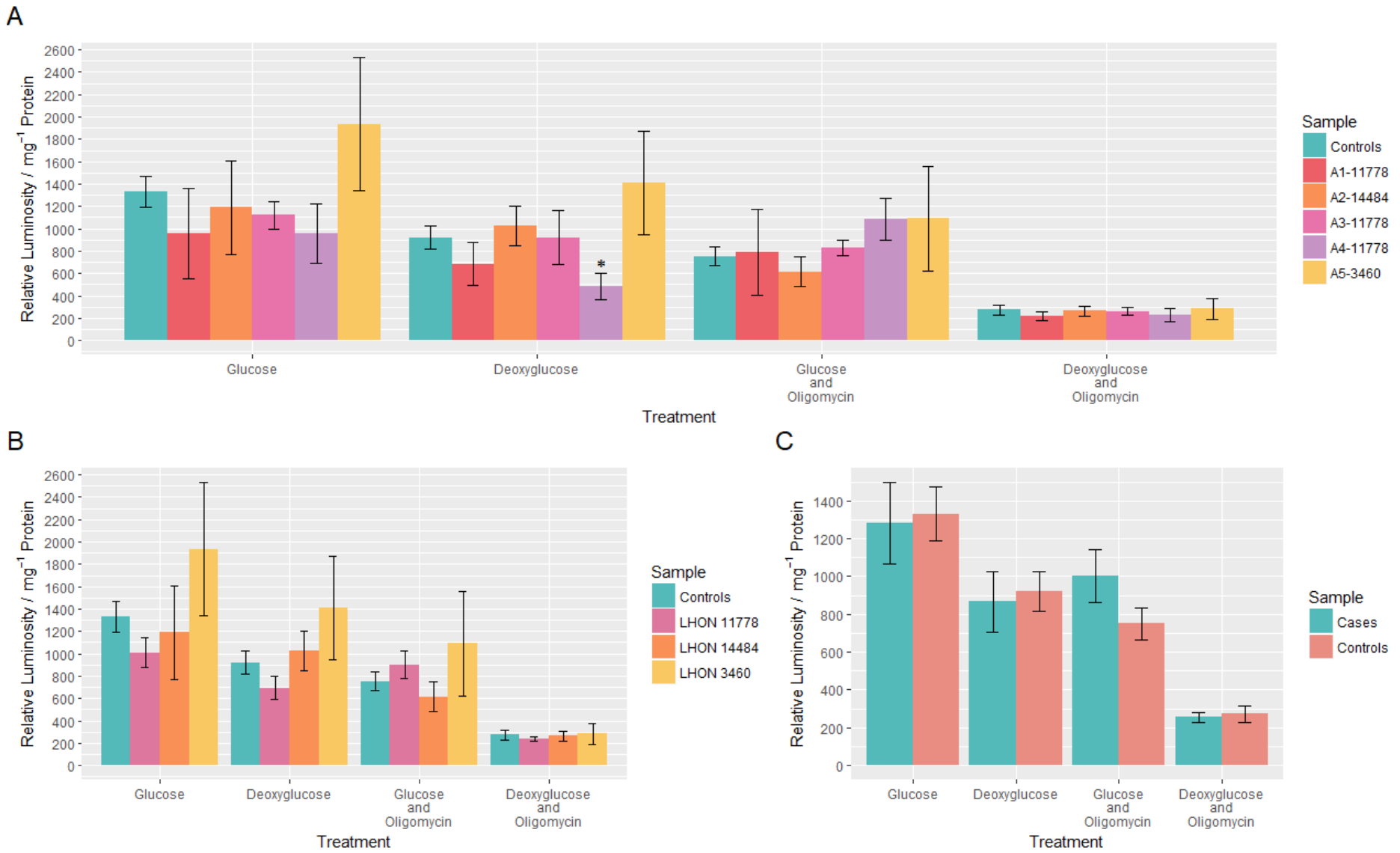

Figure 3.14: *Relative luminosity, representing ATP, normalised to mg protein. Individual cell lines after grouping the three controls (A) and grouping by mutation (B). Bars show luminosity under different drug treatments; error bars represent standard error of the mean between three biological replicates assayed at different passages. * Indicates $p \leq 0.05$.*

3.3.3 Cellular Oxygen Consumption

20,000 cells were seeded per well of a Seahorse XF96 Cell Culture Microplate prior to measurement of OCR on a Seahorse XFe96 Extracellular Flux Analyzer under both basal conditions and following sequential inhibitory drug injections. OCR measurements were normalised in Wave Desktop to mg of protein as shown in Figure 3.15.

Table S16 shows significance values. Measurements of basal respiration, ATP production, maximal respiration and spare respiratory capacity were significantly reduced in cell lines A1-11778, A4-11778 and A5-3460 (respectively, ATP production p = 0.028, 1.19e-05 and 0.001; maximal respiration p = 0.013, 0.021 and 0.009; spare respiratory capacity p = 0.016, 0.032 and 0.012) with non-mitochondrial respiration also significantly reduced in A5-3460 (p = 0.049). After grouping cell lines A1-11778, A3-11778 and A4-11778 together, only basal respiration and ATP production remained significantly reduced compared to controls (p = 0.002 and 1.25e-04 respectively).

Finally, grouping by case:control status, basal respiration and ATP production are seen to be extremely significantly reduced when compared to controls (p = 0.003 and 2.74e-04 respectively). There is a general reduction in maximal respiration, however this is not significant given the variance in the control cell lines' maximal respiration level.

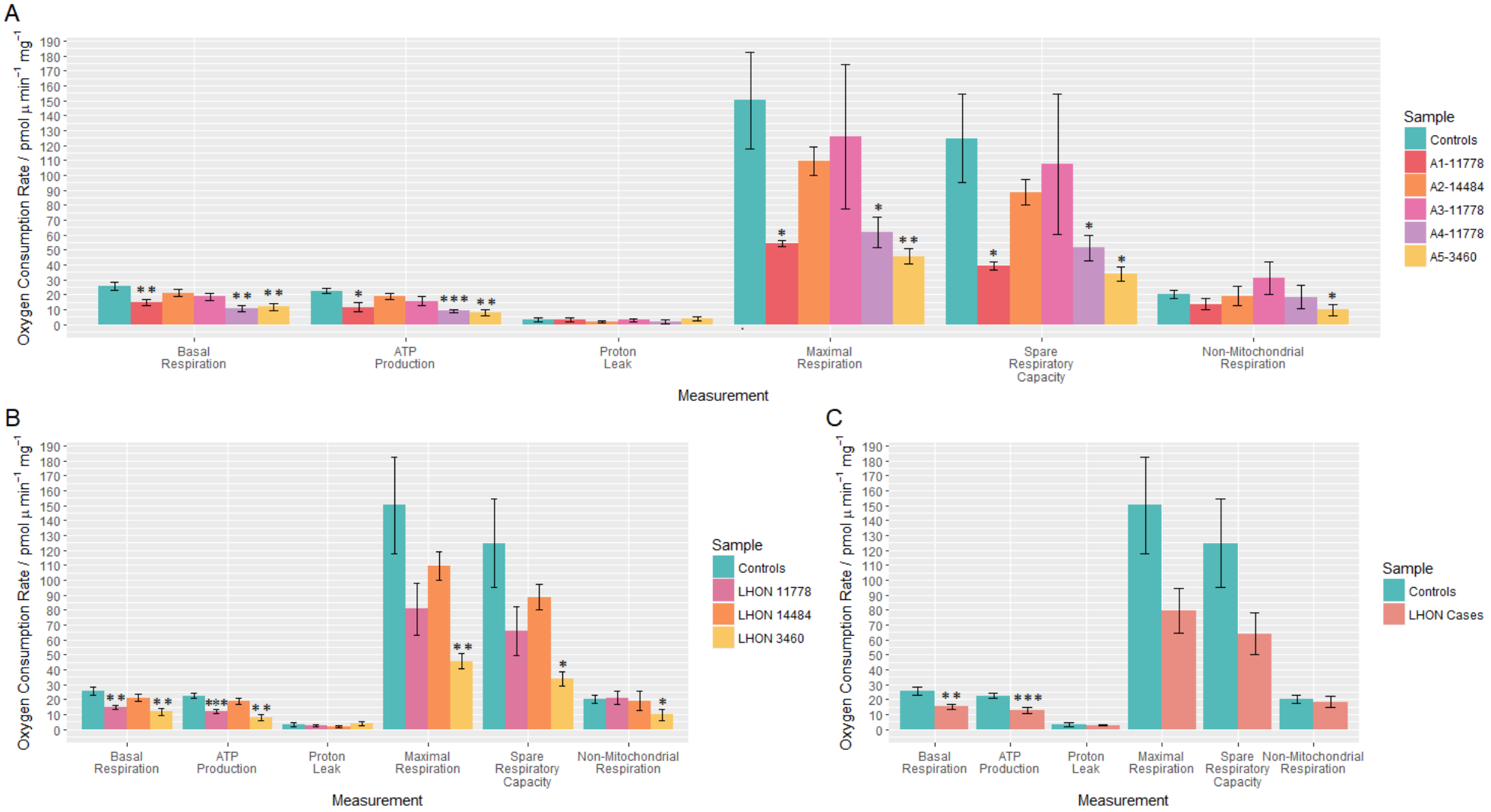

Figure 3.15: *OCR (pmol µ min $^{-1}$ mg $^{-1}$) was measured over 93 minutes. Basal respiration was determined before subsequent injections of Oligomycin A, FCCP, and Rotenone and Antimycin A to allow calculation of measurements as shown in Figure 3.1. Individual cell lines after grouping the three controls (A) and grouping by mutation (B). Error bars represent standard error of the mean between three biological replicates assayed at different passages. * Indicates $p \leq 0.05$, ** indicates $p \leq 0.005$, *** indicates $p \leq$ 5.0e-04.*

3.3.4 Calcium Homeostasis

Maximal mitochondrial calcium intake was calculated after histamine stimulation relative to controls using fluorescence intensity, as shown in Figure 3.16. After focusing the confocal microscope to the monolayer of cells, the laser was moved to non-photobleached cells, as such, the number of cells visible on the microscope varied between cell lines. A minimum of 3 cells of each cell line were used in each passage in triplicate, with counts available in Table S18.

Significance of results are shown in Table S17. There were no significant differences between cases and controls, except for cell line A5-3460 ($p = 0.004$).

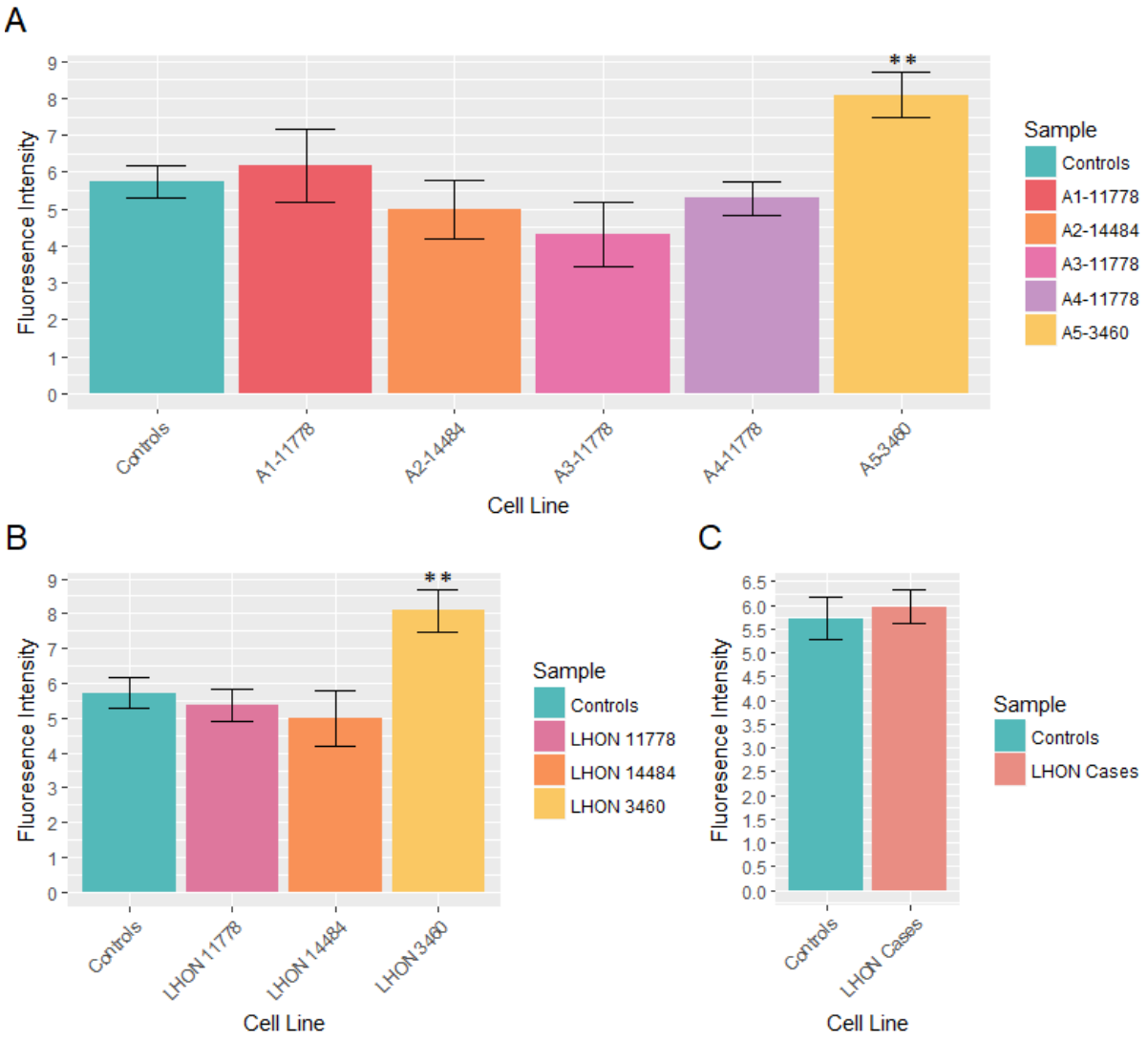

Figure 3.16: *Mitochondrial maximal calcium uptake, showing individual affected cell lines (A), grouping by mutation (B) and grouping by disease state (C). Bars show maximal mitochondrial calcium uptake after stimulation; error bars represent standard error of the mean between three biological replicates imaged at different passages. ** indicates $p \leq 0.005$.*

3.3.5 Mitochondrial Membrane Potential

Confocal microscopy visualised cells treated with TMRM to determine the $\Delta\Psi m$. TMRM fluorescence intensity is proportional to $\Delta\Psi m$ (Joshi and Bakowska, 2011) and after treatment of FCCP, baseline $\Delta\Psi m$ can be calculated as shown in Figure 3.17. No significant difference was found between controls and diseased cell lines, as shown in Figure 3.17 and Table S19. There were no significant differences between cases and controls on any of the measurements taken across any groupings.

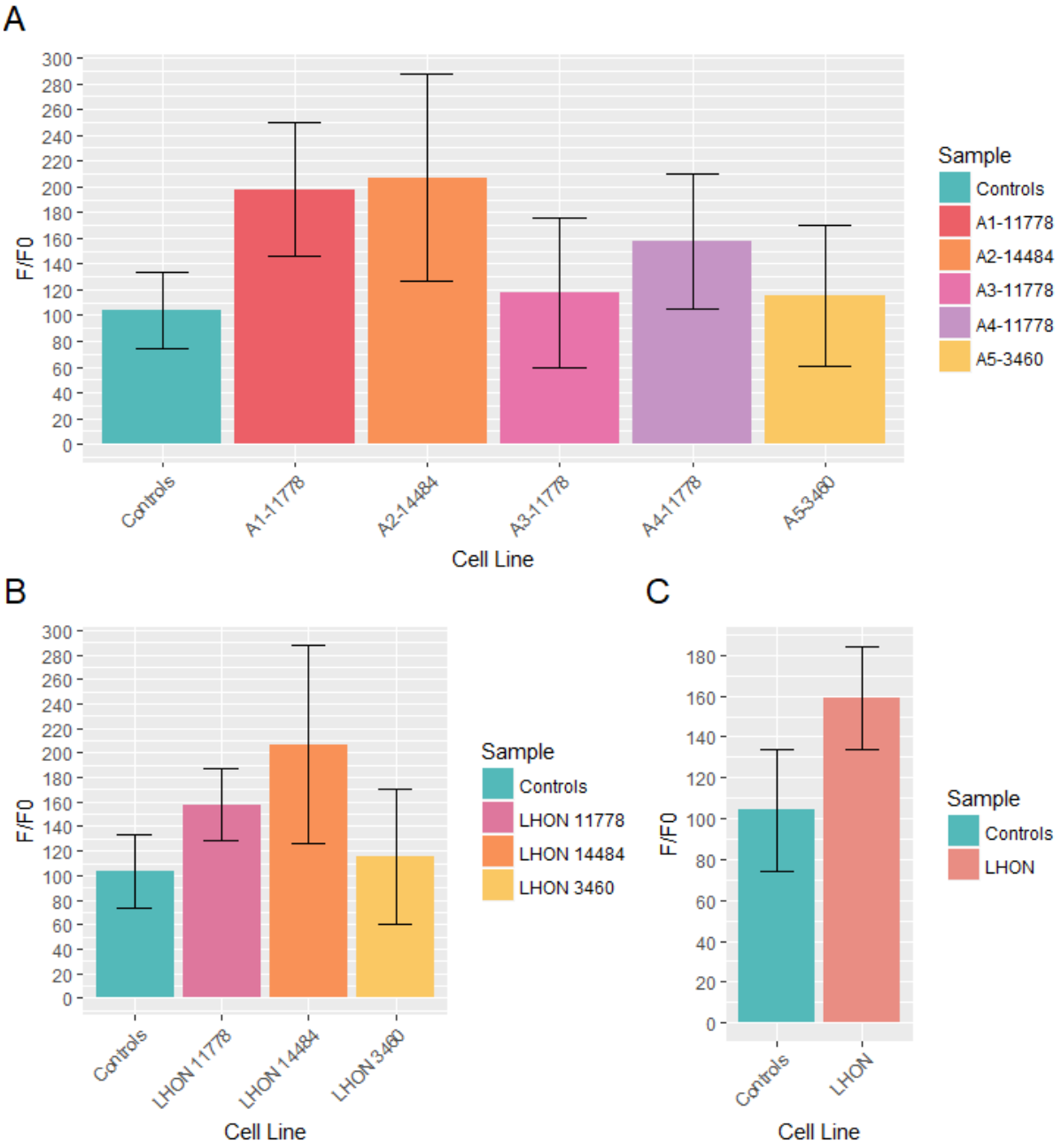

Figure 3.17: *F/F0 (fluorescence / background fluorescence) as a measurement of $\Delta\Psi m$. Individual patient cell lines after grouping the three controls (A), grouping by mutation (B) and grouping by disease state (C). Error bars represent standard error of the mean between a minimum of three biological replicates assayed at different passages.*

3.3.6 Mitochondrial Network and ER-Mitochondrial Interactions

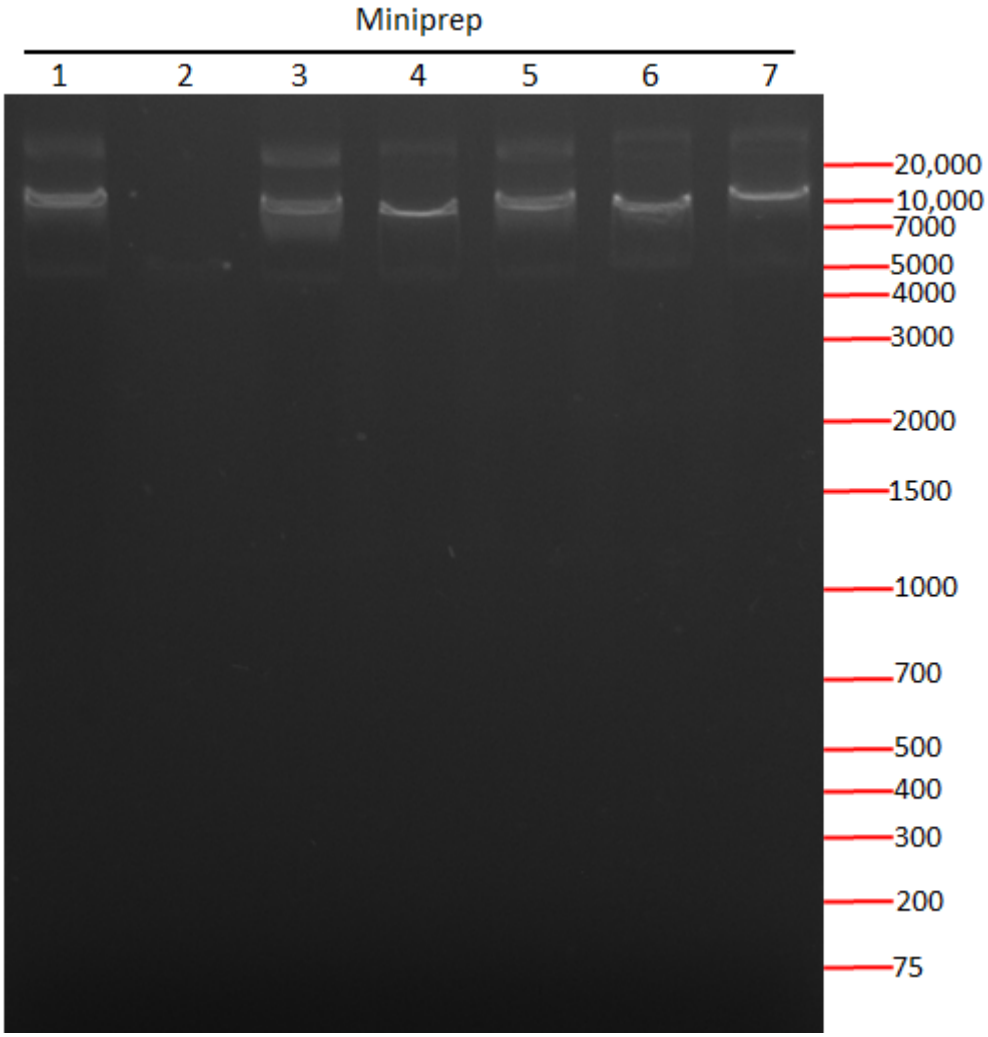

Figure 3.18: *XBaI restriction digestion of miniprepped plasmids designed for transfecting GFP-Sec61β into fibroblasts to visualise ER. GFP-Sec61β is a 5,008 bp plasmid.*

Figure 3.18 shows the partial digestion of the 5,008 bp GFP-Sec61β plasmid digestion with XBaI. GFP-Sec61β contains one restriction site for XBaI and a faint band of linear DNA is shown at ~5000 bp. The partial digest also shows other species of the same plasmids running more slowly through the gel around 11,000 bp and >20,000 bp. Minipreps from colonies 1, 3, 4, 5, 6 and 7 all incorporated the plasmid; colony 2 did not.

Mitochondrial Network

Figure 3.19 shows that cell lines A1-11778 and A4-11778 have a significant reduction in average and maximum mitochondrial network volume (average volume p-value = 0.047 and 0.013 and maximal volume p-value = 0.036 and 0.036 respectively). A1-11778's total volume is also significantly reduced when compared to controls (p-value = 0.006), however, after grouping with cell line A3-11778 as the m.11778G>A mutation, this is

no longer significant. Cell line A5-3460 shows a significant increase in mitochondrial network length (p-value = 0.024), with mitochondria more likely to be joined together, as indicated by the concurrent significant reduction in the number of fragments within the mitochondrial network (p-value = 0.016). However, after grouping the m.11778G>A mutation cell lines (Figure 3.20) or all cell lines (Figure 3.21), this significance is no longer detectable. Full significance tables and cell counts are available in the appendix, Table S21 and Table S20 respectively.

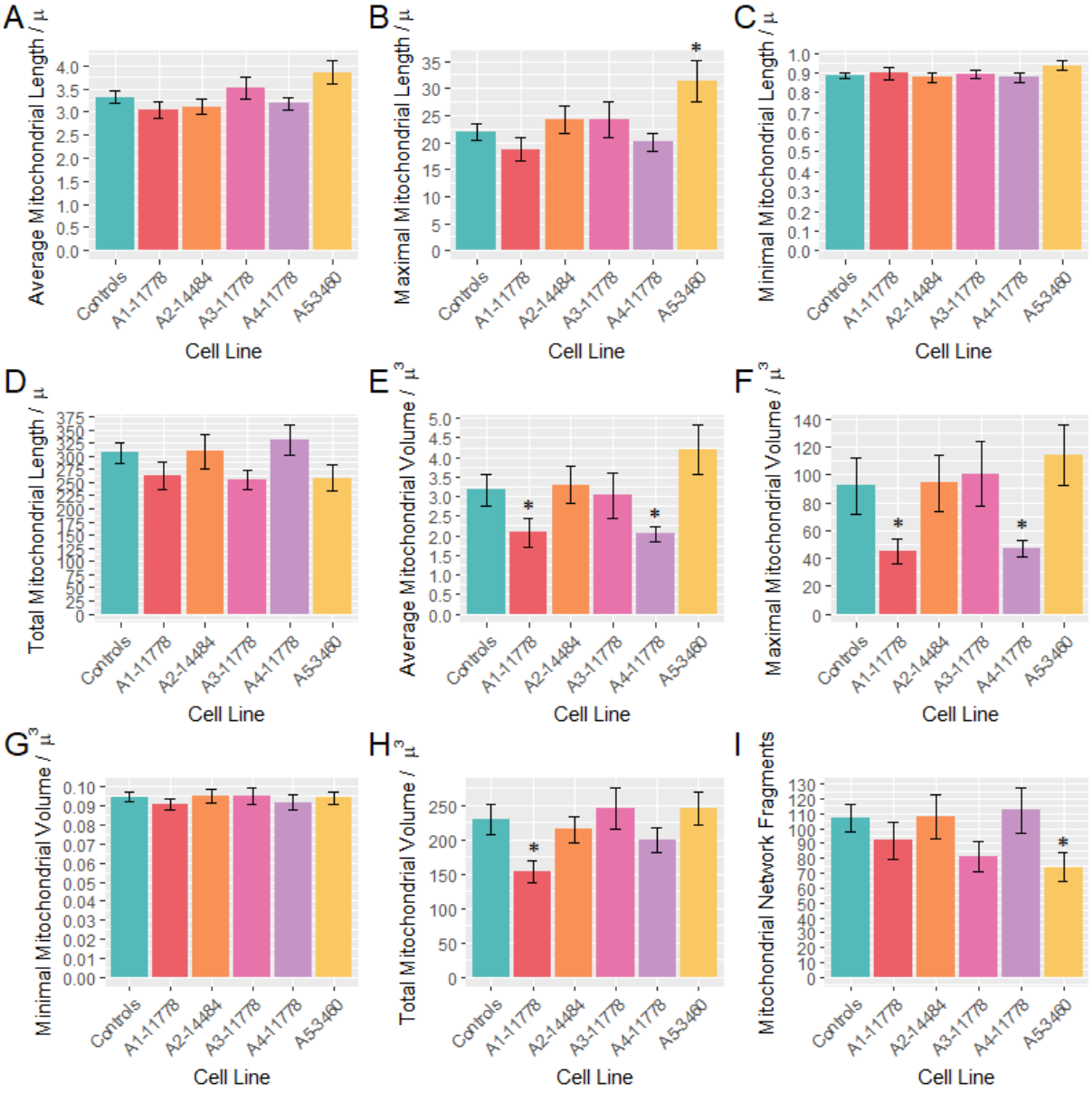

Figure 3.19: *Average mitochondrial length (A), maximal mitochondrial length (B), minimal mitochondrial length (C), total mitochondrial length (D), average mitochondrial volume (E), maximal mitochondrial volume (F), minimal mitochondrial volume (G), total mitochondrial volume (H) and mitochondrial network fragments (I) of the mitochondrial network for individual cell lines with control cell lines grouped. Error bars represent standard error of mean between a minimum of three biological replicates measured at different passages with cell counts available in Table S20. * Indicates $p \leq 0.05$.*

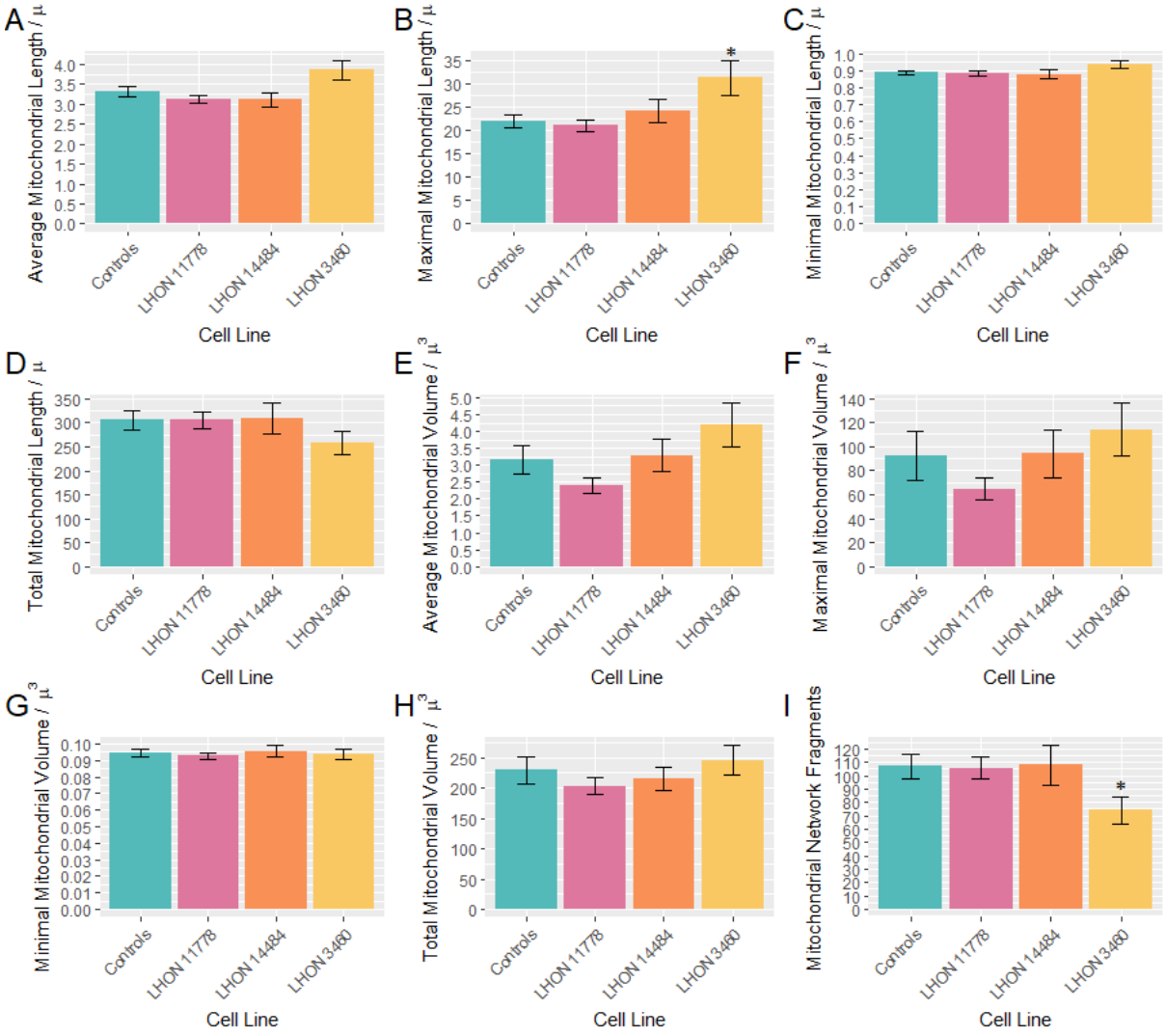

Figure 3.20: *Average mitochondrial length (A), maximal mitochondrial length (B), minimal mitochondrial length (C), total mitochondrial length (D), average mitochondrial volume (E), maximal mitochondrial volume (F), minimal mitochondrial volume (G), total mitochondrial volume (H) and mitochondrial network fragments (I) of the mitochondrial network for individual cell lines grouped by mutation status. Error bars represent standard error of mean between a minimum of three biological replicates measured at different passages with cell counts available in Table S20.*

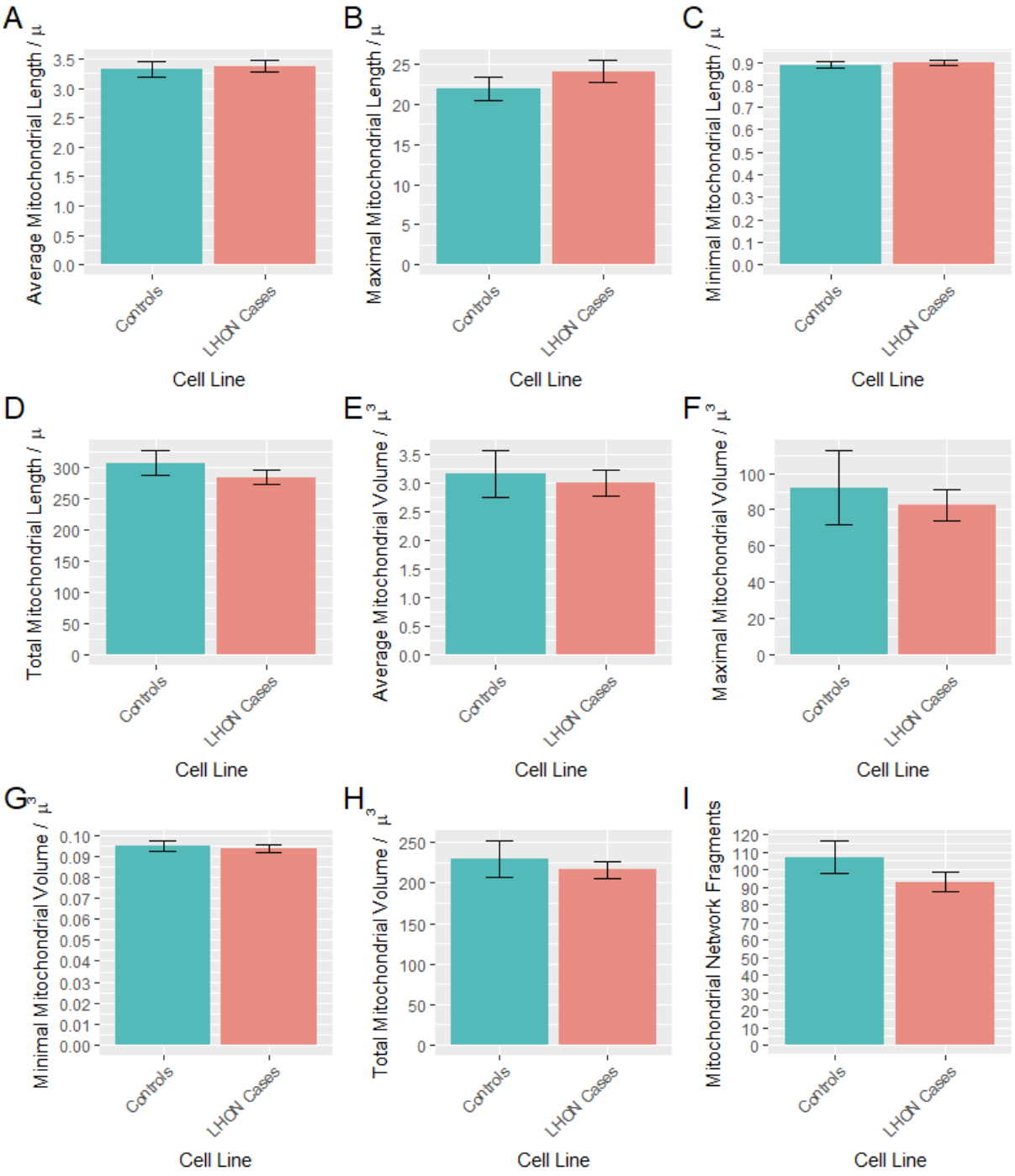

Figure 3.21: *Average mitochondrial length (A), maximal mitochondrial length (B), minimal mitochondrial length (C), total mitochondrial length (D), average mitochondrial volume (E), maximal mitochondrial volume (F), minimal mitochondrial volume (G), total mitochondrial volume (H) and mitochondrial network fragments (I) of the mitochondrial network for individual cell lines grouped by disease status. Error bars represent standard error of mean between a minimum of three biological replicates measured at different passages with cell counts available in Table S20.*

ER-Mitochondrial Interactions

Cells were prepared as described in Subsection 3.2.9 with Huygens Essential Software (SVI) used to calculate the co-localisation between the ER and mitochondrial network (Bravo et al., 2011). Figure 3.22 shows a significant increase in cell line A2-14484 in the Pearson Correlation between the ER and mitochondrial network, and Manders' coefficient M2 which represents the mitochondrial:ER co-localisation (p-value = 0.001 and 3.36e-04). A4-11778 has a significant reduction in Manders' coefficient M1 (ER:mitochondrial co-localisation) (p = 0.036), however, this is no longer significant after grouping the m.11778G>A cell lines together in Figure 3.23. After grouping all LHON cell lines together, M2 remains significantly increased (p = 0.025) as shown in 3.24. Full significance tables and data grouped by mutation available in Table S22.

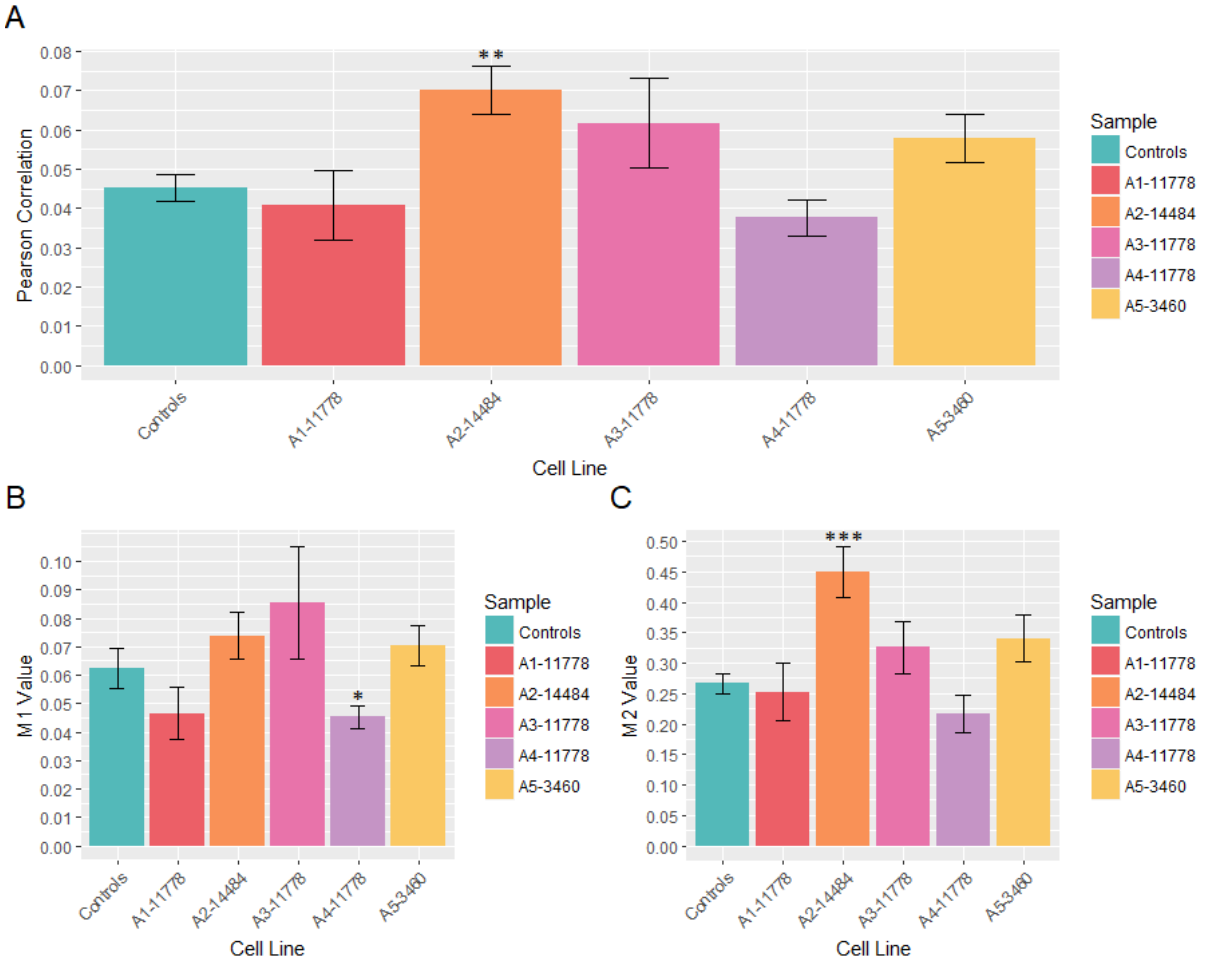

Figure 3.22: *Pearson Correlation (A), Manders' coefficient M1 (B) and Manders' coefficient M2 (C) as measured, showing controls grouped and LHON patients separate. Error bars represent standard error of the mean between a minimum of three biological replicates analysed at different passages, counts of cells analysed are available in Table S20. * Indicates p ≤ 0.05, ** indicates p ≤ 0.005, *** indicates p ≤ 5.0e-04.*

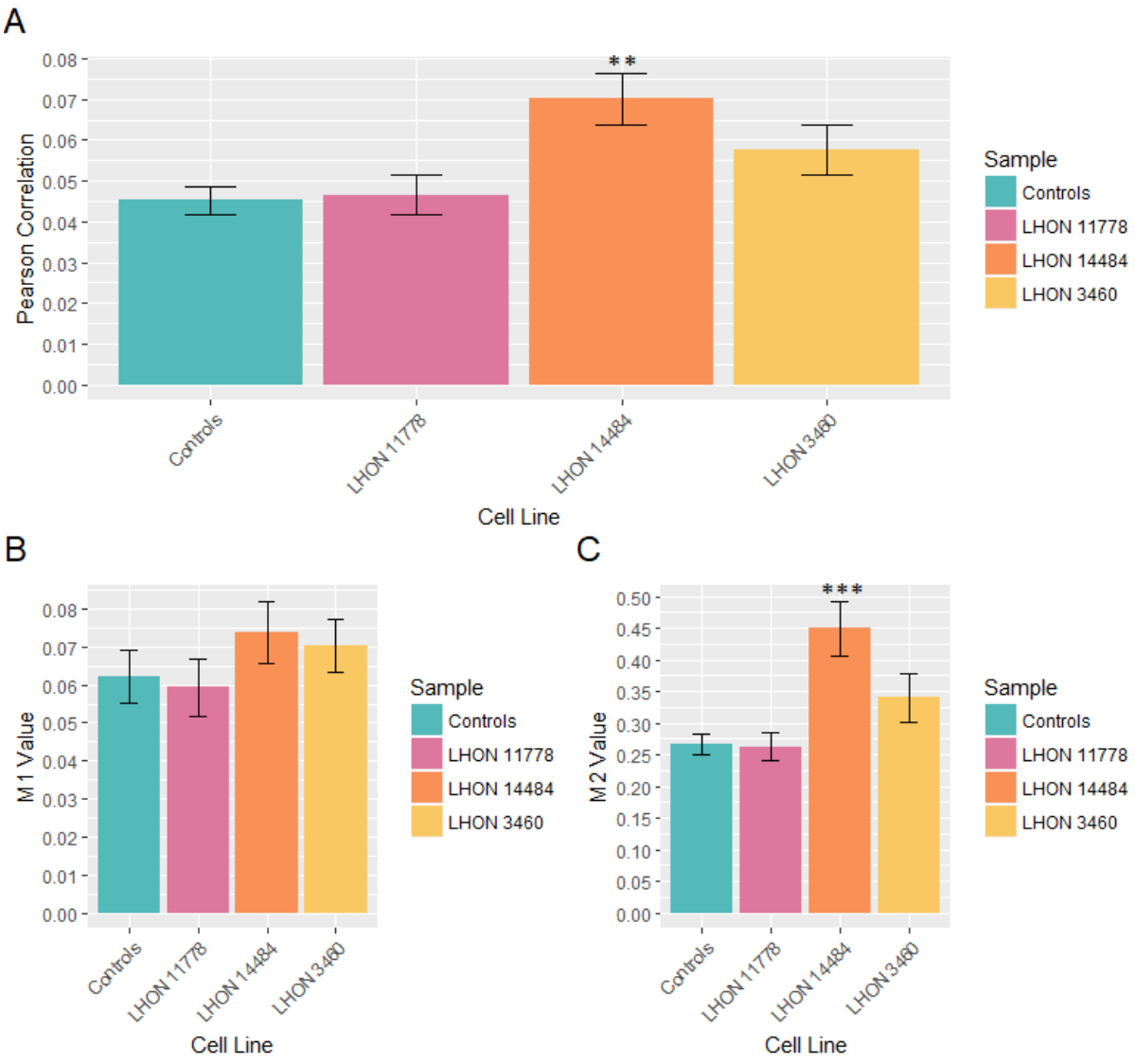

Figure 3.23: *Pearson Correlation (A), Manders' coefficient M1 (B) and Manders' coefficient M2 (C) as measured, showing controls grouped and LHON patients grouped by mutation. Error bars represent standard error of the mean between a minimum of three biological replicates analysed at different passages, counts of cells analysed are available in Table S20. ** indicates p ≤ 0.005, *** indicates p ≤ 5.0e-04.*

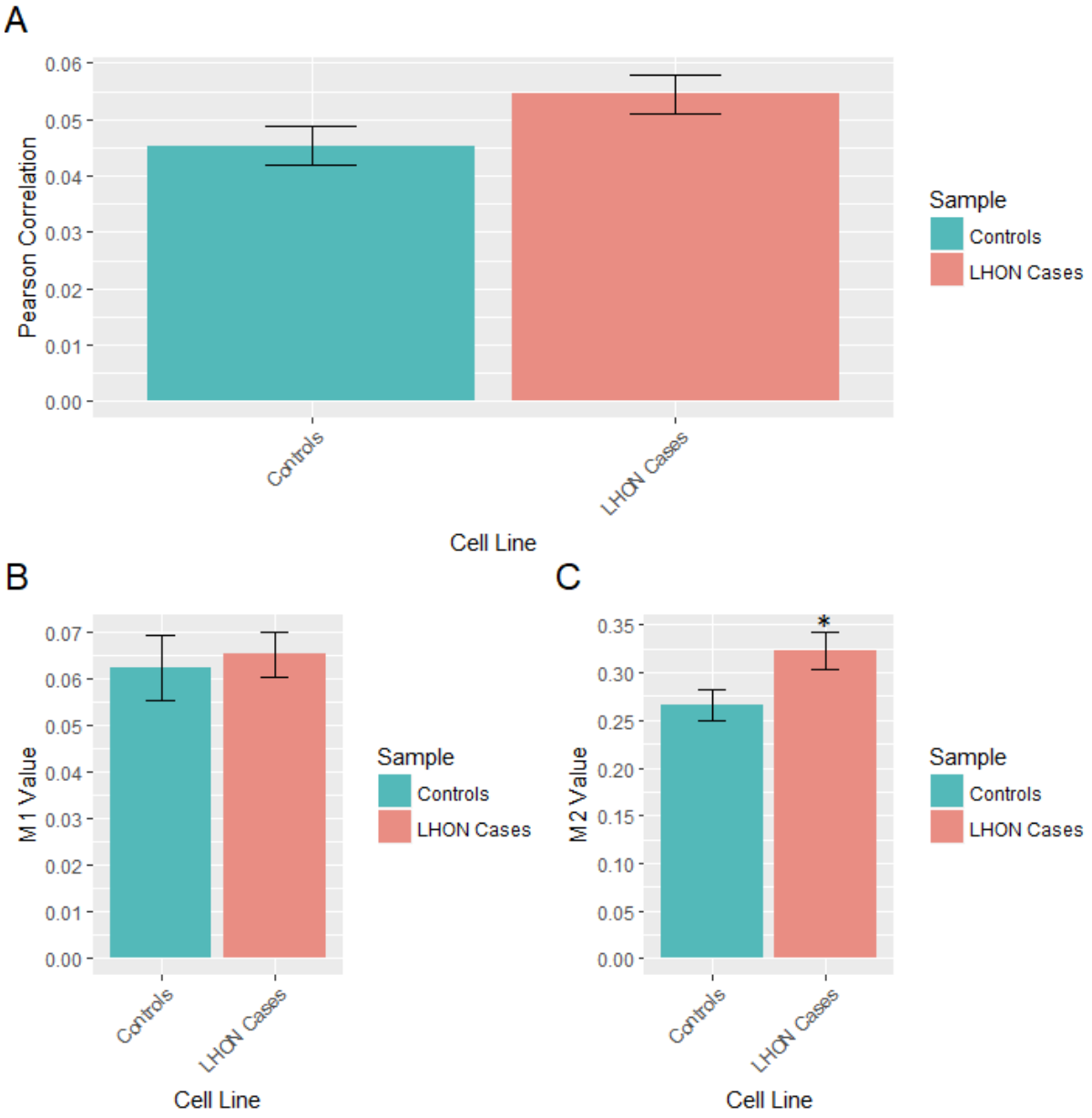

Figure 3.24: *Pearson Correlation (A), Manders' coefficient M1 (B) and Manders' coefficient M2 (C) as measured, showing controls and LHON patients grouped. Error bars represent standard error of the mean between a minimum of three biological replicates analysed at different passages, counts of cells analysed are available in Table S20. * Indicates $p \leq 0.05$.*

3.4 Discussion

3.4.1 mtDNA Copy Number

Increased mtDNA copy number has previously been declared protective towards LHON onset as observed in fibroblasts, peripheral white blood cells and skeletal muscle (Bianco et al., 2017; Giordano et al., 2014), with unaffected carriers showing a higher copy number than affected carriers or wild type controls, although this has been debated as to whether it is neuroprotective or arises as a result of carrying a LHON mutation (Finsterer, 2017; Yen et al., 2002). Increased copy number has independently been shown to ameliorate cardiomyopathy and COX deficiency symptoms within a heteroplasmic mitochondrial disease mouse (Filograna et al., 2019).

Preliminary results using the original laboratory standard assay for mtDNA copy number quantification (Grady et al., 2014; Pyle et al., 2016) did indicate that an unaffected mother had a greatly increased copy number when compared to her affected son, another m.11778G>A affected patient and also wild type controls (Figure S9). No further investigation was specifically taken into copy number in unaffected carriers due to limited availability of unaffected carrier cell lines.

Modification to the qPCR strategy was then implemented; the in-house mtDNA probe set was suboptimal for LHON mutations as a primer binding site sequence location matched the LHON position 3460 primary mutation in *MT-ND1*. Quantifying copy number in LHON samples with this mutation would result in an artificially low copy number being calculated due to the mismatch of the primer to the mutant sequence when compared to healthy controls.

This was overcome by relocating the mtDNA major arc probe set to *MT-RNR2*. The original in-house *B2M* primers were also replaced with new primers, arranged in a different position around the original probe, to prevent triplex primers being complimentary to one another as well as shortening the amplified fragment length and improving efficiency. The new probe set was successfully verified in efficacy from singleplex through to triplex (Figures 3.7 - 3.9). Both probe sets' efficiency greatly increased, with *MT-RNR2* amplifying a mean of 0.54 cycles earlier and *B2M* 3.78 cycles earlier in blood and 1.40 cycles earlier in fibroblast samples as shown in Table 3.12. Given the variance of the blood copy number measurements for *B2M* it is possible that the fibroblast measurement is more accurate, but this still indicates a detection improvement by reaching the threshold 1.40 cycles earlier. In addition to this, from in-house meta-analysis of mtDNA (kindly provided by Doctor Gavin Hudson (Newcastle University)), it was significantly less likely for a Single Nucleotide Polymorphism (SNP) to be present in the *MT-RNR2* primers/probe (1/386.5 rather than 1/8.9); dbSNP (Sherry et al., 2001) was used to ensure that the new *B2M* primers were similarly not relocated over common SNPs.

SYBR Green melt curve analysis of *B2M* (Figure 3.6) shows that the *B2M* optimisation

does not form novel primer dimers and the single melt peak indicates that only *B2M* is being successfully amplified.

The new qPCR technique was shown to be successful for quantifying LHON mtDNA copy number with the new assay more sensitive and less likely to be affected by other mtDNA sequence variability.

Using this assay to quantify LHON fibroblast copy number, results show a trend in the reduction of mitochondrial copy number in affected carriers when compared to wild type, however, this only reaches significance in the cell line A4-11778 ($p = 0.036$). As one of the three m.11778G>A cell lines, this significance is lost after grouping by mutation or looking at all LHON cell lines as a whole grouping.

No LHON cell lines showed deletion of the major arc; deletion is normalised to a control DNA blood sample - the negative deletion in LHON samples suggests that the control itself has some degree of heteroplasmy in the minor arc, with the negative deletion control showing a deletion of 65% rather than the expected 70%. Whilst mtDNA damage does occur under normal conditions (Richter et al., 1988) and is exacerbated by oxidative stress (Yakes and Van-Houten, 1997) with deletions occurring as part of a natural process of ageing (Phillips et al., 2014), large scale deletions were not expected.

3.4.2 ATP Production During Metabolic Stress

The mitochondrial respiratory chain, described in Section 1.2.1, is the principal source of ATP in the cell. LHON mutations which inhibit Complex I can limit the oxidation of NADH and electron transfer to CoQ10 (Lenaz et al., 2006) which in turn affects the downstream processes and limits resources available for production of ATP. This bioenergetic failure is known to prove fatal to cells, particularly cells with a high energy demand, such as RGCs (Osellame et al., 2012).

ATP is also known to act as a signalling molecule by ATP release from nerves to muscle tissue. Quite specifically, ATP has been shown to act as a neurotransmitter within the eye, down the optic signalling cascade, from the rod and cone cells to the brain (Khakh and Burnstock, 2009).

As such, impingement of ATP production and concentration could be causative of the LHON phenotype.

Figure 3.14 (A) does show a general decrease in most cell lines under glycolytic conditions, where it is thought that glycolysis can alleviate ATP deficiency by producing more ATP via glycolysis. In treating the cells with Deoxyglucose, glycolysis is inhibited and ATP should be produced by the mitochondrial respiratory chain. All cell lines produce less free ATP under this condition and whilst A4-11778 is significantly reduced when compared to controls, it did also have the lowest ATP measurement under glycolytic conditions.

Oligomycin A further inhibits the mitochondrial respiratory chain by blocking the proton channel of Complex V. During treatment with Glucose and Oligomycin A, cells

are dependent upon glycolysis and whilst insignificant, there is an upward trend of LHON cell lines when compared to controls. It is possible that due to Complex I defect that the trend reversal when compared to controls indicates LHON cell lines are more accustomed to glycolytic dependency.

Upon treatment with both Deoxyglucose and Oligomycin A, both glycolysis and Complex V are inhibited resulting in no production of ATP, free ATP in all cell lines is greatly reduced as cells quickly use their ATP reserves.

Baracca et al. (2005) found a severe reduction in osteosarcoma-derived rho^0 cells' ATP production however they did not find a reduction in cellular ATP content, indicating, like the data collected here, that a possible compensatory mechanism allows alleviation of low cellular ATP levels in LHON cell lines.

3.4.3 Cellular Oxygen Consumption

Mitochondrial respiration was determined using the Seahorse XFe96 Extracellular Flux Analyzer which assessed basal respiration, proton leak, ATP production, FCCP stimulated maximal respiratory capacity and spare respiratory capacity of mitochondria, alongside non-mitochondrial respiration in three control and five patient cell lines.

All LHON cell lines show a reduction in respiration, with several measurements being significant, particularly the maximal respiration and spare respiratory capacity; basal respiration and ATP production are also reduced in most cell lines, similar to that which was expected from other studies (Giorgio et al., 2012).

Figure 3.15 confirms a severe reduction in respiration, similar to that which has been seen before (Baracca et al., 2005; Brown et al., 2000). Section 3.3.2 shows that cell line A5-3460 has the greatest free ATP under glycolytic conditions, however, whilst measuring ATP production in Section 3.3.3, A5-3460 actually produces significantly less ATP than control cell lines. The results between the ATP Assay and Seahorse measurements differ in this cell line, as excluding A5-3460, the shape of the graph under glycolytic conditions (Figure 3.14) matches the shape of the graph for ATP production (Figure 3.15), indicating that ATP production could have a correlation to free cellular ATP. This is despite the ATP assay measurements indicating that there is not exclusively a direct relationship between the two as the cell lines respond differently during inhibition. This could be a biochemical response difference between the cells' responses, or that the Seahorse quantification is a more accurate measurement of cellular respiration across a range of conditions.

Interestingly, there is a range in the measurement of non-mitochondrial respiration response. Three individual cell lines are significantly reduced whilst others increase, however, after grouping by mutation, this is no longer significant. A5-3460 behaves differently between the ATP assay and Seahorse measurements, however, both A1-11778 and A4-11778, which show the lowest cellular ATP measurements under glycolytic conditions, also have the lowest non-mitochondrial respiration. It has previously been

shown that m.3460G>A fibroblasts have reduced sensitivity to rotenone (Cock et al., 1999), which potentially suggests that m.3460G>A mutations are more sensitive to further Complex I inhibition than other causative LHON mutations.

Non-mitochondrial respiration includes NADPH oxidases' activity (Brand and Nicholls, 2011) and given that NADPH oxidases produce ROS (Jiang et al., 2011) and inactivate Complex I (Kozieł et al., 2013), it is possible that LHON Complex I dysfunction results in downregulation of NADPH oxidase activity to prevent further oxidative stress and Complex I inhibition.

This was specific to the A5-3460 cell line and measurements of all cases indicated that this is not significant. This could be a peculiarity of the specific A5-3460 cell line, or indicative of a broader trend in the more severe m.3460G>A mutation which was not detectable in this experimental design.

All cell lines were cultured with antibiotics which can induce mitochondrial dysfunction and oxidative damage (Kalghatgi et al., 2013) by mitochondrial targeting, simulating the cellular phenotype of LHON. As such, these results could be exacerbated by further respiratory chain damage and ROS production.

LHON affects RGCs which experience variable ATP demand depending upon the frequency of which they must send action potentials. As such, it is important for them to maintain spare respiratory capacity and have a high maximal availability to manage increases in energy demands (Brand and Nicholls, 2011); the reduction in maximal and spare respiratory capacity within LHON patients indicates that the cells are already close to their bioenergetic limit and that they are unable to respond to further stress.

3.4.4 Calcium Homeostasis

Cells were tested for their response to histamine application which stimulates cells basal mitochondrial calcium load into their maximal uptake. This can be quantified by using Rhod-2, AM, which is a rhodamine-like fluorophore that is passively loaded into cells during incubation. Once inside the cell, the esterified AM group is cleaved to inhibit cellular removal and allow for fluorescence visualisation.

The experiment requires precise timing to ensure equal loading between cell lines and as some were approaching senescence, their calcium uptake could have been affected in the experiment. It has been acknowledged that care should be taken when acquiring mitochondrial calcium data via Rhod-2, AM imagery (Fonteriz et al., 2010).

Rhod-2, AM is known to cause modification to mitochondrial morphology and mitochondrial calcium concentration, however, this effect is "slow and limited" at 1 µM (Fonteriz et al., 2010) and Rhod-2, AM was only applied at 177 nM for this experiment, indicating that the cells would not be affected for their 30 minute incubation.

There is a high variability between cell lines with the majority of the mutant cell lines responding within the response range of the controls. The A3-11778 cell line shows the lowest uptake of calcium, however, this response does not occur in the other

m.11778G>A cell lines; A4-11778 shows a slight decrease but this is well within the range of the controls and A1-11778 is instead insignificantly increased in comparison to controls. The m.3460G>A mutation, A5-3460, is shown to significantly (0.004) increase the mitochondrial calcium uptake following histamine stimulation, however, following case:control cell groupings, this result is no longer significant. It is, however, possible that the increased biochemical response of A5-3460 is indicative of the phenotypically more severe clinical presentation (Zhuo et al., 2012).

Calcium is known to have a role in neuronal degeneration (Brini et al., 2014) and previously, LHON cybrid models' calcium deregulation has been minimised with Minocycline treatment, when compared to controls (Haroon et al., 2007), however, this study shows that only one m.3460G>A cell lines shows dysregulation of maximal mitochondrial calcium uptake following stimulation, which could again be specific to the A5-3460 cell line, or indicative increased m.3460G>A mutational burden.

As a whole, maximal calcium intake does not appear to differentiate LHON samples from healthy controls in this study.

3.4.5 Mitochondrial Membrane Potential

TMRM is accumulated within the matrix of polarised mitochondria (Kholmukhamedov et al., 2013) and is released once treated with FCCP, which uncouples the mitochondria, resulting in a loss of the proton gradient and fully depolarising the mitochondrial membrane (Dispersyn et al., 1999; Joshi and Bakowska, 2011).

Methodology for measurement of $\Delta\Psi m$ is well characterised (Joshi and Bakowska, 2011; Perry et al., 2011) and $\Delta\Psi m$ has a role in cellular permanence. Membrane permeability greatly increases by formation of the mPTP (Rao et al., 2014) and subsequent loss of $\Delta\Psi m$. This change in $\Delta\Psi m$ has been shown to cause matrix remodelling which triggers the release of cytochrome c, resulting in apoptosis (Gottlieb et al., 2003). There is conflicting evidence regarding this, with other authors indicating that apoptosis is independent of $\Delta\Psi m$ and dependent on other factors, with a decrease in $\Delta\Psi m$ occurring as a result of apoptosis, as opposed to a cause (Ly et al., 2003).

As reviewed in Section 1.3.1, fusion has been seen to generally minimise likelihood of apoptosis from occurring. MIM fusion requires an established $\Delta\Psi m$ to take place (Youle and Karbowski, 2005) and loss of $\Delta\Psi m$ selectively inhibits MIM fusion (Benard and Karbowski, 2009). Subsequently, this shift in the balance between fusion and fission would result in comparatively higher rates of mitochondrial fission - which is more likely to shift the cell fate balance towards cell death rather than survival.

Surprisingly, LHON cell lines showed no significant difference in $\Delta\Psi m$ to control cell lines but rather had a slight trend for increased $\Delta\Psi m$ which would indicate that they should actually be more resistant to apoptosis.

Other studies have shown that $\Delta\Psi m$ does decrease in LHON (Jiang et al., 2016), however, no change was found here, or in a study by Wong et al. (2002).

3.4.6 Mitochondrial Network

There is a great deal of variability between cell lines' response in experiments; LHON causative mutation has previously been indicated to affect disease severity (Howell, 1998; Yu-Wai-Man and Chinnery, 2000) however this was difficult to determine; for both the m.3460G>A and m.14484T>C mutation any significant differences could be a result of a specific cell line behaving atypically rather than that behaviour being indicative of that mutation.

MitoTracker Red, which was used to stain the mitochondria, permanence is dependent upon $\Delta\Psi$m, however, as shown in Section 3.3.6, there is no significant difference between the $\Delta\Psi$m of cases and controls so this should not affect the mitochondrial network measurements.

Mitochondrial network structure has been previously implicated in other mitochondrial optic neuropathies (Alavi and Fuhrmann, 2013) and it was possible that this could also factor into LHON disease severity (Kirches, 2011), however, whilst LHON cell lines tend to have a slightly smaller mitochondrial network volume, comprised of fewer fragments, as a whole this is not significant and differences could be exclusive to individual cell lines.

Mitochondrial fusion defects dramatically reduce cell growth rate and respiration, much like a LHON defect, however, they also result in a heterogenous mitochondrial population with reduced $\Delta\Psi$m which was not seen in Section 3.4.5, indicating that cellular fusion does not directly factor in LHON (Chen et al., 2005). This is compounded by Figure 3.21 (E) showing no reduction in mitochondrial volume between cases and controls. That being said, Figure 3.19 shows that there is a trend towards lowered mitochondrial volume in m.11778G>A cell lines with cell lines A1-11778 and A4-11778 both significantly reduced while A3-11778 mitochondrial network volume is unaffected. The correlation between the mitochondrial network response and $\Delta\Psi$m response does not appear to align with the cell lines' behaviour in each assay responding in the same direction, however.

LHON samples instead appear to have a higher rate of fusion than controls, with fewer fragments in the mitochondrial network, as seen in Figures 3.19, 3.20 and 3.21 (I), particularly in the m.3460G>A mutation sample, which again indicates that this sample responds differently to treatment compared to the other LHON samples.

It could be possible that LHON samples could upregulate fusion as a neuroprotective measure, however, further work would be needed to validate this.

3.4.7 ER-Mitochondrial Interactions

ER-mitochondrial interactions have been shown to be vital in a range of cellular functions, including Ca^{2+} signalling, the UPR^{ER} and linking in to mechanisms such as apoptosis, fusion and fission, as reviewed in Section 1.3.3.

ER-mitochondrial interactions have also been previously implicated in other mito-

chondrial optic neuropathies (Alavi and Fuhrmann, 2013) with further evidence of ER involvement in the metabolomic profile of LHON (Chao de la Barca et al., 2016). Manders' coefficient is commonly used to measure the interaction of the ER-mitochondria, as a measure of the proportion of contact between the ER structure to the mitochondria (Bravo et al., 2011).

As a whole, LHON appears to significantly increase the co-localisation of the mitochondria to the ER (M2), however, this primarily appears to be in cell lines with the m.3460G>A or m.14484T>C mutation; it is insignificantly elevated in one cell line with a m.11778G>A mutation, but insignificantly lowered in the other two. Tunicamycin, an ER stress inducer which upregulates the unfolded protein response, causes an increase in mitochondrial-ER interactions (M2 coefficient) in HeLa cells (Bravo et al., 2011); the increase of M2 in LHON cell lines suggests that ER stress could be a factor in LHON disease development or progression, as indicated previously by Chao de la Barca et al. (2016) but that this could be dependent upon the disease causing mutation.

In healthy cells, it is estimated that ~5–20% of the total mitochondrial surface is in contact with the ER at any given moment (Friedman et al., 2011); the M2 value in the control fibroblasts is ~27%, suggesting that these cell lines as a whole shows more connections between the ER to the mitochondria than previous studies have shown, but this ~5–20% figure then suggests that the LHON m.14484T>C and m.3460G>A cell lines are further increasing interactions between the organelles in comparison.

Mitochondrial-ER contact points have also been shown to often be trigger points for mitochondrial fission events (Friedman et al., 2011), however, despite the high proportion of mitochondria in contact to the ER, the number of mitochondrial fragments in these cell lines was not increased in comparison to controls, as shown in Figure 3.19.

Chapter 4 | Retinal Characterisation of Mitochondrial Disease Mouse

4.1 Introduction

Review of both subcellular systems and genetics in LHON has not yet yielded a definitive cause for the variable disease penetrance.

As such, an alternate methodology of investigating the role of mtDNA mutations at a macro systems level was considered. The mouse is known to be a good model for optic disease; there are some minor differences with anatomy, such as the murine optic nerve head opening at the nadir of the eye whilst it is off-centre in humans (Albrecht May, 2008; May and Lütjen-Drecoll, 2002), but despite this, it remains a popular model as it is more similar than many other species (Albrecht May, 2008; Krebs et al., 2017; Veleri et al., 2015).

There have been rodent models of LHON described, both a rat model (Marella et al., 2010) using the yeast *NDI1* gene, a homolog of human *MT-ND4*, and a mouse model of human *MT-ND4* by allotopic expression (Qi et al., 2007). Allotopic expression has been known as an attempted strategy LHON treatment, described in Section 1.5.5 but late stage phase III trials have been unsuccessful (GenSight Biologics, 2019).

LHON mutant m.13997G>A has also been created by fusing a cytoplast to a female mouse embryonic stem cell line which was injected into blastocysts with subsequent female carriers backcrossed for 10 generations (Lin et al., 2012). A further 150 cell lines have been described for transmitochondrial mice, with LHON m.11186G>A tested for disease phenotype (Fayzulin et al., 2015), although the LHON heteroplasmic mutation m.11186G>A also contains a secondary homoplasmic m.15581C>T mutation in the mtDNA too (Fayzulin et al., 2015).

Recently, a transgenic MitoMouse of human m.11778G>A was created by mitochondria-targeted adeno-associated virus zygote injection with female carriers backcrossed onto healthy males for 8 generations (Yu et al., 2015).

These mouse models did appear to reliably exhibit features of LHON and respond to potential drug treatments (Lin et al., 2012; Marella et al., 2010; Qi et al., 2007; Yu et al., 2015, 2018a), indicating that the systems based methodology for investigating LHON disease onset could be most effective.

The human based MitoMouse created by Yu et al. (2015) is of particular interest for being the first mouse model with both the human genotype and phenotype exhibited in

the mouse. Their later study of mitochondrially targeting the *MT-ND4* gene with adeno associated viral vector indicates that LHON gene therapy could produce a favourable clinical response.

Mutant models often have a lower fitness and reproductive capability compared to wildtype and as such, there is limited availability of mitochondrially defective mice so we were not able to characterise a specific LHON model. Instead, the well characterised $tRNA^{ALA}$ mouse was identified as a viable option for retinal characterisation for novel optic defects in $tRNA^{ALA}$ m.5024C>T and *MT-ND6* m.13715C>T (Kauppila et al., 2016). $tRNA^{ALA}$ m.5024C>T and *MT-ND6* m.13715C>T are transcribed on the same molecule and hence exist at the same level of heteroplasmy within the mouse. Further, m.13715C>T is a non-synonymous variant in *MT-ND6* - a subunit which is known to also be involved in LHON, with the LHON m.14484T>C mutation also affecting *MT-ND6*.

m.5024C>T affects the mitochondrially encoded *MT-TA* gene which encodes $tRNA^{ALA}$. $tRNA^{ALA}$ has a role in translation by decoding alanine codons and transferring an alanine amino acid to the newly synthesising amino acid chain as appropriate. The mouse was originally created by Professor James Stewart's research group (Max Planck Institute for Biology of Ageing), which originated from a cross of 'mtDNA-mutator' mice (Trifunovic et al., 2004), and was kindly gifted to Professor Michal Minczuk (University of Cambridge) who collaborated with us for retinal characterisation. At present, the mice have been shown to have reduced body mass, cardiomyopathy and impaired mitochondrial translation. Highly proliferating tissues also bias against high mutant heteroplasmy levels, indicating that heteroplasmy in the eye - with little proliferation - could increase above other tissue types (Kauppila et al., 2016).

The mouse has also been used in experiments which have targeted and corrected mutant mtDNA burden *in vivo*, with both mitochondrially targeted TALENs and ZFNs shown to be effective at reducing heteroplasmy levels (Bacman et al., 2018; Gammage et al., 2018b). Despite the newer technology of CRISPR becoming highly prevalent and popularised, it is likely not an effective strategy for mtDNA gene therapy treatments (Gammage et al., 2018a).

This project sought to determine methodology and further characterise the m.5024C>T + m.13715C>T disease mouse to ascertain whether a phenotype of retinal neuropathy could be identified and characterised. Given the variable heteroplasmy in the mouse, and the known response to TALENs and ZFNs, the long term aim was to later ascertain whether gene therapy treatments could then alleviate any retinal neuropathy by reducing mutant mitochondrial burden within a retinal phenotype (Bacman et al., 2018; Gammage et al., 2018b). LHON often exists as a homoplasmic disease, however, there are cases with reduced heteroplasmy in affected individuals (Jacobi et al., 2001; Krylova et al., 2020). As such, the variable heteroplasmy in the m.5024C>T + m.13715C>T could be used to create a scale both for the initial mutational burden and

to quantify the success of genetic rescue within retinal tissue.

4.2 METHODOLOGY

4.2.1 Mice Cohort

Tables 4.1 and 4.2 describe the mice which were respectively used for validating heteroplasmy levels between different tissue regions and retinal characterisation.

The work was performed in collaboration with Professor Michal Minczuk (University of Cambridge) who kindly shared the mice, Doctor Payam Gammage (University of Glasgow, formerly, University of Cambridge) and Beverly McCann (University of Cambridge) who originally raised the mice and determined ear heteroplasmy levels, alongside Doctor Andrew Osborne (University of Cambridge) who collected ERG measurements (Figure 4.3) and retinal tissue.

Table 4.1: *Details of quantified heteroplasmy mice.*

Mouse	Ear Clipping m.5024C>T Heteroplasmy
S1	66%
S2	56%
S3	59%
S4	63%

Table 4.2: *Heteroplasmy levels of characterised mice.*

Mouse	Mutant Heteroplasmy	Sex	Age
WT1	0%	Male	2 months
WT2	0%	Male	2 months
WT3	0%	Male	2 months
M1	81%	Male	9 months
M2	80%	Male	9 months
M3	51%	Male	24 months
M4	72%	Male	24 months
M5	68%	Male	24 months

Eye Collection

Mice were culled and eyes were extracted by Doctor Andrew Osborne.

4.2.2 Mitochondrial Heteroplasmy Level

DNA Isolation

Eyes from mice described in Table 4.1 were freshly collected and further dissected by Doctor Andrew Osborne, separating the retina and sclera of the left eye and leaving the right eye as whole tissue.

Table 4.3: *ERG measurements of characterised mice (Table 4.2) and wildtype mice. Measurements are average of both eyes taken through three biological time point triplicates for mutant mice and a single time point of four individual mice for wildtype (WT). pSTR (max), b-wave (max) and a-wave (min) represent RGC, bipolar and photoreceptor response respectively.*

Mouse	Age	pSTR (max)	pSTR (P100)	nSTR (min)	nSTR (P220)	*b*-wave (max)	*b*-wave (P90)	*a*-wave (min)
WT	5 months	35.65	27.14	-4.55	-0.71	667.54	616.88	-493.59
M3	24 months	12.71	6.75	0.89	1.20	260.70	238.75	-234.35
M4	24 months	9.89	7.76	0.93	2.13	307.99	285.22	-203.57
M5	24 months	12.05	10.18	-0.46	1.54	194.59	173.81	-183.48

DNA was then extracted from each tissue type using DNeasy Blood & Tissue Kit as per manufacturer's protocol and DNA was quantified using 8-Sample Spectrophotometer NanoDrop.

Pyrosequencing

Four technical replicates of each sample were PCR amplified using PyroMark PCR Kit (978703; QIAGEN) as per manufacturer's protocol, using the PCR reaction composition described in Table 4.4.

Table 4.4: *PCR reaction composition for pyrosequencing where water produces a reaction volume of 20 µl for pyrosequencing and 25 µl for electrophoresis. Primer sequence identity shown in Appendix Table S23.*

Volume	Component
12.5 µl	PyroMark PCR Master Mix, 2x
2.5 µl	CoralLoad Concentrate, 10x
1.5 µl	25 mM $MgCl_2$
5 µl	Q-Solution, 5x
0.5 µl	10 mM Forwards Primer
0.5 µl	10 mM Reverse Primer
x µl	25-50 ng DNA
x µl	RNase-free water

A pyrosequencing protocol was created in PyroMark Q24 Software (9019062; QIAGEN) and samples were then prepared using PyroMark Q24 Vacuum Workstation (9001516; QIAGEN) and quantified on a PyroMark Q24 (9001514; QIAGEN)), both as per manufacturer's protocol.

Table 4.5: *Pyrosequencing standard PCR thermocycling program.*

	Temperature	**Time**	
Initial Denaturation	95°C	15 min	
Amplify	94°C 60°C 72°C	30 s 30 s 30 s	45 cycles
Final Extension	70°C	10 min	
Hold	4°C	∞	

4.2.3 Eye Preparation

Eyes described in Table 4.2 were further treated within the animal facility, by Doctor Andrew Osborne, by fixing the fresh eyes in 4% Paraformaldehyde (P6148; Sigma-Aldrich) immediately following collection.

Eye Sections

24-48 hours post fixation at 4°C, the left eyes of the mice described in Table 4.2 were transferred into 30% Sucrose (S0389; Sigma-Aldrich) in PBS overnight until the tissue had sunk to the bottom of the 1.5 ml Microcentrifuge Eppendorf Safe-Lock Tube (0030120086; Eppendorf). The eyes were then transferred into Embedding Capsule (Flat Ended) (AGG3759; Agar Scientific) containing O.C.T. Compound (4583; Sakura Europe) and carefully orientating the pupil to be perpendicular to the bottom of the Embedding Capsule (Flat Ended) before snap freezing on dry ice. These were stored at -20°C until cryosectioning.

Samples were sectioned on an OTF5000 Cryostat Microtome (Bright Instruments) with a 3P Anti-Roll System CE, Glass 70 mm (14047742497; Leica Microsystems), taking 11 µm sections and collecting onto Microscope Slides (630-1985; Gerhard Menzel GMBH) in a series of 6 slides, each containing a range of sections across the whole eye. Samples were left to air dry for 4 hours before transferral into a -20°C freezer until staining.

Samples were equilibrated to room temperature before staining. They were then washed for 15 minutes, three times, in PBS on a Mini Orbital Shaker SO5 (Stuart Scientific) at a slow speed before drying, demarcating the outer slide boundary with a Microscope Slide Marking Pen (Magnacol) and applying 500 µl blocking buffer (2% Bovine Serum Albumin (A0149; Sigma-Aldrich), 0.3% Triton and 5% Normal Goat Serum (G9023; Sigma-Aldrich) in PBS). This was incubated on the orbital shaker for one hour before the blocking buffer was replaced with the primary antibody.

One series of slides were stained with Mouse Anti-βIII Tubulin mAb (G7121; Promega) and another with Mouse mAb Anti Rhodopsin (1D4, C-Terminal) (kindly gifted from

Professor Mike Cheetham (University College London), who received it as a gift from Professor Robert Molday (University of British Columbia)) at a dilution of 1:500 for Mouse Anti-βIII Tubulin mAb and 1:1000 for Mouse mAb Anti Rhodopsin (1D4, C-Terminal), both in blocking buffer. 400 µl of the primary antibody solution was incubated in the dark overnight at 4°C on the orbital shaker.

All subsequent steps proceeded whilst limiting light exposure to the slides. The slides were washed three times, each for 15 minutes on the orbital shaker and secondary antibodies were prepared for both series of slides. Goat anti-Mouse IgG (H+L) Highly Cross-Adsorbed Secondary Antibody, Alexa Fluor 555 (A-21424; Invitrogen) at a 1:500 dilution in blocking buffer was prepared for both the Mouse Anti-βIII Tubulin mAb and Mouse mAb Anti Rhodopsin (1D4, C-Terminal). Both secondary solutions also added a 1:8000 dilution of DAPI Solution (1 mg/mL) (62248; Thermo Fisher Scientific) and 500 µl of each secondary antibody to the slides before incubating at room temperature for two hours on the orbital shaker.

The slides were then washed three times, each for 20 minutes, with PBS on the orbital shaker prior to mounting with FluorSave Reagent (345789; Merck Millipore) and an SLS Select Coverslips No 1, 24x50mm (MIC3234 ; Scientific Laboratory Supplies).

The prepared slides were then kept in darkness and dried overnight before storing at 4°C until imaging.

Flat Mounts

2 hours post fixation at room temperature, the right eyes from the M3:M5 mice, as described in Table 4.2 were transferred into 50 mm Single Vent Shallow (10mm) Petri Dish (SC266; Sterilin) filed with PBS. The cornea was punctured using a Hypodermic Needle 27G (0.4 x 20 mm) (Terumo) and the retina was dissected out using Dumont #5 Forceps Biologie Dumostar (11295-10; InterFocus) and Vannas Spring Scissors, Straight 3mm Cutting Edge (15000-00; InterFocus). Cuts were made from the edge of the retina towards optic nerve head, located in the centre of the mouse retina, to form the 'petals' of the flattened tissue. This was then placed onto a Membrane Filter, 0.8 µm pore size, gridded (AABG01300; MF-Millipore™) and the filter was placed into a Nunc Cell-Culture Treated Multidish (142475; Thermo Fisher Scientific) with 500 µl of PBS. Retinas were stored at 4°C until staining.

For staining, retinas were equilibrated to room temperature and washed twice, for 10 minutes, in 250 µl PBS with 0.5% Triton and placed on a slow moving orbital shaker. Retinas were permeated by freezing for 10 minutes at -70°C in 350 µl PBS with 0.5% Triton. Care was taken to ensure that the entire retina was submerged prior to freezing. This is vital for staining nuclear proteins.

The retinas were quickly thawed at room temperature by adding 500 µl PBS with 0.5% Triton and slowly shook until they finished thawing. They were washed twice for an additional 10 minutes in 250 µl PBS with 0.5% Triton on the orbital shaker.

Retinas were blocked in 500 µl Blocking Buffer (2% BSA, 2% Triton and 10% Normal Donkey Serum (D9663; Sigma-Aldrich) in PBS) for 1 hour on the orbital shaker before incubating in the primary antibody within darkness. A 1:300 dilution of Goat Brn-3a Antibody (C-20) (sc-31984; Santa Cruz Biotechnology) in Blocking Buffer was used for 2 hours on the orbital shaker at room temperature before shaking overnight at 4°C. During all subsequent stages, care was taken to minimise sample light exposure.

The next morning, retinas were rinsed for 5 minutes in 1 ml PBS with 2% Triton and a further three 30 minute washes took place using 1 ml PBS with 0.5% Triton, all at room temperature on the slow orbital shaker.

A 1:500 dilution of Donkey anti-Goat IgG (H+L) Cross-Adsorbed Secondary Antibody, Alexa Fluor 555 (A-21432; Invitrogen) secondary antibody in PBS with 2% Triton was added before incubating for two hours on the orbital shaker. They were then washed three times for 30 minutes in 1 ml PBS on the orbital shaker. For the final 30 minute wash, a 1:10,000 dilution of DAPI Solution (1 mg/mL) was added.

The retinas were carefully transferred, RGC layer upwards, onto a microscope slide. A fine paint brush was used to smooth the tissue and a Kimwipes Delicate Task Wipers, 1-Ply (06-666; Kimberly-Clark Professional) was used to blot excess liquid. FluorSave Reagent was carefully added and an SLS Select Coverslips No 1, 24x50mm placed on top, taking care to prevent bubbles and air dried overnight.

The prepared slides were then kept in darkness and stored at 4°C until imaging.

4.2.4 Quantification

Sections

Sections were imaged using a Zeiss LSM 880 AxioObserver confocal microscope (Carl Zeiss MicroImaging) equipped with a Nikon Plan-Apochromat 63x/1.4 numerical aperture oil immersion objective, averaging fluoresence across two image replicates. A range of tile scans, with 15% image over lap, Z-stacks, with 0.95 µm steps through the section, and tiled Z-stacks were taken.

CZI files were imported into ZEN 2.6 18299.3 (blue edition) (Carl Zeiss Microscopy GmbH), stitched as necessary, and best fit channel scaling was applied. Each individual channel was then exported as uncompressed TIFF file format.

TIFF files were imported into Fiji (ImageJ 1.52i) (Schindelin et al., 2012) and a maximum projection was performed on stacks for RGC counting and length measurements. ONL and INL cells were quantified from a single stack slice. Cells were converted to a binary mask following signal multiplication, Gaussian blurring - to remove noise - raising contrast and multiplying again. ONL and INL were auto thresholded via "default white" and "triangle white" methods respectively with a further Gaussian blur and image contrasting.

The binary mask was opened (eroded then dilated), cell holes were filled and a watershed was applied to separate any conjoined cells. Within the 11 µm section, RGCs

existed in a monolayer, so the length in which the cells were counted was measured. ONL and INL cells were dense and a region was highlighted, measured and the cells within the region counted by analysing particles larger than 50 or 150 pixel units for ONL and INL respectively.

Retinal cell layers' length was also measured in Fiji, using the maximal projection of Rhodopsin stained sections to measure the PRs, ONL and OPL. Tubulin stained slides' maximum projections were used to measure the INL, IPL and RGC layer.

All quantification steps were performed blinded to the sample identity as control or mutant.

Whole Mounts

Whole mounts were imaged on a Dragonfly Spinning Disk Imaging System (Andor Technologies Ltd.) comprised of a Nikon Ti-E microscope, Nikon Plan-Apochromat 40×/1.3 numerical aperture oil immersion objective and an Andor iXon EMCCD Camera. Z-stacks were taken at 0.12 µm steps across the depth of the tissue, ~500 steps and a staged montage was taken across the width and length of the tissue in a grid with 10% overlap between tiles, using Fusion Version 1.5.0.7 (Andor Technology Ltd.).

Images were initially reviewed in Imaris Bitplane 9.1.2 to stitch the tiles and quantify RGC counts.

Individual tiles were imported into Fiji (ImageJ 1.52i) (Schindelin et al., 2012) via the Bio-Formats Importer and a maximum intensity projection was performed across the Z-stacks on the Brn3-a channel. The individual tiles were then stitched together in a grid, using a 10% overlap and fusion by linear blending with a regression threshold of 0.15, maximum/average displacement threshold of 2.5 and absolute displacement threshold of 3.5 (Preibisch et al., 2009). Following stitching, the images were converted to binary masks and holes within the cells were filled. Images were cleaned by performing a binary opening to remove isolated pixel noise and smooth the cell edges. A watershed transformation was then used to create cell boundaries for cells which appeared conjoined within the binary image. Particles larger than 100 pixel units were then measured and analysed.

Total tissue cell counts were calculated, then a 1000x1000 pixel section was taken in quadruplicate for points close to the optic nerve head, the outside edge of the retina and the centre of the tissue, with care taken to avoid obvious venous routes and secondary artefacts in the tissue structure. Cells were again quantified in this region and the length across the entire flattened retina and optic nerve head were measured in technical quadruplicate.

All quantification steps were performed blinded to the sample identity as control or mutant.

4.3 RESULTS

4.3.1 Mitochondrial Heteroplasmy Level

Table 4.6: *m.5024C>T heteroplasmy levels of quantified heteroplasmic mice cohort in ear clippings, sclera, retina and whole eye; mean of technical quadruplicates.*

Mouse	Ear Heteroplasmy	Sclera Heteroplasmy	Retina Heteroplasmy	Eye Heteroplasmy
S1	66%	66%	66%	66%
S2	56%	56%	56%	55%
S3	59%	62%	64%	64%
S4	63%	66%	65%	65%

Mitochondrial heteroplasmy level was compared between the ear and eye, with further tissue stratification into whole eye, retina and sclera. As shown in Table 4.6, there are no significant differences between heteroplasmy levels in the ear, eye or different eye sections.

4.3.2 Sections

Measurement Validation

As shown in Figure 4.1, staining patterns allowed for clear demarcation of retinal layers. Methods for quantifying cell counts are shown in Figures 4.2, 4.3 and 4.4 for ONL, INL and RGC layers respectively. Methodology allowed for clear demarcation and identification of cells without human bias within the counting process.

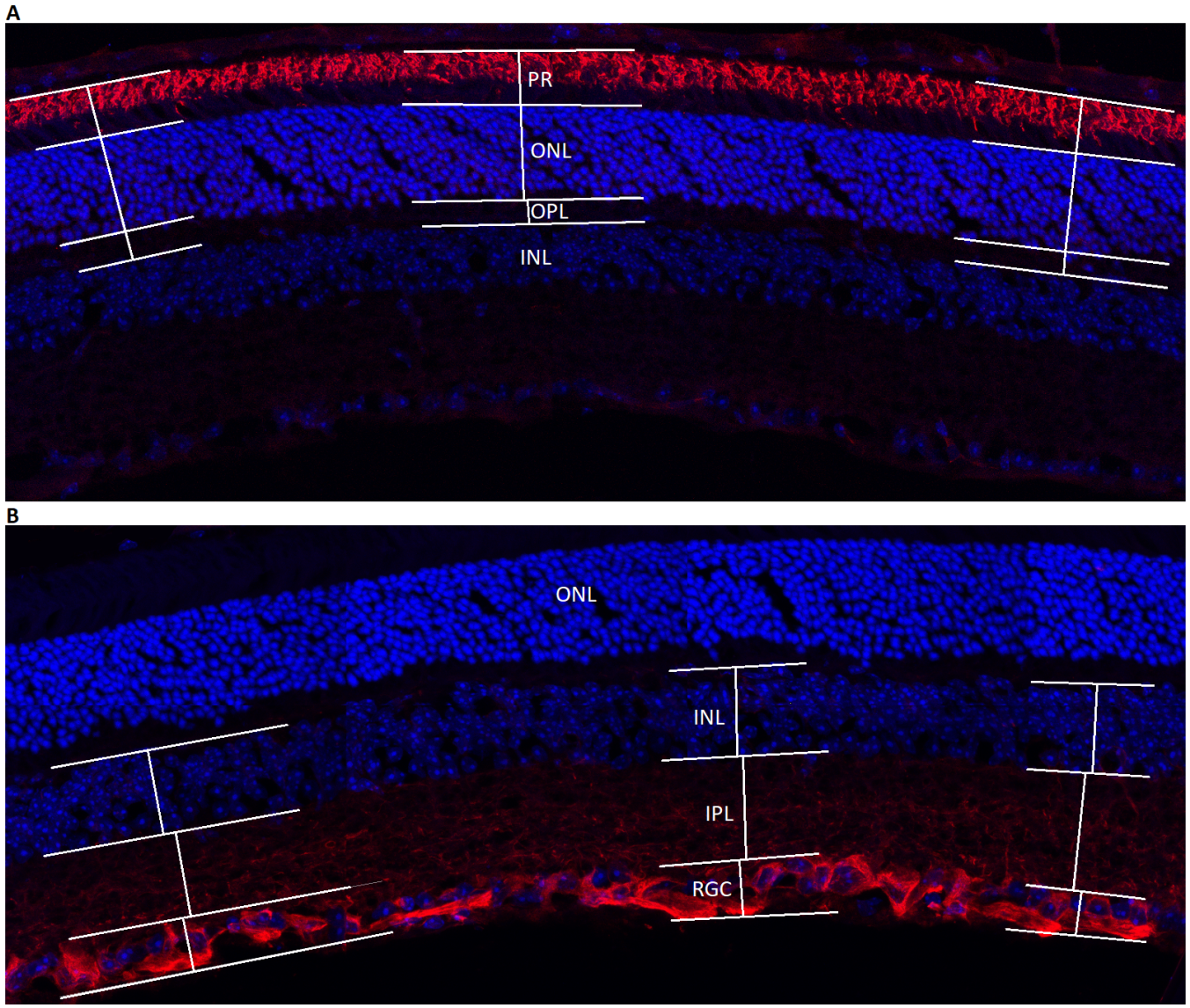

Figure 4.1: *Measuring lengths of (A) PR layer, ONL and OPL, and (B) INL, IPL and RGC layer, in cells stained against Rhodopsin (1D4, C-Terminal) (red) and DAPI (blue). Lines were drawn parallel to each layer and the length was measured perpendicularly to the line with triplicate measurements.*

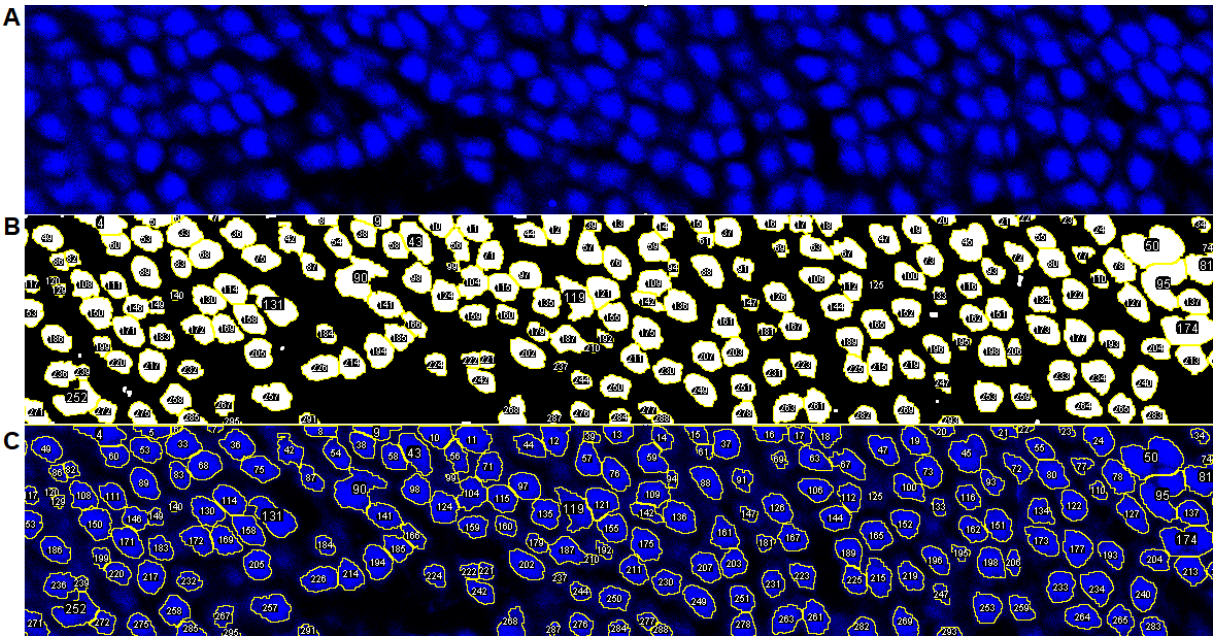

Figure 4.2: *Validation of ONL cell quantification in a single stack slice; original image (A), binary mask after processing image B, mapping counted cells of binary mask back onto original image (C).*

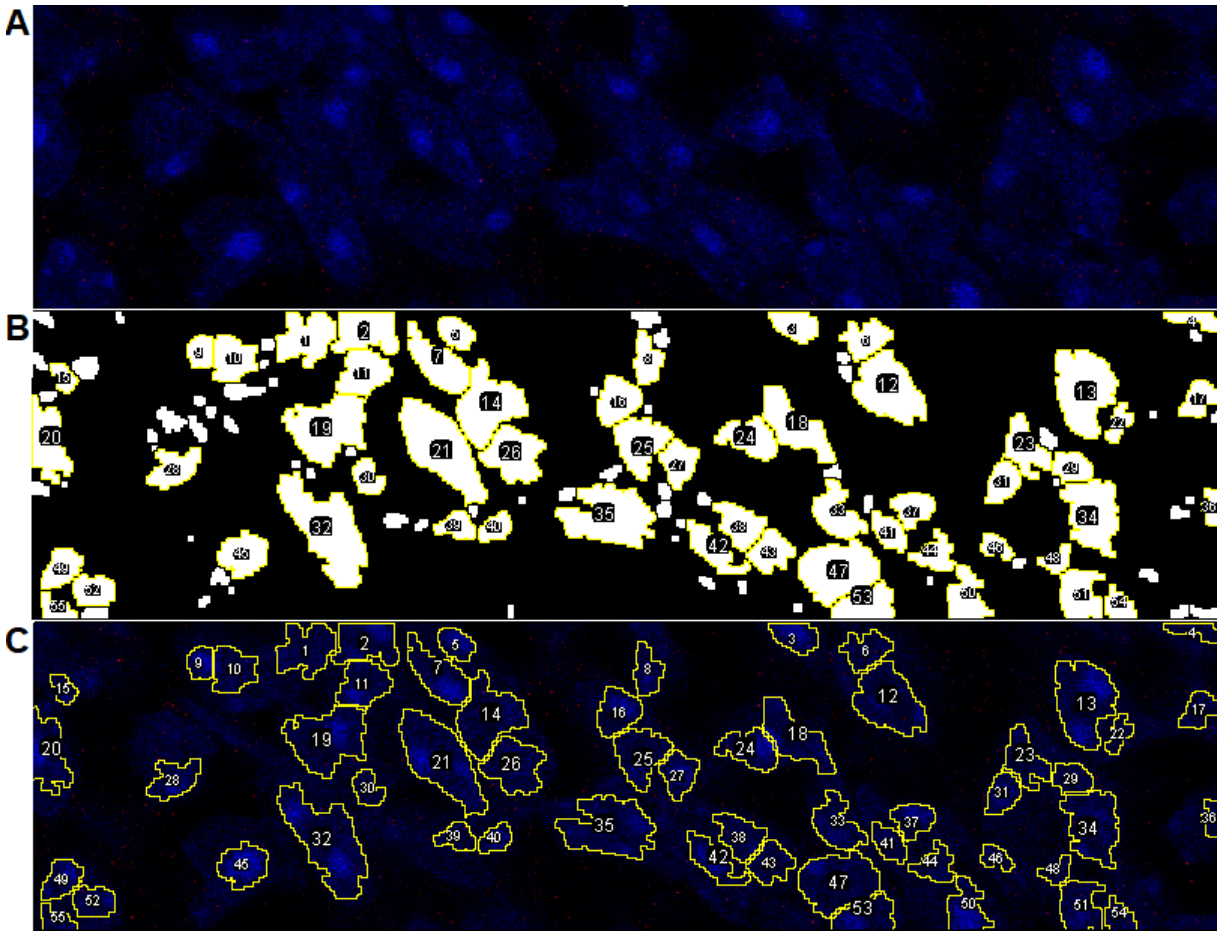

Figure 4.3: *Validation of INL cell quantification in a single stack slice; original image (A), binary mask after processing image B, mapping counted cells of binary mask back onto original image (C).*

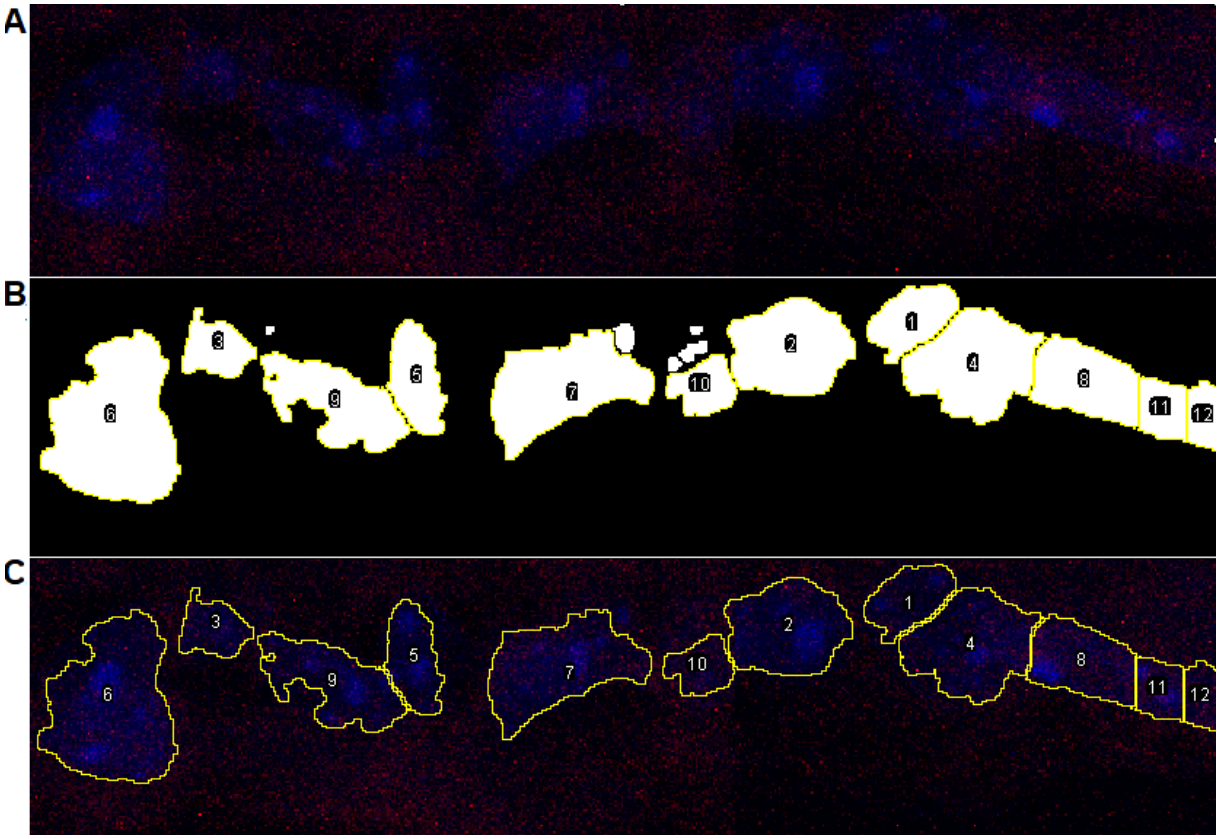

Figure 4.4: *Validation of RGC cell quantification in a single stack slice; original image (A), binary mask after processing image B, mapping counted cells of binary mask back onto original image (C).*

Tissue Morphology

Tissue cross-sections were shown as whole eye tile scans in Figures 4.5 and 4.6. Selected regions from Z-stack tile scans are then magnified in Figures 4.7- 4.14.

Tissue morphology in wildtype samples (Figures 4.7, 4.8 and 4.9) were highly ordered with good separation between retinal layers.

Samples M1 and M2 (Figures 4.10 and 4.11) had several small spaces which appear within the ONL and INL.

Sample M3 (Figure 4.12) was visibly more tortured across the whole eye and there were a number of spaces in the ONL and INL.

Sample M4 (Figure 4.13) was visibly ragged across the whole eye and with lots of spaces in the ONL and INL.

Sample M5 (Figure 4.13) was openly vacuous with spaces, variability is the size of the layers and cell types transitioning between layers with less clear layer boundaries.

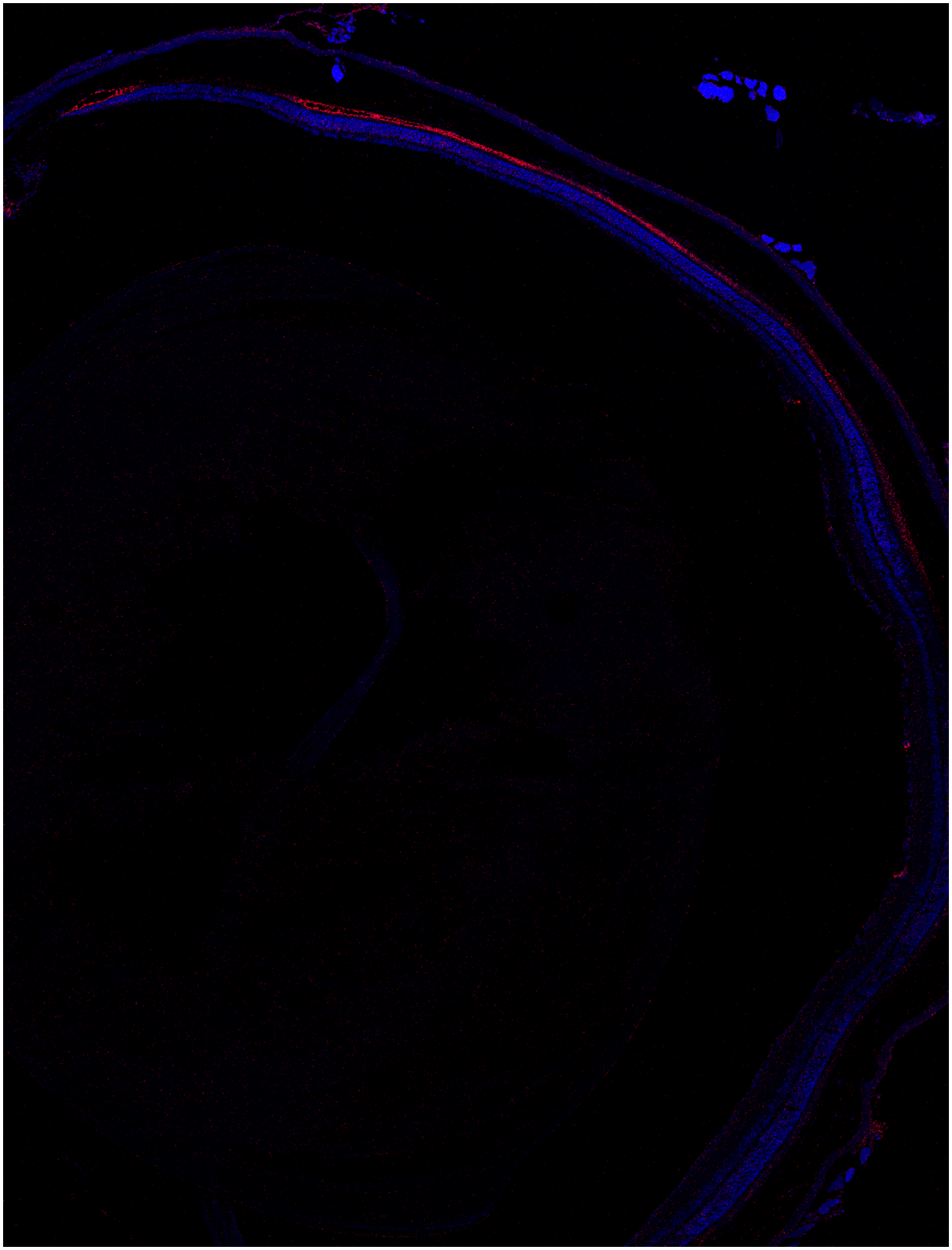

Figure 4.5: *Whole eye sectioned tile scan, stained against Rhodopsin (1D4, C-Terminal) (red) and DAPI (blue). Red staining indicates the PR layer, with all cell nuclei stained by DAPI; gross morphology of tissue structure shown.*

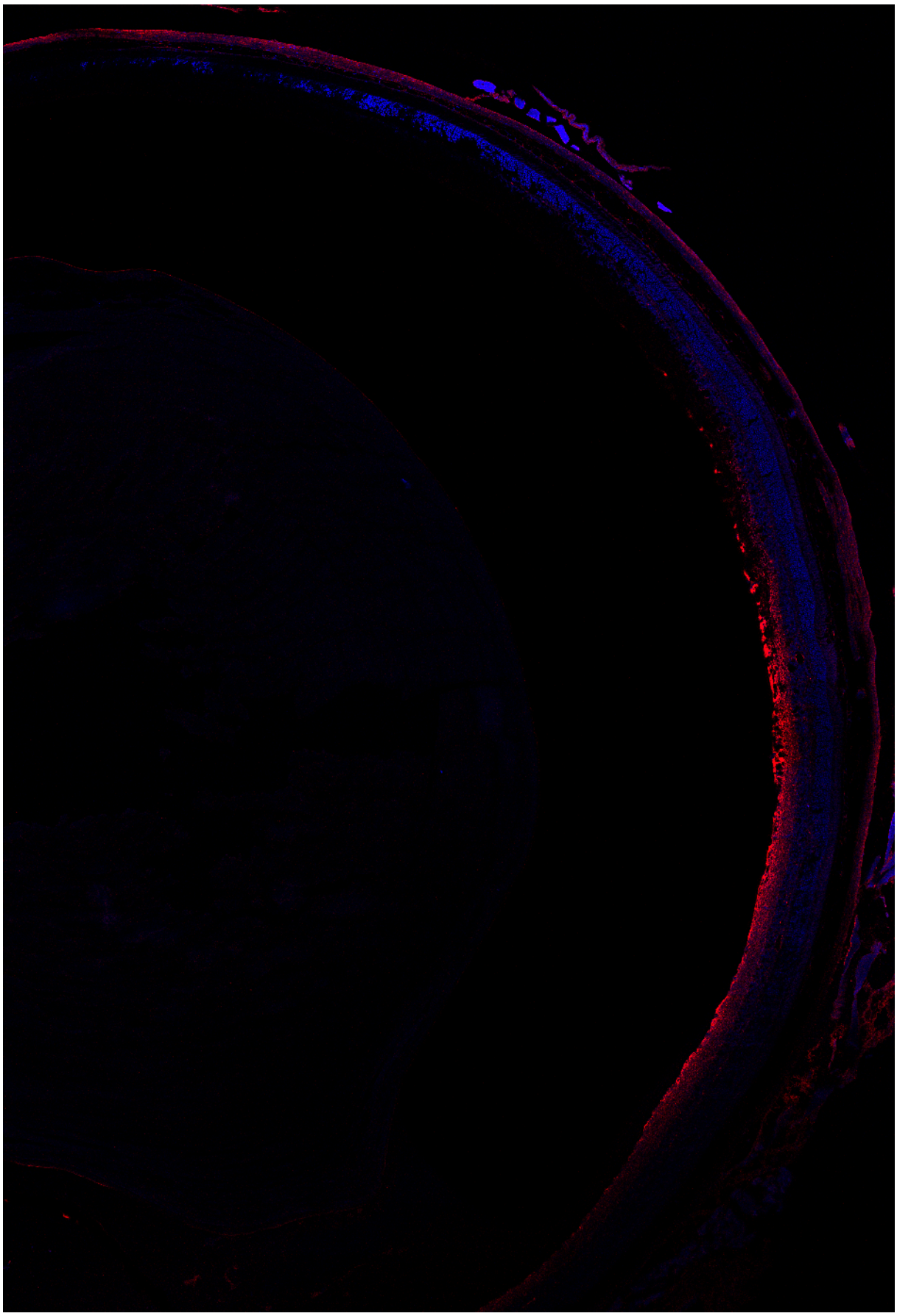

Figure 4.6: *Whole eye sectioned tile scan, stained against Tubulin (βIII) (red) and DAPI (blue). Red staining indicates the RGC layer, with all cell nuclei stained by DAPI; gross morphology of tissue structure shown.*

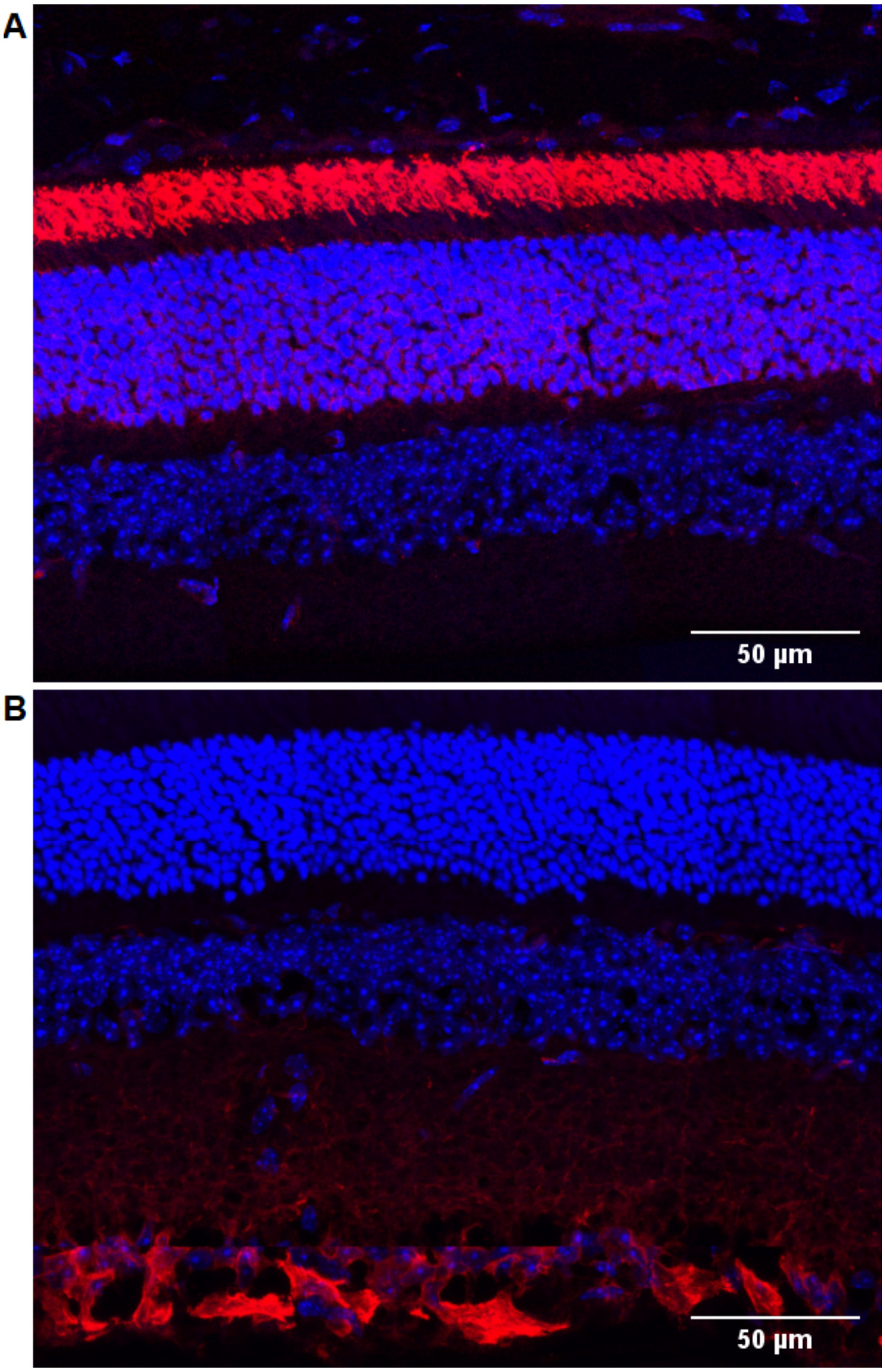

Figure 4.7: *WT1 retinal section stained against Rhodopsin (1D4, C-Terminal) (red)and DAPI (blue) (A) and Tubulin (βIII) (red) and DAPI (blue) (B).*

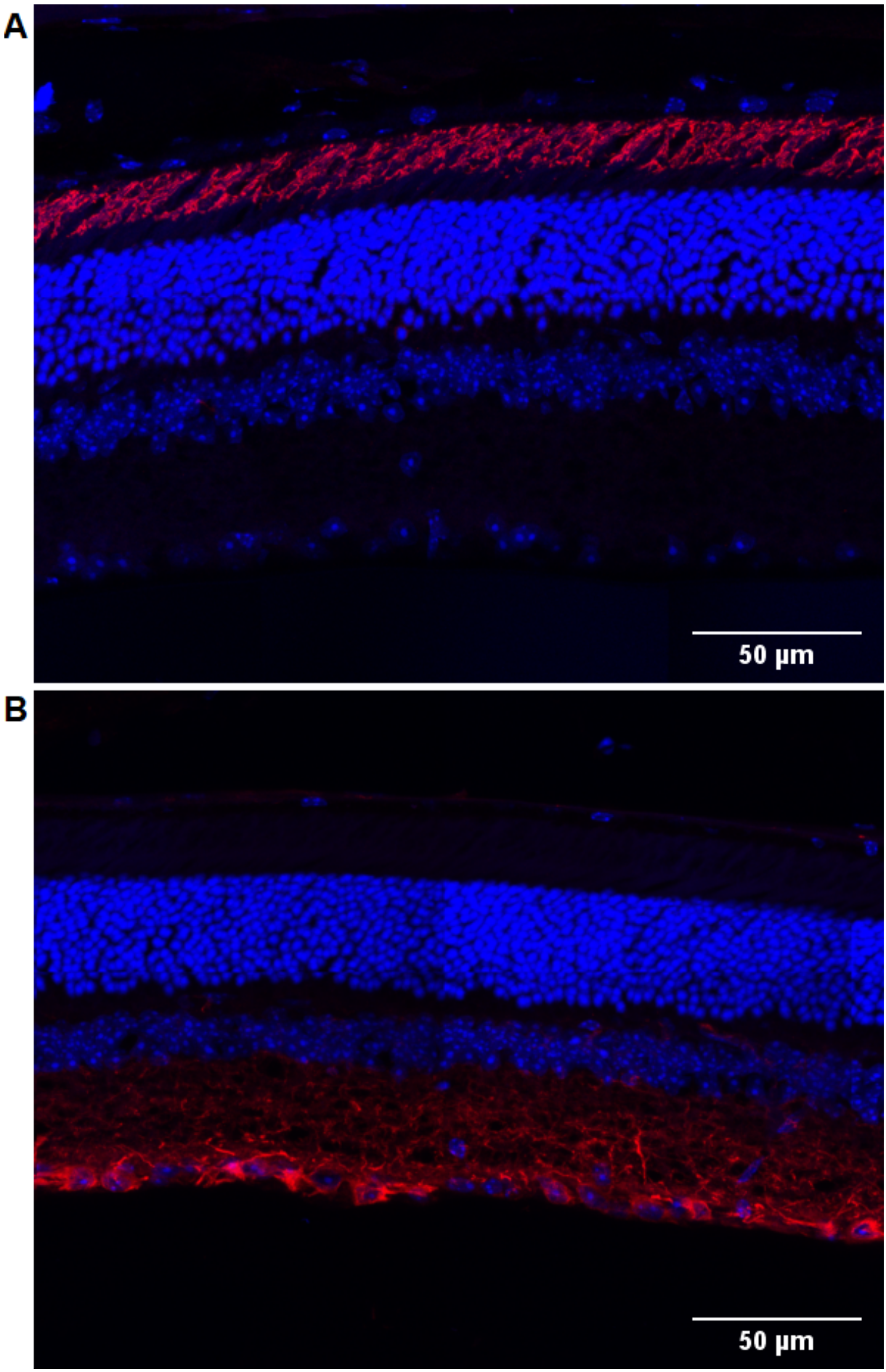

Figure 4.8: *WT2 retinal section stained against Rhodopsin (1D4, C-Terminal) (red)and DAPI (blue) (A) and Tubulin (βIII) (red) and DAPI (blue) (B).*

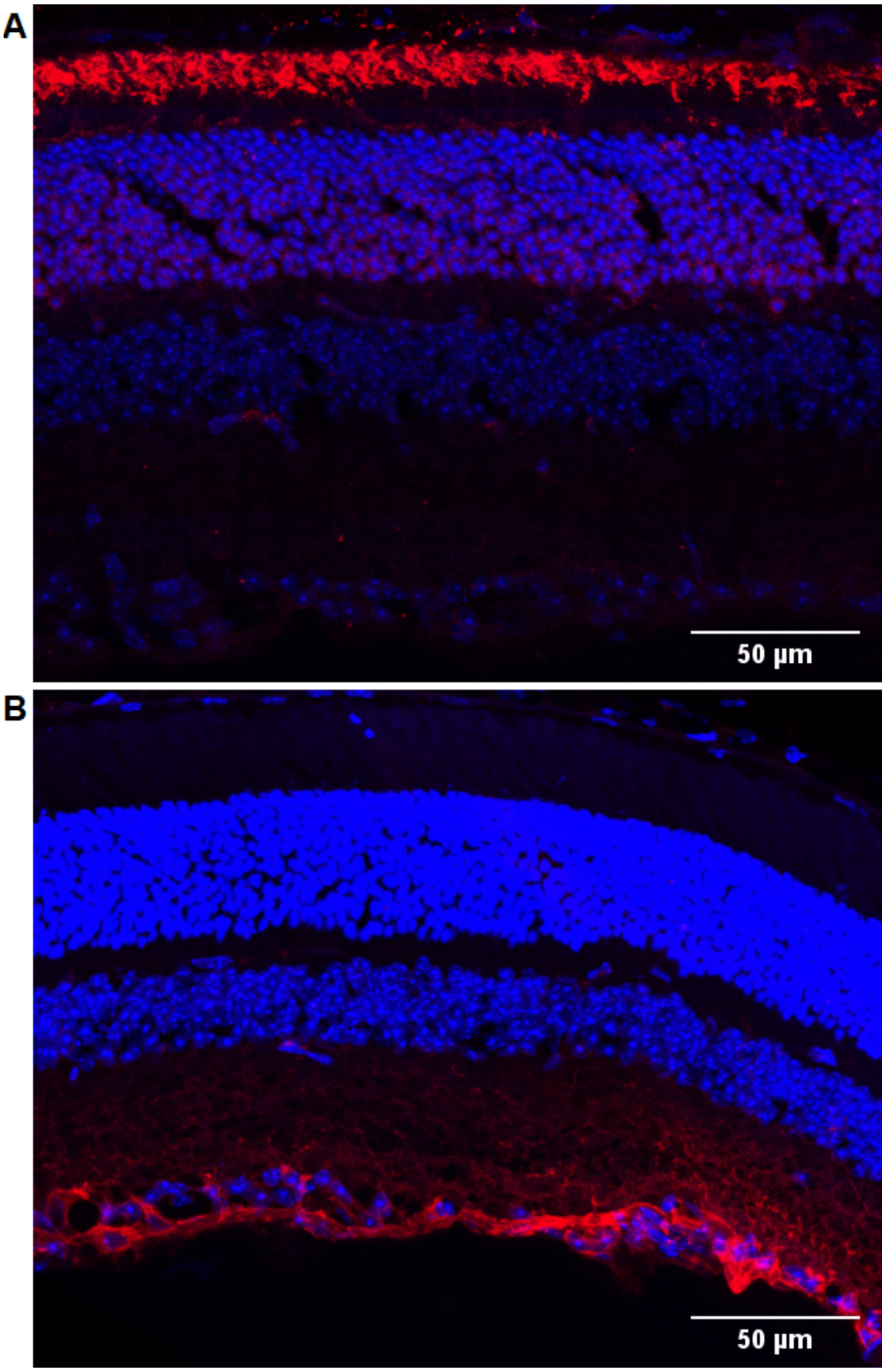

Figure 4.9: *WT3 retinal section stained against Rhodopsin (1D4, C-Terminal) (red)and DAPI (blue) (A) and Tubulin (βIII) (red) and DAPI (blue) (B).*

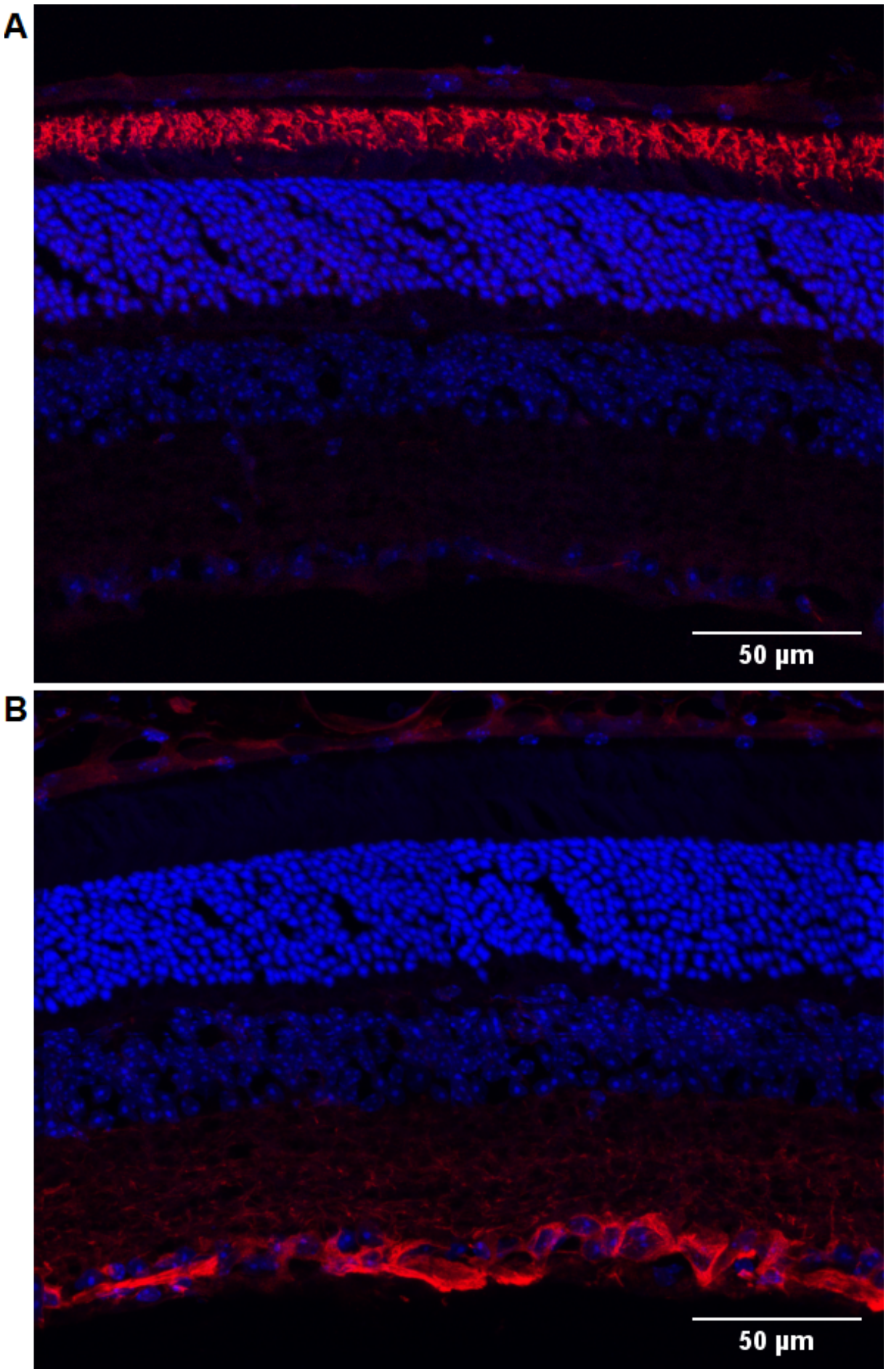

Figure 4.10: *M1 retinal section stained against Rhodopsin (1D4, C-Terminal) (red)and DAPI (blue) (A) and Tubulin (βIII) (red) and DAPI (blue) (B).*

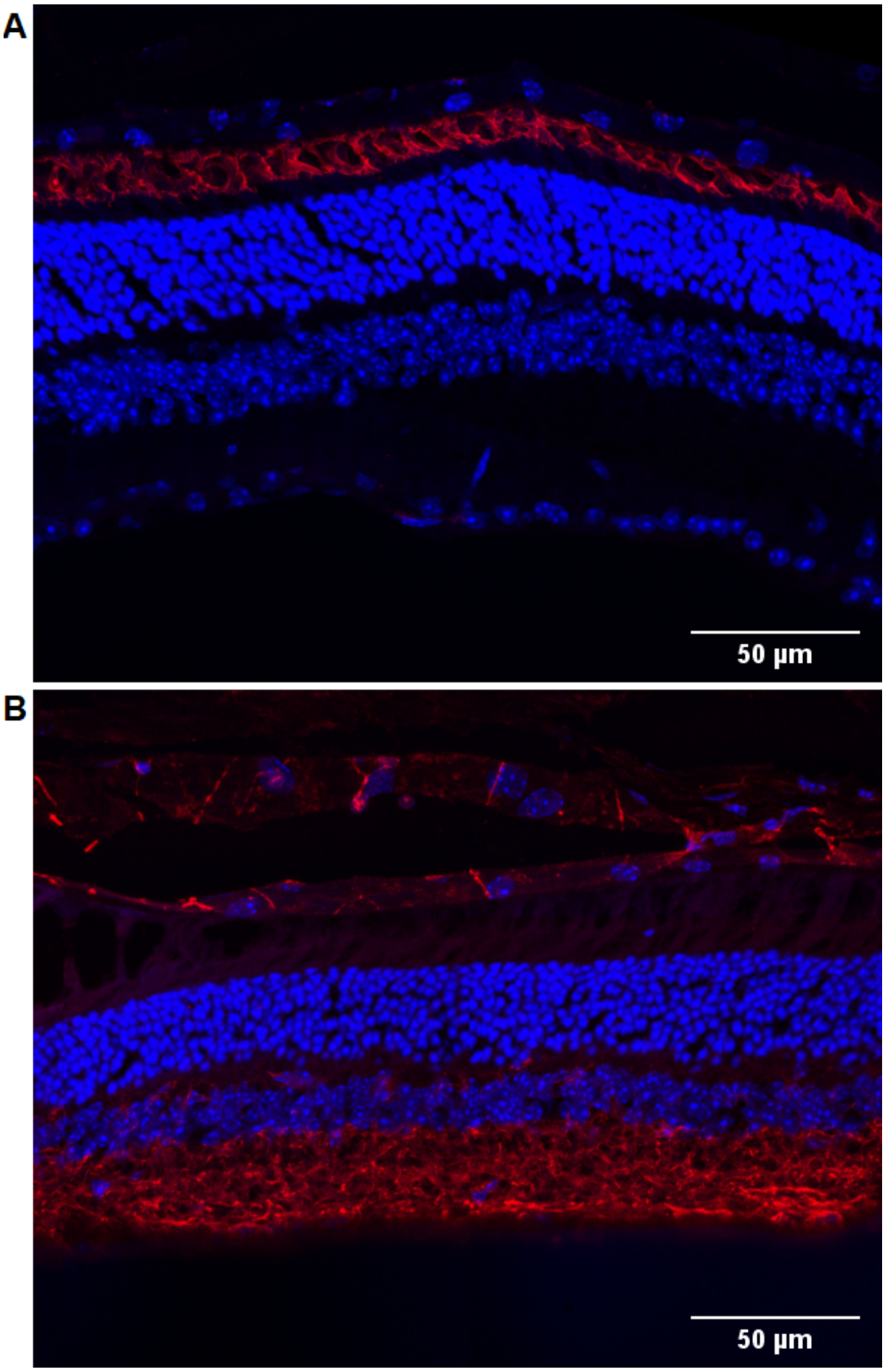

Figure 4.11: *M2 retinal section stained against Rhodopsin (1D4, C-Terminal) (red)and DAPI (blue) (A) and Tubulin (βIII) (red) and DAPI (blue) (B).*

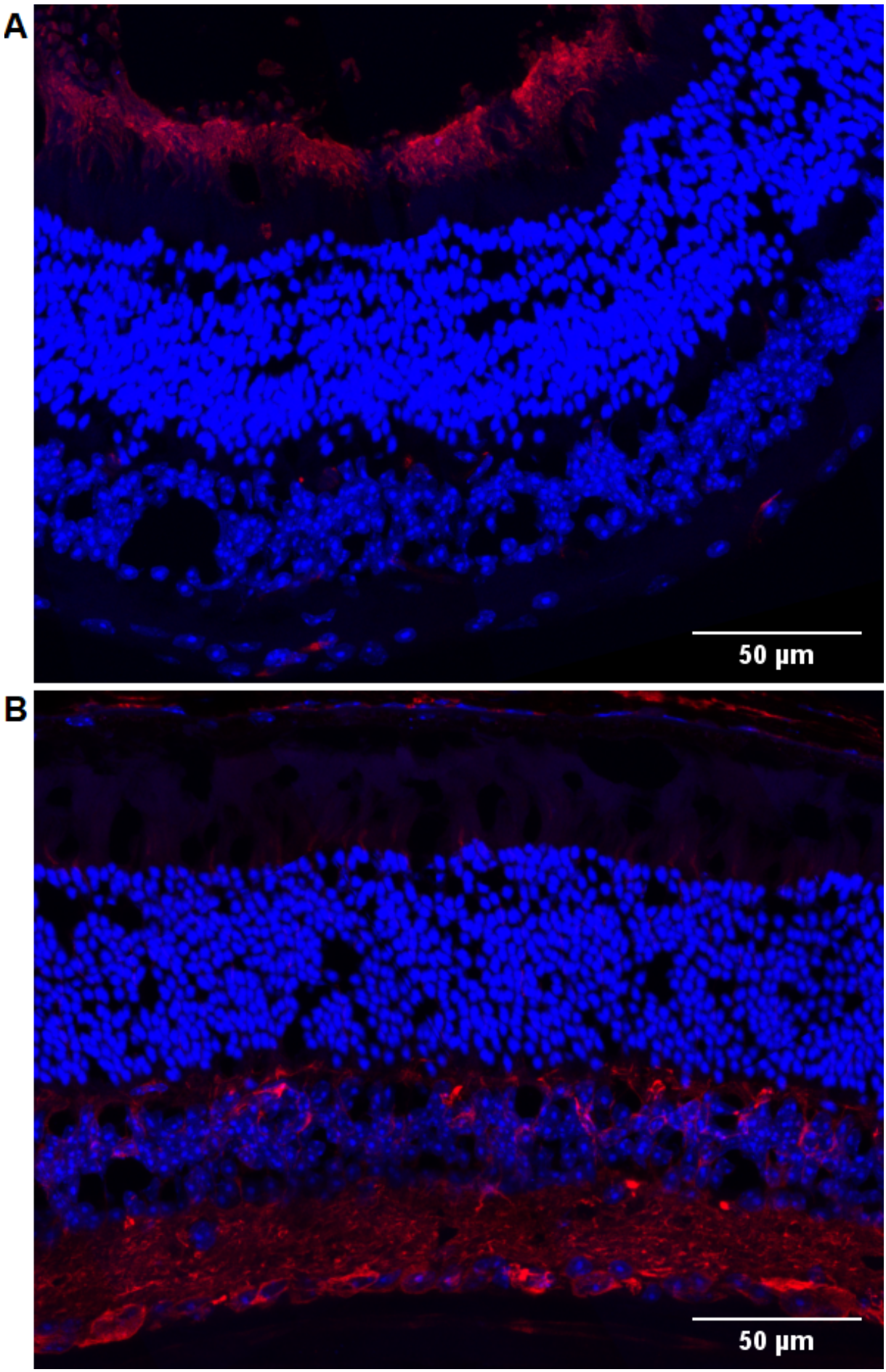

Figure 4.12: *M3 retinal section stained against Rhodopsin (1D4, C-Terminal) (red)and DAPI (blue) (A) and Tubulin (βIII) (red) and DAPI (blue) (B).*

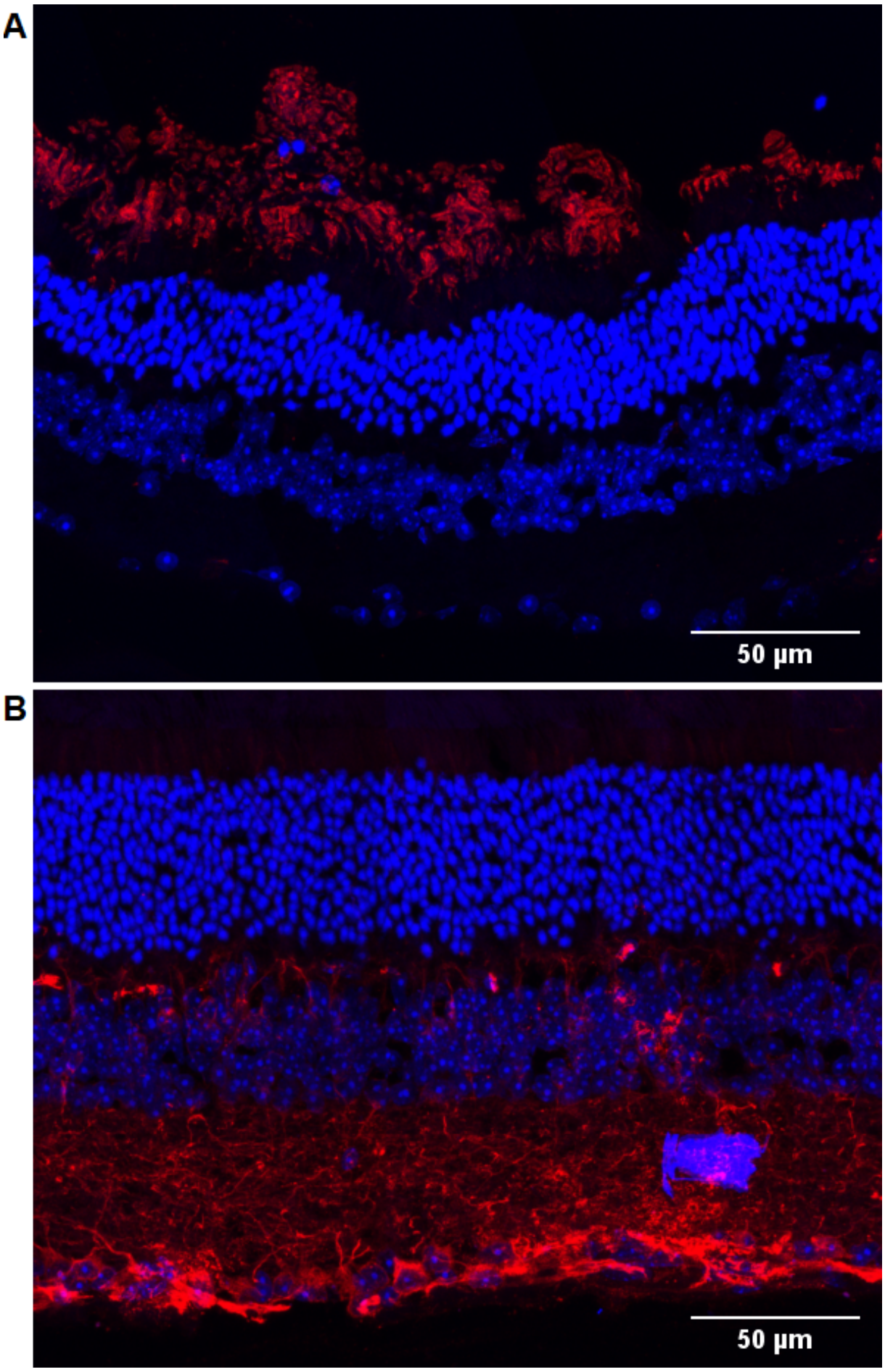

Figure 4.13: *M4 retinal section stained against Rhodopsin (1D4, C-Terminal) (red)and DAPI (blue) (A) and Tubulin (βIII) (red) and DAPI (blue) (B).*

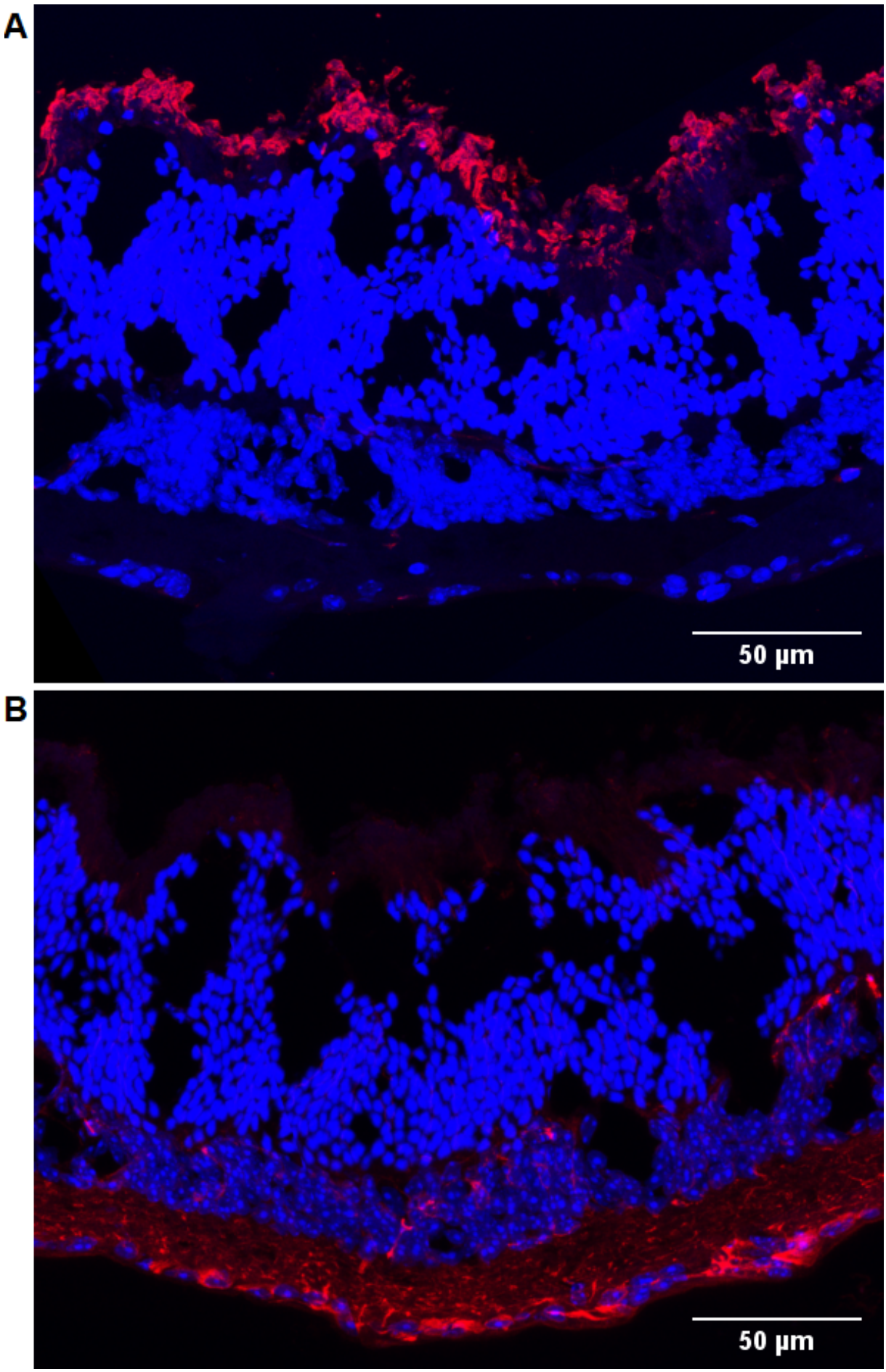

Figure 4.14: *M5 retinal section stained against Rhodopsin (1D4, C-Terminal) (red)and DAPI (blue) (A) and Tubulin (βIII) (red) and DAPI (blue) (B).*

Quantification

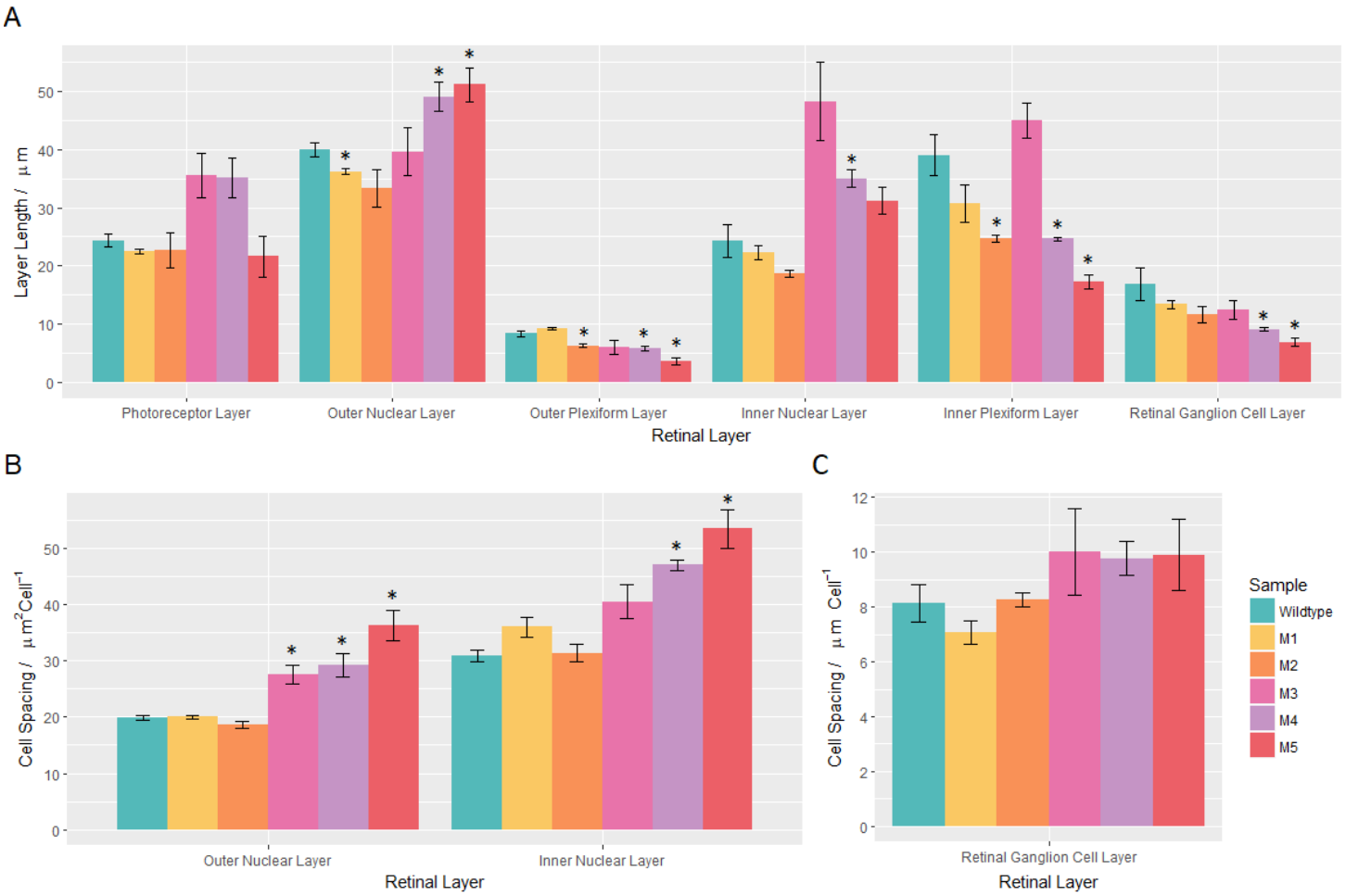

Figure 4.15: *Measurements of retinal sections layer length in wildtype and individual heteroplasmic mice eye samples (A), then respective cell spacing area for the INL and ONL (B) and length for cell spacing in the RGC layer (C).*

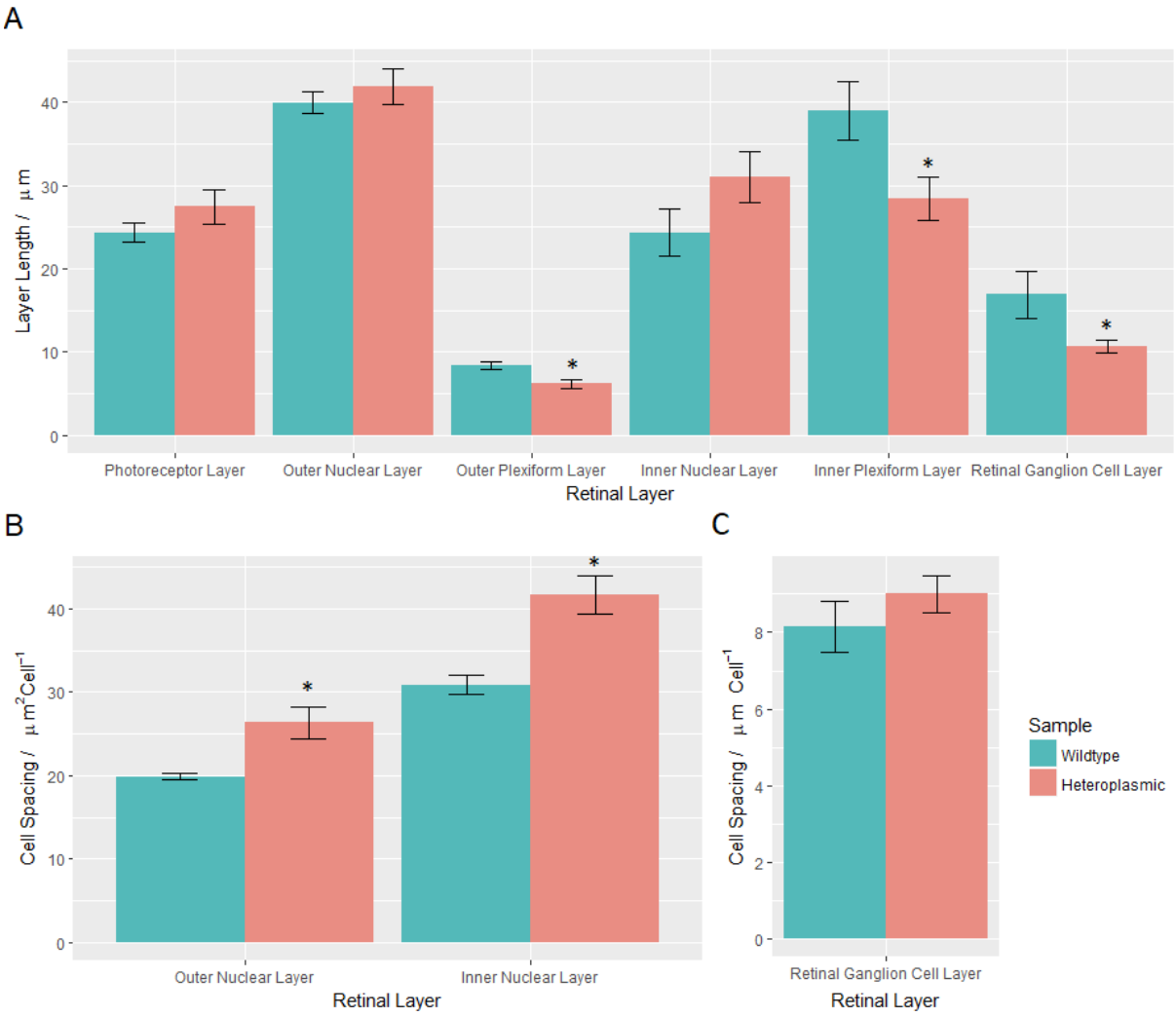

Figure 4.16: *Measurements of retinal sections layer length in wildtype and grouped heteroplasmic mice eye samples (A), then respective cell spacing area for the INL and ONL (B) and length for cell spacing in the RGC layer (C).*

Measurements of each retinal layer from mice described in Table 4.2 were taken as shown in Figures 4.15 and 4.16 (A) and significance is shown in Table S24. The area that a single cell occupies was also measured for the INL and ONL (B). The length that a cell occupied was then measured for the RGC layer (C) and significance is shown in Table S25.

There is no significant difference in the length of the PR layer in any sample, however, ONL lengths are significantly different in samples M1, M4 and M5 (respectively p = 0.020, 0.046 and 0.042).

OPL and IPL length is significantly reduced in samples M2, M4 and M5 (respectively OPL p = 0.005, 0.007 and 0.001; IPL p = 0.003, 0.003 and 1.96e-04); OPL and IPL lengths are significantly different in heteroplasmic samples as a whole (p = 0.008 and 0.028 respectively).

M4 INL length is significantly increased from wildtype (p = 0.009) and both M4 and M5 are reduced in RGC layer (respectively p = 0.025 and 0.008).

There is no significant difference in the length of which a single cell occupies in the RGC layer between heteroplasmic samples and wildtype. The area in which cells occupy in the ONL and INL, however, are significantly increased in samples M4, M5 and comparing heteroplasmic samples to wildtype (respectively, ONL p = 0.041 and 0.025; INL p = 3.51e-06 and 0.015); M3 ONL is also significantly increased to the wildtype controls (p = 0.042). Overall, both ONL and INL cell area is significantly increased (p = 0.004 and p = 4.00e-04).

4.3.3 Whole Mounts

Image Processing Optimisation

As seen in Figure 4.17, the Imaris Bitplane software did not successfully stitch the individual tiles in the correct layout. It did successfully group the whole mount tiles together, however, the outer boundary is clearly disordered and the venous internal structure is disjointed.

Imaris Bitplane then selected regions of interest to quantify as shown in Figure 4.18 and an increased magnification of a region in Figure 4.19. Figure 4.19 shows that the detected cells are not representative of the positioning or count of the real cells.

Figure 4.20 shows Fiji stitching the tiles together and subsequent conversion to a binary mask, following processing methodology. Outer flat mount boundary appears precisely ordered and inner venous structure is continuous, indicating that both inner and outer tiles are correctly stitched and that the binary mask is a good representation of the original tissue. Figure 4.21 shows a magnification of the binary mask cell detection and the cell counting appears to be more accurate than the regions quantified in Imaris Bitplane.

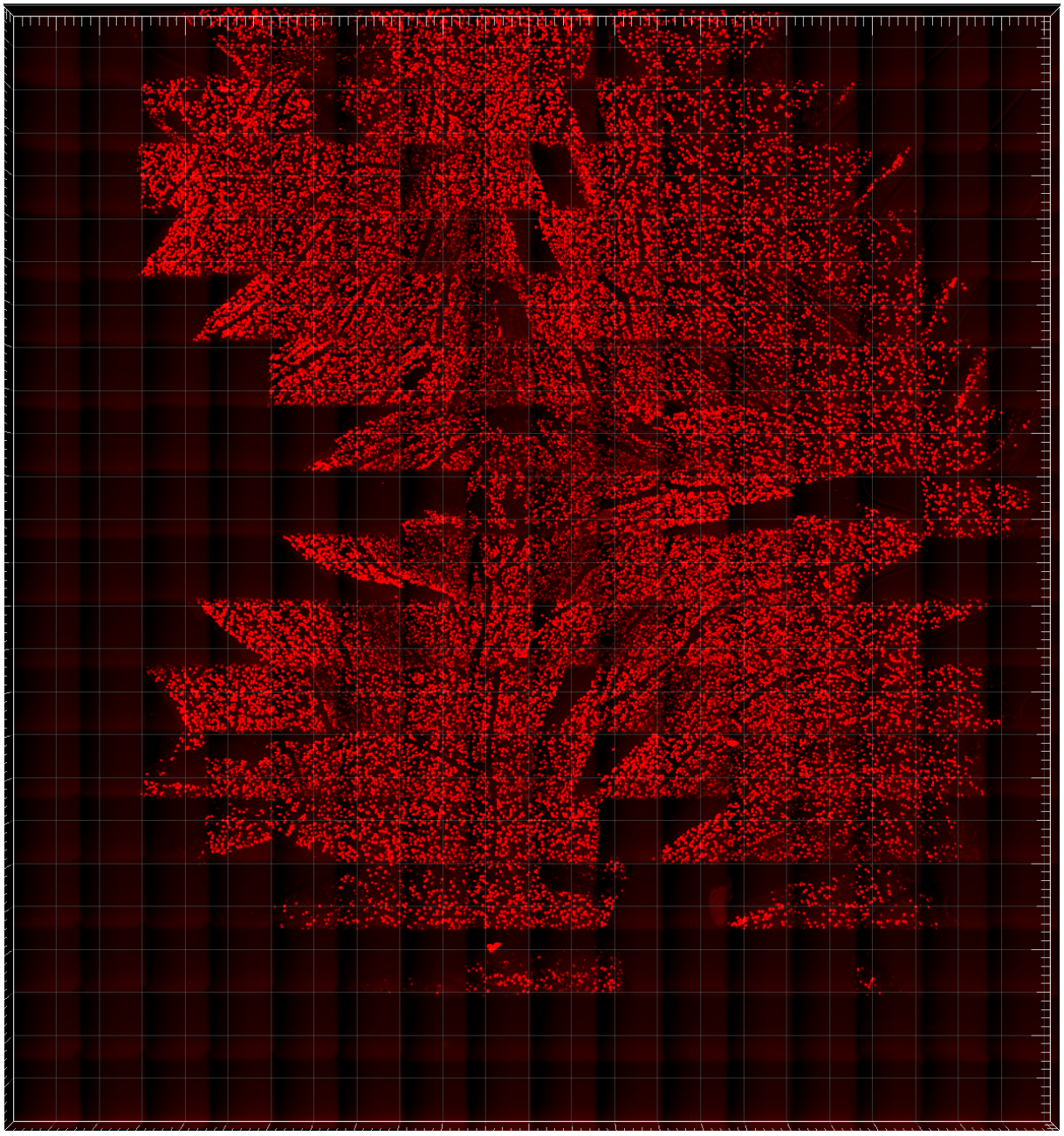

Figure 4.17: *Imaris Bitplane software stitching together the individual tiles from whole mount tissue.*

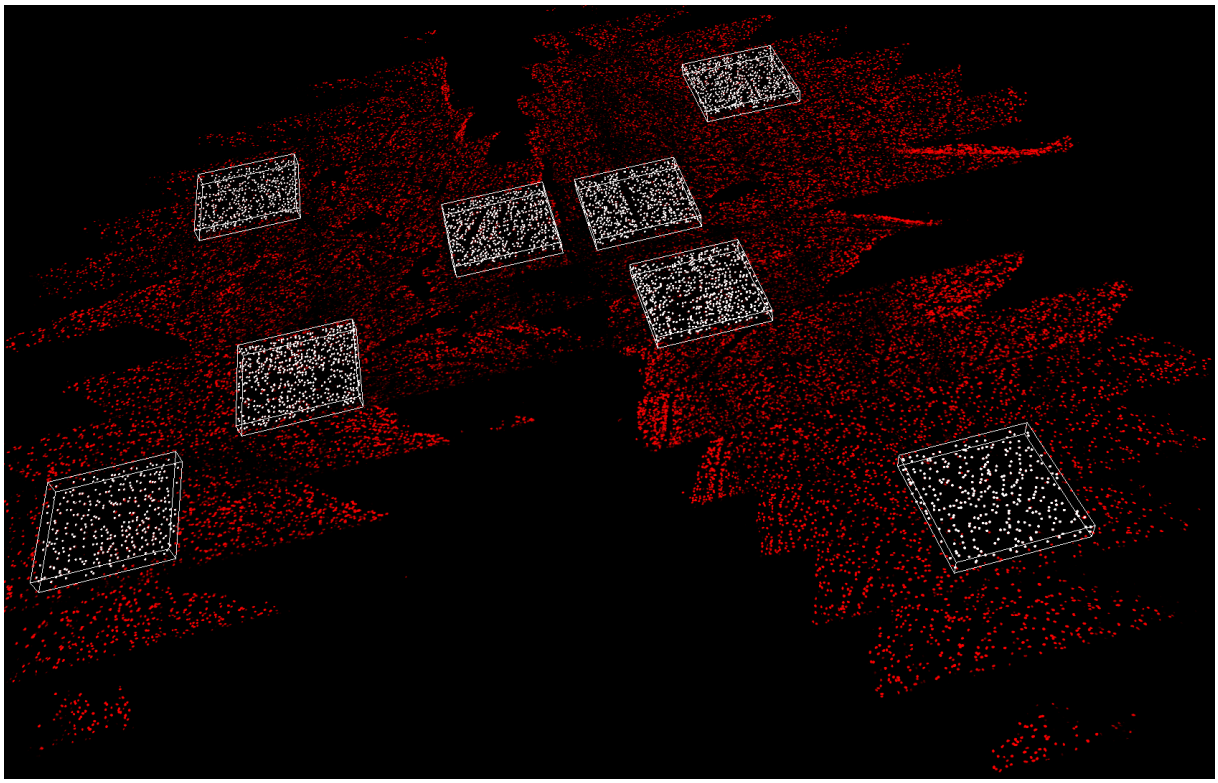

Figure 4.18: *Imaris Bitplane software assigning spots to detected cells.*

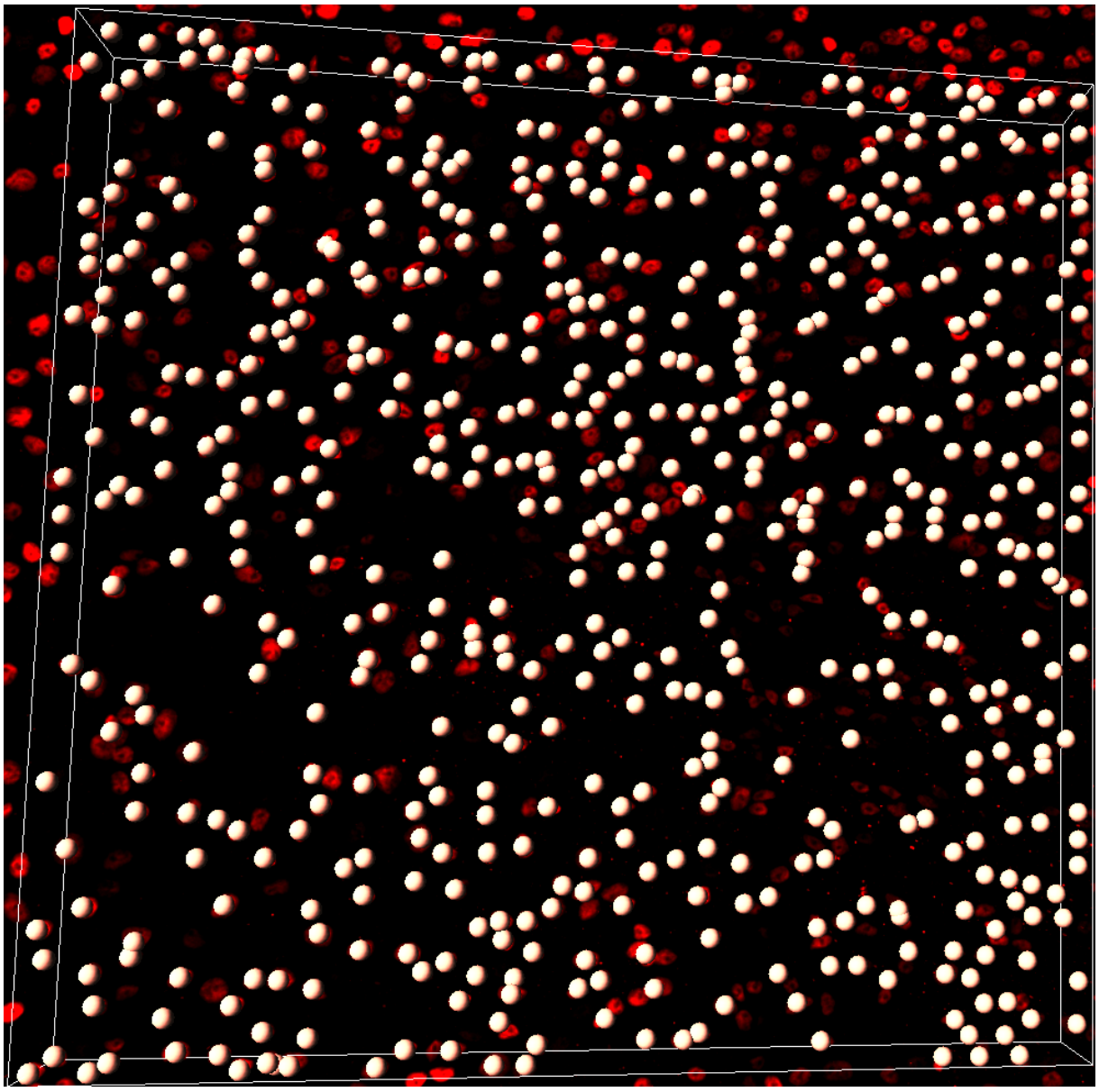

Figure 4.19: *A magnification of a selected region of interest showing the real cells and cells detected by Imaris.*

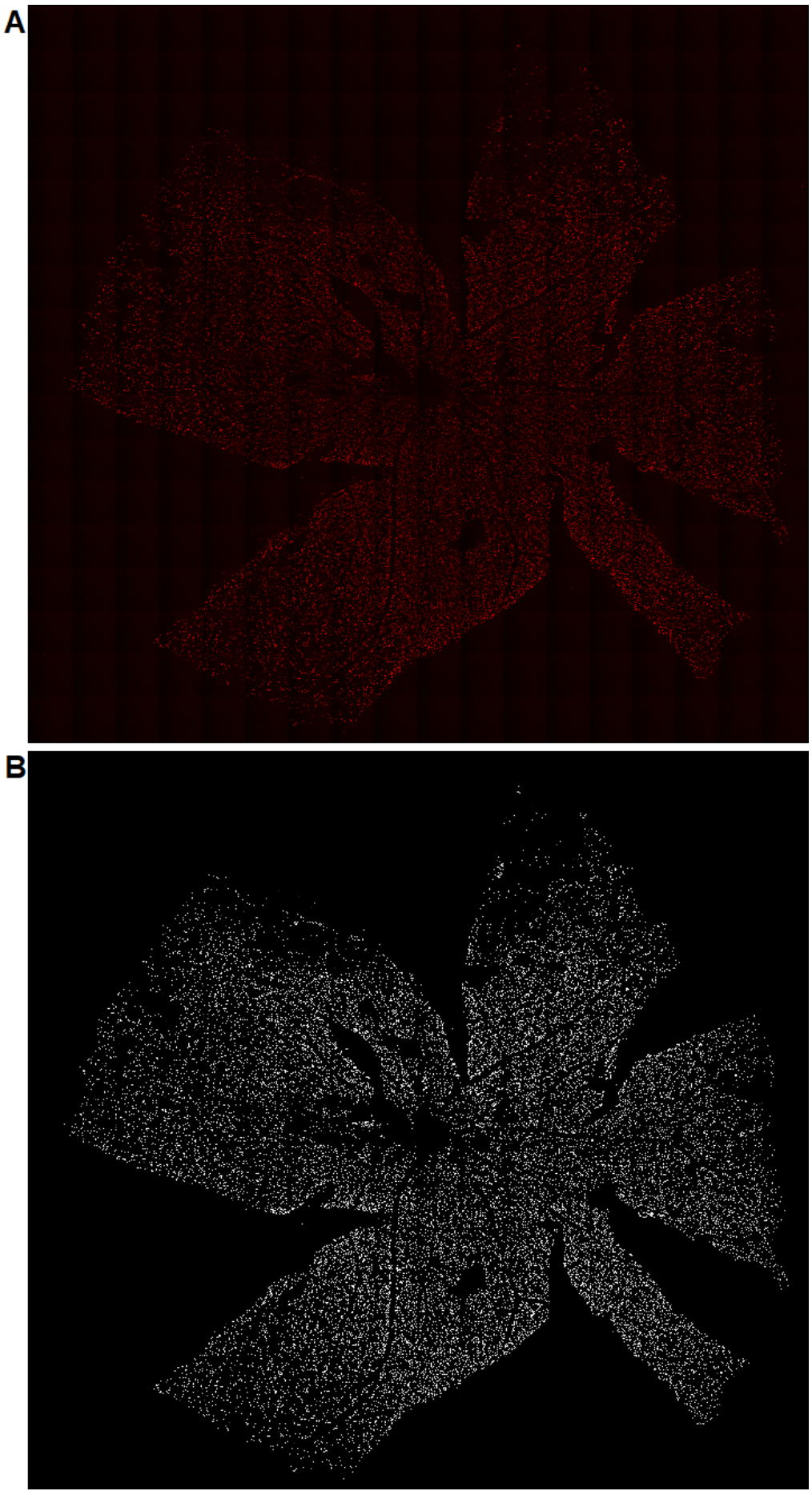

Figure 4.20: *Fiji stitching whole mount tiles into one image (A) and conversion to a binary mark (B).*

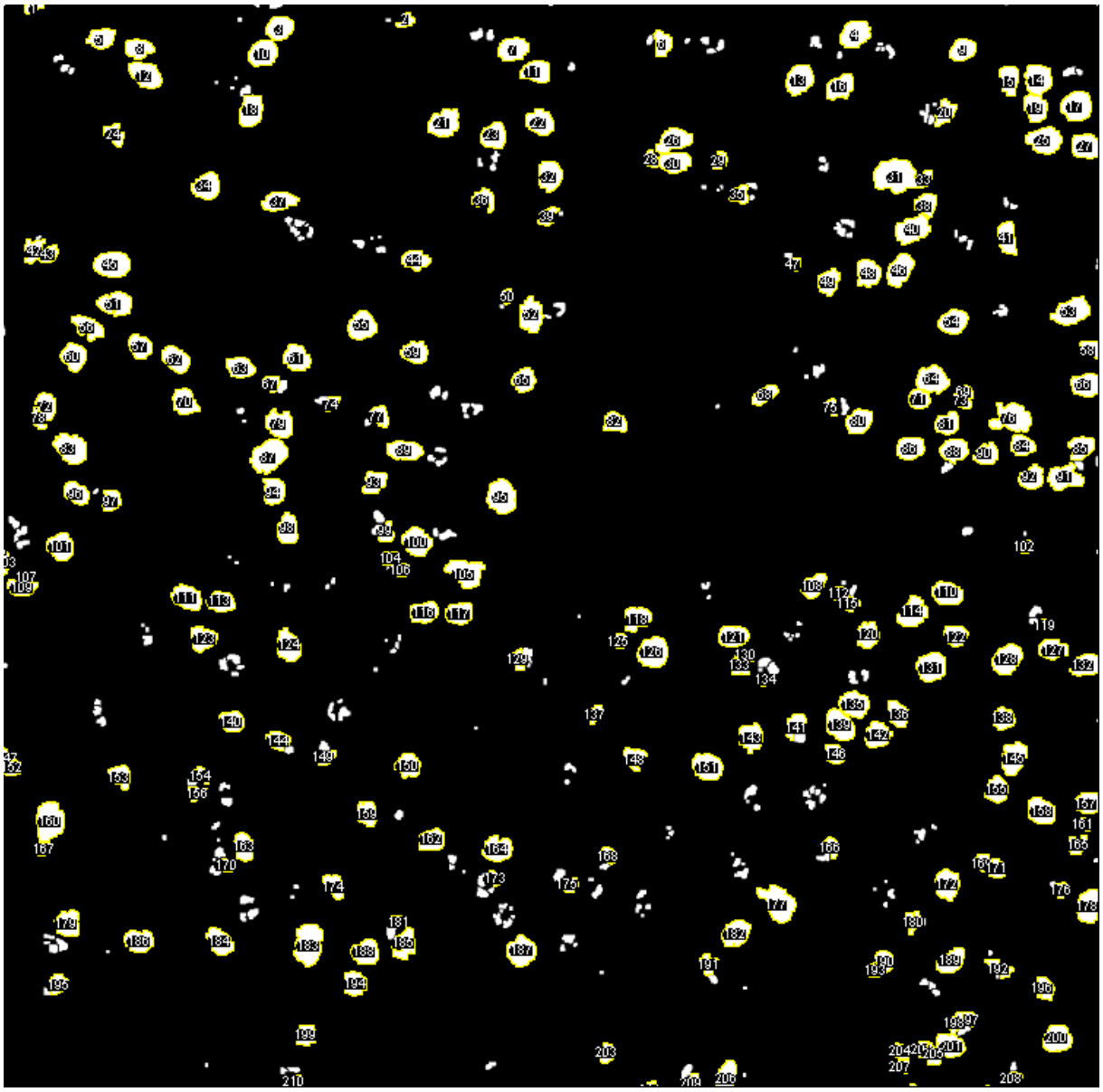

Figure 4.21: *A magnification of the binary mask created in Fiji after optimising and counting cells.*

Flat Mount Morphology

Figures 4.22, 4.23 and 4.24 show the final binary masks which were analysed for each of the tissues, including tissue macro structure.

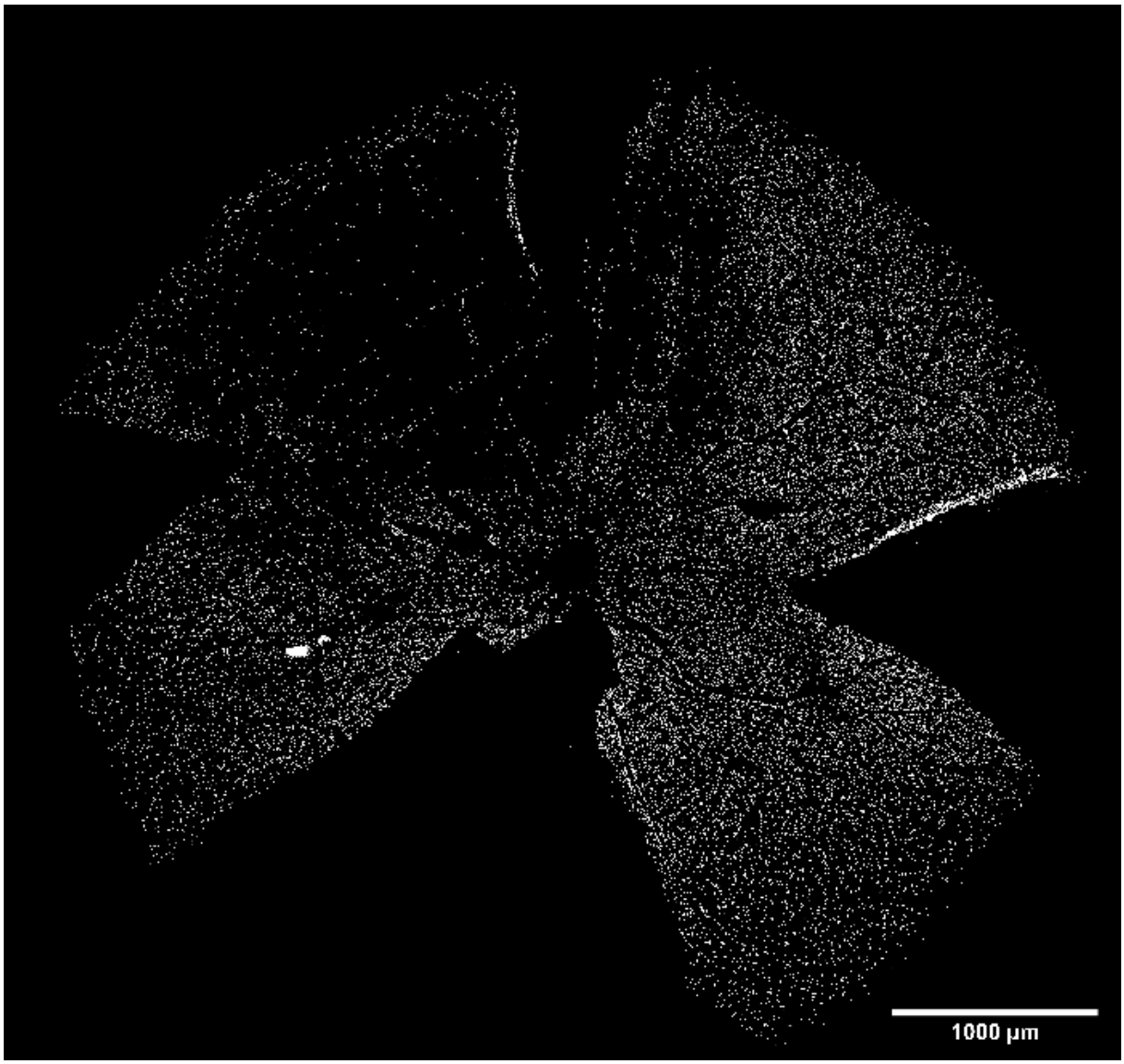

Figure 4.22: *Final image for the M3 flat mount.*

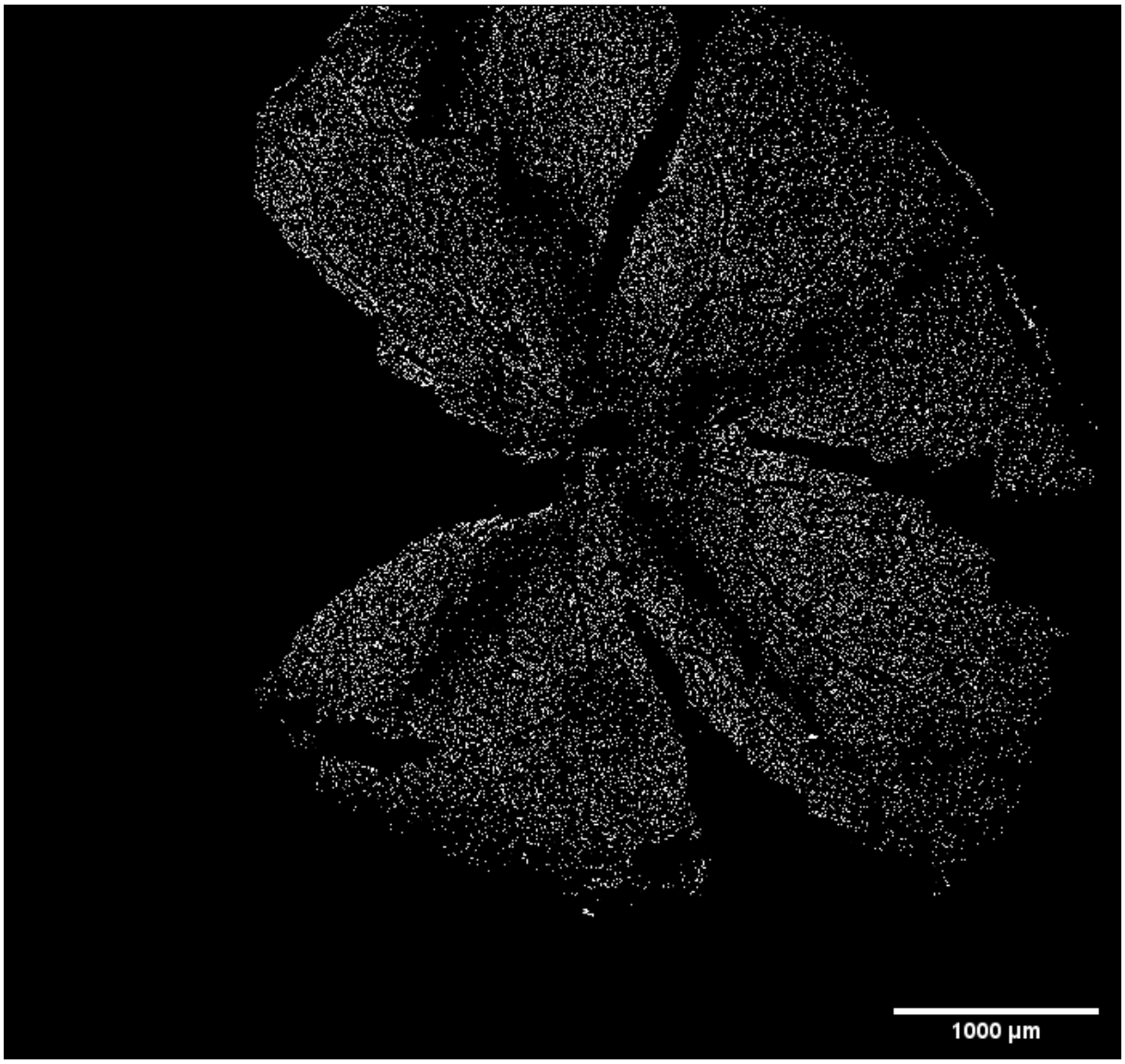

Figure 4.23: *Final image for the M4 flat mount.*

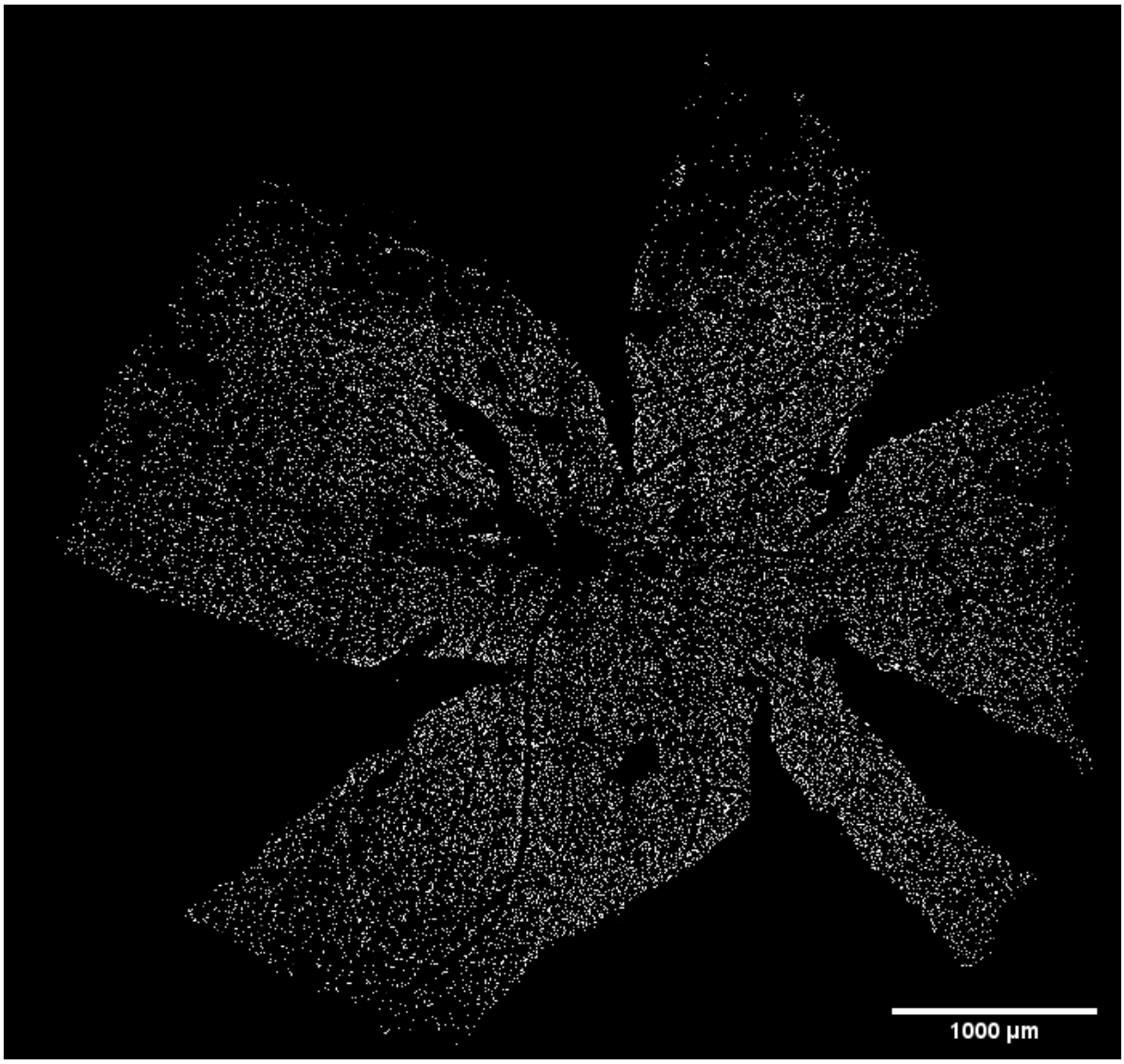

Figure 4.24: *Final image for the M5 flat mount.*

Quantification

No comparatively healthy tissues were collected in this manner so no quantitative statistical tests can be undertaken for this aspect of the project. Qualitative analysis will be discussed in Section 4.4.3.

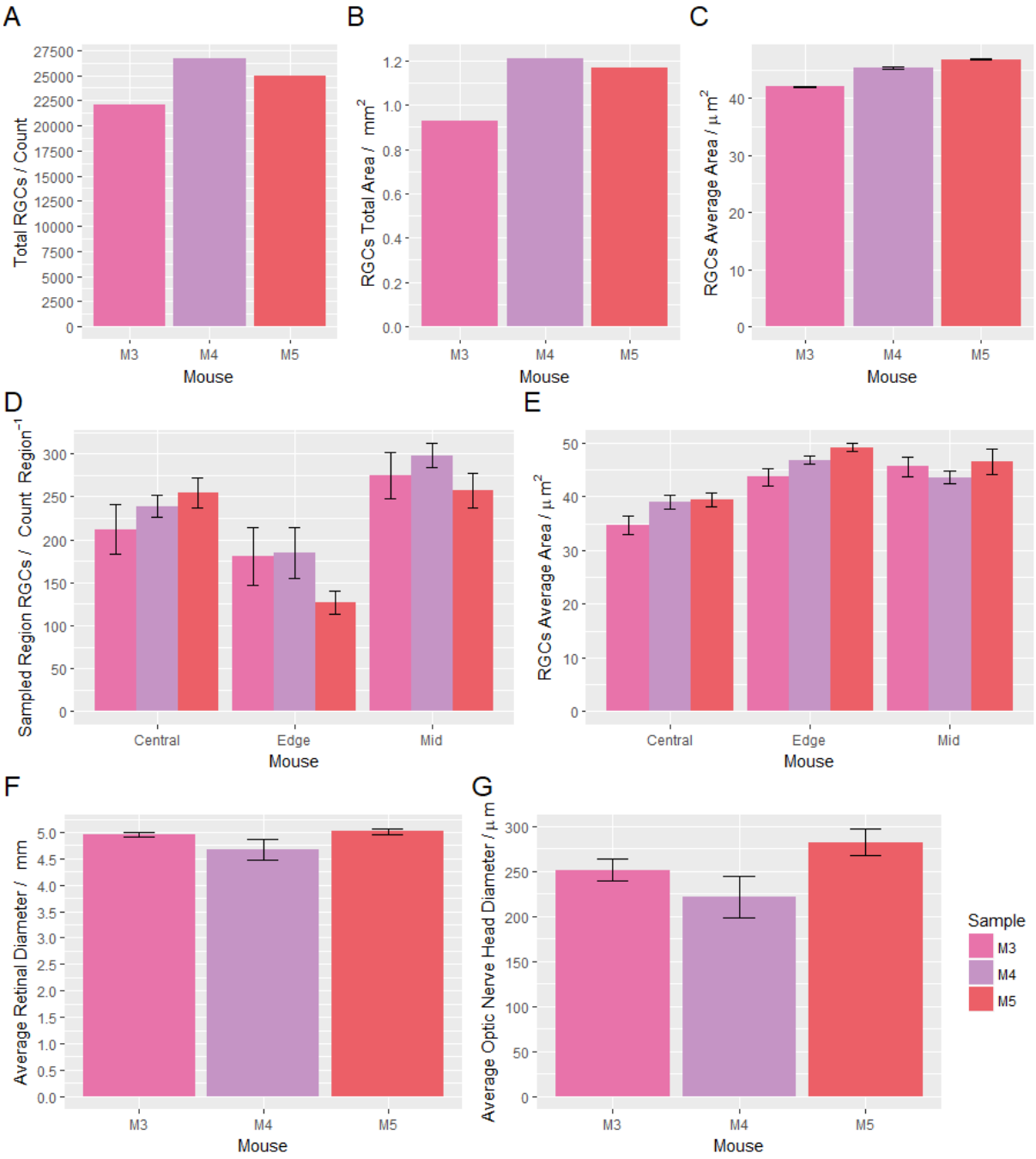

Figure 4.25: *Quantified measurements of whole mounts by showing total RGC count (A), the total area within the tissue covered by RGCs (B), average area (size) of RGCs within the tissue, error bars represent standard error of mean across each cell (C). Looking at quadruplicate regions cocircular to the optic nerve head in positions close to the optic nerve head (Central), close to the edge of the tissue (Edge) and between the two positions (Mid), the average number of cells within a within a 1000x1000 pixel region (105,625 µm^2) (D), average area (size) of RGCs in the sampled area by region (E); error bars represent standard error of mean across quadruplicate measures of the tissue in different samples. Average retinal diameter (F) and average optic nerve head diameter (G); error bars represent standard error of mean across quadruplicate measurements of the tissue through differing orientations.*

4.4 Discussion

4.4.1 Mitochondrial Heteroplasmy Level

It was important to determine the heteroplasmy levels across the eyes of the mouse as tissue preparation methods for microscopy work does not normally produce leftover retinal tissue and the preparation methods make the sample unsuitable for subsequent DNA sequencing.

As the heteroplasmic bottleneck occurs immediately following creation of the egg cell and each time a cell divides, splitting the mitochondrial population into different cells, cells of a different embryonic origin are more likely to have differing heteroplasmy levels than those which arose from a more recent cell division event. As such, the eyes were separated into retinal and sclera, as they are of different embryonic developmental origin, namely, the anterior neural plate and periocular mesenchyme respectively (Heavner and Pevny, 2012; Kanakubo et al., 2006).

The outer ear clipping, arising from the second arch neural crest in mice (Anthwal and Thompson, 2016), is further developmentally distinct, and depending upon the variability of mtDNA heteroplasmy across the differing samples, it could affect the suitability of an ear clipping as a measure of retinal heteroplasmy.

As Table 4.6 shows, there is little difference in heteroplasmy levels across any of the sampled regions, disregarding the minor variation which could inherently occur by technical error and the sequencing methodology accuracy.

This means that ear clipping heteroplasmy measurements are an appropriate measure of heteroplasmy in the eye. This was particularly relevant for the m.5024C>T + m.13715C>T mouse as it has been shown to have variable heteroplasmy levels (Kauppila et al., 2016).

4.4.2 Sections

Cell quantification and measurements were taken whilst blinded to the sample identity so no human bias could occur from knowledge of sample mutational load. Further, cell counting was undertaken by an automated process which identified and counted the cells without further human input beyond highlighting the appropriate region of interest for each retinal layer. The described methodologies appear to be an effective and efficient manner of retinal cell quantification and size quantification.

Results indicate that the m.5024C>T + m.13715C>T mouse could have a cellular ocular phenotype with the tissue morphology particularly disrupted in the M3, M4 and M5 heteroplasmic mice, of 51%, 72% and 68% heteroplasmy respectively. Unexpectedly, M1 and M2, at 81% and 80% heteroplasmic burden, did not have such an obvious cellular impairment and in all regions they appeared to have a better cellular structure than the other mutant samples.

More contradictorily, the cellular response of M1 and M2 appeared to often act in

an inverse direction of M3, M4 and M5 when comparing against controls as baseline measurements. The most severe retinal defects appeared to be tortuosity of the retinal tissue and gaping holes within the INL and particularly within the ONL. Unlike LHON which preferentially affects RGCs (Sadun et al., 2000; Ventura et al., 2005; Yu-Wai-Man et al., 2009), the m.5024C>T + m.13715C>T mouse does not appear to have a significant effect on RGCs' morphology, spacing or quantity. Similarly, the PR layer is not affected in size whilst LHON has been shown to affect colour perception (Yu-Wai-Man et al., 2009).

M3:M5 have wider retinal layers, as seen in Figure 4.15 (A), particularly in the ONL and INL, which could arise as a result of the m.5024C>T + m.13715C>T mutations. Further, they have many vacuous spaces and a lower cell density, as seen in Figure 4.15 (B). M1 and M2 did not have such severe vacuity, as seen within Figure 4.15, however, M1 did have a significant reduction of the INL and OPL length and significantly more dense cells within the ONL; M2 also had a reduction of the IPL.

M3:M5 increase in size whilst reducing cellular density whereas M1 and M2 sometimes exhibited increased cell density and reduced layer size. M1 and M2 arise from much younger mice (9 months) whilst M3:M5 are over twice the age (24 months) and this could have affected expression as either a natural occurrence in elderly mice or that the m.5024C>T + m.13715C>T mouse optic phenotype is only exhibited in elderly mice, much like age-related macular degeneration.

ERG measurements were only collected in mice M3:M5, however, as shown in Table 4.3, mice do exhibit significant visual reduction when compared to wildtype mice in both RGC, bipolar and PR response measurements.

4.4.3 Flat Mounts

Present methodology often takes a number of confocal microscope images to quantify RGC density across whole mounts (Osborne et al., 2018), however, on a 40x magnification, it is difficult to ascertain the exact microscope positioning in the tissue as switching between 40x and a lower magnification requires the addition or removal of oil and cleaning of the microscope, losing tissue positioning.

As such, this project sought to devise methodology whereby the whole retina RGC count and distribution could be identified.

Staining of RGCs occurred as previously described (Osborne et al., 2018), however, rather than single plane microscope images in selected regions, Z-stacks were taken across the entirety of the tissue.

Some difficulty was observed in this, with M3 appearing to have a region which was deeper than the Z-stack depth meaning that the total RGC cell count was likely inaccurate. M4 also could have possibly underestimated cell counts by cropping an outer edge of the tissue, however, despite this, the tissue can be clearly observed.

Initial analysis used proprietary Imaris Bitplane 9.1.2 software which came bundled

with the Dragonfly Spinning Disk Imaging System microscope, however, both the stitching and cell detection quality appeared to be extremely poor, as seen in Figures 4.17 and 4.19. In addition to this, the final tile scan was 80 GB in file size and computational processing was met with difficulty.

As such, new methodologies were applied using Fiji (ImageJ 1.52i) (Schindelin et al., 2012). Tiles were first stitched together in 3D before a maximal projection was applied to compress the file size. As seen in live tissue, and Figures 4.18:4.24, RGCs exist in a monolayer which means that reducing the vertical dimension minimised loss of information. It did lose the 3D structure which was available in Imaris Bitplane, however, the tissue is already a flat mounted representation of the natural cup-like structure and this reduction allowed functional analysis to continue. Further, the improved cell counting methodology would allow for more accurate counting of the cell counts.

It is possible that the cell counting in single confocal images could be as accurate, however, it does not have the entire tissue view, or definitive positioning of tiles to count in. The RGCs positioning leaves spaces for the circulatory system and tissue can be damaged in collection, resulting in a number of spaces which would create artefacts for the analysis.

Due to the extensive time on the microscope, the tissue was at risk of photobleaching and subsequent imaging would not be as effective. For further work, it would be recommended to increase the Goat Brn-3a Antibody (C-20) concentration as original staining was not excessively bright or saturating the microscope's detection limit. This increased brightness could help remove the apparent fracturing of some cells in Figure 4.21 or a further image processing step of Gaussian blur and reduction of the pixel threshold for cell detection could be applied. The present methodology could underestimate cells, however, it is automated and unbiased across the tissue so all samples would be equally affected.

Due to limited time and sample availability, only samples M3, M4 and M5 were analysed in this manner and no wildtypes were observed to measure a baseline against. Despite this, M3 appears to have fewer RGCs than both M4 and M5; whilst the total RGC count could be an artefact of the reduced Z-dimensionality, Figure 4.25 (E), indicates that this reduction occurred in both the central and edge of the tissue selected regions. No regions were selected within the reduced Z-dimension region of M3. RGCs appeared to also be smaller in M3 than M4 and M5; this could be indicative of different subpopulations of RGCs, such as midget cells being more prevalent, however that was not guaranteed by the limited staining.

Mice retinas have previously been estimated to have ~70,000 RGCs (Dräger and Olsen, 1981), which is much greater than the total RGC counts in the heteroplasmic samples (Figure 4.25 (A)), however, the staining methodology affects total RGC count numbers; Brn3a was used as a marker of total retinal RGC count, however, Brn3a is

expressed in the RGCs of the principal retinothalamic/retinocollicular pathway mediating cortical vision but not the RGCs which serve subcortical visuomotor and circadian functions (Quina et al., 2005). As such, it is likely an under-representation of total retinal RGC count, but a more accurate representation of the effect of RGC in vision. However, 85% of mouse retinal RGCs are believed to express Brn3a (Rodriguez et al., 2014) so it still seems that the total RGC count is greatly reduced in the heteroplasmic mice (~32,000 RGC in the most RGC populous retina after factoring that 15% would be undetected by Brn3a staining) compared to the ~70,000 RGCs counted by Dräger and Olsen (1981). Hedberg-Buenz et al. (2016) predicted ~55,000 RGCs per normal mouse retina with an estimated ~16,000 RGCs in 16-month-old DBA/2J mice with glaucoma; the heteroplasmic mice did not have such a significant reduction to total healthy RGC counts, however, they definitely have fewer RGCs than healthy mice retinas. However, there is variation in cell counts of the GCL between different mouse strains (Chen et al., 2016).

The whole eyeball appeared to be of a similar size in all samples and it is difficult to ascertain whether there was a difference in the size of the optic nerve head; the optic nerve head was an ovaloid shape rather than circular, resulting in a large variability of the measurements.

Despite the limited sample numbers, this appears to be an excellent methodology for RGC counting and identification. Further samples, particularly of wildtypes, could additionally validate this strategy for cell counting.

Chapter 5 | Evaluation

5.1 LHON Disease Penetrance

This study further updated the penetrance of LHON on a range of different populations and discovered that the LHON primary mitochondrial mutation and mother's disease status has a high significance in determining LHON penetrance. Further, whilst different mitochondrial mutations do have different penetrances, our cohort found that overall penetrance in females is closer to ~20% rather than the previously estimated ~10% (Yu-Wai-Man et al., 2003, 2009). Penetrance has likely shifted given the improvement in genetic diagnostic techniques and expansion of pedigrees to limit ascertainment bias.

This further compounds that different mitochondrial mutations can be more severe than others (Zhuo et al., 2012), with a higher penetrance in the m.3460G>A mutation than the other variants which were observed in multiple families. It indicates that it is further possible that different mtDNA and nDNA variants work in an additive model to cause LHON disease onset (Caporali et al., 2018).

It would be interesting to further inspect this data for mitochondrial haplogroups and ascertain whether it associates with primary LHON mutation, m.14484T>C is particularly associated with an mtDNA founder effect in regions like French-Canada (Howell et al., 2003; Macmillan et al., 2000b). Similarly m.11778G>A is associated with East Asian founder events (Sudoyo et al., 2002). While no families of East Asian descent were included within our cohort, the addition of pedigrees which are genetically more distant would allow for a greater understanding of which variants control LHON disease onset by alleles being identical by state within both cohorts. Prising apart the significance of LHON primary mutation, nDNA background and haplogroup could provide further evidence for new hypothesised genes which affect penetrance.

Haplogroup data is not presently available for several of the families in this study and few samples have had nDNA characterised, so this was not possible within the present study. DNA samples, however, are available for many of the patients so this could be a beneficial future study to inspect both nDNA for genetic and epigenetic modifications which affect LHON disease expression.

As we identified that mother's disease status is highly significant in predicting LHON disease onset, it is possible that further mtDNA and nDNA variants are inherited from the mother either on a genetic or epigenetic level as a result of being raised in a

similar environment to the mother. As Biobanks expand and multigenerational DNA samples become available, additional work which focuses on identifying alleles which are identical by descent in affected mothers and offspring could map to genes which explain the missing heritability in LHON.

We further investigated the statistical likelihood of an X-linked modifier gene moderating LHON disease onset, as regularly previously hypothesised (Chen and Denton, 1991; Hudson et al., 2005; Phasukkijwatana et al., 2010; Qu et al., 2010; Shankar et al., 2008; Vilkki et al., 1991), by following the Bu and Rotter (1991) methodology. Similar to Bu and Rotter (1991), we found it statistically significant that males in our cohort developed LHON depending upon their inheritance of a mutant X-linked allele. The penetrance and probability that a female will be affected was also similar between studies (0.176 to Bu and Rotter's (1991) 0.111 measurement).

Our cohort, however, had a much higher proportion of affected females (0.230 compared to 0.093) and the frequency of the hypothetical X-linked allele was much more common (0.283 to 0.076). We find our value for the hypothetical gene frequency to be far more likely than the original measurement as at a gene frequency of 0.076; we would expect LHON penetrance to greatly reduce in generations following a LHON patient as it is quite likely that the mutant X-linked allele would not be transmitted multiple generations and that the father would likely contribute a healthy X allele every time a daughter is born. The pedigree penetrance indicates that this is not the case as we often see LHON onset in multiple subsequent generations, and an X-linked gene of 28.3% population frequency could potentially be inherited from either parent.

In addition to this, a number of issues in the original study methodology were identified and confirmed with thanks by Doctors Joanna Howson (University of Cambridge) and Ian Wilson (Newcastle University). This included their ascertainment bias correction, Chi-Squared test formula (different between pooled and individual male sibships with one doubling the standard Chi-Squared test formula to make a four-tailed test) and their goodness-of-fit test defining the null hypothesis to be that male LHON onset to be dependent upon their inheritance of the mutant X-linked allele whilst this would often be the alternate hypothesis given that an X-linked model has not previously been robustly confirmed. Additionally, it assumes that all mitochondrial mutations are of an equivalent burden and that X-inactivation is random, however, abnormal X chromosomes are preferentially silenced (Shvetsova et al., 2019).

We are confident in the replication, however, statistical methods have developed in the last 20 years and we would like to pursue further analysis of our cohort using a more robust, modern methodology which could allow for more confidence in the modelling process. We would also like to further investigate the stratification by mutation type instead of country of collection as our evidence suggests that the specific mutation has a greater impact on the penetrance of LHON than where the pedigree was collected. Further, we would like to further investigate how haplogroup background affects pen-

etrance after stratifying by the specific LHON mutation as additive models of LHON disease onset may arise by specific combinations, as evidenced by specific haplogroups having a greater impact on LHON disease onset by specific mutation types (Carelli et al., 2006; Hudson et al., 2007; Kaewsutthi et al., 2011).

Identification of LHON nDNA variants identified a number of novel hypothetical modifier genes which are over-represented in a range of pathways when compared to the expected proportion of each gene set to be returned, given the submitted gene list count. Interestingly, comparing against MSigDB's C2 curated gene sets of chemical and genetic perturbations the gene sets returned were related to cell survival, and a gene set which becomes hypermethylated in breast progenitor cells when pre-exposed to estradiol (which targets ERB) (Cheng et al., 2008), linking to the investigation of ERB as a target in LHON treatment (Giordano et al., 2011; Pisano et al., 2015).

Further gene sets included neurogenesis, cell signalling, oxidative stress, and cell death when comparing against MSigDB's C5 GO gene sets of biological processes. Given that there are 7,350 potential gene sets which could be returned through this analysis, the returned 26 gene set pathways appear to be quite similar and relevant to LHON disease onset as a disease which affects RGCs through a Complex I defect, or OXPHOS deficiency. Neurogenesis was also further confirmed by PANTHER's Overrepresentation Test, indicating that the identified genes are relevant to neurological pathways.

Some difficulties were met through this investigation for power constraints as Section 2.3.3 only had 1 unaffected male sample after QC, limiting the tests which could be used to analyse the data. With only one male and 7 unaffected females, testing for disease status in the whole data set would more readily detect the great difference between methylation of the X chromosome between male and female samples. Additionally, there was difficulty in obtaining clinical data so information about patients' smoking habits were not always available despite the significance that it had on methylation patterns.

Further, BeadChips were initially prepared in 2010 and samples were not randomised when plated, meaning that all families and similarly, primary LHON mutation, were clustered together on the chips. This meant that including Family, Mutation or Batch as a covariate normalised the effects of all three. The three BeadChips were measured on the same day, on the same machine but another plate was measured between the first and second BeadChip and looking at control probes a batch effect is definitely observable (data not included). Following this, there is a great variability in pipelines used to process BeadChips; the HumanMethylation27 BeadChip is the second generation chip and the majority of papers and packages available on Bioconductor (Huber et al., 2015) deal with the 450k array and quality control steps are now much more rigorous than that which was initially used with the 27k array. Further, most packages are not compatible with the 27k array so additional steps were necessary to

improve the data quality, however some, such as normalising sample methylation to methylation patterns of blood cell counts or predicted blood cell counts (Houseman et al., 2012) were not possible.

As such, to compensate for this low power, candidate differential methylation regression analysis looked at genes which appeared significantly methylated regardless of the covariates included in the model as no methylation appeared significant in any singular linear model following Benjamini–Hochberg correction for multiple testing.

Exome analysis was also limited by investigation of only three unaffected carrier samples, compared to the 25 affected samples, which resulted in 3,833 genes being returned as containing unique variants which were exclusively present in cases or unaffected carriers.

Despite this, the cross-matching of the two analyses returned 29 hypermethylated and 17 hypomethylated genes which contained unique variants between the LHON patients and carriers that could be either causative or protective and downstream pathway analysis predominantly returns gene sets which appear highly relevant to LHON. Given the number of potential gene sets screened, if the discovered genes occurred by chance, we would also expect to see less logical gene set pathways returned by chance but they mostly appear relevant. Further investigation into the variants would need to be undertaken for confirmation, however, they are an optimistic starting point, given the lack of success in other genetic screenings. Specifically investigating gene function, multiple genes were directly known to cause retinal defects and further genes impaired both mitochondrial and neuronal function, indicating that these genes do seem to specifically affect mechanisms which are known to be involved in LHON. We would like to validate our findings by investigating these genes for differential variants and methylation patterns between LHON patients and an unaffected sibling of the same sex, to match for nuclear background, haplogroup and methylation patterns which are caused by age and sex. Our candidate gene list is a novel finding for the LHON research field and if validated, it could be a breakthrough in understanding LHON disease onset.

In addition to this, we did some preliminary work investigating methylation patterns of the mtDNA which successfully isolated high purity mtDNA without nuclear contamination and bisulphite converted the samples. Unfortunately, this method had a very low yield and samples failed NGSeq due to low sample concentration. Following the success in investigating nDNA methylation for potential LHON modifier genes, we would suggest that further investigation of mtDNA methylation as a factor in LHON penetrance as an additive model should be performed (Caporali et al., 2018). Our experimental design was successful in preparing high quality yields of pure mtDNA isolates but found difficulty in preparing large yield volumes. We would recommend sequencing higher concentrations of sample and ensuring all stages after DNA extraction are performed in laminar flow hood to prevent external mtDNA contamination.

5.2 Functional Characterisation of LHON Fibroblasts

Many different cellular pathways were characterised within this project. The most useful of which is likely the qPCR work which identifies a novel qPCR methodology for quantifying mitochondrial copy number within LHON fibroblasts. This removes the bias from previously described methods which mostly use a *MT-ND1* probe which overlays the LHON primary mutation, m.3460G>A, (Grady et al., 2014; Pyle et al., 2016).

Additionally, *B2M* primers were optimised, showing a much greater affinity and sensitivity in quantifying the nDNA copy number.

Our new assay can be used to quantify mtDNA copy number in all of the common LHON disease causing variants without under representing any of the mutations when compared to each other.

Beyond the preliminary review of LHON asymptomatic carrier's copy number in Figure S9 and specifically the A4-11778 cell line's copy number, there was no significant difference between cases and controls.

A4-11778 was also found to be particularly affected by deoxyglucose, indicating that it favours ATP production through glycolysis rather than OXPHOS when compared to the ratio in other cell lines. It also has a significant reduction of Manders' coefficient M1, indicating that most of the ER did not make contact with the mitochondrial network. This could be a result of the decreased size of the mitochondrial network in A4-11778, which was found to have reduced average and maximum mitochondrial network volumes despite the overall increase in mtDNA copy number. A1-11778 had a similar reduction in average and maximum mitochondrial network volumes without the increased mtDNA copy number or M1 or M2 measurements.

A5-3460 shows significantly increased M2 value, mitochondrial network length and reduced mitochondrial network fragments alongside an upregulated maximal calcium uptake. Despite these changes, there is no difference in the ER-mitochondrial interactions or $\Delta\Psi$m, suggesting that increased mitochondrial fusion occurs independently of ER or Ca^{2+} signalling and $\Delta\Psi$m.

$\Delta\Psi$m was not found to be any different between cases and controls and there was limited importance of ATP generation.

A2-14484 exhibits a significant increase in Manders' coefficient M2 but is otherwise indistinguishable from control cell lines. However, M2 values as a whole are increased in LHON samples, indicating that LHON increases mitochondria-ER interactions.

The most dramatic responses were seen in LHON cellular oxygen consumption, with greatly reduced basal respiration, ATP production, maximal respiration and spare respiratory capacity in cell lines A1-11778, A4-11778 and A5-3460. For the m.11778G>A mutant group, basal respiration and ATP production remained significantly reduced but A3-11778 maximal respiration and spare respiratory capacity was not impacted by LHON. Non-mitochondrial respiration was also significantly reduced in A5-3460.

As a whole, the greatest LHON phenotype was seen in cell lines A4-11778 and A5-

3460. A2-14484 had a very mild phenotype, which matches the favourable prognosis for this mutation in patients (Riordan-Eva et al., 1995).

Patient blood samples indicated that they were homoplasmic for the LHON mutation, as such, they should not have been affected by differing heteroplasmy levels between biological replicates - improving the quality of the results.

Due to limited study scope and singular cell lines for both the m.3460G>A and m.14484T>C mutations, it is impossible to determine whether any significant differences are cell line specific or a particular feature of that mutation.

The cell lines were also fibroblasts, which are asymptomatic to the LHON mutation within affected LHON patient phenotypes, rather than the more sensitive neurological cell types. It is possible that further work could be done in iPSCs which would show this neuronal sensitivity to LHON mutations. Three LHON iPSC models are now available (Bahr et al., 2020) which would exhibit the tissue specificity of LHON and allow for a more accurate representation of LHON disease phenotype characterisation. In Section 4, the mouse model for mitochondrial disease introduces a holistic systems approach to see how the pathways directly interact with each other, rather than different assays being performed on different passages of cells. Additionally, with oestrogen implicated as having a role in LHON development, a mouse model would allow for further pathways to be analysed that are presently disregarded in isolated cell studies. Due to limited LHON cell line availability, this could have been particularly impactful in this study given that all control cell lines were of female origin compared to the affected cell lines arising from male patients; with the discordance in penetrance between male and female LHON. Whilst within an isolated system and not exposed to mass influxes of hormonal stimulation from other tissues, given the differential penetrance of LHON between males and females, it would be beneficial to match the sex of case and control samples or study males and females separately.

As a whole, this study succeeded in characterising specific LHON primary fibroblast cell lines across a broad scope of biological responses.

Whilst we report a quantifiable difference in LHON cases to controls under Seahorse XFe96 Extracellular Flux Analyzer measurements, other pathways had a limited response and we would recommend that further cell work investigate established iPSC lines. Given the specificity of cell types affected within LHON, with midget RGCs primarily being affected, and the differences between fibroblast and neuronal cell types, particularly myelination and mitochondrial distribution, it is possible that further pathways are affected but that our model failed to exhibit symptoms due to cell type differences.

We would recommend our novel qPCR assay for quantification of LHON mitochondrial copy number in future experiments. Our cells could also be directly investigated with drug treatments to ascertain whether the treatment could prevent cell death, but we would recommend limiting investigation to determining OXPHOS response and

using a more sensitive model for investigation of other biological pathways.

5.3 Retinal Characterisation of Mitochondrial Disease Mouse

Cellular morphology indicates that the m.5024C>T + m.13715C>T mouse does have an ocular phenotype. In collaboration with Doctors Andrew Osborne (University of Cambridge) and Payam Gammage (University of Glasgow), this was further confirmed by ERG measurements in the live mice, as shown in Table 4.3. Wildtype comparisons are only 5 months old and not strain-matched, so the measurements are not directly comparable. Despite this, the visual reduction can be clearly seen and is further confirmed by measurements by Brandli and Stone (2015) as indicative of measurements taken in mice retinas damaged by light. Of note, the heteroplasmic mice were much older than the wildtype controls (roughly 9 or 24 months compared to two months).

Despite this, retinal thickness is often observed to shrink with age (Nieves-Moreno et al., 2018) with certain layers being differentially affected in disease, such as the thickening of the RPE in age-related macular degeneration (Brandl et al., 2019) and this is the opposite of what we observed in our oldest mice, indicating that it may not be an age related devolution.

Further work would be greatly improved by collection of mice at more similar life stage to ensure that observed differences are not a result of the elderly mouse naturally developing visual defects. Of note, the sectioned mutant tissue appeared greatly more tortured than the wildtype and further work could measure the sum of angles across the eye whilst normalising for the retinal curvature. Further, mutant tissue had a much greater variability in the lengths of the retinal layers than the wildtype and analysis of variance could further indicate that the mutations destabilise a normally highly ordered and regular tissue.

At present, a phenotype has been clearly observed and it would be interesting so see whether this continues in additional samples and following genetic rescue by TALENs or ZFNs (Bacman et al., 2018; Gammage et al., 2018b).

This would require a much larger mouse cohort to compare intraocular injection of one retina against the untreated eye as flat mount and tissue section preparations would then have to be observed in separate cohorts. We would recommend ageing the mice to 24 months as our cohort found that the phenotype was most significant in the elderly mice. Other mouse models of retinal disease have also found that phenotype is age dependent (John et al., 1998) and given that our phenotype increased in severity with age, it is possible that sacrificing the mice at an earlier date could fail to capture the phenotype.

The new methodology for measuring RGC density and volume appears greatly improved, allowing for total retinal cell counts and confidence in regional selection accuracy. More interestingly, further staining could be applied and it would allow for

a mosaic pattern of different sub-population of RGCs across the whole eye. As the retina contains different populations of RGCs across the eye, it could be possible that one sub-population is more affected by mitochondrial disease than the others.

Given that midget cells, which are more commonly positioned around the central papillomacular bundle, are primarily affected in LHON (Pavlidis et al., 2006; Sadun et al., 2000), this methodology could allow for validation of this hypothesis and visualisation of possible compensatory mechanisms.

Of note, Figure 4.25 (E) shows that the size of each RGC within the central region are smaller in all three samples than the edge and middle RGCs, this could indicate that there is a greater proportion of midget cells in the central region than the outer regions, as previously described by Pavlidis et al. (2006); Sadun et al. (2000).

The RPE was also collected alongside the retina, however, extreme difficulty was encountered by the dark tissue colouration. Brightfield microscopy was attempted to observe the cell structure, however, it was not optimised and no conclusions could be drawn. Our methodology allows for RPE collection but further optimisation would be required to allow for whole RPE flat mount imaging.

The limited sample availability meant that no analysis between wildtype and m.5024C>T + m.13715C>T mutant could be observed from flat mount macro structure and addition of wildtype samples would immediately improve analytic options. Given that M3:M5 only has a heteroplasmy range of 21%, with three samples, it is not possible to plot whether there is a heteroplasmy threshold or whether the differing heteroplasmy affects the samples as a range of 21% difference in the mutational burden is the equivalent that the sample with the lowest mutational burden (M3, 51%) contains 71% of the mutational burden captured in the sample with the greatest mutational burden (M4,72%).

The characterisation of the m.5024C>T + m.13715C>T mouse has been particularly interesting, and whilst replication is necessary, it has been confirmed to have a visual defect which particularly affects cells within the ONL, OPL and INL in aged mice. For this model, further investigation is needed to ascertain whether it arises as a late-onset disease phenotype or a natural ageing progression. For LHON specific studies, further work using one of the other LHON mice described in Section 4.1 could allow for LHON specific analysis and comparative analysis of the result of varying mitochondrial mutations on retinal phenotype.

We have established a technical framework which displays whole eye RGC distribution and counts; this could readily be adapted to co-stain the tissue for specific neurological markers and subsets of RGC sub-populations could be further identified. This framework could be applied to a specific LHON mouse model to characterise disease and allow for drug treatment in a live, holistic system, and the characterisation of the m.5024C>T + m.13715C>T mouse shows that it exhibits a previously unknown retinal phenotype whilst aged.

5.4 Concluding Remarks

LHON is a crippling disease for those affected and both patients and their families' quality of life is greatly reduced. With extremely limited treatment strategies, further investigation is necessary and this project sought to characterise LHON penetrance and identify novel predictive variants. Further, accurate characterisation of the phenotype on a cellular level is necessary for drug design and to target involved mechanisms.

Whilst rare disease is often considered to be 'simple', this is clearly not the case in LHON and identification of novel genetic features would also allow for improved genetic counselling if it were possible to more accurately predict disease development.

As outlined in Section 1.6, this project sought to explore fundamental pathological mechanisms which contribute to retinal defects by combining a systematic analysis of pathophysiological mechanisms using *in vitro* models and analysis of the underlying genomic traits associated with LHON.

We have identified 45 candidate genes which appear relevant in LHON disease progression, with pathway over-representation showing that the majority of identified pathways were clearly relevant and the others relate to a broader function in cellular mechanisms. Whilst further assessment in a different cohort is necessary to fully validate these candidate modifier genes, with 3/45 already known to specifically cause optic neuropathy and others implicated in cell fate, oxidative phosphorylation, and highly significant in neurogenesis, they do appear to be a favourable route of investigation.

Given that affected mothers are more likely to transmit LHON to their offspring, it is possible that some of the missing heritability of LHON is through heritable modifier genes exerting a subtle influence in likelihood of disease onset.

We specifically characterised known LHON fibroblast cell lines and found that they behaved as expected of LHON cell lines, with a significant reduction in respiratory capabilities but limited significance in other measured assays. Given these limitations, we would recommend further work to investigate other models, such as iPSCs, as tissue specificity potentially limits the phenotype expression in other biological pathways.

We specifically validated a new qPCR assay to allow for accurate quantification of mtDNA across the three most common LHON primary mutations - m.11778G>A, m.3460G>A and m.14484T>C. This improved the likelihood of positioning the primers and probes over a known SNP from ~1/8.9 to ~1/386.5 for one of the mitochondrial primers and we also altered our *B2M* primer set to improve efficiency with the new primer set reaching the detectable threshold 1.4-3.78 cycles earlier depending on the sample DNA source.

Finally, we investigated a m.5024C>T + m.13715C>T mitochondrial disease mouse for a retinal phenotype and identified a reduction in retinal functionality both *in vivo* and at a cellular level. Despite limited sample size, power calculations indicated that reduction in ERG measurements were so significant that live mice carrying the m.5024C>T

+ m.13715C>T mutations are functionally affected with reduced vision. Cellular investigations were less significant with a phenotype appearing to only develop in aged mice. This could be either late disease onset or natural visual loss through ageing as wildtype controls were not age matched, but in addition to the highly disordered tissue sections, we found a thickening of the retinal layers which is the opposite of the common age-related retinal shrinkage. The technical framework which was established within this mouse model could readily be applied to other mouse models of retinal disease, including a LHON specific one. It offers new opportunities to understand the retinal mosaicism and evolution of retinal disease onset.

We cannot fully ascertain whether measurements occur as a result of genetic defects or as a result of underlying disease pathogenesis, however, with identification of new candidate genes for LHON and methods to quantify mitochondrial copy number and characterise retinal phenotype within a mouse model, we are hopeful in eventual improvement of diagnostic and treatment options.

Bibliography

Abu-Amero, K. K., Bosley, T. M., Bohlega, S., and McLean, D. (2005). Complex I respiratory defect in LHON plus dystonia with no mitochondrial DNA mutation. *The British journal of ophthalmology*, 89(10):1380–1381.

Acosta-Alvear, D., Zhou, Y., Blais, A., Tsikitis, M., Lents, N. H., Arias, C., Lennon, C. J., Kluger, Y., and Dynlacht, B. D. (2007). XBP1 Controls Diverse Cell Type- and Condition-Specific Transcriptional Regulatory Networks. *Molecular Cell*, 27(1):53–66.

Alavi, M. V. and Fuhrmann, N. (2013). Dominant optic atrophy, OPA1, and mitochondrial quality control: understanding mitochondrial network dynamics. *Molecular Neurodegeneration*, 8(1):32.

Albrecht May, C. (2008). Comparative anatomy of the optic nerve head and inner retina in non-primate animal models used for glaucoma research. *The open ophthalmology journal*, 2:94–101.

Alexandre, A., Reynafarje, B., and Lehninger, A. L. (1978). Stoichiometry of vectorial H+ movements coupled to electron transport and to ATP synthesis in mitochondria. *Proceedings of the National Academy of Sciences of the United States of America*, 75(11):5296–5300.

An Roinn Sláinte Department of Health (2017). General Scheme of the Assisted Human Reproduction Bill. *An Roinn Sláinte Bill*.

Anderson, S., Bankier, A. T., Barrell, B. G., de Bruijn, M. H. L., Coulson, A. R., Drouin, J., Eperon, I. C., Nierlich, D. P., Roe, B. A., Sanger, F., Schreier, P. H., Smith, A. J. H., Staden, R., and Young, I. G. (1981). Sequence and organization of the human mitochondrial genome. *Nature*, 290(5806):457–465.

Angebault, C., Fauconnier, J., Patergnani, S., Rieusset, J., Danese, A., Affortit, C. A., Jagodzinska, J., Mégy, C., Quiles, M., Cazevieille, C., Korchagina, J., Bonnet-Wersinger, D., Milea, D., Hamel, C., Pinton, P., Thiry, M., Lacampagne, A., Delprat, B., and Delettre, C. (2018). ER-mitochondria cross-talk is regulated by the Ca2+ sensor NCS1 and is impaired in Wolfram syndrome. *Science Signaling*, 11(553):eaaq1380.

Angebault, C., Gueguen, N., Desquiret-Dumas, V., Chevrollier, A., Guillet, V., Verny, C., Cassereau, J., Ferre, M., Milea, D., Amati-Bonneau, P., Bonneau, D., Procaccio,

V., Reynier, P., and Loiseau, D. (2011). Idebenone increases mitochondrial complex I activity in fibroblasts from LHON patients while producing contradictory effects on respiration. *BMC Research Notes*, 4(1):557.

Anthwal, N. and Thompson, H. (2016). The development of the mammalian outer and middle ear. *Journal of anatomy*, 228(2):217–232.

Australian Bureau of Statistics (2016). 2016 Census - Tasmania.

Bacman, S. R., Kauppila, J. H. K., Pereira, C. V., Nissanka, N., Miranda, M., Pinto, M., Williams, S. L., Larsson, N.-G., Stewart, J. B., and Moraes, C. T. (2018). MitoTALEN reduces mutant mtDNA load and restores tRNAAla levels in a mouse model of heteroplasmic mtDNA mutation. *Nature Medicine*, 24(11):1696–1700.

Bahr, T., Welburn, K., Donnelly, J., and Bai, Y. (2020). Emerging model systems and treatment approaches for Leber's hereditary optic neuropathy: Challenges and opportunities. *Biochimica et Biophysica Acta (BBA) - Molecular Basis of Disease*, 1866(6):165743.

Balciuniene, J. and Balciunas, D. (2019). A Nuclear mtDNA Concatemer (Mega-NUMT) Could Mimic Paternal Inheritance of Mitochondrial Genome .

Baracca, A., Solaini, G., Sgarbi, G., Lenaz, G., Baruzzi, A., Schapira, A., Martinuzzi, A., and Carelli, V. (2005). Severe impairment of complex i–driven adenosine triphosphate synthesis in leber hereditary optic neuropathy cybrids. *Archives of Neurology*, 62(5):730–736.

Barboni, P., Savini, G., Valentino, M. L., La Morgia, C., Bellusci, C., De Negri, A. M., Sadun, F., Carta, A., Carbonelli, M., Sadun, A. A., and Carelli, V. (2006). Leber's Hereditary Optic Neuropathy with Childhood Onset. *Investigative Ophthalmology & Visual Science*, 47(12):5303–5309.

Basso, V., Marchesan, E., Peggion, C., Chakraborty, J., von Stockum, S., Giacomello, M., Ottolini, D., Debattisti, V., Caicci, F., Tasca, E., Pegoraro, V., Angelini, C., Antonini, A., Bertoli, A., Brini, M., and Ziviani, E. (2018). Regulation of ER-mitochondria contacts by Parkin via Mfn2. *Pharmacological Research*, 138:43–56.

Battisti, C., Formichi, P., Cardaioli, E., Bianchi, S., Mangiavacchi, P., Tripodi, S. A., Tosi, P., and Federico, A. (2004). Cell response to oxidative stress induced apoptosis in patients with Leber's hereditary optic neuropathy. *Journal of Neurology, Neurosurgery & Psychiatry*, 75(12):1731 LP – 1736.

Bayrhuber, M., Meins, T., Habeck, M., Becker, S., Giller, K., Villinger, S., Vonrhein, C., Griesinger, C., Zweckstetter, M., and Zeth, K. (2008). Structure of the human voltage-dependent anion channel. *Proceedings of the National Academy of Sciences*, 105(40):15370 LP – 15375.

Bellizzi, D., D'Aquila, P., Scafone, T., Giordano, M., Riso, V., Riccio, A., and Passarino, G. (2013). The Control Region of Mitochondrial DNA Shows an Unusual CpG and Non-CpG Methylation Pattern. *DNA Research*.

Benard, G. and Karbowski, M. (2009). Mitochondrial fusion and division: Regulation and role in cell viability. *Seminars in cell & developmental biology*, 20(3):365–374.

Benz, R. (1990). Biophysical properties of porin pores from mitochondrial outer membrane of eukaryotic cells. *Experientia*, 46(2):131–137.

Berg, J. M., Tymoczko, J. L., and Stryer, L. (2002). Photoreceptor Molecules in the Eye Detect Visible Light.

Berson, A., Nativio, R., Berger, S. L., and Bonini, N. M. (2018). Epigenetic Regulation in Neurodegenerative Diseases. *Trends in Neurosciences*, 41(9):587–598.

Beurel, E. and Jope, R. S. (2006). The Paradoxical Pro- and Anti-apoptotic Actions of GSK3 in the Intrinsic and Extrinsic Apoptosis Signaling Pathways. *Progress in Neurobiology*, 79(4):173–189.

Bezawork-Geleta, A., Rohlena, J., Dong, L., Pacak, K., and Neuzil, J. (2017). Mitochondrial Complex II: At the Crossroads. *Trends in Biochemical Sciences*, 42(4):312–325.

Bianco, A., Bisceglia, L., Russo, L., Palese, L. L., D'Agruma, L., Emperador, S., Montoya, J., Guerriero, S., and Petruzzella, V. (2017). High Mitochondrial DNA Copy Number Is a Protective Factor From Vision Loss in Heteroplasmic Leber's Hereditary Optic Neuropathy (LHON)High mtDNA Content Protects From LHON Vision Loss. *Investigative Ophthalmology & Visual Science*, 58(4):2193–2197.

Bianco, A., Martínez-Romero, I., Bisceglia, L., D'Agruma, L., Favia, P., Ruiz-Pesini, E., Guerriero, S., Montoya, J., and Petruzzella, V. (2015). Mitochondrial DNA copy number differentiates the Leber's hereditary optic neuropathy affected individuals from the unaffected mutation carriers. *Brain*.

Bianco, A., Valletti, A., Longo, G., Bisceglia, L., Montoya, J., Emperador, S., Guerriero, S., and Petruzzella, V. (2018). Mitochondrial DNA copy number in affected and unaffected LHON mutation carriers. *BMC research notes*, 11(1):911.

Bogenhagen, D. F. (2012). Mitochondrial DNA nucleoid structure. *Biochimica et Biophysica Acta (BBA) - Gene Regulatory Mechanisms*, 1819(9–10):914–920.

Bouquet, C., Vignal Clermont, C., Galy, A., Fitoussi, S., Blouin, L., Munk, M. R., Valero, S., Meunier, S., Katz, B., Sahel, J. A., and Thomasson, N. (2019). Immune Response and Intraocular Inflammation in Patients With Leber Hereditary Optic Neuropathy Treated With Intravitreal Injection of Recombinant Adeno-Associated

Virus 2 Carrying the ND4 Gene: A Secondary Analysis of a Phase 1/2 Clinical TrialOutcomes i. *JAMA Ophthalmology*, 137(4):399–406.

Brand, M. and Nicholls, D. (2011). Assessing mitochondrial dysfunction in cells. *Biochemical Journal*, 435(Pt 2):297–312.

Brandl, C., Brücklmayer, C., Günther, F., Zimmermann, M. E., Küchenhoff, H., Helbig, H., Weber, B. H. F., Heid, I. M., and Stark, K. J. (2019). Retinal Layer Thicknesses in Early Age-Related Macular Degeneration: Results From the German AugUR StudyRetinal Layer Thicknesses in Early AMD. *Investigative Ophthalmology & Visual Science*, 60(5):1581–1594.

Brandli, A. and Stone, J. (2015). Using the Electroretinogram to Assess Function in the Rodent Retina and the Protective Effects of Remote Limb Ischemic Preconditioning. *Journal of visualized experiments : JoVE*, 100:e52658–e52658.

Brandt, U. and Zickermann, V. (2013). Respiratory Chain Complex. In Lane, M. D., editor, *Encyclopedia of Biological Chemistry*, pages 87–91. Academic Press, Waltham.

Bravo, R., Parra, V., Gatica, D., Rodriguez, A. E., Torrealba, N., Paredes, F., Wang, Z. V., Zorzano, A., Hill, J. A., Jaimovich, E., Quest, A. F. G., and Lavandero, S. (2013). Endoplasmic reticulum and the unfolded protein response: dynamics and metabolic integration. *International review of cell and molecular biology*, 301:215–290.

Bravo, R., Vicencio, J. M., Parra, V., Troncoso, R., Munoz, J. P., Bui, M., Quiroga, C., Rodriguez, A. E., Verdejo, H. E., Ferreira, J., Iglewski, M., Chiong, M., Simmen, T., Zorzano, A., Hill, J. A., Rothermel, B. A., Szabadkai, G., and Lavandero, S. (2011). Increased ER–mitochondrial coupling promotes mitochondrial respiration and bioenergetics during early phases of ER stress. *Journal of Cell Science*, 124(13):2143–2152.

Brawn, K. and Fridovich, I. (1981). DNA strand scission by enzymically generated oxygen radicals. *Archives of Biochemistry and Biophysics*, 206(2):414–419.

Breitling, L., Yang, R., Korn, B., Burwinkel, B., and Brenner, H. (2011). Tobacco-Smoking-Related Differential DNA Methylation: 27K Discovery and Replication. *American Journal of Human Genetics*, 88(4):450–457.

Brini, M., Calì, T., Ottolini, D., and Carafoli, E. (2014). Neuronal calcium signaling: function and dysfunction. *Cellular and Molecular Life Sciences*, 71(15):2787–2814.

Britti, E., Delaspre, F., Tamarit, J., and Ros, J. (2018). Mitochondrial calcium signalling and neurodegenerative diseases. *Neuronal Signaling*, 2(4):NS20180061.

Broad Institute (2016). Picard toolkit.

Brown, M. D., Starikovskaya, E., Derbeneva, O., Hosseini, S., Allen, J. C., Mikhailovskaya, I. E., Sukernik, R. I., and Wallace, D. C. (2002). The role of mtDNA background in disease expression: a new primary LHON mutation associated with Western Eurasian haplogroup J. *Human Genetics*, 110(2):130–138.

Brown, M. D., Sun, F., and Wallace, D. C. (1997). Clustering of Caucasian Leber hereditary optic neuropathy patients containing the 11778 or 14484 mutations on an mtDNA lineage. *American journal of human genetics*, 60(2):381–387.

Brown, M. D., Trounce, I. A., Jun, A. S., Allen, J. C., and Wallace, D. C. (2000). Functional Analysis of Lymphoblast and Cybrid Mitochondria Containing the 3460, 11778, or 14484 Leber's Hereditary Optic Neuropathy Mitochondrial DNA Mutation. *Journal of Biological Chemistry*, 275(51):39831–39836.

Bu, X. D. and Rotter, J. I. (1991). X chromosome-linked and mitochondrial gene control of Leber hereditary optic neuropathy: evidence from segregation analysis for dependence on X chromosome inactivation. *Proceedings of the National Academy of Sciences of the United States of America*, 88(18):8198–8202.

Bui, M., Gilady, S. Y., Fitzsimmons, R. E. B., Benson, M. D., Lynes, E. M., Gesson, K., Alto, N. M., Strack, S., Scott, J. D., and Simmen, T. (2010). Rab32 Modulates Apoptosis Onset and Mitochondria-associated Membrane (MAM) Properties. *Journal of Biological Chemistry*, 285(41):31590–31602.

Burton, P. R., Palmer, L. J., Jacobs, K., Keen, K. J., Olson, J. M., and Elston, R. C. (2000). Ascertainment adjustment: where does it take us? *American journal of human genetics*, 67(6):1505–1514.

Calvo, S. E., Clauser, K. R., and Mootha, V. K. (2016). MitoCarta2.0: an updated inventory of mammalian mitochondrial proteins. *Nucleic Acids Research*, 44(Database issue):D1251–D1257.

Campbell, C. T., Kolesar, J. E., and Kaufman, B. A. (2012). Mitochondrial transcription factor A regulates mitochondrial transcription initiation, DNA packaging, and genome copy number. *Biochimica et Biophysica Acta (BBA) - Gene Regulatory Mechanisms*, 1819(9–10):921–929.

Caporali, L., Iommarini, L., La Morgia, C., Olivieri, A., Achilli, A., Maresca, A., Valentino, M. L., Capristo, M., Tagliavini, F., Del Dotto, V., Zanna, C., Liguori, R., Barboni, P., Carbonelli, M., Cocetta, V., Montopoli, M., Martinuzzi, A., Cenacchi, G., De Michele, G., Testa, F., Nesti, A., Simonelli, F., Porcelli, A. M., Torroni, A., and Carelli, V. (2018). Peculiar combinations of individually non-pathogenic missense mitochondrial DNA variants cause low penetrance Leber's hereditary optic neuropathy. *PLoS genetics*, 14(2):e1007210–e1007210.

Carden, T., Singh, B., Mooga, V., Bajpai, P., and Singh, K. K. (2017). Epigenetic modification of miR-663 controls mitochondria-to-nucleus retrograde signaling and tumor progression. *The Journal of biological chemistry*, 292(50):20694–20706.

Carelli, V., Achilli, A., Valentino, M. L., Rengo, C., Semino, O., Pala, M., Olivieri, A., Mattiazzi, M., Pallotti, F., Carrara, F., Zeviani, M., Leuzzi, V., Carducci, C., Valle, G., Simionati, B., Mendieta, L., Salomao, S., Belfort Jr., R., Sadun, A. A., and Torroni, A. (2006). Haplogroup Effects and Recombination of Mitochondrial DNA: Novel Clues from the Analysis of Leber Hereditary Optic Neuropathy Pedigrees. *The American Journal of Human Genetics*, 78(4):564–574.

Carelli, V., La Morgia, C., Valentino, M. L., Rizzo, G., Carbonelli, M., De Negri, A. M., Sadun, F., Carta, A., Guerriero, S., Simonelli, F., Sadun, A. A., Aggarwal, D., Liguori, R., Avoni, P., Baruzzi, A., Zeviani, M., Montagna, P., and Barboni, P. (2011). Idebenone Treatment In Leber's Hereditary Optic Neuropathy. *Brain*, 134(9):e188–e188.

Carelli, V., Ross-Cisneros, F. N., and Sadun, A. A. (2004). Mitochondrial dysfunction as a cause of optic neuropathies. *Prog Retin Eye Res*, 23.

Carelli, V., Valentino, M. L., Liguori, R., Meletti, S., Vetrugno, R., Provini, F., Mancardi, G. L., Bandini, F., Baruzzi, A., and Montagna, P. (2001). Leber's hereditary optic neuropathy (LHON/11778) with myoclonus: report of two cases. *Journal of Neurology, Neurosurgery & Psychiatry*, 71(6):813 LP – 816.

Castegna, A., Iacobazzi, V., and Infantino, V. (2015). The mitochondrial side of epigenetics. *Physiological Genomics*, 47(8):299 LP – 307.

Chalmers, R. M. and Schapira, A. H. V. (1999). Clinical, biochemical and molecular genetic features of Leber's hereditary optic neuropathy. *Biochimica et Biophysica Acta (BBA) - Bioenergetics*, 1410(2):147–158.

Chance, B., Sies, H., and Boveris, A. (1979). Hydroperoxide metabolism in mammalian organs. *Physiological Reviews*, 59(3):527–605.

Chao de la Barca, J. M., Simard, G., Amati-Bonneau, P., Safiedeen, Z., Prunier-Mirebeau, D., Chupin, S., Gadras, C., Tessier, L., Gueguen, N., Chevrollier, A., Desquiret-Dumas, V., Ferré, M., Bris, C., Kouassi Nzoughet, J., Bocca, C., Leruez, S., Verny, C., Miléa, D., Bonneau, D., Lenaers, G., Martinez, M. C., Procaccio, V., and Reynier, P. (2016). The metabolomic signature of Leber's hereditary optic neuropathy reveals endoplasmic reticulum stress. *Brain*, 139(11):2864–2876.

Chen, H. and Chan, D. C. (2006). Critical dependence of neurons on mitochondrial dynamics. *Current Opinion in Cell Biology*, 18(4):453–459.

Chen, H., Chomyn, A., and Chan, D. C. (2005). Disruption of Fusion Results in Mitochondrial Heterogeneity and Dysfunction. *Journal of Biological Chemistry*, 280(28):26185–26192.

Chen, J. D. and Denton, M. J. (1991). X-chromosomal gene in Leber hereditary optic neuroretinopathy. *American journal of human genetics*, 49(3):692–693.

Chen, L., Zhao, Y., and Zhang, H. (2016). Comparative Anatomy of the Trabecular Meshwork, the Optic Nerve Head and the Inner Retina in Rodent and Primate Models Used for Glaucoma Research.

Cheng, A. S. L., Culhane, A. C., Chan, M. W. Y., Venkataramu, C. R., Ehrich, M., Nasir, A., Rodriguez, B. A. T., Liu, J., Yan, P. S., Quackenbush, J., Nephew, K. P., Yeatman, T. J., and Huang, T. H.-M. (2008). Epithelial progeny of estrogen-exposed breast progenitor cells display a cancer-like methylome. *Cancer research*, 68(6):1786–1796.

Chestnut, B. A., Chang, Q., Price, A., Lesuisse, C., Wong, M., and Martin, L. J. (2011). Epigenetic Regulation of Motor Neuron Cell Death Through DNA Methylation. *The Journal of neuroscience : the official journal of the Society for Neuroscience*, 31(46):16619–16636.

Chinnery, P. F. (2000). Mitochondrial Disorders Overview.

Chinnery, P. F., Brown, D. T., Andrews, R. M., Singh-Kler, R., Riordan-Eva, P., Lindley, J., Applegarth, D. A., Turnbull, D. M., and Howell, N. (2001). The mitochondrial ND6 gene is a hot spot for mutations that cause Leber's hereditary optic neuropathy. *Brain*, 124(1):209–218.

Chinnery, P. F. and Gomez-Duran, A. (2018). Oldies but Goldies mtDNA Population Variants and Neurodegenerative Diseases .

Chinnery, P. F. and Turnbull, D. M. (2001). Epidemiology and treatment of mitochondrial disorders. *American Journal of Medical Genetics*, 106(1):94–101.

Choi, Y.-S., Hoon Jeong, J., Min, H.-K., Jung, H.-J., Hwang, D., Lee, S.-W., and Kim Pak, Y. (2011). Shot-gun proteomic analysis of mitochondrial D-loop DNA binding proteins: identification of mitochondrial histones. *Molecular BioSystems*, 7(5):1523–1536.

Chowdhury, S. R., binti Ismail, A., Chee, S. C., bin Laupa, M. S., binti Jaffri, F., Mohmad Saberi, S. E., and Hj Idrus, R. B. (2015). One-Step Purification of Human Skeletal Muscle Myoblasts and Subsequent Expansion Using Laminin-Coated Surface. *Tissue Engineering Part C: Methods*, 21(11):1135–1142.

Clapham, D. E. (2007). Calcium Signaling. *Cell*, 131(6):1047–1058.

Clayton, D. A. (2000). Vertebrate Mitochondrial DNA—A Circle of Surprises. *Experimental Cell Research*, 255(1):4–9.

Cock, H. R., Cooper, J. M., and Schapira, A. H. V. (1999). Functional consequences of the 3460-bp mitochondrial DNA mutation associated with Leber's hereditary optic neuropathy. *Journal of the Neurological Sciences*, 165(1):10–17.

Cock, H. R., Tabrizi, S. J., Cooper, J. M., and Schapira, A. H. V. (1998). The influence of nuclear background on the biochemical expression of 3460 Leber's hereditary optic neuropathy. *Annals of Neurology*, 44(2):187–193.

Cole, L. W. (2016). The Evolution of Per-cell Organelle Number.

Consortium, T. U. (2018). UniProt: a worldwide hub of protein knowledge. *Nucleic Acids Research*, 47(D1):D506–D515.

Coppedè, F. and Stoccoro, A. (2019). Mitoepigenetics and Neurodegenerative Diseases.

Cortelli, P., Montagna, P., Pierangeli, G., Lodi, R., Barboni, P., Liguori, R., Carelli, V., Iotti, S., Zaniol, P., Lugaresi, E., and Barbiroli, B. (1997). Clinical and brain bioenergetics improvement with idebenone in a patient with Leber's hereditary optic neuropathy: a clinical and ³¹P-MRS study. *Journal of the Neurological Sciences*, 148(1):25–31.

Craven, L., Tuppen, H. A., Greggains, G. D., Harbottle, S. J., Murphy, J. L., Cree, L. M., Murdoch, A. P., Chinnery, P. F., Taylor, R. W., Lightowlers, R. N., Herbert, M., and Turnbull, D. M. (2010). Pronuclear transfer in human embryos to prevent transmission of mitochondrial DNA disease. *Nature*, 465:82.

Crawford, N., Prendergast, D., Oehlert, J. W., Shaw, G. M., Stevenson, D. K., Rappaport, N., Sirota, M., Tishkoff, S. A., and Sondheimer, N. (2018). Divergent Patterns of Mitochondrial and Nuclear Ancestry Are Associated with the Risk for Preterm Birth. *The Journal of pediatrics*, 194:40–46.e4.

Cruz-Bermúdez, A., Vicente-Blanco, R. J., Hernández-Sierra, R., Montero, M., Alvarez, J., González Manrique, M., Blázquez, A., Martín, M. A., Ayuso, C., Garesse, R., and Fernández-Moreno, M. A. (2016). Functional Characterization of Three Concomitant MtDNA LHON Mutations Shows No Synergistic Effect on Mitochondrial Activity. *PLoS ONE*, 11(1):e0146816.

Cukras, C., Gaasterland, T., Lee, P., Gudiseva, H. V., Chavali, V. R. M., Pullakhandam, R., Maranhao, B., Edsall, L., Soares, S., Reddy, G. B., Sieving, P. A., and Ayyagari, R. (2012). Exome analysis identified a novel mutation in the RBP4 gene in a consanguineous pedigree with retinal dystrophy and developmental abnormalities. *PloS one*, 7(11):e50205–e50205.

Cyranoski, D. (2017). Japanese man is first to receive 'reprogrammed' stem cells from another person. *Nature*.

Dacey, D. M. and Petersen, M. R. (1992). Dendritic field size and morphology of midget and parasol ganglion cells of the human retina. *Proceedings of the National Academy of Sciences of the United States of America*, 89(20):9666–9670.

Damirchi, A. (2012). Mitochondrial Biogenesis in Skeletal Muscle: Exercise and Aging. In Babaei, P., editor, *Skeletal Muscle - From Myogenesis to Clinical Relations*, page Ch. 10. IntechOpen, Rijeka.

Davis, S., Du, P., Bilke, S., Triche, T., and Bootwalla, M. (2017). methylumi: Handle Illumina methylation data. *Bioconductor*.

de Brito, O. M. and Scorrano, L. (2008). Mitofusin 2 tethers endoplasmic reticulum to mitochondria. *Nature*, 456:605.

De Grey, A. D. N. J. (2005). Reactive Oxygen Species Production in the Mitochondrial Matrix: Implications for the Mechanism of Mitochondrial Mutation Accumulation. *Rejuvenation Research*, 8(1):13–17.

De Vivo, D. C. and DiMauro, S. (1990). Mitochondrial Defects of Brain and Muscle. *Neonatology*, 58(suppl 1(Suppl. 1):54–69.

DeMarini, D. M. (2004). Genotoxicity of tobacco smoke and tobacco smoke condensate: a review. *Mutation Research/Reviews in Mutation Research*, 567(2):447–474.

Deveraux, Q. L., Roy, N., Stennicke, H. R., Van Arsdale, T., Zhou, Q., Srinivasula, S. M., Alnemri, E. S., Salvesen, G. S., and Reed, J. C. (1998). IAPs block apoptotic events induced by caspase-8 and cytochrome c by direct inhibition of distinct caspases. *The EMBO journal*, 17(8):2215–2223.

Dewson, G. and Kluck, R. M. (2009). Mechanisms by which Bak and Bax permeabilise mitochondria during apoptosis. *Journal of Cell Science*, 122(16):2801 LP – 2808.

Di Noia, M. A., Todisco, S., Cirigliano, A., Rinaldi, T., Agrimi, G., Iacobazzi, V., and Palmieri, F. (2014). The human SLC25A33 and SLC25A36 genes of solute carrier family 25 encode two mitochondrial pyrimidine nucleotide transporters. *The Journal of biological chemistry*, 289(48):33137–33148.

Diaz, F., Bayona-Bafaluy, M. P., Rana, M., Mora, M., Hao, H., and Moraes, C. T. (2002). Human mitochondrial DNA with large deletions repopulates organelles faster than full-length genomes under relaxed copy number control. *Nucleic Acids Research*, 30(21):4626–4633.

Dieteren, C. E. J., Willems, P. H. G. M., Vogel, R. O., Swarts, H. G., Fransen, J., Roepman, R., Crienen, G., Smeitink, J. A. M., Nijtmans, L. G. J., and Koopman, W. J. H. (2008). Subunits of Mitochondrial Complex I Exist as Part of Matrix- and Membrane-associated Subcomplexes in Living Cells. *Journal of Biological Chemistry*, 283(50):34753–34761.

Ding, W.-X. and Yin, X.-M. (2012). Mitophagy: mechanisms, pathophysiological roles, and analysis. *Biological chemistry*, 393(7):547–564.

Dispersyn, G., Nuydens, R., Connors, R., Borgers, M., and Geerts, H. (1999). Bcl-2 protects against FCCP-induced apoptosis and mitochondrial membrane potential depolarization in PC12 cells. *Biochimica et Biophysica Acta (BBA) - General Subjects*, 1428(2):357–371.

Distelmaier, F., Valsecchi, F., Liemburg-Apers, D. C., Lebiedzinska, M., Rodenburg, R. J., Heil, S., Keijer, J., Fransen, J., Imamura, H., Danhauser, K., Seibt, A., Viollet, B., Gellerich, F. N., Smeitink, J. A. M., Wieckowski, M. R., Willems, P. H. G. M., and Koopman, W. J. H. (2015). Mitochondrial dysfunction in primary human fibroblasts triggers an adaptive cell survival program that requires AMPK-α. *Biochimica et Biophysica Acta (BBA) - Molecular Basis of Disease*, 1852(3):529–540.

Divakaruni, A. S. and Brand, M. D. (2011). The Regulation and Physiology of Mitochondrial Proton Leak. *Physiology*, 26(3):192–205.

Do, M. T. H. and Yau, K.-W. (2010). Intrinsically Photosensitive Retinal Ganglion Cells. *Physiological Reviews*, 90(4):1547–1581.

Dong, Y., Yoshitomi, T., Hu, J.-F., and Cui, J. (2017). Long noncoding RNAs coordinate functions between mitochondria and the nucleus. *Epigenetics & chromatin*, 10(1):41.

Dräger, U. C. and Olsen, J. F. (1981). Ganglion cell distribution in the retina of the mouse. *Investigative Ophthalmology & Visual Science*, 20(3):285–293.

Du, P., Kibbe, W. A., and Lin, S. M. (2008). lumi: a pipeline for processing Illumina microarray. *Bioinformatics*, 24(13):1547–1548.

Du, P., Zhang, X., Huang, C.-C., Jafari, N., Kibbe, W. A., Hou, L., and Lin, S. M. (2010). Comparison of Beta-value and M-value methods for quantifying methylation levels by microarray analysis. *BMC Bioinformatics*, 11(1):587.

Duda, P. and Jan Zrzavý (2016). Human population history revealed by a supertree approach. *Scientific Reports*, 6:29890.

Elmore, S. (2007). Apoptosis: a review of programmed cell death. *Toxicologic pathology*, 35(4):495–516.

Elson, J. L., Andrews, R. M., Chinnery, P. F., Lightowlers, R. N., Turnbull, D. M., and Howell, N. (2001). Analysis of European mtDNAs for recombination. *American journal of human genetics*, 68(1):145–153.

Elzey, B. D., Griffith, T. S., Herndon, J. M., Barreiro, R., Tschopp, J., and Ferguson, T. A. (2001). Regulation of Fas Ligand-Induced Apoptosis by TNF. *The Journal of Immunology*, 167(6):3049 LP – 3056.

Emperador, S., López-Gallardo, E., Hernández-Ainsa, C., Habbane, M., Montoya, J., Bayona-Bafaluy, M. P., and Ruiz-Pesini, E. (2019). Ketogenic treatment reduces the percentage of a LHON heteroplasmic mutation and increases mtDNA amount of a LHON homoplasmic mutation. *Orphanet Journal of Rare Diseases*, 14(1):150.

eSight Corp (2019). eSight.

European Medicines Agency (2015). Raxone (Idebenone).

Falkenberg, M. (2018). Mitochondrial DNA replication in mammalian cells: overview of the pathway. *Essays in biochemistry*, 62(3):287–296.

Fauser, S., Luberichs, J., Besch, D., and Leo-Kottler, B. (2002a). Sequence analysis of the complete mitochondrial genome in patients with Leber's hereditary optic neuropathy lacking the three most common pathogenic DNA mutations. *Biochemical and Biophysical Research Communications*, 295(2):342–347.

Fauser, S., Luberichs, J., Besch, D., and Leo-Kottler, B. (2002b). Sequence analysis of the complete mitochondrial genome in patients with Leber's hereditary optic neuropathy lacking the three most common pathogenic DNA mutations. *Biochemical and Biophysical Research Communications*, 295(2):342–347.

Fayzulin, R. Z., Perez, M., Kozhukhar, N., Spadafora, D., Wilson, G. L., and Alexeyev, M. F. (2015). A method for mutagenesis of mouse mtDNA and a resource of mouse mtDNA mutations for modeling human pathological conditions. *Nucleic Acids Research*, 43(9):e62–e62.

Fernández-Vizarra, E. and Zeviani, M. (2015). Nuclear gene mutations as the cause of mitochondrial complex III deficiency .

Ferrea, S. and Winterer, G. (2009). Neuroprotective and Neurotoxic Effects of Nicotine. *Pharmacopsychiatry*, 42(06):255–265.

Field, G. D. and Chichilnisky, E. J. (2007). Information Processing in the Primate Retina: Circuitry and Coding. *Annual Review of Neuroscience*, 30(1):1–30.

Filograna, R., Koolmeister, C., Upadhyay, M., Pajak, A., Clemente, P., Wibom, R., Simard, M. L., Wredenberg, A., Freyer, C., Stewart, J. B., and Larsson, N. G. (2019). Modulation

of mtDNA copy number ameliorates the pathological consequences of a heteroplasmic mtDNA mutation in the mouse. *Science advances*, 5(4):eaav9824–eaav9824.

Finsterer, J. (2017). Do High mtDNA Copy Numbers Truly Prevent LHON Manifestations? *Investigative Ophthalmology & Visual Science*, 58(10):4076.

Finsterer, J. and Zarrouk-Mahjoub, S. (2018). Increased mtDNA Copy Number Does Not Protect Against LHON. *Investigative Ophthalmology & Visual Science*, 59(1):330.

Fonseca, T. B., Sánchez-Guerrero, Á., Milosevic, I., and Raimundo, N. (2019). Mitochondrial fission requires DRP1 but not dynamins. *Nature*, 570(7761):E34–E42.

Fonteriz, R. I., de la Fuente, S., Moreno, A., Lobatón, C. D., Montero, M., and Alvarez, J. (2010). Monitoring mitochondrial [Ca2+] dynamics with rhod-2, ratiometric pericam and aequorin. *Cell Calcium*, 48(1):61–69.

Freedom Scientific Inc (2019a). JAWS, Job Access With Speech.

Freedom Scientific Inc (2019b). ZoomText Magnifier/Reader.

Friedman, J. R., Lackner, L. L., West, M., DiBenedetto, J. R., Nunnari, J., and Voeltz, G. K. (2011). ER tubules mark sites of mitochondrial division. *Science (New York, N.Y.)*, 334(6054):358–362.

Froehlich, J. M., Seiliez, I., Gabillard, J.-C., and Biga, P. R. (2014). Preparation of Primary Myogenic Precursor Cell/Myoblast Cultures from Basal Vertebrate Lineages. *Journal of Visualized Experiments : JoVE*, 30(86):51354.

Fu, J., Jin, Y., and Arend, L. J. (2003). Smac3, a Novel Smac/DIABLO Splicing Variant, Attenuates the Stability and Apoptosis-inhibiting Activity of X-linked Inhibitor of Apoptosis Protein. *Journal of Biological Chemistry*, 278(52):52660–52672.

Fukui, H. and Moraes, C. T. (2009). Mechanisms of formation and accumulation of mitochondrial DNA deletions in aging neurons. *Human molecular genetics*, 18(6):1028–1036.

Furuichi, K., Kokubo, S., Hara, A., Imamura, R., Wang, Q., Kitajima, S., Toyama, T., Okumura, T., Matsushima, K., Suda, T., Mukaida, N., Kaneko, S., and Wada, T. (2012). Fas Ligand Has a Greater Impact than TNF-α on Apoptosis and Inflammation in Ischemic Acute Kidney Injury. *Nephron extra*, 2(1):27–38.

Galluzzi, L., Kepp, O., and Kroemer, G. (2014). 5 - Pathophysiology of Cancer Cell Death. In Niederhuber, J. E., Armitage, J. O., Doroshow, J. H., Kastan, M. B., and Tepper, J. E. B. T., editors, *Abeloff's Clinical Oncology*, pages 69–77.e3. Elsevier, Philadelphia, fifth edn edition.

Gammage, P. A. and Frezza, C. (2019). Mitochondrial DNA: the overlooked oncogenome? *BMC Biology*, 17(1):53.

Gammage, P. A., Moraes, C. T., and Minczuk, M. (2018a). Mitochondrial Genome Engineering: The Revolution May Not Be CRISPR-Ized. *Trends in genetics : TIG*, 34(2):101–110.

Gammage, P. A., Viscomi, C., Simard, M.-L., Costa, A. S. H., Gaude, E., Powell, C. A., Van Haute, L., McCann, B. J., Rebelo-Guiomar, P., Cerutti, R., Zhang, L., Rebar, E. J., Zeviani, M., Frezza, C., Stewart, J. B., and Minczuk, M. (2018b). Genome editing in mitochondria corrects a pathogenic mtDNA mutation in vivo. *Nature Medicine*, 24(11):1691–1695.

Gatliff, J. and Campanella, M. (2015). TSPO is a REDOX regulator of cell mitophagy. *Biochemical Society Transactions*, 43(4):543–552.

Gatliff, J., East, D. A., Singh, A., Alvarez, M. S., Frison, M., Matic, I., Ferraina, C., Sampson, N., Turkheimer, F., and Campanella, M. (2017). A role for TSPO in mitochondrial Ca(2+) homeostasis and redox stress signaling. *Cell death & disease*, 8(6):e2896–e2896.

Gavathiotis, E., Reyna, D. E., Davis, M. L., Bird, G. H., and Walensky, L. D. (2010). BH3-triggered structural reorganization drives the activation of proapoptotic BAX. *Molecular cell*, 40(3):481–492.

Gaweda-Walerych, K. and Zekanowski, C. (2013). The impact of mitochondrial DNA and nuclear genes related to mitochondrial functioning on the risk of Parkinson's disease. *Current genomics*, 14(8):543–559.

GenSight Biologics (2019). Long-term Follow-up of ND4 LHON Subjects Treated With GS010 Ocular Gene Therapy in the RESCUE or REVERSE Phase III Clinical Trials.

Gertz, J., Varley, K. E., Reddy, T. E., Bowling, K. M., Pauli, F., Parker, S. L., Kucera, K. S., Willard, H. F., and Myers, R. M. (2011). Analysis of DNA Methylation in a Three-Generation Family Reveals Widespread Genetic Influence on Epigenetic Regulation. *PLOS Genetics*, 7(8):e1002228.

Ghosh, S., Sengupta, S., and Scaria, V. (2014). Comparative analysis of human mitochondrial methylomes shows distinct patterns of epigenetic regulation in mitochondria. *Mitochondrion*, 18:58–62.

Ghosh, S., Singh, K. K., Sengupta, S., and Scaria, V. (2015). Mitoepigenetics: The different shades of grey. *Mitochondrion*.

Giachin, G., Bouverot, R., Acajjaoui, S., Pantalone, S., and Soler-López, M. (2016). Dynamics of Human Mitochondrial Complex I Assembly: Implications for Neurodegenerative Diseases .

Giacomello, M. and Pellegrini, L. (2016). The coming of age of the mitochondria-ER contact: a matter of thickness. *Cell death and differentiation*, 23(9):1417–1427.

Giordano, C., Iommarini, L., Giordano, L., Maresca, A., Pisano, A., Valentino, M. L., Caporali, L., Liguori, R., Deceglie, S., Roberti, M., Fanelli, F., Fracasso, F., Ross-Cisneros, F. N., D'Adamo, P., Hudson, G., Pyle, A., Yu-Wai-Man, P., Chinnery, P. F., Zeviani, M., Salomao, S. R., Berezovsky, A., Belfort, R., Ventura, D. F., Moraes, M., Moraes Filho, M., Barboni, P., Sadun, F., De Negri, A., Sadun, A. A., Tancredi, A., Mancini, M., D'Amati, G., Loguercio Polosa, P., Cantatore, P., and Carelli, V. (2014). Efficient mitochondrial biogenesis drives incomplete penetrance in Leber's hereditary optic neuropathy. *Brain*, 137(2):335–353.

Giordano, C., Montopoli, M., Perli, E., Orlandi, M., Fantin, M., Ross-Cisneros, F. N., Caparrotta, L., Martinuzzi, A., Ragazzi, E., Ghelli, A., Sadun, A. A., D'Amati, G., and Carelli, V. (2011). Oestrogens ameliorate mitochondrial dysfunction in Leber's hereditary optic neuropathy. *Brain*, 134(1):220–234.

Giordano, L., Deceglie, S., D'Adamo, P., Valentino, M. L., La Morgia, C., Fracasso, F., Roberti, M., Cappellari, M., Petrosillo, G., Ciaravolo, S., Parente, D., Giordano, C., Maresca, A., Iommarini, L., Del Dotto, V., Ghelli, A. M., Salomao, S. R., Berezovsky, A., Belfort, R., Sadun, A. A., Carelli, V., Loguercio Polosa, P., and Cantatore, P. (2015). Cigarette toxicity triggers Leber's hereditary optic neuropathy by affecting mtDNA copy number, oxidative phosphorylation and ROS detoxification pathways. *Cell Death & Disease*, 6(12):e2021.

Giorgio, V., Petronilli, V., Ghelli, A., Carelli, V., Rugolo, M., Lenaz, G., and Bernardi, P. (2012). The effects of idebenone on mitochondrial bioenergetics. *Biochimica et Biophysica Acta (BBA) - Bioenergetics*, 1817(2):363–369.

Glick, D., Barth, S., and Macleod, K. F. (2010). Autophagy: cellular and molecular mechanisms. *The Journal of pathology*, 221(1):3–12.

Goldman, D. (2014). Muller glial cell reprogramming and retina regeneration. *Nat Rev Neurosci*, 15(7):431–442.

Gorman, G. S. and Taylor, R. W. (2011). Mitochondrial DNA abnormalities in ophthalmological disease. *Saudi Journal of Ophthalmology*, 25(4):395–404.

Gottlieb, E., Armour, S. M., Harris, M. H., and Thompson, C. B. (2003). Mitochondrial membrane potential regulates matrix configuration and cytochrome c release during apoptosis. *Cell Death And Differentiation*, 10:709.

Grady, J. P., Murphy, J. L., Blakely, E. L., Haller, R. G., Taylor, R. W., Turnbull, D. M., and Tuppen, H. A. L. (2014). Accurate Measurement of Mitochondrial DNA Deletion Level and Copy Number Differences in Human Skeletal Muscle. *PLoS ONE*, 9(12):e114462.

Grimm, S. A., Shimbo, T., Takaku, M., Thomas, J. W., Auerbach, S., Bennett, B. D., Bucher, J. R., Burkholder, A. B., Day, F., Du, Y., Duncan, C. G., French, J. E., Foley, J. F., Li, J., Merrick, B. A., Tice, R. R., Wang, T., Xu, X., Barnabas, B. B., Bouffard, G. G., Brooks, S. Y., Coleman, H., Dekhtyar, L., Guan, X., Han, J., Ho, S.-l., Legaspi, R., Maduro, Q. L., Masiello, C. A., McDowell, J. C., Montemayor, C., Park, M., Riebow, N. L., Schandler, K., Scharer, C., Schmidt, B., Sison, C., Stantripop, S., Thomas, P. J., Vemulapalli, M., Young, A. C., Bushel, P. R., Fargo, D. C., Mullikin, J. C., Wade, P. A., and Program, N. C. S. (2019). DNA methylation in mice is influenced by genetics as well as sex and life experience. *Nature Communications*, 10(1):305.

Gross, A., McDonnell, J. M., and Korsmeyer, S. J. (1999). BCL-2 family members and the mitochondria in apoptosis. *Genes & Development*, 13(15):1899–1911.

Guha, M. and Avadhani, N. G. (2013). Mitochondrial retrograde signaling at the crossroads of tumor bioenergetics, genetics and epigenetics. *Mitochondrion*, 13(6):577–591.

Guy, J., Feuer, W. J., Davis, J. L., Porciatti, V., Gonzalez, P. J., Koilkonda, R. D., Yuan, H., Hauswirth, W. W., and Lam, B. L. (2017). Gene Therapy for Leber Hereditary Optic Neuropathy: Low- and Medium-Dose Visual Results. *Ophthalmology*, 124(11):1621–1634.

Haile, Y., Deng, X., Ortiz-Sandoval, C., Tahbaz, N., Janowicz, A., Lu, J.-Q., Kerr, B. J., Gutowski, N. J., Holley, J. E., Eggleton, P., Giuliani, F., and Simmen, T. (2017). Rab32 connects ER stress to mitochondrial defects in multiple sclerosis. *Journal of neuroinflammation*, 14(1):19.

Halestrap, A. P. (2006). Calcium, mitochondria and reperfusion injury: a pore way to die. *Biochemical Society Transactions*, 34(2):232 LP – 237.

Hall, E., Volkov, P., Dayeh, T., Esguerra, J. L. S., Salö, S., Eliasson, L., Rönn, T., Bacos, K., and Ling, C. (2014). Sex differences in the genome-wide DNA methylation pattern and impact on gene expression, microRNA levels and insulin secretion in human pancreatic islets. *Genome Biology*, 15(12):522.

Halliwell, B. and Aruoma, O. I. (1991). DNA damage by oxygen-derived species. Its mechanism and measurement in mammalian systems. *FEBS Letters*, 281(1-2):9–19.

Haroon, M. F., Fatima, A., Schöler, S., Gieseler, A., Horn, T. F. W., Kirches, E., Wolf, G., and Kreutzmann, P. (2007). Minocycline, a possible neuroprotective agent in Leber's hereditary optic neuropathy (LHON): Studies of cybrid cells bearing 11778 mutation. *Neurobiology of Disease*, 28(3):237–250.

Heavner, W. and Pevny, L. (2012). Eye Development and Retinogenesis. *Cold Spring Harbor Perspectives in Biology*, 4(12).

Hedberg-Buenz, A., Christopher, M. A., Lewis, C. J., Fernandes, K. A., Dutca, L. M., Wang, K., Scheetz, T. E., Abràmoff, M. D., Libby, R. T., Garvin, M. K., and Anderson, M. G. (2016). Quantitative measurement of retinal ganglion cell populations via histology-based random forest classification. *Experimental eye research*, 146:370–385.

Hekimi, S., Wang, Y., and Noë, A. (2016). Mitochondrial ROS and the Effectors of the Intrinsic Apoptotic Pathway in Aging Cells: The Discerning Killers! *Frontiers in genetics*, 7:161.

Herrmann, J. M. and Riemer, J. (2010). The Intermembrane Space of Mitochondria. *Antioxidants & Redox Signaling*, 13(9):1341–1358.

Hetz, C., Bernasconi, P., Fisher, J., Lee, A.-H., Bassik, M. C., Antonsson, B., Brandt, G. S., Iwakoshi, N. N., Schinzel, A., Glimcher, L. H., and Korsmeyer, S. J. (2006). Proapoptotic BAX and BAK Modulate the Unfolded Protein Response by a Direct Interaction with IRE1α. *Science*, 312(5773):572 LP – 576.

Hirst, J. (2013). Mitochondrial Complex I. *Annual Review of Biochemistry*, 82(1):551–575.

Hirst, J. and Roessler, M. M. (2015). Energy conversion, redox catalysis and generation of reactive oxygen species by respiratory complex I. *Biochimica et Biophysica Acta (BBA) - Bioenergetics*.

Hitchcock, D. B. (2009). Yates and Contingency Tables: 75 Years Later (2009). *Electronic Journal for History of Probability and Statistics*, 5(2).

Holt, I. J., Lorimer, H. E., and Jacobs, H. T. (2000). Coupled Leading- and Lagging-Strand Synthesis of Mammalian Mitochondrial DNA. *Cell*, 100(5):515–524.

Horsthemke, B. (2018). A critical view on transgenerational epigenetic inheritance in humans. *Nature communications*, 9(1):2973.

Houseman, E. A., Accomando, W. P., Koestler, D. C., Christensen, B. C., Marsit, C. J., Nelson, H. H., Wiencke, J. K., and Kelsey, K. T. (2012). DNA methylation arrays as surrogate measures of cell mixture distribution. *BMC Bioinformatics*, 13(1):86.

Howell, N. (1998). Leber hereditary optic neuropathy: respiratory chain dysfunction and degeneration of the optic nerve. *Vision Research*, 38(10):1495–1504.

Howell, N., Halvorson, S., Burns, J., McCullough, D. A., and Paulton, J. (1993). When does bilateral optic atrophy become Leber hereditary optic neuropathy? *American Journal of Human Genetics*, 53(4):959–963.

Howell, N., Miller, N. R., Mackey, D. A., Arnold, A., Herrnstadt, C., Williams, I. M., and Kubacka, I. (2002). Lightning Strikes Twice: Leber Hereditary Optic Neuropathy Families with Two Pathogenic mtDNA Mutations. *Journal of Neuro-Ophthalmology*, 22(4).

Howell, N., Oostra, R.-J., Bolhuis, P. A., Spruijt, L., Clarke, L. A., Mackey, D. A., Preston, G., and Herrnstadt, C. (2003). Sequence Analysis of the Mitochondrial Genomes from Dutch Pedigrees with Leber Hereditary Optic Neuropathy. *The American Journal of Human Genetics*, 72(6):1460–1469.

Huber, W., Carey, V. J., Gentleman, R., Anders, S., Carlson, M., Carvalho, B. S., Bravo, H. C., Davis, S., Gatto, L., Girke, T., Gottardo, R., Hahne, F., Hansen, K. D., Irizarry, R. A., Lawrence, M., Love, M. I., MacDonald, J., Obenchain, V., Oleś, A. K., Pagès, H., Reyes, A., Shannon, P., Smyth, G. K., Tenenbaum, D., Waldron, L., and Morgan, M. (2015). Orchestrating high-throughput genomic analysis with Bioconductor. *Nature methods*, 12(2):115–121.

Hudson, G., Carelli, V., Spruijt, L., Gerards, M., Mowbray, C., Achilli, A., Pyle, A., Elson, J., Howell, N., La Morgia, C., Valentino, M. L., Huoponen, K., Savontaus, M.-L., Nikoskelainen, E., Sadun, A. A., Salomao, S. R., Belfort Jr., R., Griffiths, P., Man, P. Y. W., de Coo, R. F. M., Horvath, R., Zeviani, M., Smeets, H. J. T., Torroni, A., and Chinnery, P. F. (2007). Clinical Expression of Leber Hereditary Optic Neuropathy Is Affected by the Mitochondrial DNA Haplogroup Background. *The American Journal of Human Genetics*, 81(2):228–233.

Hudson, G., Keers, S., Yu-Wai-Man, P., Griffiths, P., Huoponen, K., Savontaus, M.-L., Nikoskelainen, E., Zeviani, M., Carrara, F., Horvath, R., Karcagi, V., Spruijt, L., de Coo, I. F. M., Smeets, H. J. M., and Chinnery, P. F. (2005). Identification of an X-chromosomal locus and haplotype modulating the phenotype of a mitochondrial DNA disorder. *American journal of human genetics*, 77(6):1086–1091.

Hüttemann, M., Pecina, P., Rainbolt, M., Sanderson, T. H., Kagan, V. E., Samavati, L., Doan, J. W., and Lee, I. (2011). The multiple functions of cytochrome c and their regulation in life and death decisions of the mammalian cell: From respiration to apoptosis. *Mitochondrion*, 11(3):369–381.

Iacobazzi, V., Castegna, A., Infantino, V., and Andria, G. (2013). Mitochondrial DNA methylation as a next-generation biomarker and diagnostic tool. *Molecular Genetics and Metabolism*, 110(1–2):25–34.

Igney, F. H. and Krammer, P. H. (2002). Death and anti-death: tumour resistance to apoptosis. *Nature Reviews Cancer*, 2(4):277–288.

Integrated DNA Technologies (2017). OligoAnalyzer 3.1.

Ishihara, N., Eura, Y., and Mihara, K. (2004). Mitofusin 1 and 2 play distinct roles in mitochondrial fusion reactions via GTPase activity. *Journal of Cell Science*, 117(26):6535 LP – 6546.

Ito, Y. A. and Di Polo, A. (2017). Mitochondrial dynamics, transport, and quality control: A bottleneck for retinal ganglion cell viability in optic neuropathies. *Mitochondrion*, 36:186–192.

Jacob, W. A., Bakker, A., Hertsens, R. C., and Biermans, W. (1994). Mitochondrial matrix granules: Their behavior during changing metabolic situations and their relationship to contact sites between inner and outer mitochondrial membranes. *Microscopy Research and Technique*, 27(4):307–318.

Jacobi, F. K., Leo-Kottler, B., Mittelviefhaus, K., Zrenner, E., Meyer, J., Pusch, C. M., and Wissinger, B. (2001). Segregation Patterns and Heteroplasmy Prevalence in Leber's Hereditary Optic Neuropathy. *Investigative Ophthalmology & Visual Science*, 42(6):1208–1214.

Jaña, F., Bustos, G., Rivas, J., Cruz, P., Urra, F., Basualto-Alarcón, C., Sagredo, E., Ríos, M., Lovy, A., Dong, Z., Cerda, O., Madesh, M., and Cárdenas, C. (2019). Complex I and II are required for normal mitochondrial Ca2+ homeostasis. *Mitochondrion*, 49:73–82.

Jankauskaitė, E., Bartnik, E., and Kodroń, A. (2017). Investigating Leber's hereditary optic neuropathy: Cell models and future perspectives. *Mitochondrion*, 32:19–26.

Jastroch, M., Divakaruni, A. S., Mookerjee, S., Treberg, J. R., and Brand, M. D. (2010). Mitochondrial proton and electron leaks. *Essays in biochemistry*, 47:53–67.

Jeppesen, D. K., Bohr, V. A., and Stevnsner, T. (2011). DNA Repair Deficiency in Neurodegeneration. *Progress in Neurobiology*, 94(2):166–200.

Ji, F., Sharpley, M. S., Derbeneva, O., Alves, L. S., Qian, P., Wang, Y., Chalkia, D., Lvova, M., Xu, J., Yao, W., Simon, M., Platt, J., Xu, S., Angelin, A., Davila, A., Huang, T., Wang, P. H., Chuang, L.-M., Moore, L. G., Qian, G., and Wallace, D. C. (2012). Mitochondrial DNA variant associated with Leber hereditary optic neuropathy and high-altitude Tibetans. *Proceedings of the National Academy of Sciences of the United States of America*, 109(19):7391–7396.

Jiang, F., Zhang, Y., and Dusting, G. J. (2011). NADPH Oxidase-Mediated Redox Signaling: Roles in Cellular Stress Response, Stress Tolerance, and Tissue Repair. *Pharmacological Reviews*, 63(1):218–242.

Jiang, P., Liang, M., Zhang, C., Zhao, X., He, Q., Cui, L., Liu, X., Sun, Y.-H., Fu, Q., Ji, Y., Bai, Y., Huang, T., and Guan, M.-X. (2016). Biochemical evidence for a mitochondrial genetic modifier in the phenotypic manifestation of Leber's hereditary optic neuropathy-associated mitochondrial DNA mutation. *Human Molecular Genetics*.

John, S. W., Smith, R. S., Savinova, O. V., Hawes, N. L., Chang, B., Turnbull, D., Davisson, M., Roderick, T. H., and Heckenlively, J. R. (1998). Essential iris atrophy pigment dispersion and glaucoma in DBA/2J mice.

Johns, D. R. and Berman, J. (1991). Alternative, simultaneous complex I mitochondrial DNA mutations in Leber's hereditary optic neuropathy. *Biochemical and Biophysical Research Communications*, 174(3):1324–1330.

Joshi, D. C. and Bakowska, J. C. (2011). Determination of Mitochondrial Membrane Potential and Reactive Oxygen Species in Live Rat Cortical Neurons. *Journal of Visualized Experiments : JoVE*, 23(51):2704.

Joshi, S. and Kermode, A. G. (2019). Harding's disease: an important MS mimic. *BMJ Case Reports*, 12(3):e228337.

Jurkute, N., Harvey, J., and Yu-Wai-Man, P. (2019). Treatment strategies for Leber hereditary optic neuropathy. *Current Opinion in Neurology*, 32(1).

Kaati, G., Bygren, L. O., Pembrey, M., and Sjöström, M. (2007). Transgenerational response to nutrition, early life circumstances and longevity. *European Journal Of Human Genetics*, 15:784.

Kaewsutthi, S., Phasukkijwatana, N., Joyjinda, Y., Chuenkongkaew, W., Kunhapan, B., Tun, A. W., Suktitipat, B., and Lertrit, P. (2011). Mitochondrial Haplogroup Background May Influence Southeast Asian G11778A Leber Hereditary Optic Neuropathy. *Investigative Ophthalmology & Visual Science*, 52(7):4742–4748.

Kalghatgi, S., Spina, C. S., Costello, J. C., Liesa, M., Morones-Ramirez, J. R., Slomovic, S., Molina, A., Shirihai, O. S., and Collins, J. J. (2013). Bactericidal Antibiotics Induce Mitochondrial Dysfunction and Oxidative Damage in Mammalian Cells. *Science translational medicine*, 5(192):192ra85–192ra85.

Kalkavan, H. and Green, D. R. (2017). MOMP, cell suicide as a BCL-2 family business. *Cell Death And Differentiation*, 25:46.

Kanakubo, S., Nomura, T., Yamamura, K.-i., Miyazaki, J.-i., Tamai, M., and Osumi, N. (2006). Abnormal migration and distribution of neural crest cells in Pax6 heterozygous mutant eye, a model for human eye diseases. *Genes to Cells*, 11(8):919–933.

Karanjia, R., Tran, J., Chu, E. R., Gale, J., Frousiakis, S. E., Pouw, A., Wa, C. A., Moraes, M., Salomao, S. R., and Carelli, V. (2014). Although smoking and alcohol are known to increase incidence of Leber's Hereditary Optic Neuropathy (LHON) only smoking increases severity of LHON. *Investigative Ophthalmology & Visual Science*, 55(6203).

Karbowski, M., Arnoult, D., Chen, H., Chan, D. C., Smith, C. L., and Youle, R. J. (2004). Quantitation of mitochondrial dynamics by photolabeling of individual organelles shows that mitochondrial fusion is blocked during the Bax activation phase of apoptosis. *The Journal of cell biology*, 164(4):493–499.

Karbowski, M. and Youle, R. J. (2003). Dynamics of mitochondrial morphology in healthy cells and during apoptosis. *Cell Death Differ*, 10(8):870–880.

Kauppila, J., Baines, H., Bratic, A., Simard, M.-L., Freyer, C., Mourier, A., Stamp, C., Filograna, R., Larsson, N.-G., Greaves, L., and Stewart, J. (2016). A Phenotype-Driven Approach to Generate Mouse Models with Pathogenic mtDNA Mutations Causing Mitochondrial Disease. *Cell Reports*, 16(11):2980–2990.

Kay, J. N., Chu, M. W., and Sanes, J. R. (2012). MEGF10 and MEGF11 mediate homotypic interactions required for mosaic spacing of retinal neurons. *Nature*, 483(7390):465–469.

Kaykas, A., Yang-Snyder, J., Héroux, M., Shah, K. V., Bouvier, M., and Moon, R. T. (2004). Mutant Frizzled 4 associated with vitreoretinopathy traps wild-type Frizzled in the endoplasmic reticulum by oligomerization. *Nature Cell Biology*, 6(1):52–58.

Keinan, N., Tyomkin, D., and Shoshan-Barmatz, V. (2010). Oligomerization of the Mitochondrial Protein Voltage-Dependent Anion Channel Is Coupled to the Induction of Apoptosis. *Molecular and Cellular Biology*, 30(24):5698–5709.

Kerrison, J. B., Howell, N., Miller, N. R., Hirst, L., and Green, W. R. (1995). Leber Hereditary Optic Neuropathy: Electron Microscopy and Molecular Genetic Analysis of a Case. *Ophthalmology*, 102(10):1509–1516.

Khakh, B. S. and Burnstock, G. (2009). The Double Life of ATP. *Scientific American*, 301(6):84–92.

Kholmukhamedov, A., Schwartz, J. M., and Lemasters, J. J. (2013). MitoTracker Probes and Mitochondrial Membrane Potential. *Shock (Augusta, Ga.)*, 39(6):543.

Kim, U. S., Jurkute, N., and Yu-Wai-Man, P. (2018). Leber Hereditary Optic Neuropathy—Light at the End of the Tunnel? *The Asia-Pacific Journal of Ophthalmology*, 7(4).

Kinnally, K. W., Peixoto, P. M., Ryu, S.-Y., and Dejean, L. M. (2011). Is mPTP the gatekeeper for necrosis, apoptosis, or both? *Biochimica et biophysica acta*, 1813(4):616–622.

Kirches, E. (2011). LHON: Mitochondrial Mutations and More. *Current Genomics*, 12(1):44–54.

Kirkman, M. A., Yu-Wai-Man, P., Korsten, A., Leonhardt, M., Dimitriadis, K., De Coo, I. F., Klopstock, T., and Chinnery, P. F. (2009). Gene–environment interactions in Leber hereditary optic neuropathy. *Brain*, 132(9):2317–2326.

Klopstock, T., Metz, G., Yu-Wai-Man, P., Büchner, B., Gallenmüller, C., Bailie, M., Nwali, N., Griffiths, P. G., von Livonius, B., Reznicek, L., Rouleau, J., Coppard, N., Meier, T., and Chinnery, P. F. (2013). Persistence of the treatment effect of idebenone in Leber's hereditary optic neuropathy. *Brain : a journal of neurology*, 136(Pt 2):e230–e230.

Klopstock, T., Yu-Wai-Man, P., Dimitriadis, K., Rouleau, J., Heck, S., Bailie, M., Atawan, A., Chattopadhyay, S., Schubert, M., Garip, A., Kernt, M., Petraki, D., Rummey, C., Leinonen, M., Metz, G., Griffiths, P. G., Meier, T., and Chinnery, P. F. (2011). A randomized placebo-controlled trial of idebenone in Leber's hereditary optic neuropathy. *Brain*.

Koboldt, D. C., Zhang, Q., Larson, D. E., Shen, D., McLellan, M. D., Lin, L., Miller, C. A., Mardis, E. R., Ding, L., and Wilson, R. K. (2012). VarScan 2: somatic mutation and copy number alteration discovery in cancer by exome sequencing. *Genome research*, 22(3):568–576.

Kögel, D. and Prehn, J. H. (2013). Caspase-Independent Cell Death Mechanisms.

Kolb, H. and Marshak, D. (2003). The midget pathways of the primate retina. *Documenta Ophthalmologica*, 106(1):67–81.

Kolb, H., Nelson, R., and Mariani, A. (1981). Amacrine cells, bipolar cells and ganglion cells of the cat retina: A Golgi study. *Vision Research*, 21(7):1081–1114.

Koopman, W. J. H., Beyrath, J., Fung, C.-W., Koene, S., Rodenburg, R. J., Willems, P. H. G. M., and Smeitink, J. A. M. (2016). Mitochondrial disorders in children: toward development of small-molecule treatment strategies. *EMBO Molecular Medicine*, 8(4):311–327.

Kowald, A. and Kirkwood, T. B. L. (2013). Mitochondrial mutations and aging: random drift is insufficient to explain the accumulation of mitochondrial deletion mutants in short-lived animals. *Aging Cell*, 12(4):728–731.

Kozieł, R., Pircher, H., Kratochwil, M., Lener, B., Hermann, M., Dencher, N., and Jansen-Dürr, P. (2013). Mitochondrial respiratory chain complex I is inactivated by NADPH oxidase Nox4. *Biochemical Journal*, 452(2):231–239.

Krebs, M. P., Collin, G. B., Hicks, W. L., Yu, M., Charette, J. R., Shi, L. Y., Wang, J., Naggert, J. K., Peachey, N. S., and Nishina, P. M. (2017). Mouse models of human ocular disease for translational research. *PLOS ONE*, 12(8):e0183837.

Krylova, T. D., Sheremet, N. L., Tabakov, V. Y., Lyamzaev, K. G., Itkis, Y. S., Tsygankova, P. G., Andreeva, N. A., Shmelkova, M. S., Nevinitsyna, T. A., Kadyshev, V. V., and Zakharova, E. Y. (2020). Three rare pathogenic mtDNA substitutions in LHON patients with low heteroplasmy. *Mitochondrion*, 50:139–144.

Kühlbrandt, W. (2015). Structure and function of mitochondrial membrane protein complexes. *BMC Biology*, 13(1):89.

Kukat, C., Wurm, C. A., Spåhr, H., Falkenberg, M., Larsson, N.-G., and Jakobs, S. (2011). Super-resolution microscopy reveals that mammalian mitochondrial nucleoids have a uniform size and frequently contain a single copy of mtDNA. *Proceedings of the National Academy of Sciences*, 108(33):13534–13539.

Leber, T. (1871). Ueber hereditäre und congenital-angelegte Sehnervenleiden. *Albrecht von Graefes Archiv für Ophthalmologie*, 17(2):249–291.

Lee, A.-H., Iwakoshi, N. N., and Glimcher, L. H. (2003). XBP-1 Regulates a Subset of Endoplasmic Reticulum Resident Chaperone Genes in the Unfolded Protein Response. *Molecular and Cellular Biology*, 23(21):7448 LP – 7459.

Lee, K.-S., Huh, S., Lee, S., Wu, Z., Kim, A.-K., Kang, H.-Y., and Lu, B. (2018). Altered ER-mitochondria contact impacts mitochondria calcium homeostasis and contributes to neurodegeneration in vivo in disease models. *Proceedings of the National Academy of Sciences of the United States of America*, 115(38):E8844–E8853.

Lenaz, G., Fato, R., Genova, M. L., Bergamini, C., Bianchi, C., and Biondi, A. (2006). Mitochondrial Complex I: Structural and functional aspects. *Biochimica et Biophysica Acta (BBA) - Bioenergetics*, 1757(9):1406–1420.

Levin, L. A. (2007). Mechanisms of Retinal Ganglion Specific-Cell Death in Leber Hereditary Optic Neuropathy. *Transactions of the American Ophthalmological Society*, 105:379–391.

LHON Society (2020). About LHON.

Li, C., Bai, Y., Liu, H., Zuo, X., Yao, H., Xu, Y., and Cao, M. (2013). Comparative study of microRNA profiling in keloid fibroblast and annotation of differential expressed microRNAs. *Acta Biochimica et Biophysica Sinica*, 45(8):692–699.

Li, D., Carozza, R. B., Shatos, M. A., Hodges, R. R., and Dartt, D. A. (2012a). Effect of Histamine on Ca2+-Dependent Signaling Pathways in Rat Conjunctival Goblet Cells. *Investigative Ophthalmology & Visual Science*, 53(11):6928–6938.

Li, H. and Durbin, R. (2009). Fast and accurate short read alignment with Burrows-Wheeler transform. *Bioinformatics (Oxford, England)*, 25(14):1754–1760.

Li, H., Handsaker, B., Wysoker, A., Fennell, T., Ruan, J., Homer, N., Marth, G., Abecasis, G., Durbin, R., and Subgroup, . G. P. D. P. (2009). The Sequence Alignment/Map format and SAMtools. *Bioinformatics (Oxford, England)*, 25(16):2078–2079.

Li, P., Jiao, J., Gao, G., and Prabhakar, B. S. (2012b). Control of mitochondrial activity by miRNAs. *Journal of Cellular Biochemistry*, 113(4):1104–1110.

Li, P., Nijhawan, D., Budihardjo, I., Srinivasula, S. M., Ahmad, M., Alnemri, E. S., and Wang, X. (1997). Cytochrome c and dATP-Dependent Formation of Apaf-1/Caspase-9 Complex Initiates an Apoptotic Protease Cascade. *Cell*, 91(4):479–489.

Li, Q. and Wang, K. (2017). InterVar: Clinical Interpretation of Genetic Variants by the 2015 ACMG-AMP Guidelines. *American journal of human genetics*, 100(2):267–280.

Li, Y., D'Aurelio, M., Deng, J.-H., Park, J.-S., Manfredi, G., Hu, P., Lu, J., and Bai, Y. (2007). An Assembled Complex IV Maintains the Stability and Activity of Complex I in Mammalian Mitochondria. *Journal of Biological Chemistry*, 282(24):17557–17562.

Lin, C. S., Sharpley, M. S., Fan, W., Waymire, K. G., Sadun, A. A., Carelli, V., Ross-Cisneros, F. N., Baciu, P., Sung, E., McManus, M. J., Pan, B. X., Gil, D. W., MacGregor, G. R., and Wallace, D. C. (2012). Mouse mtDNA mutant model of Leber hereditary optic neuropathy. *Proceedings of the National Academy of Sciences*, 109(49):20065 LP – 20070.

Liu, B., Du, Q., Chen, L., Fu, G., Li, S., Fu, L., Zhang, X., Ma, C., and Bin, C. (2016). CpG methylation patterns of human mitochondrial DNA. *Scientific Reports*, 6:23421.

Liu, S., Sarkar, C., Dinizo, M., Faden, A. I., Koh, E. Y., Lipinski, M. M., and Wu, J. (2015). Disrupted autophagy after spinal cord injury is associated with ER stress and neuronal cell death. *Cell death & disease*, 6(1):e1582–e1582.

Llòria, X., Catarino, C., Silva, M., and Klopstock, T. (2017). Idebenone is effective and well tolerated in Leber's hereditary optic neuropathy (LHON): Long-term results of real world clinical practice. *Acta Ophthalmologica*, 95(S259).

Lomonosova, E. and Chinnadurai, G. (2008). BH3-only proteins in apoptosis and beyond: an overview. *Oncogene*, 27 Suppl 1(Suppl 1):S2–S19.

Losón, O. C., Song, Z., Chen, H., and Chan, D. C. (2013). Fis1, Mff, MiD49, and MiD51 mediate Drp1 recruitment in mitochondrial fission. *Molecular biology of the cell*, 24(5):659–667.

Lott, M. T., Leipzig, J. N., Derbeneva, O., Xie, H. M., Chalkia, D., Sarmady, M., Procaccio, V., and Wallace, D. C. (2013). mtDNA Variation and Analysis Using Mitomap and Mitomaster. *Current protocols in bioinformatics*, 44(123):1.23.1–1.23.26.

Lovell, J. F., Billen, L. P., Bindner, S., Shamas-Din, A., Fradin, C., Leber, B., and Andrews, D. W. (2008). Membrane Binding by tBid Initiates an Ordered Series of Events Culminating in Membrane Permeabilization by Bax. *Cell*, 135(6):1074–1084.

Luo, S., Valencia, C. A., Zhang, J., Lee, N.-C., Slone, J., Gui, B., Wang, X., Li, Z., Dell, S., Brown, J., Chen, S. M., Chien, Y.-H., Hwu, W.-L., Fan, P.-C., Wong, L.-J., Atwal, P. S., and Huang, T. (2018). Biparental Inheritance of Mitochondrial DNA in Humans. *Proceedings of the National Academy of Sciences*, 115(51):13039 LP – 13044.

Ly, J. D., Grubb, D. R., and Lawen, A. (2003). The mitochondrial membrane potential ($\Delta\psi$m) in apoptosis; an update. *Apoptosis*, 8(2):115–128.

Lyseng-Williamson, K. A. (2016). Idebenone: A Review in Leber's Hereditary Optic Neuropathy. *Drugs*, 76(7):805–813.

Ma, C., Liu, Y., Neumann, S., and Gao, X. (2017). Nicotine from cigarette smoking and diet and Parkinson disease: a review. *Translational Neurodegeneration*, 6(1):18.

Ma, D. K., Marchetto, M. C., Guo, J. U., Ming, G.-l., Gage, F. H., and Song, H. (2010). Epigenetic choreographers of neurogenesis in the adult mammalian brain. *Nature Neuroscience*, 13:1338.

Macmillan, C., Johns, T. A., Fu, K., and Shoubridge, E. A. (2000a). Predominance of the T14484C Mutation in French-Canadian Families with Leber Hereditary Optic Neuropathy Is Due to a Founder Effect. *American Journal of Human Genetics*, 66(1):332–335.

Macmillan, C., Johns, T. A., Fu, K., and Shoubridge, E. A. (2000b). Predominance of the T14484C mutation in French-Canadian families with Leber hereditary optic neuropathy is due to a founder effect. *American journal of human genetics*, 66(1):332–335.

Maeda, A., Mandai, M., and Takahashi, M. (2019). Gene and Induced Pluripotent Stem Cell Therapy for Retinal Diseases. *Annual Review of Genomics and Human Genetics*, 20(1):201–216.

Majander, A., Bowman, R., Poulton, J., Antcliff, R. J., Reddy, M. A., Michaelides, M., Webster, A. R., Chinnery, P. F., Votruba, M., Moore, A. T., and Yu-Wai-Man, P. (2017). Childhood-onset Leber hereditary optic neuropathy. *British Journal of Ophthalmology*, 101(11):1505 LP – 1509.

Malladi, S., Challa-Malladi, M., Fearnhead, H. O., and Bratton, S. B. (2009). The Apaf-1*procaspase-9 apoptosome complex functions as a proteolytic-based molecular timer. *The EMBO journal*, 28(13):1916–1925.

Mandai, M., Watanabe, A., Kurimoto, Y., Hirami, Y., Morinaga, C., Daimon, T., Fujihara, M., Akimaru, H., Sakai, N., Shibata, Y., Terada, M., Nomiya, Y., Tanishima, S., Nakamura, M., Kamao, H., Sugita, S., Onishi, A., Ito, T., Fujita, K., Kawamata, S., Go, M. J., Shinohara, C., Hata, K.-i., Sawada, M., Yamamoto, M., Ohta, S., Ohara, Y., Yoshida, K., Kuwahara, J., Kitano, Y., Amano, N., Umekage, M., Kitaoka, F., Tanaka, A., Okada, C., Takasu, N., Ogawa, S., Yamanaka, S., and Takahashi, M. (2017). Autologous Induced Stem-Cell–Derived Retinal Cells for Macular Degeneration. *New England Journal of Medicine*, 376(11):1038–1046.

Manev, H., Dzitoyeva, S., and Chen, H. (2012). Mitochondrial DNA: A Blind Spot in Neuroepigenetics. *Biomolecular concepts*, 3(2):107–115.

Mannella, C. A. (2006). The relevance of mitochondrial membrane topology to mitochondrial function. *Biochimica et Biophysica Acta (BBA) - Molecular Basis of Disease*, 1762(2):140–147.

Mannella, C. A., Pfeiffer, D. R., Bradshaw, P. C., Moraru, I. I., Slepchenko, B., Loew, L. M., Hsieh, C.-e., Buttle, K., and Marko, M. (2001). Topology of the Mitochondrial Inner Membrane: Dynamics and Bioenergetic Implications. *IUBMB Life*, 52(3-5):93–100.

Marchi, S., Patergnani, S., and Pinton, P. (2014). The endoplasmic reticulum–mitochondria connection: One touch, multiple functions. *Biochimica et Biophysica Acta (BBA) - Bioenergetics*, 1837(4):461–469.

Marella, M., Seo, B. B., Thomas, B. B., Matsuno-Yagi, A., and Yagi, T. (2010). Successful Amelioration of Mitochondrial Optic Neuropathy Using the Yeast NDI1 Gene in a Rat Animal Model. *PLOS ONE*, 5(7):e11472.

Maresca, A. (2011). *Pathogenetic mechanisms in mitochondrial opticneuropathies*. PhD thesis, Università di Bologna.

Martel, C., Wang, Z., and Brenner, C. (2014). VDAC phosphorylation, a lipid sensor influencing the cell fate. *Mitochondrion*, 19, Part A:69–77.

Marthandan, S., Baumgart, M., Priebe, S., Groth, M., Schaer, J., Kaether, C., Guthke, R., Cellerino, A., Platzer, M., Diekmann, S., and Hemmerich, P. (2016). Conserved Senescence Associated Genes and Pathways in Primary Human Fibroblasts Detected by RNA-Seq. *PLOS ONE*, 11(5):e0154531.

Masland, R. H. (2001). Neuronal diversity in the retina. *Current Opinion in Neurobiology*, 11(4):431–436.

Matilainen, O., Quirós, P. M., and Auwerx, J. (2017). Mitochondria and Epigenetics – Crosstalk in Homeostasis and Stress. *Trends in Cell Biology*, 27(6):453–463.

Matsuura, K., Canfield, K., Feng, W., and Kurokawa, M. (2016). Chapter Two - Metabolic Regulation of Apoptosis in Cancer. In Jeon, K. W., Galluzzi, L. B. T. I. R. o. C., and Biology, M., editors, *International Review of Cell and Molecular Biology*, volume 327, pages 43–87. Academic Press.

May, C. A. and Lütjen-Drecoll, E. (2002). Morphology of the Murine Optic Nerve. *Investigative Ophthalmology & Visual Science*, 43(7):2206–2212.

McCommis, K. S. and Baines, C. P. (2012). The role of VDAC in cell death: Friend or foe? *Biochimica et Biophysica Acta (BBA) - Biomembranes*, 1818(6):1444–1450.

McCommis, K. S. and Finck, B. N. (2015). Mitochondrial pyruvate transport: a historical perspective and future research directions. *The Biochemical journal*, 466(3):443–454.

McEntyre, J. (1998). Linking up with entrez. *Trends in Genetics*, 14(1):39–40.

McLelland, G.-L., Goiran, T., Yi, W., Dorval, G., Chen, C. X., Lauinger, N. D., Krahn, A. I., Valimehr, S., Rakovic, A., Rouiller, I., Durcan, T. M., Trempe, J.-F., and Fon, E. A. (2018). Mfn2 ubiquitination by PINK1/parkin gates the p97-dependent release of ER from mitochondria to drive mitophagy. *eLife*, 7:e32866.

Menshikova, E. V., Ritov, V. B., Fairfull, L., Ferrell, R. E., Kelley, D. E., and Goodpaster, B. H. (2006). Effects of exercise on mitochondrial content and function in aging human skeletal muscle. *The journals of gerontology. Series A, Biological sciences and medical sciences*, 61(6):534–540.

Meyerson, C., Van Stavern, G., and McClelland, C. (2015). Leber hereditary optic neuropathy: current perspectives. *Clinical ophthalmology (Auckland, N.Z.)*, 9:1165–1176.

Mi, H., Muruganujan, A., Ebert, D., Huang, X., and Thomas, P. D. (2018). PANTHER version 14: more genomes, a new PANTHER GO-slim and improvements in enrichment analysis tools. *Nucleic Acids Research*, 47(D1):D419–D426.

Mi, H. and Thomas, P. (2009). PANTHER Pathway: An Ontology-Based Pathway Database Coupled with Data Analysis Tools BT - Protein Networks and Pathway Analysis. *Methods Mol Biol*, pages 123–140.

Millis, A. J. T. and Pious, D. A. (1973). Oxidative phosphorylation in mitochondria isolated from human fibroblasts. *Biochimica et Biophysica Acta (BBA) - Bioenergetics*, 292(1):73–77.

Mimaki, M., Ikota, A., Sato, A., Komaki, H., Akanuma, J., Nonaka, I., and Goto, Y. (2003). A double mutation (G11778A and G12192A) in mitochondrial DNA associated with Leber's hereditary optic neuropathy and cardiomyopathy. *Journal of Human Genetics*, 48(1):47–50.

Mimaki, M., Wang, X., McKenzie, M., Thorburn, D. R., and Ryan, M. T. (2012). Understanding mitochondrial complex I assembly in health and disease. *Biochimica et Biophysica Acta (BBA) - Bioenergetics*, 1817(6):851–862.

Mizushima, N., Levine, B., Cuervo, A. M., and Klionsky, D. J. (2008). Autophagy fights disease through cellular self-digestion. *Nature*, 451(7182):1069–1075.

Mohajeri, M., Martín-Jiménez, C., Barreto, G. E., and Sahebkar, A. (2019). Effects of estrogens and androgens on mitochondria under normal and pathological conditions. *Progress in Neurobiology*, 176:54–72.

Monick, M. M., Beach, S. R. H., Plume, J., Sears, R., Gerrard, M., Brody, G. H., and Philibert, R. A. (2012). Coordinated Changes in AHRR Methylation in Lymphoblasts and Pulmonary Macrophages from Smokers. *American Journal of Medical Genetics*, 159B(2):141–151.

Mootha, V. K., Lindgren, C. M., Eriksson, K.-F., Subramanian, A., Sihag, S., Lehar, J., Puigserver, P., Carlsson, E., Ridderstrale, M., Laurila, E., Houstis, N., Daly, M. J., Patterson, N., Mesirov, J. P., Golub, T. R., Tamayo, P., Spiegelman, B., Lander, E. S., Hirschhorn, J. N., Altshuler, D., and Groop, L. C. (2003). PGC-1[alpha]-responsive genes involved in oxidative phosphorylation are coordinately downregulated in human diabetes. *Nat Genet*, 34(3):267–273.

Morgia, C. L., Achilli, A., Iommarini, L., Barboni, P., Pala, M., Olivieri, A., Zanna, C., Vidoni, S., Tonon, C., Lodi, R., Vetrugno, R., Mostacci, B., Liguori, R., Carroccia, R., Montagna, P., Rugolo, M., Torroni, A., and Carelli, V. (2008). Rare mtDNA variants in Leber hereditary optic neuropathy families with recurrence of myoclonus. *Neurology*, 70(10):762 LP – 770.

Morris, B. and Votruba, M. (2012). Leber's optic neuropathy – visual return on alcohol cessation. *Acta Ophthalmologica*, 90(7):e568–e568.

Morris, T. J. and Beck, S. (2015). Analysis pipelines and packages for Infinium HumanMethylation450 BeadChip (450k) data. *Methods*, 72:3–8.

Mossman, J. A., Ge, J. Y., Navarro, F., and Rand, D. M. (2019). Mitochondrial DNA Fitness Depends on Nuclear Genetic Background in Drosophila. *G3: Genes | Genomes | Genetics*, 9(4):1175 LP – 1188.

Muñoz-Pinedo, C., Guío-Carrión, A., Goldstein, J. C., Fitzgerald, P., Newmeyer, D. D., and Green, D. R. (2006). Different mitochondrial intermembrane space proteins are released during apoptosis in a manner that is coordinately initiated but can vary in duration. *Proceedings of the National Academy of Sciences of the United States of America*, 103(31):11573–11578.

National Institutes of Health (2020). ClinicalTrials.gov.

National Institutes of Health (NIH) (2020). Genetic Testing Registry.

National Library of Medicine (US) (2019). Familial exudative vitreoretinopathy.

Nechushtan, A., Smith, C. L., Lamensdorf, I., Yoon, S. H., and Youle, R. J. (2001). Bax and Bak coalesce into novel mitochondria-associated clusters during apoptosis. *The Journal of cell biology*, 153(6):1265–1276.

Neumann, S., Hüser, L., Ondreka, K., Auler, N., and Haverkamp, S. (2016). Cell type-specific bipolar cell input to ganglion cells in the mouse retina. *Neuroscience*, 316:420–432.

Neuspiel, M., Zunino, R., Gangaraju, S., Rippstein, P., and McBride, H. (2005). Activated Mitofusin 2 Signals Mitochondrial Fusion, Interferes with Bax Activation, and Reduces Susceptibility to Radical Induced Depolarization. *Journal of Biological Chemistry*, 280(26):25060–25070.

Newman, N. J. (2009). Leber hereditary optic neuropathy: bad habits, bad vision? *Brain : a journal of neurology*, 132(Pt 9):2306–2308.

Nicholls, T. J. and Minczuk, M. (2014). In D-loop: 40years of mitochondrial 7S DNA. *Experimental Gerontology*, 56:175–181.

Nickla, D. L. and Wallman, J. (2010). The Multifunctional Choroid. *Progress in Retinal and Eye Research*, 29(2):144–168.

Nieves-Moreno, M., Martínez-de-la Casa, J. M., Morales-Fernández, L., Sánchez-Jean, R., Sáenz-Francés, F., and García-Feijoó, J. (2018). Impacts of age and sex on retinal layer thicknesses measured by spectral domain optical coherence tomography with Spectralis. *PloS one*, 13(3):e0194169–e0194169.

Nikoskelainen, E. K., Marttila, R. J., Huoponen, K., Juvonen, V., Lamminen, T., Sonninen, P., and Savontaus, M. L. (1995). Leber's "plus": neurological abnormalities in patients with Leber's hereditary optic neuropathy. *Journal of Neurology, Neurosurgery & Psychiatry*, 59(2):160 LP – 164.

Nilsson, E. E., Sadler-Riggleman, I., and Skinner, M. K. (2018). Environmentally induced epigenetic transgenerational inheritance of disease. *Environmental Epigenetics*, 4(2).

Nino, C. L., Perez, G. F., Isaza, N., Gutierrez, M. J., Gomez, J. L., and Nino, G. (2018). Characterization of Sex-Based Dna Methylation Signatures in the Airways During Early Life. *Scientific reports*, 8(1):5526.

Niyazov, D. M., Kahler, S. G., and Frye, R. E. (2016). Primary Mitochondrial Disease and Secondary Mitochondrial Dysfunction: Importance of Distinction for Diagnosis and Treatment. *Molecular syndromology*, 7(3):122–137.

Noack, H., Bednarek, T., Heidler, J., Ladig, R., Holtz, J., and Szibor, M. (2006). TFAM-dependent and independent dynamics of mtDNA levels in C2C12 myoblasts caused by redox stress. *Biochimica et Biophysica Acta (BBA) - General Subjects*, 1760(2):141–150.

NuEyes (2019). NuEyes.

Ogata, M., Hino, S.-i., Saito, A., Morikawa, K., Kondo, S., Kanemoto, S., Murakami, T., Taniguchi, M., Tanii, I., Yoshinaga, K., Shiosaka, S., Hammarback, J. A., Urano, F., and Imaizumi, K. (2006). Autophagy is activated for cell survival after endoplasmic reticulum stress. *Molecular and cellular biology*, 26(24):9220–9231.

Okie, J. G., Smith, V. H., and Martin-Cereceda, M. (2016). Major evolutionary transitions of life, metabolic scaling and the number and size of mitochondria and chloroplasts. *Proceedings. Biological sciences*, 283(1831):20160611.

O'Leary, N. A., Wright, M. W., Brister, J. R., Ciufo, S., Haddad, D., McVeigh, R., Rajput, B., Robbertse, B., Smith-White, B., Ako-Adjei, D., Astashyn, A., Badretdin, A., Bao, Y., Blinkova, O., Brover, V., Chetvernin, V., Choi, J., Cox, E., Ermolaeva, O., Farrell, C. M., Goldfarb, T., Gupta, T., Haft, D., Hatcher, E., Hlavina, W., Joardar, V. S., Kodali, V. K., Li, W., Maglott, D., Masterson, P., McGarvey, K. M., Murphy, M. R., O'Neill, K., Pujar, S., Rangwala, S. H., Rausch, D., Riddick, L. D., Schoch, C., Shkeda, A., Storz, S. S., Sun, H., Thibaud-Nissen, F., Tolstoy, I., Tully, R. E., Vatsan, A. R., Wallin, C., Webb, D., Wu, W., Landrum, M. J., Kimchi, A., Tatusova, T., DiCuccio, M., Kitts, P., Murphy, T. D., and Pruitt, K. D. (2016). Reference sequence (RefSeq) database at NCBI: current status, taxonomic expansion, and functional annotation. *Nucleic acids research*, 44(D1):D733–D745.

Oostra, R. J., Bolhuis, P. A., Wijburg, F. A., Zorn-Ende, G., and Bleeker-Wagemakers, E. M. (1994). Leber's hereditary optic neuropathy: correlations between mitochondrial genotype and visual outcome. *Journal of Medical Genetics*, 31(4):280 LP – 286.

Orssaud, C. (2018). Cardiac Disorders in Patients With Leber Hereditary Optic Neuropathy. *Journal of Neuro-Ophthalmology*, 38(4):466–469.

Osborne, A., Khatib, T. Z., Songra, L., Barber, A. C., Hall, K., Kong, G. Y. X., Widdowson, P. S., and Martin, K. R. (2018). Neuroprotection of retinal ganglion cells by a novel gene therapy construct that achieves sustained enhancement of brain-derived neurotrophic factor/tropomyosin-related kinase receptor-B signaling. *Cell Death & Disease*, 9(10):1007.

Osellame, L. D., Blacker, T. S., and Duchen, M. R. (2012). Cellular and molecular mechanisms of mitochondrial function. *Best Practice & Research. Clinical Endocrinology & Metabolism*, 26(6):711–723.

Otera, H., Wang, C., Cleland, M. M., Setoguchi, K., Yokota, S., Youle, R. J., and Mihara, K. (2010). Mff is an essential factor for mitochondrial recruitment of Drp1 during mitochondrial fission in mammalian cells. *The Journal of Cell Biology*, 191(6):1141 LP – 1158.

Ott, M., Gogvadze, V., Orrenius, S., and Zhivotovsky, B. (2007). Mitochondria, oxidative stress and cell death. *Apoptosis*, 12(5):913–922.

Pacheu-Grau, D., Rucktäschel, R., and Deckers, M. (2018). Mitochondrial dysfunction and its role in tissue-specific cellular stress. *Cell stress*, 2(8):184–199.

Pagliarini, D. J., Calvo, S. E., Chang, B., Sheth, S. A., Vafai, S. B., Ong, S.-E., Walford, G. A., Sugiana, C., Boneh, A., Chen, W. K., Hill, D. E., Vidal, M., Evans, J. G., Thorburn, D. R., Carr, S. A., and Mootha, V. K. (2008). A mitochondrial protein compendium elucidates complex I disease biology. *Cell*, 134(1):112–123.

Pala, M., Olivieri, A., Achilli, A., Accetturo, M., Metspalu, E., Reidla, M., Tamm, E., Karmin, M., Reisberg, T., Hooshiar Kashani, B., Perego, U. A., Carossa, V., Gandini, F., Pereira, J. B., Soares, P., Angerhofer, N., Rychkov, S., Al-Zahery, N., Carelli, V., Sanati, M. H., Houshmand, M., Hatina, J., Macaulay, V., Pereira, L., Woodward, S. R., Davies, W., Gamble, C., Baird, D., Semino, O., Villems, R., Torroni, A., and Richards, M. B. (2012). Mitochondrial DNA signals of late glacial recolonization of Europe from near eastern refugia. *American journal of human genetics*, 90(5):915–924.

Panning, B. (2008). X-chromosome inactivation: the molecular basis of silencing. *Journal of Biology*, 7(8):30.

Pasquali-Ronchetti, I., Greenawalt, J. W., and Carafoli, E. (1969). On the nature of the dense matrix granules of normal mitochondria. *The Journal of cell biology*, 40(2):565–568.

Patterson, M. C. and Percy, A. K. (2015). Chapter 19 - Peripheral Neuropathy in Inherited Metabolic Disease. In Darras, B. T., Jones, H. R., Ryan, M. M., and De Vivo Childhood, and Adolescence (Second Edition), D. C. B. T. N. D. o. I., editors, *Neuromuscular Disorders of Infancy, Childhood, and Adolescence*, pages 353–378. Academic Press, San Diego, second edn edition.

Pavlidis, M., Stupp, T., and Hummeke, M. (2006). Morphometric examination of human and monkey retinal ganglion cells within the papillomacular area. *Retina*, 26(4):445–453.

Pedram, A., Razandi, M., Wallace, D. C., and Levin, E. R. (2006). Functional estrogen receptors in the mitochondria of breast cancer cells. *Molecular biology of the cell*, 17(5):2125–2137.

Pemp, B., Kircher, K., and Reitner, A. (2019). Visual function in chronic Leber's hereditary optic neuropathy during idebenone treatment initiated 5 to 50 years after onset. *Graefe's Archive for Clinical and Experimental Ophthalmology*, 257(12):2751–2757.

Perfettini, J.-L., Roumier, T., and Kroemer, G. (2005). Mitochondrial fusion and fission in the control of apoptosis. *Trends in Cell Biology*, 15(4):179–183.

Perry, S. W., Norman, J. P., Barbieri, J., Brown, E. B., and Gelbard, H. A. (2011). Mitochondrial membrane potential probes and the proton gradient: a practical usage guide. *BioTechniques*, 50(2):98–115.

Pfeffer, G., Burke, A., Yu-Wai-Man, P., Compston, D. A. S., and Chinnery, P. F. (2013). Clinical features of MS associated with Leber hereditary optic neuropathy mtDNA mutations. *Neurology*, 81(24):2073–2081.

Pfeffer, S., Woellhaf, M. W., Herrmann, J. M., and Förster, F. (2015). Organization of the mitochondrial translation machinery studied in situ by cryoelectron tomography. *Nature Communications*, 6:6019.

Phasukkijwatana, N., Kunhapan, B., Stankovich, J., Chuenkongkaew, W. L., Thomson, R., Thornton, T., Bahlo, M., Mushiroda, T., Nakamura, Y., Mahasirimongkol, S., Tun, A. W., Srisawat, C., Limwongse, C., Peerapittayamongkol, C., Sura, T., Suthammarak, W., and Lertrit, P. (2010). Genome-wide linkage scan and association study of PARL to the expression of LHON families in Thailand. *Human Genetics*, 128(1):39–49.

Phillips, N. R., Sprouse, M. L., and Roby, R. K. (2014). Simultaneous quantification of mitochondrial DNA copy number and deletion ratio: A multiplex real-time PCR assay. *Scientific Reports*, 4:3887.

Pickard, G. E. and Sollars, P. J. (2012). Intrinsically Photosensitive Retinal Ganglion Cells. In Nilius, B., Amara, G. S., Gudermann, T., Jahn, R., Lill, R., Offermanns, S., and Petersen, H. O., editors, *Reviews of Physiology, Biochemistry and Pharmacology: Volume 162*, pages 59–90. Springer Berlin Heidelberg, Berlin, Heidelberg.

Pinelli, M., Carissimo, A., Cutillo, L., Lai, C.-H., Mutarelli, M., Moretti, M. N., Singh, M. V., Karali, M., Carrella, D., Pizzo, M., Russo, F., Ferrari, S., Ponzin, D., Angelini, C., Banfi, S., and di Bernardo, D. (2016). An atlas of gene expression and gene co-regulation in the human retina. *Nucleic Acids Research*, 44(12):5773–5784.

Pinto, M. and Moraes, C. T. (2014). Mitochondrial genome changes and neurodegenerative diseases. *Biochimica et Biophysica Acta (BBA) - Molecular Basis of Disease*, 1842(8):1198–1207.

Pisano, A., Preziuso, C., Iommarini, L., Perli, E., Grazioli, P., Campese, A. F., Maresca, A., Montopoli, M., Masuelli, L., Sadun, A. A., D'Amati, G., Carelli, V., Ghelli, A., and Giordano, C. (2015). Targeting estrogen receptor β as preventive therapeutic strategy for Leber's hereditary optic neuropathy. *Human Molecular Genetics*.

Popgeorgiev, N., Jabbour, L., and Gillet, G. (2018). Subcellular Localization and Dynamics of the Bcl-2 Family of Proteins. *Frontiers in cell and developmental biology*, 6:13.

Preibisch, S., Saalfeld, S., and Tomancak, P. (2009). Globally optimal stitching of tiled 3D microscopic image acquisitions. *Bioinformatics (Oxford, England)*, 25(11):1463–1465.

Price, E. M. and Robinson, W. P. (2018). Adjusting for Batch Effects in DNA Methylation Microarray Data, a Lesson Learned.

Puomila, A., Hamalainen, P., Kivioja, S., Savontaus, M.-L., Koivumaki, S., Huoponen, K., and Nikoskelainen, E. (2007). Epidemiology and penetrance of Leber hereditary optic neuropathy in Finland. *Eur J Hum Genet*, 15(10):1079–1089.

Purves, D., Augustine, G. J., and Fitzpatrick, D. (2001). Cones and Color Vision.

Putney, J. W. and Tomita, T. (2012). Phospholipase C signaling and calcium influx. *Advances in biological regulation*, 52(1):152–164.

Pyle, A., Anugrha, H., Kurzawa-Akanbi, M., Yarnall, A., Burn, D., and Hudson, G. (2016). Reduced mitochondrial DNA copy number is a biomarker of Parkinson's disease. *Neurobiology of Aging*, 38:216.e7–216.e10.

Qi, X., Sun, L., Lewin, A. S., Hauswirth, W. W., and Guy, J. (2007). The Mutant Human ND4 Subunit of Complex I Induces Optic Neuropathy in the Mouse. *Investigative Ophthalmology & Visual Science*, 48(1):1–10.

Qu, J., Wang, Y., Tong, Y., Zhou, X., Zhao, F., Yang, L., Zhang, S., Zhang, J., West, C. E., and Guan, M.-X. (2010). Leber's hereditary optic neuropathy affects only female matrilineal relatives in two Chinese families. *Investigative ophthalmology & visual science*, 51(10):4906–4912.

Quina, L. A., Pak, W., Lanier, J., Banwait, P., Gratwick, K., Liu, Y., Velasquez, T., O'Leary, D. D. M., Goulding, M., and Turner, E. E. (2005). Brn3a-Expressing Retinal Ganglion Cells Project Specifically to Thalamocortical and Collicular Visual Pathways. *The Journal of Neuroscience*, 25(50):11595 LP – 11604.

Ranieri, M., Brajkovic, S., Riboldi, G., Ronchi, D., Rizzo, F., Bresolin, N., Corti, S., and Comi, G. P. (2013). Mitochondrial Fusion Proteins and Human Diseases. *Neurology Research International*.

Ranieri, M., Brajkovic, S., Riboldi, G., Ronchi, D., Rizzo, F., Bresolin, N., Corti, S., and Comi, G. P. (2014). Mitochondrial Fission and Fusion in Human Diseases. *New England Journal of Medicine*, 370(11):1073–1074.

Rao, V. K., Carlson, E. A., and Yan, S. S. (2014). Mitochondrial permeability transition pore is a potential drug target for neurodegeneration. *Biochimica et Biophysica Acta (BBA) - Molecular Basis of Disease*, 1842(8):1267–1272.

Rebelo, A. P., Williams, S. L., and Moraes, C. T. (2009). In vivo methylation of mtDNA reveals the dynamics of protein–mtDNA interactions. *Nucleic Acids Research*, 37(20):6701–6715.

Riccio, A. (2010). Dynamic epigenetic regulation in neurons: enzymes, stimuli and signaling pathways. *Nature Neuroscience*, 13:1330.

Richards, M., Macaulay, V., Torroni, A., and Bandelt, H.-J. (2002). In Search of Geographical Patterns in European Mitochondrial DNA. *The American Journal of Human Genetics*, 71(5):1168–1174.

Richter, C., Park, J. W., and Ames, B. N. (1988). Normal oxidative damage to mitochondrial and nuclear DNA is extensive. *Proceedings of the National Academy of Sciences of the United States of America*, 85(17):6465–6467.

Rieusset, J. (2018). The role of endoplasmic reticulum-mitochondria contact sites in the control of glucose homeostasis: an update. *Cell Death & Disease*, 9(3):388.

Rimessi, A., Giorgi, C., Pinton, P., and Rizzuto, R. (2008). The versatility of mitochondrial calcium signals: From stimulation of cell metabolism to induction of cell death. *Biochimica et Biophysica Acta (BBA) - Bioenergetics*, 1777(7–8):808–816.

Riordan-Eva, P., Sanders, M. D., Govan, G. G., Sweeney, M. G., Costa, J. D., and Harding, A. E. (1995). The clinical features of Leber's hereditary optic neuropathy defined by the presence of a pathogenic mitochondrial DNA mutation. *Brain*, 118(2):319–337.

Rishishwar, L. and Jordan, I. K. (2017). Implications of human evolution and admixture for mitochondrial replacement therapy. *BMC genomics*, 18(1):140.

Ritchie, M. E., Phipson, B., Wu, D., Hu, Y., Law, C. W., Shi, W., and Smyth, G. K. (2015). limma powers differential expression analyses for RNA-sequencing and microarray studies. *Nucleic Acids Research*, 43(7):e47–e47.

Rizzuto, R., Marchi, S., Bonora, M., Aguiari, P., Bononi, A., De Stefani, D., Giorgi, C., Leo, S., Rimessi, A., Siviero, R., Zecchini, E., and Pinton, P. (2009). Ca(2+) transfer from the ER to mitochondria: when, how and why. *Biochimica et biophysica acta*, 1787(11):1342–1351.

Roberts, D. L., Merrison, W., MacFarlane, M., and Cohen, G. M. (2001). The inhibitor of apoptosis protein-binding domain of Smac is not essential for its proapoptotic activity. *The Journal of cell biology*, 153(1):221–228.

Rodriguez, A. R., de Sevilla Müller, L. P., and Brecha, N. C. (2014). The RNA binding protein RBPMS is a selective marker of ganglion cells in the mammalian retina. *The Journal of comparative neurology*, 522(6):1411–1443.

Rohde, M. C., Corydon, T. J., Hansen, J., Pedersen, C. B., Schmidt, S. P., Gregersen, N., and Banner, J. (2014). Characteristics of human infant primary fibroblast cultures from Achilles tendons removed post-mortem. *Forensic Science International*, 234(Supplement C):149–153.

Romano, S. N. and Gorelick, D. A. (2018). Crosstalk between nuclear and G protein-coupled estrogen receptors. *General and comparative endocrinology*, 261:190–197.

Rooney, J. P., Ryde, I. T., Sanders, L. H., Howlett, E. H., Colton, M. D., Germ, K. E., Mayer, G. D., Greenamyre, J. T., and Meyer, J. N. (2015). PCR Based Determination of Mitochondrial DNA Copy Number in Multiple Species. *Methods in molecular biology (Clifton, N.J.)*, 1241:23–38.

Roostalu, U., Kutuev, I., Loogväli, E.-L., Metspalu, E., Tambets, K., Reidla, M., Khusnutdinova, E. K., Usanga, E., Kivisild, T., and Villems, R. (2006). Origin and Expansion of Haplogroup H, the Dominant Human Mitochondrial DNA Lineage in West Eurasia: The Near Eastern and Caucasian Perspective. *Molecular Biology and Evolution*, 24(2):436–448.

Rosenberg, T., Nørby, S., Schwartz, M., Saillard, J., Magalhães, P. J., Leroy, D., Kann, E. C., and Duno, M. (2016). Prevalence and Genetics of Leber Hereditary Optic Neuropathy in the Danish Population Prevalence and Genetics of LHON. *Investigative Ophthalmology & Visual Science*, 57(3):1370–1375.

Rossi, E. A., Chung, M., Dubra, A., Hunter, J. J., Merigan, W. H., and Williams, D. R. (2011). Imaging retinal mosaics in the living eye. *Eye*, 25(3):301–308.

Rossignol, R., Faustin, B., Rocher, C., Malgat, M., Mazat, J.-P., and Letellier, T. (2003). Mitochondrial threshold effects. *The Biochemical journal*, 370(Pt 3):751–762.

Roussel, B. D., Kruppa, A. J., Miranda, E., Crowther, D. C., Lomas, D. A., and Marciniak, S. J. (2013). Endoplasmic reticulum dysfunction in neurological disease. *The Lancet Neurology*, 12(1):105–118.

Rozpedek, W., Pytel, D., Mucha, B., Leszczynska, H., Diehl, J. A., and Majsterek, I. (2016). The Role of the PERK/eIF2α/ATF4/CHOP Signaling Pathway in Tumor Progression During Endoplasmic Reticulum Stress. *Current molecular medicine*, 16(6):533–544.

Ryter, S. W., Kim, H. P., Hoetzel, A., Park, J. W., Nakahira, K., Wang, X., and Choi, A. M. K. (2006). Mechanisms of Cell Death in Oxidative Stress. *Antioxidants & Redox Signaling*, 9(1):49–89.

Sabbah, H. N., Gupta, R. C., Kohli, S., Wang, M., Hachem, S., and Zhang, K. (2016). Chronic Therapy With Elamipretide (MTP-131), a Novel Mitochondria-Targeting Peptide, Improves Left Ventricular and Mitochondrial Function in Dogs With Advanced Heart Failure. *Circulation. Heart failure*, 9(2):e002206–e002206.

Sadakierska-Chudy, A., Frankowska, M., and Filip, M. (2014). Mitoepigenetics and drug addiction. *Pharmacology & Therapeutics*, 144(2):226–233.

Sadun, A. and Kim, A. (2010). Chapter 43 - Leber's hereditary optic neuropathy. In Levin, L. A. and Albert, D. M. B. T. O. D., editors, *Ocular Disease*, pages 330–336. W.B. Saunders, Edinburgh.

Sadun, A. A., Carelli, V., Salomao, S. R., Berezovsky, A., Quiros, P. A., Sadun, F., DeNegri, A.-M., Andrade, R., Moraes, M., Passos, A., Kjaer, P., Pereira, J., Valentino, M. L., Schein, S., and Belfort, R. (2003). Extensive investigation of a large Brazilian pedigree of 11778/haplogroup J Leber hereditary optic neuropathy. *American Journal of Ophthalmology*, 136(2):231–238.

Sadun, A. A., Chicani, C., Ross-Cisneros, F. N., Barboni, P., Thoolen, M., Shrader, W., Kubis, K., Carelli, V., and Miller, G. (2012). EFfect of epi-743 on the clinical course of the mitochondrial disease leber hereditary optic neuropathy. *Archives of Neurology*, 69(3):331–338.

Sadun, A. A., Win, P. H., Ross-Cisneros, F. N., Walker, S. O., and Carelli, V. (2000). Leber's hereditary optic neuropathy differentially affects smaller axons in the optic nerve. *Transactions of the American Ophthalmological Society*, 98:223–235.

Sanchez, R. N., Smith, A. J., Carelli, V., Sadun, A. A., and Keltner, J. L. (2006). Leber Hereditary Optic Neuropathy Possibly Triggered by Exposure to Tire Fire. *Journal of Neuro-Ophthalmology*, 26(4):268–272.

Schenkel, L. C. and Bakovic, M. (2014). Formation and regulation of mitochondrial membranes. *International journal of cell biology*, 2014:709828.

Schindelin, J., Arganda-Carreras, I., Frise, E., Kaynig, V., Longair, M., Pietzsch, T., Preibisch, S., Rueden, C., Saalfeld, S., Schmid, B., Tinevez, J.-Y., White, D. J., Hartenstein, V., Eliceiri, K., Tomancak, P., and Cardona, A. (2012). Fiji: an open-source platform for biological-image analysis. *Nat Meth*, 9(7):676–682.

Schneider, V. A., Graves-Lindsay, T., Howe, K., Bouk, N., Chen, H.-C., Kitts, P. A., Murphy, T. D., Pruitt, K. D., Thibaud-Nissen, F., Albracht, D., Fulton, R. S., Kremitzki,

M., Magrini, V., Markovic, C., McGrath, S., Steinberg, K. M., Auger, K., Chow, W., Collins, J., Harden, G., Hubbard, T., Pelan, S., Simpson, J. T., Threadgold, G., Torrance, J., Wood, J., Clarke, L., Koren, S., Boitano, M., Li, H., Chin, C.-S., Phillippy, A. M., Durbin, R., Wilson, R. K., Flicek, P., and Church, D. M. (2016). Evaluation of GRCh38 and de novo haploid genome assemblies demonstrates the enduring quality of the reference assembly. *bioRxiv*, page 72116.

Scottish Medicines Consortium (2017). Idebenone (Raxone).

Seahorse Bioscience (2015). XF Cell Mito Stress Test Profile.

Shamas-Din, A., Brahmbhatt, H., Leber, B., and Andrews, D. W. (2011). BH3-only proteins: Orchestrators of apoptosis. *Biochimica et Biophysica Acta (BBA) - Molecular Cell Research*, 1813(4):508–520.

Shamas-Din, A., Kale, J., Leber, B., and Andrews, D. W. (2013). Mechanisms of action of Bcl-2 family proteins. *Cold Spring Harbor perspectives in biology*, 5(4):a008714–a008714.

Shankar, S. P., Fingert, J. H., Carelli, V., Valentino, M. L., King, T. M., Daiger, S. P., Salomao, S. R., Berezovsky, A., Belfort, R., Braun, T. A., Sheffield, V. C., Sadun, A. A., and Stone, E. M. (2008). Evidence for a Novel X-Linked Modifier Locus for Leber Hereditary Optic Neuropathy. *Ophthalmic Genetics*, 29(1):17–24.

Sharma, L. K., Tiwari, M., Rai, N. K., and Bai, Y. (2018). Mitophagy activation repairs Leber's hereditary optic neuropathy-associated mitochondrial dysfunction and improves cell survival. *Human Molecular Genetics*, 28(3):422–433.

Sherry, S. T., Ward, M.-H., Kholodov, M., Baker, J., Phan, L., Smigielski, E. M., and Sirotkin, K. (2001). dbSNP: the NCBI database of genetic variation. *Nucleic Acids Research*, 29(1):308–311.

Shock, L. S., Thakkar, P. V., Peterson, E. J., Moran, R. G., and Taylor, S. M. (2011). DNA methyltransferase 1, cytosine methylation, and cytosine hydroxymethylation in mammalian mitochondria. *Proceedings of the National Academy of Sciences*, 108(9):3630–3635.

Shvetsova, E., Sofronova, A., Monajemi, R., Gagalova, K., Draisma, H. H. M., White, S. J., Santen, G. W. E., Chuva de Sousa Lopes, S. M., Heijmans, B. T., van Meurs, J., Jansen, R., Franke, L., Kiełbasa, S. M., den Dunnen, J. T., 't Hoen, P. A. C., Heijmans, B. T., 't Hoen, P. A. C., van Meurs, J., Boomsma, D. I., Pool, R., van Dongen, J., Hottenga, J. J., van Greevenbroek, M. M. J., Stehouwer, C. D. A., van der Kallen, C. J. H., Schalkwijk, C. G., Wijmenga, C., Zhernakova, S., Tigchelaar, E. F., Slagboom, P. E., Beekman, M., Deelen, J., van Heemst, D., Veldink, J. H., van den Berg, L. H., van Duijn, C. M., Hofman, B. A., Uitterlinden, A. G., Jhamai, P. M., Verbiest, M., Suchiman, H. E. D., Verkerk, M., van der Breggen, R., van Rooij, J., Lakenberg, N.,

Mei, H., Bot, J., Zhernakova, D. V., van 't Hof, P., Deelen, P., Nooren, I., Moed, M., Vermaat, M., Luijk, R., Jan Bonder, M., van Iterson, M., van Dijk, F., van Galen, M., Arindrarto, W., Kiełbasa, S. M., Swertz, M. A., van Zwet, E. W., Isaacs, A., Jansen, R., Franke, L., Francioli, L. C., Menelaou, A., Pulit, S. L., van Dijk, F., Palamara, P. F., Elbers, C. C., Neerincx, P. B., Ye, K., Guryev, V., Kloosterman, W. P., Deelen, P., Abdellaoui, A., van Leeuwen, E. M., van Oven, M., Vermaat, M., Li, M., Laros, J. F., Karssen, L. C., Kanterakis, A., Amin, N., Hottenga, J. J., Lameijer, E. W., Kattenberg, M., Dijkstra, M., Byelas, H., van Setten, J., van Schaik, B. D., Bot, J., Nijman, I. J., Renkens, I., Marschall, T., Schönhuth, A., Hehir-Kwa, J. Y., Handsaker, R. E., Polak, P., Sohail, M., Vuzman, D., Hormozdiari, F., van Enckevort, D., Mei, H., Koval, V., Moed, M. H., van der Velde, K. J., Rivadeneira, F., Estrada, K., Medina-Gomez, C., Isaacs, A., McCarroll, S. A., Beekman, M., de Craen, A. J., Suchiman, H. E., Hofman, B. A., Oostra, B., Uitterlinden, A. G., Willemsen, G., Platteel, M., Veldink, J. H., van den Berg, L. H., Pitts, S. J., Potluri, S., Sundar, P., Cox, D. R., Sunyaev, S. R., den Dunnen, J. T., Stoneking, M., de Knijff, P., Kayser, M., Li, Q., Li, Y., Du, Y., Chen, R., Cao, H., Li, N., Cao, S., Wang, J., Bovenberg, J. A., Pe'er, I., Slagboom, P. E., van Duijn, C. M., Boomsma, D. I., van Ommen, G. J., de Bakker, P. I., Swertz, M. A., Wijmenga, C., Consortium, B., and Consortium, G. (2019). Skewed X-inactivation is common in the general female population. *European Journal of Human Genetics*, 27(3):455–465.

Signes, A. and Fernandez-Vizarra, E. (2018). Assembly of mammalian oxidative phosphorylation complexes I–V and supercomplexes. *Essays In Biochemistry*, 62(3):255 LP – 270.

Singapore Bioethics Advisory Committee (2018). Public Consultation on Ethical, Legal and Social Issues Arising from Mitochondrial Genome Replacement Technology. *Bioethics Advisory Committee Press Releases*.

Singh, M. S., Park, S. S., Albini, T. A., Canto-Soler, M. V., Klassen, H., MacLaren, R. E., Takahashi, M., Nagiel, A., Schwartz, S. D., and Bharti, K. (2019). Retinal stem cell transplantation: Balancing safety and potential. *Progress in Retinal and Eye Research*, page 100779.

Singmann, P., Shem-Tov, D., Wahl, S., Grallert, H., Fiorito, G., Shin, S.-Y., Schramm, K., Wolf, P., Kunze, S., Baran, Y., Guarrera, S., Vineis, P., Krogh, V., Panico, S., Tumino, R., Kretschmer, A., Gieger, C., Peters, A., Prokisch, H., Relton, C. L., Matullo, G., Illig, T., Waldenberger, M., and Halperin, E. (2015). Characterization of whole-genome autosomal differences of DNA methylation between men and women. *Epigenetics & Chromatin*, 8(1):43.

Sinicrope, F. A., Rego, R. L., Okumura, K., Foster, N. R., O'Connell, M. J., Sargent, D. J., and Windschitl, H. E. (2008). Prognostic impact of bim, puma, and noxa expression

in human colon carcinomas. *Clinical cancer research : an official journal of the American Association for Cancer Research*, 14(18):5810–5818.

Smolková, K. and Ježek, P. (2012). The Role of Mitochondrial NADPH-Dependent Isocitrate Dehydrogenase in Cancer Cells. *International journal of cell biology*, 2012:273947.

Soares, P., Alshamali, F., Pereira, J. B., Fernandes, V., Silva, N. M., Afonso, C., Costa, M. D., Musilová, E., Macaulay, V., Richards, M. B., Černý, V., and Pereira, L. (2011). The Expansion of mtDNA Haplogroup L3 within and out of Africa. *Molecular Biology and Evolution*, 29(3):915–927.

Sokol, A. M., Sztolsztener, M. E., Wasilewski, M., Heinz, E., and Chacinska, A. (2014). Mitochondrial protein translocases for survival and wellbeing. *FEBS Letters*, 588(15):2484–2495.

Song, K. (2012). Diagram of a typical animal cell.

Song, K. (2013). Diagrammatic structural features of a mitochondrion.

Spinazzola, A. and Zeviani, M. (2009). Mitochondrial Diseases: A Cross-Talk Between Mitochondrial and Nuclear Genomes BT - Inherited Neuromuscular Diseases: Translation from Pathomechanisms to Therapies. *Adv Exp Med Biol*, pages 69–84.

Stealth BioTherapeutics Inc. (2019). A Study Investigating the Safety, Tolerability, and Efficacy of MTP-131 Topical Ophthalmic Solution for the Treatment of Leber's Hereditary Optic Neuropathy.

Stelzer, G., Rosen, N., Plaschkes, I., Zimmerman, S., Twik, M., Fishilevich, S., Stein, T. I., Nudel, R., Lieder, I., Mazor, Y., Kaplan, S., Dahary, D., Warshawsky, D., Guan-Golan, Y., Kohn, A., Rappaport, N., Safran, M., and Lancet, D. (2016). The GeneCards Suite: From Gene Data Mining to Disease Genome Sequence Analyses. *Current Protocols in Bioinformatics*, 54(1):1.30.1–1.30.33.

Strauss, K. A., DuBiner, L., Simon, M., Zaragoza, M., Sengupta, P. P., Li, P., Narula, N., Dreike, S., Platt, J., Procaccio, V., Ortiz-González, X. R., Puffenberger, E. G., Kelley, R. I., Morton, D. H., Narula, J., and Wallace, D. C. (2013). Severity of cardiomyopathy associated with adenine nucleotide translocator-1 deficiency correlates with mtDNA haplogroup. *Proceedings of the National Academy of Sciences*, 110(9):3453 LP – 3458.

Strauss, O. (2005). The Retinal Pigment Epithelium in Visual Function. *Physiological Reviews*, 85(3):845–881.

Subramanian, A., Tamayo, P., Mootha, V. K., Mukherjee, S., Ebert, B. L., Gillette, M. A., Paulovich, A., Pomeroy, S. L., Golub, T. R., Lander, E. S., and Mesirov, J. P. (2005). Gene set enrichment analysis: A knowledge-based approach for interpreting genome-wide

expression profiles. *Proceedings of the National Academy of Sciences*, 102(43):15545–15550.

Sudoyo, H., Suryadi, H., Lertrit, P., Pramoonjago, P., Lyrawati, D., and Marzuki, S. (2002). Asian-specific mtDNA backgrounds associated with the primary G11778A mutation of Leber's hereditary optic neuropathy. *Journal of Human Genetics*, 47(11):594–604.

Suen, D.-F., Norris, K. L., and Youle, R. J. (2008). Mitochondrial dynamics and apoptosis. *Genes & development*, 22(12):1577–1590.

Suthammarak, W., Yang, Y.-Y., Morgan, P. G., and Sedensky, M. M. (2009). Complex I function is defective in complex IV-deficient Caenorhabditis elegans. *The Journal of biological chemistry*, 284(10):6425–6435.

Szabadkai, G., Bianchi, K., Várnai, P., De Stefani, D., Wieckowski, M. R., Cavagna, D., Nagy, A. I., Balla, T., and Rizzuto, R. (2006). Chaperone-mediated coupling of endoplasmic reticulum and mitochondrial Ca2+ channels. *The Journal of cell biology*, 175(6):901–911.

Szegezdi, E., Logue, S. E., Gorman, A. M., and Samali, A. (2006). Mediators of endoplasmic reticulum stress-induced apoptosis. *EMBO reports*, 7(9):880–885.

Taanman, J.-W. (1999). The mitochondrial genome: structure, transcription, translation and replication. *Biochimica et Biophysica Acta (BBA) - Bioenergetics*, 1410(2):103–123.

Tabas, I. and Ron, D. (2011). Integrating the mechanisms of apoptosis induced by endoplasmic reticulum stress. *Nature cell biology*, 13(3):184–190.

Tachibana, M., Sparman, M., Sritanaudomchai, H., Ma, H., Clepper, L., Woodward, J., Li, Y., Ramsey, C., Kolotushkina, O., and Mitalipov, S. (2009). Mitochondrial gene replacement in primate offspring and embryonic stem cells. *Nature*, 461:367.

Tait, S. W. G. and Green, D. R. (2010). Mitochondria and cell death: outer membrane permeabilization and beyond. *Nature Reviews Molecular Cell Biology*, 11:621.

Takashima, A. (2001). Establishment of Fibroblast Cultures. In *Current Protocols in Cell Biology*. John Wiley & Sons, Inc.

Talhout, R., Schulz, T., Florek, E., van Benthem, J., Wester, P., and Opperhuizen, A. (2011). Hazardous compounds in tobacco smoke. *International journal of environmental research and public health*, 8(2):613–628.

Tan, W. and Colombini, M. (2007). VDAC closure increases calcium ion flux. *Biochimica et biophysica acta*, 1768(10):2510–2515.

Taylor, R. W., Jobling, M. S., Turnbull, D. M., and Chinnery, P. F. (2003). Frequency of rare mitochondrial DNA mutations in patients with suspected Leber's hereditary optic neuropathy. *Journal of Medical Genetics*, 40(7):e85.

The European DNA Profiling Group, Gruppo Ematologi Forensi Italiani, and Grupo Español y Portugués de la ISFG (2016). EMPOP Mitochondrial DNA Population Database.

The Japan Times (2019). Osaka University team conducts world's first iPS transplant for corneal disease.

Thompson, B. (1988). Misuse of chi-square contingency-table test statistics.

Thuerauf, D. J., Marcinko, M., Belmont, P. J., and Glembotski, C. C. (2007). Effects of the Isoform-specific Characteristics of ATF6α and ATF6β on Endoplasmic Reticulum Stress Response Gene Expression and Cell Viability. *Journal of Biological Chemistry*, 282(31):22865–22878.

Torroni, A., Petrozzi, M., D'Urbano, L., Sellitto, D., Zeviani, M., Carrara, F., Carducci, C., Leuzzi, V., Carelli, V., Barboni, P., De Negri, A., and Scozzari, R. (1997). Haplotype and phylogenetic analyses suggest that one European-specific mtDNA background plays a role in the expression of Leber hereditary optic neuropathy by increasing the penetrance of the primary mutations 11778 and 14484. *American Journal of Human Genetics*, 60(5):1107–1121.

Touleimat, N. and Tost, J. (2012). Complete pipeline for Infinium® Human Methylation 450K BeadChip data processing using subset quantile normalization for accurate DNA methylation estimation. *Epigenomics*, 4(3):325–341.

Traboulsi, E. I. (2012). *Genetic diseases of the eye*. Oxford University Press, USA.

Trifunovic, A., Wredenberg, A., Falkenberg, M., Spelbrink, J. N., Rovio, A. T., Bruder, C. E., Bohlooly-Y, M., Gidlöf, S., Oldfors, A., Wibom, R., Törnell, J., Jacobs, H. T., and Larsson, N.-G. (2004). Premature ageing in mice expressing defective mitochondrial DNA polymerase. *Nature*, 429(6990):417–423.

Tsao, K., Aitken, P., and Johns, D. (1999). Smoking as an aetiological factor in a pedigree with Leber's hereditary optic neuropathy. *The British Journal of Ophthalmology*, 83(5):577–581.

Tubbs, E. and Rieusset, J. (2017). Metabolic signaling functions of ER–mitochondria contact sites: role in metabolic diseases. *Journal of Molecular Endocrinology*, 58(2):R87–R106.

Twig, G., Elorza, A., Molina, A. J. A., Mohamed, H., Wikstrom, J. D., Walzer, G., Stiles, L., Haigh, S. E., Katz, S., Las, G., Alroy, J., Wu, M., Py, B. F., Yuan, J., Deeney, J. T., Corkey,

B. E., and Shirihai, O. S. (2008a). Fission and selective fusion govern mitochondrial segregation and elimination by autophagy. *The EMBO Journal*, 27(2):433–446.

Twig, G., Hyde, B., and Shirihai, O. S. (2008b). Mitochondrial fusion, fission and autophagy as a quality control axis: The bioenergetic view. *Biochimica et Biophysica Acta (BBA) - Bioenergetics*, 1777(9):1092–1097.

Tzagoloff, A. (1982). Mitochondrial Structure and Compartmentalization. In Tzagoloff, A., editor, *Mitochondria*, pages 15–38. Springer US, Boston, MA.

United Kingdom Houses of Parliament (2015). Regulations, The Human Fertilisation and Embryology (Mitochondrial Donation). *The National Archives*, 572.

van der Bliek, A. M., Shen, Q., and Kawajiri, S. (2013). Mechanisms of Mitochondrial Fission and Fusion. *Cold Spring Harbor Perspectives in Biology*, 5(6).

van der Wijst, M. G. P. and Rots, M. G. (2015). Mitochondrial epigenetics: an overlooked layer of regulation? *Trends in Genetics*, 31(7):353–356.

van Heesbeen, H. J. and Smidt, M. P. (2019). Entanglement of Genetics and Epigenetics in Parkinson's Disease .

Veleri, S., Lazar, C. H., Chang, B., Sieving, P. A., Banin, E., and Swaroop, A. (2015). Biology and therapy of inherited retinal degenerative disease: insights from mouse models. *Disease Models & Mechanisms*, 8(2):109 LP – 129.

Ventura, D. F., Quiros, P., Carelli, V., Salomao, S. R., Gualtieri, M., Oliveira, A. G. F., Costa, M. F., Berezovsky, A., Sadun, F., de Negri, A. M., and Sadun, A. A. (2005). Chromatic and Luminance Contrast Sensitivities in Asymptomatic Carriers from a Large Brazilian Pedigree of 11778 Leber Hereditary Optic Neuropathy. *Investigative Ophthalmology & Visual Science*, 46(12):4809–4814.

Vignal, C., Uretsky, S., Fitoussi, S., Galy, A., Blouin, L., Girmens, J.-F., Bidot, S., Thomasson, N., Bouquet, C., Valero, S., Meunier, S., Combal, J.-P., Gilly, B., Katz, B., and Sahel, J.-A. (2018). Safety of rAAV2/2-ND4 Gene Therapy for Leber Hereditary Optic Neuropathy. *Ophthalmology*, 125(6):945–947.

Vilkki, J., Ott, J., Savontaus, M. L., Aula, P., and Nikoskelainen, E. K. (1991). Optic atrophy in Leber hereditary optic neuroretinopathy is probably determined by an X-chromosomal gene closely linked to DXS7. *American journal of human genetics*, 48(3):486–491.

Villegas, J. and McPhaul, M. (2001). Establishment and Culture of Human Skin Fibroblasts. In *Current Protocols in Molecular Biology*. John Wiley & Sons, Inc.

Vivian, C. J., Brinker, A. E., Graw, S., Koestler, D. C., Legendre, C., Gooden, G. C., Salhia, B., and Welch, D. R. (2017). Mitochondrial Genomic Backgrounds Affect Nuclear DNA Methylation and Gene Expression. *Cancer research*, 77(22):6202–6214.

Voeltz, G. K., Prinz, W. A., Shibata, Y., Rist, J. M., and Rapoport, T. A. (2006). A class of membrane proteins shaping the tubular endoplasmic reticulum. *Cell*, 124(3):573–586.

von Graefe, A. (1858). Ein ungewoehnlicher Fall von hereditaerer Amaurose. *Arch. Ophthalmol.*, 4:266–268.

Voskoboinik, I., Whisstock, J. C., and Trapani, J. A. (2015). Perforin and granzymes: function, dysfunction and human pathology. *Nature Reviews Immunology*, 15:388.

Wallace, D. C. and Chalkia, D. (2013). Mitochondrial DNA Genetics and the Heteroplasmy Conundrum in Evolution and Disease. *Cold Spring Harbor Perspectives in Biology*, 5(11):a021220.

Wallace, D. C. and Fan, W. (2010). Energetics, epigenetics, mitochondrial genetics. *Mitochondrion*, 10(1):12–31.

Walter, P. and Ron, D. (2011). The Unfolded Protein Response: From Stress Pathway to Homeostatic Regulation. *Science*, 334(6059):1081 LP – 1086.

Wan, X., Pei, H., Zhao, M.-j., Yang, S., Hu, W.-k., He, H., Ma, S.-q., Zhang, G., Dong, X.-y., Chen, C., Wang, D.-w., and Li, B. (2016). Efficacy and Safety of rAAV2-ND4 Treatment for Leber's Hereditary Optic Neuropathy. *Scientific Reports*, 6:21587.

Wang, C., Liu, Z., and Huang, X. (2012). Rab32 Is Important for Autophagy and Lipid Storage in Drosophila. *PLOS ONE*, 7(2):e32086.

Wang, T., Sha, H., Ji, D., Zhang, H., Chen, D., Cao, Y., and Zhu, J. (2014). Polar Body Genome Transfer for Preventing the Transmission of Inherited Mitochondrial Diseases. *Cell*, 157(7):1591–1604.

Wang, Y. E., Marinov, G. K., Wold, B. J., and Chan, D. C. (2013). Genome-Wide Analysis Reveals Coating of the Mitochondrial Genome by TFAM. *PLoS ONE*, 8(8):e74513.

Wang, Z., Wu, X., and Wang, Y. (2018). A framework for analyzing DNA methylation data from Illumina Infinium HumanMethylation450 BeadChip. *BMC Bioinformatics*, 19(5):115.

Wang, Z., Ying, Z., Bosy-Westphal, A., Zhang, J., Schautz, B., Later, W., Heymsfield, S. B., and Müller, M. J. (2010). Specific metabolic rates of major organs and tissues across adulthood: evaluation by mechanistic model of resting energy expenditure. *The American journal of clinical nutrition*, 92(6):1369–1377.

Wassle, H. (2004). Parallel processing in the mammalian retina. *Nat Rev Neurosci*, 5(10):747–757.

Watson, N. V. and Breedlove, S. M. (2012). *The Mind's Machine: Foundations of Brain and Behavior*. Sinauer Associates, 1st edition.

Wei, W., Gomez-Duran, A., Hudson, G., and Chinnery, P. F. (2017). Background sequence characteristics influence the occurrence and severity of disease-causing mtDNA mutations. *PLOS Genetics*, 13(12):e1007126.

Westphal, D., Dewson, G., Czabotar, P. E., and Kluck, R. M. (2011). Molecular biology of Bax and Bak activation and action. *Biochimica et Biophysica Acta (BBA) - Molecular Cell Research*, 1813(4):521–531.

Whelan, S. P. and Zuckerbraun, B. S. (2013). Mitochondrial Signaling: Forwards, Backwards, and In Between. *Oxidative Medicine and Cellular Longevity*, 2013(351613):10.

Wirth, C., Brandt, U., Hunte, C., and Zickermann, V. (2016). Structure and function of mitochondrial complex I. *Biochimica et Biophysica Acta (BBA) - Bioenergetics*, 1857(7):902–914.

Wolter, K. G., Hsu, Y. T., Smith, C. L., Nechushtan, A., Xi, X. G., and Youle, R. J. (1997). Movement of Bax from the cytosol to mitochondria during apoptosis. *The Journal of cell biology*, 139(5):1281–1292.

Wong, A., Cortopassi, G. A., Collins-Schramm, H. E., Cavelier, L., Savontaus, M.-L., McGrogan, M., and Seldin, M. F. (2002). Differentiation-specific effects of LHON mutations introduced into neuronal NT2 cells. *Human Molecular Genetics*, 11(4):431–438.

Wong, R. C. B., Lim, S. Y., Hung, S. S. C., Jackson, S., Khan, S., Van Bergen, N. J., De Smit, E., Liang, H. H., Kearns, L. S., Clarke, L., Mackey, D. A., Hewitt, A. W., Trounce, I. A., and Pébay, A. (2017). Mitochondrial replacement in an iPSC model of Leber's hereditary optic neuropathy. *Aging*, 9(4):1341–1350.

Woś, M., Szczepanowska, J., Pikuła, S., Tylki-Szymańska, A., Zabłocki, K., and Bandorowicz-Pikuła, J. (2016). Mitochondrial dysfunction in fibroblasts derived from patients with Niemann-Pick type C disease. *Archives of Biochemistry and Biophysics*, 593(Supplement C):50–59.

Wright, D. C., Han, D.-H., Garcia-Roves, P. M., Geiger, P. C., Jones, T. E., and Holloszy, J. O. (2007). Exercise-induced Mitochondrial Biogenesis Begins before the Increase in Muscle PGC-1α Expression. *Journal of Biological Chemistry*, 282(1):194–199.

Wu, C.-C. and Bratton, S. B. (2013). Regulation of the intrinsic apoptosis pathway by reactive oxygen species. *Antioxidants & redox signaling*, 19(6):546–558.

Xia, M., Zhang, Y., Jin, K., Lu, Z., Zeng, Z., and Xiong, W. (2019). Communication between mitochondria and other organelles: a brand-new perspective on mitochondria in cancer. *Cell & Bioscience*, 9(1):27.

Xu, X., Ichida, J. M., Allison, J. D., Boyd, J. D., Bonds, A. B., and Casagrande, V. A. (2001). A comparison of koniocellular, magnocellular and parvocellular receptive field properties in the lateral geniculate nucleus of the owl monkey (Aotus trivirgatus). *The Journal of Physiology*, 531(Pt 1):203–218.

Xue, L., Fletcher, G. C., and Tolkovsky, A. M. (1999). Autophagy Is Activated by Apoptotic Signalling in Sympathetic Neurons: An Alternative Mechanism of Death Execution. *Molecular and Cellular Neuroscience*, 14(3):180–198.

Yakes, F. M. and Van-Houten, B. (1997). Mitochondrial DNA damage is more extensive and persists longer than nuclear DNA damage in human cells following oxidative stress. *Proceedings of the National Academy of Sciences of the United States of America*, 94(2):514–519.

Yang, T.-C., Yarmishyn, A. A., Yang, Y.-P., Lu, P.-C., Chou, S.-J., Wang, M.-L., Lin, T.-C., Hwang, D.-K., Chou, Y.-B., Chen, S.-J., Yu, W.-K., Wang, A.-G., Hsu, C.-C., and Chiou, S.-H. (2020). Mitochondrial transport mediates survival of retinal ganglion cells in affected LHON patients. *Human Molecular Genetics*, 29(9):1454–1464.

Yang, Z. and Klionsky, D. J. (2009). An overview of the molecular mechanism of autophagy. *Current topics in microbiology and immunology*, 335:1–32.

Yasukawa, T., Reyes, A., Cluett, T. J., Yang, M.-Y., Bowmaker, M., Jacobs, H. T., and Holt, I. J. (2006). Replication of vertebrate mitochondrial DNA entails transient ribonucleotide incorporation throughout the lagging strand. *The EMBO Journal*, 25(22):5358–5371.

Ye, K., Lu, J., Ma, F., Keinan, A., and Gu, Z. (2014). Extensive pathogenicity of mitochondrial heteroplasmy in healthy human individuals. *Proceedings of the National Academy of Sciences*, 111(29):10654 LP – 10659.

Yeatts, K., Sly, P., Shore, S., Weiss, S., Martinez, F., Geller, A., Bromberg, P., Enright, P., Koren, H., Weissman, D., and Selgrade, M. (2006). A brief targeted review of susceptibility factors, environmental exposures, asthma incidence, and recommendations for future asthma incidence research. *Environmental health perspectives*, 114(4):634–640.

Yen, M.-Y., Chen, C.-S., Wang, A.-G., and Wei, Y.-H. (2002). Increase of mitochondrial DNA in blood cells of patients with Leber's hereditary optic neuropathy with 11778 mutation. *British Journal of Ophthalmology*, 86(9):1027 LP – 1030.

Yorimitsu, T., Nair, U., Yang, Z., and Klionsky, D. J. (2006). Endoplasmic reticulum stress triggers autophagy. *The Journal of biological chemistry*, 281(40):30299–30304.

Yoshida, H., Okada, T., Haze, K., Yanagi, H., Yura, T., Negishi, M., and Mori, K. (2000). ATF6 activated by proteolysis binds in the presence of NF-Y (CBF) directly to the cis-acting element responsible for the mammalian unfolded protein response. *Molecular and cellular biology*, 20(18):6755–6767.

Youle, R. J. and Karbowski, M. (2005). Mitochondrial fission in apoptosis. *Nature Reviews Molecular Cell Biology*, 6(8):657–663.

Youle, R. J. and van der Bliek, A. M. (2012). Mitochondrial fission, fusion, and stress. *Science*, 337.

Yu, H., Koilkonda, R. D., Chou, T.-H., Porciatti, V., Mehta, A., Hentall, I. D., Chiodo, V. A., Boye, S. L., Hauswirth, W. W., Lewin, A. S., and Guy, J. (2015). Consequences of zygote injection and germline transfer of mutant human mitochondrial DNA in mice. *Proceedings of the National Academy of Sciences of the United States of America*, 112(42):E5689–E5698.

Yu, H., Porciatti, V., Lewin, A., Hauswirth, W., and Guy, J. (2018a). Longterm Reversal of Severe Visual Loss by Mitochondrial Gene Transfer in a Mouse Model of Leber Hereditary Optic Neuropathy. *Scientific Reports*, 8(1):5587.

Yu, L., Chen, Y., and Tooze, S. A. (2018b). Autophagy pathway: Cellular and molecular mechanisms. *Autophagy*, 14(2):207–215.

Yu, Z., Sheng, H., Liu, S., Zhao, S., Glembotski, C. C., Warner, D. S., Paschen, W., and Yang, W. (2017). Activation of the ATF6 branch of the unfolded protein response in neurons improves stroke outcome. *Journal of cerebral blood flow and metabolism : official journal of the International Society of Cerebral Blood Flow and Metabolism*, 37(3):1069–1079.

Yu-Wai-Man, P. and Chinnery, P. F. (2000). Leber Hereditary Optic Neuropathy.

Yu-Wai-Man, P. and Chinnery, P. F. (2011). Leber Hereditary Optic Neuropathy - Therapeutic Challenges and Early Promise. *Taiwan journal of ophthalmology*, 1(1):12–15.

Yu-Wai-Man, P., Griffiths, P. G., Brown, D. T., Howell, N., Turnbull, D. M., and Chinnery, P. F. (2003). The Epidemiology of Leber Hereditary Optic Neuropathy in the North East of England. *American Journal of Human Genetics*, 72(2):333–339.

Yu-Wai-Man, P., Griffiths, P. G., Hudson, G., and Chinnery, P. F. (2009). Inherited mitochondrial optic neuropathies. *Journal of Medical Genetics*, 46(3):145–158.

Yu-Wai-Man, P., Klopstock, T., Metz, G., Büchner, B., Gallenmüller, C., Bailie, M., Nwali, N., Griffiths, P. G., von Livonius, B., Reznicek, L., Rouleau, J., Coppard, N., Meier, T., and Chinnery, P. F. (2013). Idebenone treatment for Leber hereditary optic neuropathy — Past, present, and future. *Mitochondrion*, 13(6):901.

Yu-Wai-Man, P., Soiferman, D., Moore, D. G., Burté, F., and Saada, A. (2017). Evaluating the therapeutic potential of idebenone and related quinone analogues in Leber hereditary optic neuropathy. *Mitochondrion*, 36:36–42.

Yu-Wai-Man, P., Turnbull, D. M., and Chinnery, P. F. (2002). Leber hereditary optic neuropathy. *Journal of Medical Genetics*, 39(3):162–169.

Yu-Wai-Man, P., Votruba, M., Moore, A. T., and Chinnery, P. F. (2014). Treatment strategies for inherited optic neuropathies: past, present and future. *Eye*, 28(5):521–537.

Yuan, L.-J., Wang, X.-W., Wang, H.-T., Zhang, M., Sun, J.-W., and Chen, W.-F. (2019). G protein-coupled estrogen receptor is involved in the neuroprotective effect of IGF-1 against MPTP/MPP+-induced dopaminergic neuronal injury. *The Journal of Steroid Biochemistry and Molecular Biology*, 192:105384.

Zaidi, A. A. and Makova, K. D. (2019). Investigating mitonuclear interactions in human admixed populations. *Nature Ecology & Evolution*, 3(2):213–222.

Zhang, J., Liu, H., Luo, S., Lu, Z., Chávez-Badiola, A., Liu, Z., Yang, M., Merhi, Z., Silber, S. J., Munné, S., Konstantinidis, M., Wells, D., Tang, J. J., and Huang, T. (2017). Live birth derived from oocyte spindle transfer to prevent mitochondrial disease. *Reproductive BioMedicine Online*, 34(4):361–368.

Zhang, Y., Tian, Z., Yuan, J., Liu, C., Liu, H. L., Ma, S. Q., and Li, B. (2018). The Progress of Gene Therapy for Leber's Optic Hereditary Neuropathy. *Current gene therapy*, 17(4):320–326.

Zhao, X., Zhang, Y., Lu, L., and Yang, H. (2020). Therapeutic Effects of Idebenone on Leber Hereditary Optic Neuropathy. *Current Eye Research*, pages 1–9.

Zhuo, Y., Luo, H., and Zhang, K. (2012). Leber hereditary optic neuropathy and oxidative stress. *Proceedings of the National Academy of Sciences of the United States of America*, 109(49):19882–19883.

Appendices

LHON Disease Penetrance

Familial Disease Penetrance

Figure S1: *Counts of LHON affected patients by the age that they develop at within a cohort of 133 Italian and 111 British affected LHON patients. Splitting by gender (A) and further splitting by country of origin (B).*

Nuclear DNA Variants

Table S1: *2-sample test for equality of proportions with Yates Correction between affected and unaffected mothers, total and stratifying by mutation group.*

	Stratification	**P-Value**
Total	Total Offspring	8.43e-09
	Sons	5.60e-04
	Daughters	7.62e-05
m.11778G>A	Total Offspring	0.001
	Sons	0.125
	Daughters	0.008
m.3460G>A	Total Offspring	0.001
	Sons	0.025
	Daughters	0.046
UK	Total Offspring	0.002
	Sons	0.014
	Daughters	0.186
Finnish	Total Offspring	5.43e-05
	Sons	0.041
	Daughters	0.001

Table S2: *Illumina Infinium HumanMethylation27 BeadChip probe distribution, after quality control.*

Chromosome	**Count**	**Chromosome**	**Count**
1	2863	13	490
2	1682	14	824
3	1498	15	822
4	992	16	1192
5	1141	17	1575
6	1477	18	390
7	1241	19	1896
8	929	20	880
9	1063	21	311
10	1034	22	642
11	1714	X	1046
12	1511	Y	7

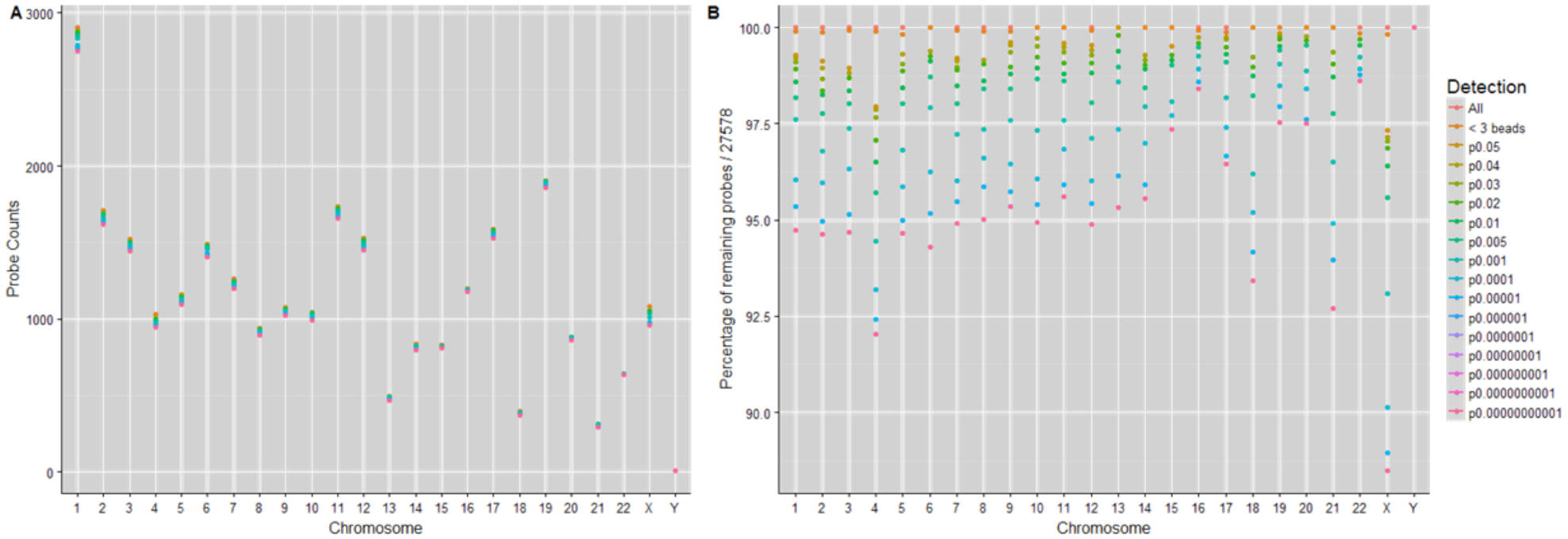

Figure S2: *Probes per chromosome (A) and percentages remaining (B) at different detection thresholds.*

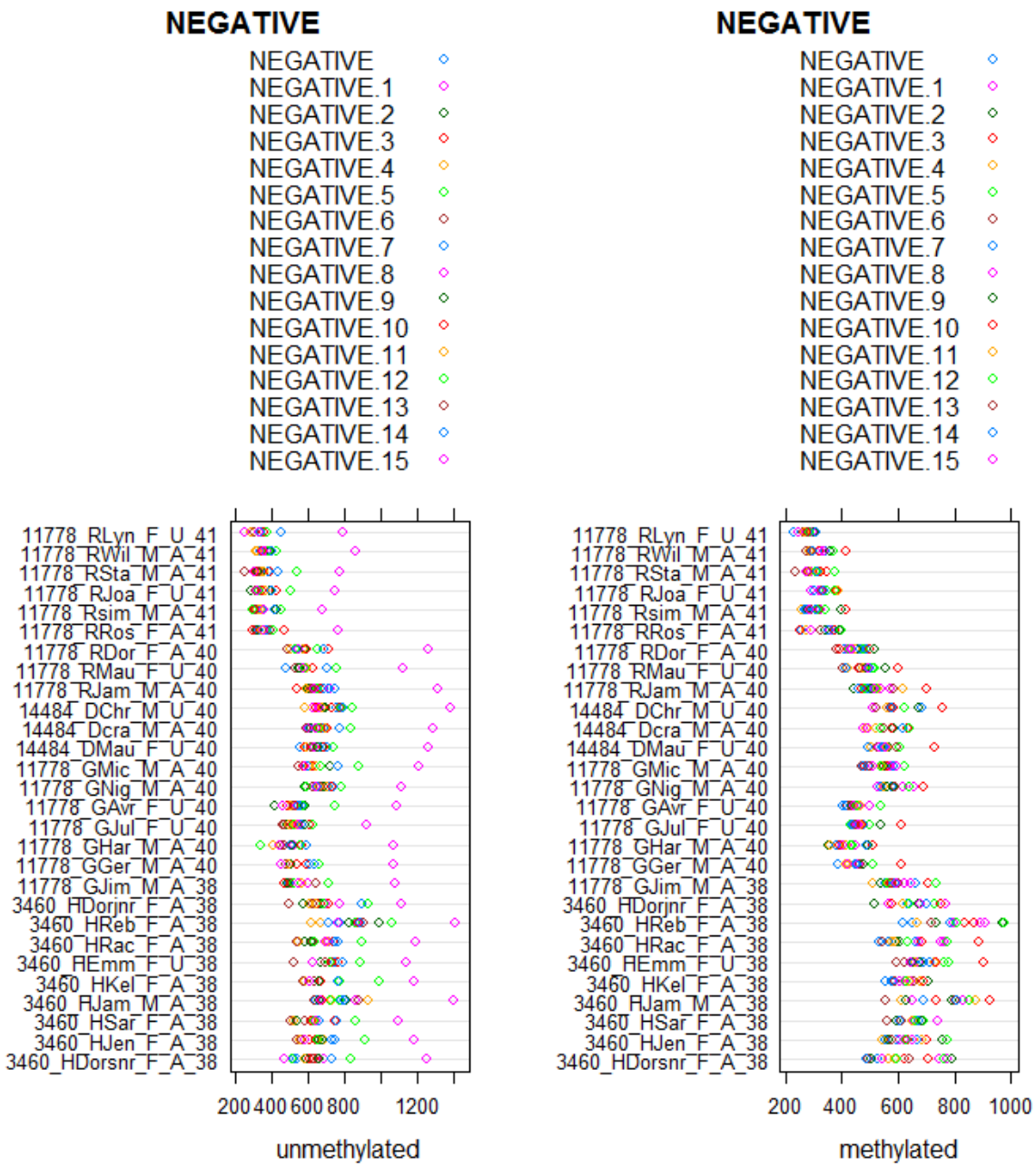

Figure S3: *Negative control probes of the Illumina Infinium HumanMethylation27 BeadChips used within this study. Note the final number in the sample identifier indicators which array it was loaded onto and the variation of measurements between batches.*

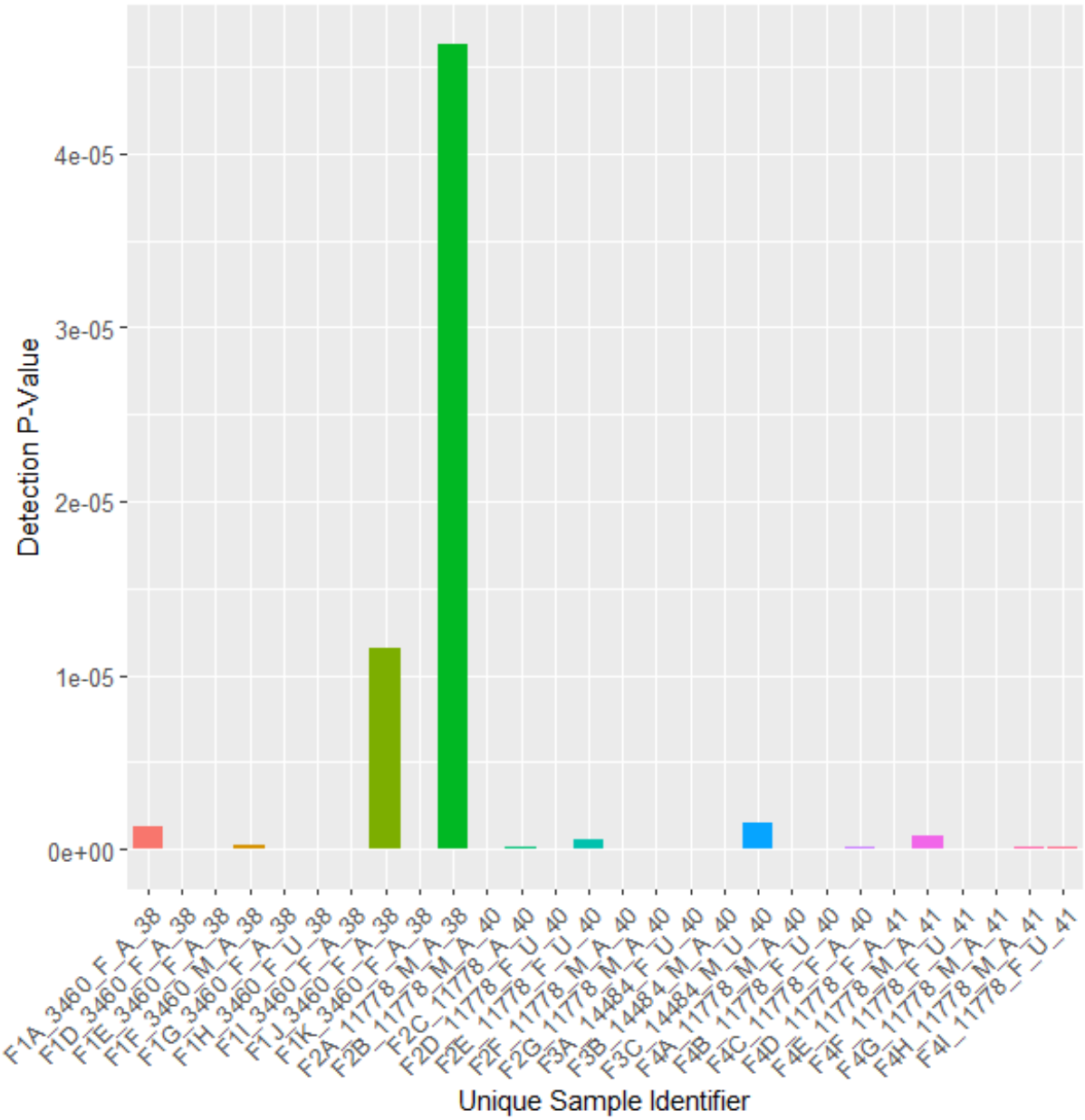

Figure S4: *P-Value of methylation beta value per sample.*

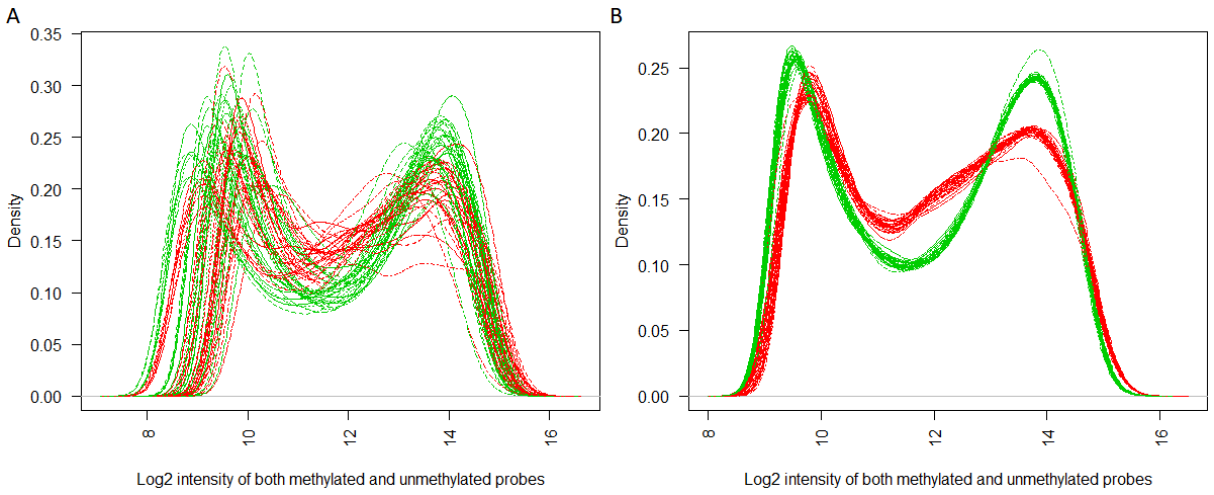

Figure S5: *Density distribution of two colour channels; before (A) and after (B) quantile normalisation.*

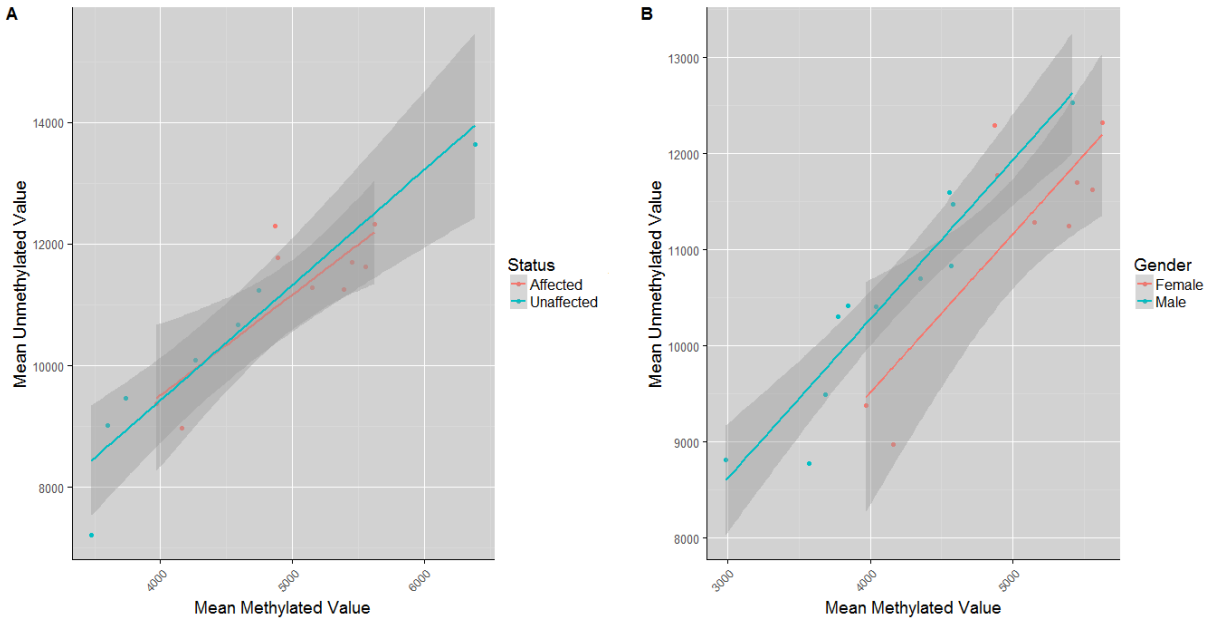

Figure S6: *Global methylation patterns by disease status and gender.*

Table S3: *Differentially hypermethylated genes in LHON patients compared to unaffected carriers, emphasising hypermethylation in males compared to females out of a maximum of 40 tests. Mitochondrial genes identified from MitoCarta 2.0 (Calvo et al., 2016; Pagliarini et al., 2008) and retinal genes identified from TIGEM (Pinelli et al., 2016).*

Gene	Hypomethylated in Males	Hypermethylated in Males	Mitochondrial	Retinal
ECT2	40	NA	NA	YES
C20orf102	NA	NA	NA	NA
FGF20	NA	NA	NA	NA
GJA7	NA	NA	NA	NA
GNAI1	NA	NA	NA	YES
IPO9	NA	NA	NA	YES
KCNE1L	NA	40	NA	NA
TSPAN32	NA	NA	NA	NA
WIRE	NA	NA	NA	NA
ZNF273	NA	NA	NA	YES
CMTM6	NA	NA	NA	YES
FLJ30834	40	NA	NA	NA
NSF	NA	NA	NA	YES
RAB32	NA	NA	YES	YES
FZD1	40	NA	NA	NA
NFATC2IP	40	NA	NA	YES
GRB10	NA	NA	NA	YES
HLA-C	39	NA	NA	YES
HGF	40	NA	NA	YES
PCDHGC4	NA	NA	NA	YES
AIRE	40	NA	NA	NA
BMP8A	NA	NA	NA	NA
LOC349136	39	NA	NA	NA
MEGF10	40	NA	NA	YES
SCN4B	40	NA	NA	YES
SCUBE3	40	NA	NA	NA
SLC25A36	NA	NA	YES	YES
SLC6A3	NA	NA	NA	NA
TLX2	40	NA	NA	YES
NETO1	NA	NA	NA	YES
C1orf85	NA	NA	NA	YES
C20orf98	NA	NA	NA	NA
LAMC2	NA	NA	NA	NA
TMEM34	NA	NA	NA	NA
C3orf15	NA	NA	NA	NA
IRF6	40	NA	NA	YES
NIPA1	40	NA	NA	YES
THRB	40	NA	NA	YES
ADCY2	NA	NA	NA	YES
GPR157	NA	NA	NA	NA
LPPR4	39	NA	NA	NA
ITGA1	39	NA	NA	YES
RBP4	NA	NA	NA	NA
GPM6A	NA	NA	NA	YES

Table S4: *Differentially hypomethylated genes in LHON patients compared to unaffected carriers, emphasising hypomethylation in males compared to females out of a maximum of 40 tests. Mitochondrial genes identified from MitoCarta 2.0 (Calvo et al., 2016; Pagliarini et al., 2008) and retinal genes identified from TIGEM (Pinelli et al., 2016).*

Gene	Hypomethylated in Males	Hypermethylated in Males	Mitochondrial	Retinal
BXDC1	NA	40	NA	NA
EFNB1	40	NA	NA	YES
COPB2	NA	NA	NA	YES
DNASE1L1	40	NA	NA	YES
EVL	NA	NA	NA	YES
GPR37L1	NA	NA	NA	YES
IDH3G	40	NA	YES	YES
IGSF8	NA	NA	NA	YES
IQSEC1	NA	NA	NA	YES
LINS1	NA	NA	NA	NA
RUNX3	NA	NA	NA	NA
SLC6A18	NA	NA	NA	NA
STK6	NA	NA	NA	NA
TFAP4	NA	NA	NA	YES
PHYH	NA	NA	YES	YES
RAB32	NA	NA	YES	YES
SN	NA	NA	NA	NA
FLJ10996	NA	NA	NA	NA
TNS3	NA	NA	NA	YES
LOC317671	NA	NA	NA	NA
DNAJB13	NA	NA	NA	NA
C20orf75	NA	NA	NA	NA
NANP	NA	39	NA	NA

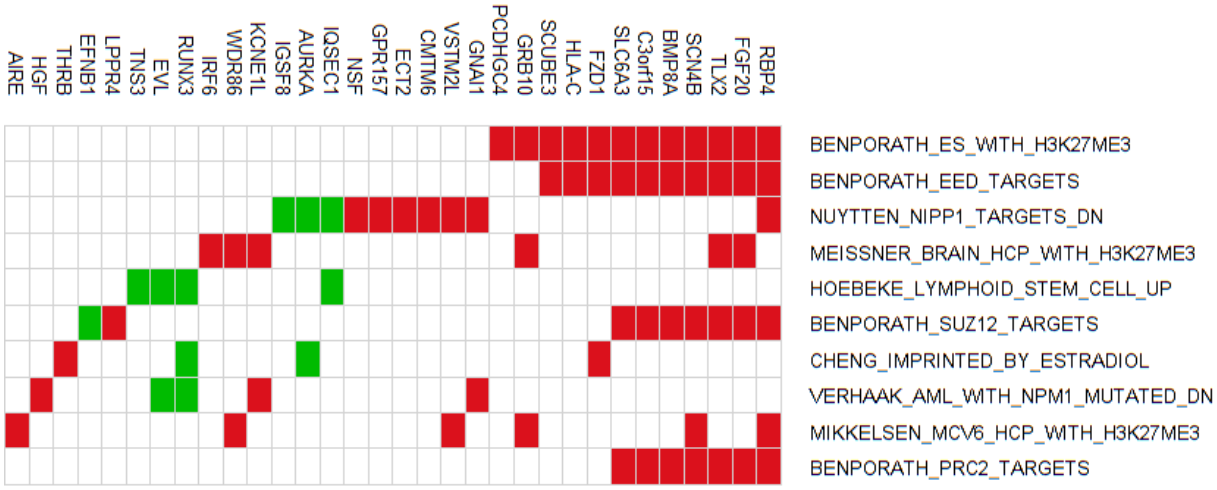

Figure S7: *Matches of LHON hypermethylated (red) and hypomethylated (genes) in MSigDB's C2 curated gene sets of chemical and genetic perturbations (3302 gene sets).*

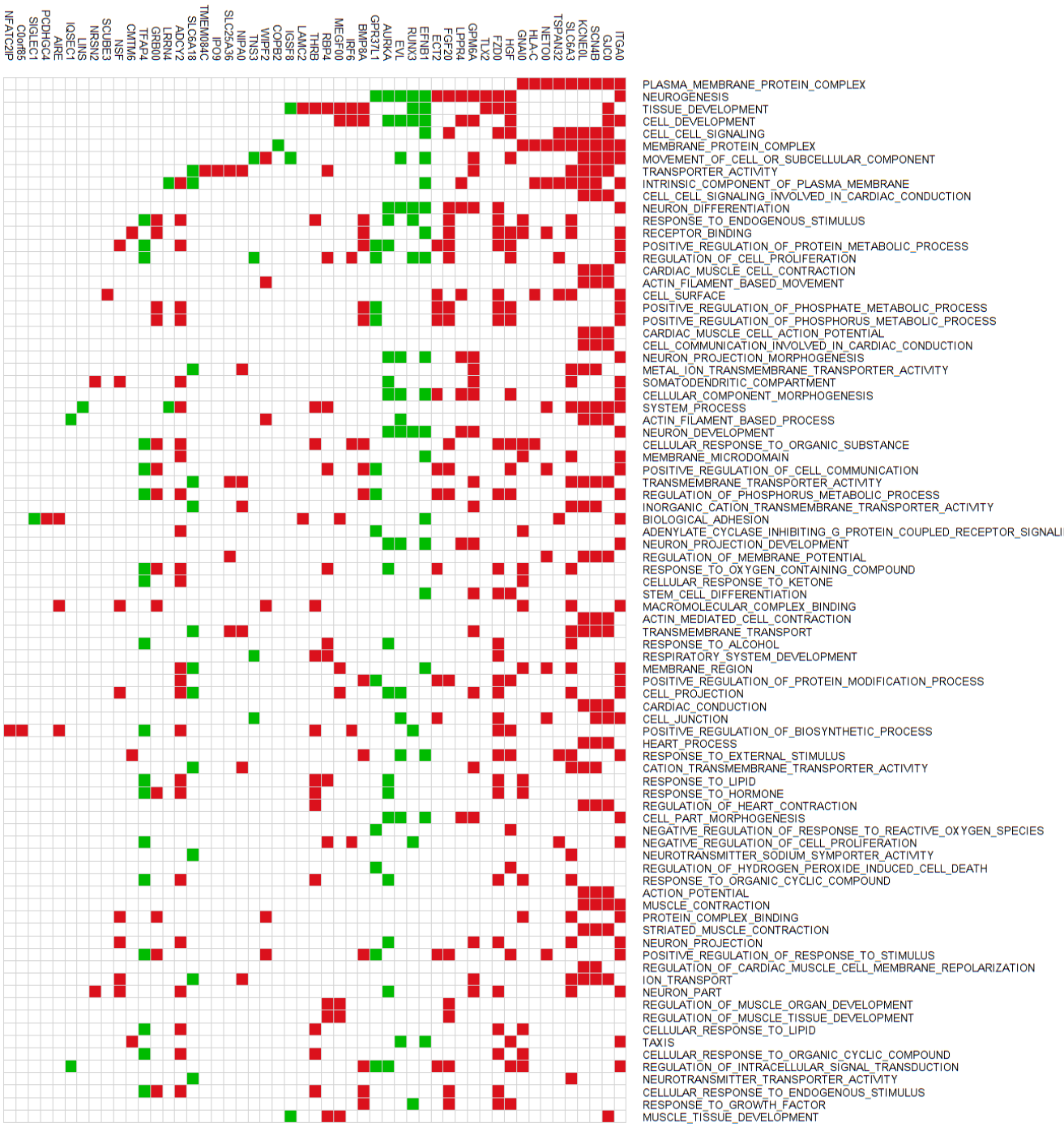

Figure S8: *Matches of LHON hypermethylated (red) and hypomethylated (genes) in MSigDB's C5 GO gene sets of biological processes (7350 gene sets).*

Table S5: *GO C2 curated gene sets of chemical and genetic perturbations gene sets which are over-represented in genes which show differential methylation between LHON patients and carriers, and contain exome variants which uniquely appear in patients compared to carriers in a dominant or recessive model. k = cross-matched genes and K = number of genes in the gene set.*

Gene Set	**k**	**k/K**	**p-value**	**FDR q-value**
Benporath_Es_With_H3K27Me3	9	0.008	1.12E-06	3.71E-03
Hoebeke_Lymphoid_Stem_Cell_Up	4	0.041	2.60E-06	4.29E-03
Benporath_Eed_Targets	8	0.008	7.78E-06	8.57E-03
Nuytten_Nipp1_Targets_Dn	7	0.008	1.75E-05	1.45E-02
Ingram_Shh_Targets_Dn	3	0.048	3.34E-05	2.21E-02
Rodrigues_Thyroid_Carcinoma_Up	2	0.133	9.76E-05	4.85E-02
Verhaak_Aml_With_Npm1_Mutated_Dn	4	0.016	1.05E-04	4.85E-02
Meissner_Brain_Hcp_With_H3K27Me3	4	0.015	1.30E-04	4.85E-02
Boylan_Multiple_Myeloma_C_D_Dn	4	0.015	1.42E-04	4.85E-02
Rodrigues_Thyroid_Carcinoma_Anaplastic_Dn	5	0.010	1.64E-04	4.85E-02
Cheng_Imprinted_By_Estradiol	3	0.027	1.76E-04	4.85E-02
Jackson_Dnmt1_Targets_Dn	2	0.100	1.76E-04	4.85E-02
Chiba_Response_To_Tsa_Dn	2	0.095	1.95E-04	4.94E-02

Table S6: *GO C5 Biological Process Complete gene sets which are over-represented in genes which show differential methylation between LHON patients and carriers, and contain exome variants which uniquely appear in patients compared to carriers in a dominant or recessive model. k = cross-matched genes and K = number of genes in the gene set.*

Gene Set	k	k/K	p-value	FDR q-value
Neurogenesis	14	0.009	2.19e-10	1.26e-06
Neuron_Differentiation	13	0.010	3.43e-10	1.26e-06
Neuron_Development	10	0.009	8.55e-08	2.09e-04
Locomotion	12	0.006	2.47e-07	4.54e-04
Cellular_Response_To_Antibiotic	5	0.034	3.45e-07	5.07e-04
Response_To_Drug	9	0.009	5.37e-07	5.61e-04
Regulation_Of_Cell_Population_Proliferation	11	0.006	5.73e-07	5.61e-04
Cell_Motility	11	0.006	6.10e-07	5.61e-04
Response_To_Antibiotic	6	0.018	7.99e-07	6.53e-04
Positive_Regulation_Of_Signalling	11	0.006	1.11e-06	8.19e-04
Cellular_Response_To_Drug	6	0.017	1.46e-06	9.78e-04
Regulation_Of_Neuron_Differentiation	7	0.011	3.12e-06	1.91e-03
Cell_Cell_Signalling	10	0.006	3.39e-06	1.92e-03
Regulation_Of_Phosphorus_Metabolic_Process	10	0.006	4.42e-06	2.32e-03
Positive_Regulation_Of_Phosphorus_Metabolic_Process	8	0.007	9.28e-06	4.55e-03
Cellular_Component_Morphogenesis	8	0.007	1.14e-05	5.23e-03
Cell_Projection_Organization	9	0.006	1.34e-05	5.80e-03
Protein_Phosphorylation	10	0.005	1.63e-05	6.66e-03
Positive_Regulation_Of_Protein_Modification_Process	8	0.007	2.18e-05	8.45e-03
Negative_Regulation_Of_Response_To_Oxidative_Stress	3	0.054	2.35e-05	8.62e-03
Positive_Regulation_Of_Protein_Metabolic_Process	9	0.006	2.46e-05	8.62e-03
Response_To_Endogenous_Stimulus	9	0.006	2.65e-05	8.84e-03
Regulation_Of_Nervous_System_Development	7	0.008	2.83e-05	9.03e-03
Regulation_Of_Cell_Development	7	0.008	3.35e-05	1.03e-02
Cell_Part_Morphogenesis	6	0.009	4.91e-05	1.32e-02
Muscle_Organ_Development	5	0.012	5.02e-05	1.32e-02
Response_To_Forskolin	2	0.182	5.13e-05	1.32e-02
Positive_Regulation_Of_ Multicellular_Organismal_Process	9	0.005	5.15e-05	1.32e-02
Regulation_Of_Oxidative_Stress_Induced_Cell_Death	3	0.041	5.20e-05	1.32e-02
Regulation_Of_Protein_Modification_Process	9	0.005	6.31e-05	1.54e-02
Enzyme_Linked_Receptor_Protein_Signalling_Pathway	7	0.007	6.50e-05	1.54e-02
Regulation_Of_Cell_Differentiation	9	0.005	6.85e-05	1.57e-02
Striated_Muscle_Cell_Proliferation	3	0.037	7.10e-05	1.57e-02
Response_To_Platelet_Aggregation_Inhibitor	2	0.154	7.26e-05	1.57e-02
Response_To_Growth_Factor	6	0.008	7.68e-05	1.61e-02
Adenylate_Cyclase_Inhibiting_G_Protein _Coupled_Receptor_Signalling_Pathway	3	0.034	9.39e-05	1.92e-02
Negative_Regulation_Of_Cell_Population_Proliferation	6	0.008	9.78e-05	1.94e-02
Cell_Death_In_Response_To_Oxidative_Stress	3	0.033	1.00e-04	1.94e-02
Cellular_Response_To_Oxygen_Containing_Compound	7	0.006	1.05e-04	1.97e-02
Cellular_Response_To_Ketone	3	0.032	1.10e-04	1.98e-02
Regulation_Of_Response_To_Oxidative_Stress	3	0.032	1.10e-04	1.98e-02
Cellular_Response_To_Hydrogen_Peroxide	3	0.030	1.29e-04	2.25e-02
Regulation_Of_Response_To_Drug	3	0.030	1.37e-04	2.34e-02
Positive_Regulation_Of_Rna_Biosynthetic_Process	8	0.005	1.45e-04	2.42e-02
Response_To_Oxygen_Containing_Compound	8	0.005	1.55e-04	2.54e-02
Positive_Regulation_Of_Nervous_System_Development	5	0.009	1.73e-04	2.77e-02
Cellular_Response_To_Oxidative_Stress	4	0.013	2.12e-04	3.32e-02
Negative_Regulation_Of_ Multicellular_Organismal_Process	7	0.005	2.39e-04	3.60e-02
Regulation_Of_Cell_Death	8	0.005	2.40e-04	3.60e-02
Negative_Regulation_Of_Cellular_Response_To_Drug	2	0.083	2.55e-04	3.75e-02
Activation_Of_Protein_Kinase_Activity	4	0.012	3.16e-04	4.55e-02

Table S7: *Genes contributing to GO C5 Biological Process Complete pathways which are over-represented in PANTHER over-representation test.*

Generation of Neurons	**Neurogenesis**	**Methylation**
RUNX3	RUNX3	Hypomethylated
GPM6A	GPM6A	Hypermethylated
EVL	EVL	Hypomethylated
THRB	THRB	Hypermethylated
EFNB1	EFNB1	Hypomethylated
TLX2	TLX2	Hypermethylated
FZD1	FZD1	Hypermethylated
FGF20	FGF20	Hypermethylated
ITGA1	ITGA1	Hypermethylated
GRB10	GRB10	Hypermethylated
ECT2	ECT2	Hypermethylated
HGF	HGF	Hypermethylated
GPR37L1	GPR37L1	Hypomethylated
	GPR157	Hypermethylated

Cross-Matched Gene Summaries

Investigating genes at an individual level, following gene summaries have been adapted from GeneCards (Stelzer et al., 2016), Entrez (RefSeq) (McEntyre, 1998; O'Leary et al., 2016) and UniProtKB/Swiss-Prot (Consortium, 2018) to identify relevant functional details.

ADCY2

Adenylate Cyclase 2 is a Protein Coding gene. Among its related pathways are RET signalling and Oocyte meiosis. GO annotations related to this gene include protein heterodimerisation activity and phosphorus-oxygen lyase activity. This gene encodes a member of the family of adenylate cyclases, which are membrane-associated enzymes that catalyze the formation of the secondary messenger cyclic adenosine monophosphate. This enzyme is insensitive to Ca^{2+}/calmodulin, and is stimulated by the G protein beta and gamma subunit complex.

AIRE

Autoimmune Regulator is a Protein Coding gene. Diseases associated with *AIRE* include Autoimmune Polyendocrine Syndrome, Type I, With Or Without Reversible Metaphyseal Dysplasia and Hypoparathyroidism, Familial Isolated. Among its related pathways are Ubiquitin mediated proteolysis and Primary immunodeficiency. GO annotations related to this gene include identical protein binding and transcription regulatory region DNA binding. Mutations in this gene cause the rare autosomal-recessive systemic autoimmune disease termed autoimmune polyendocrinopathy with candidiasis and ectodermal dystrophy.

BMP8A

Bone Morphogenetic Protein 8a is a Protein Coding gene. Among its related pathways are G-Protein-Coupled Receptor (GPCR) Pathway and Nanog in Mammalian Embryonic Stem Cell Pluripotency. GO annotations related to this gene include cytokine activity and Transforming Growth Factor-β (TGF-β) receptor binding. This gene encodes a secreted ligand of the TGF-β superfamily of proteins. Ligands of this family bind various TGF-β receptors leading to recruitment and activation of SMAD family transcription factors that regulate gene expression. Plays a role in calcium regulation and bone homeostasis (By similarity). Signalling protein involved in regulation of thermogenesis and energy balance.

CMTM6

CKLF Like MARVEL Transmembrane Domain Containing 6 is a Protein Coding gene. Among its related pathways are Innate Immune System. GO annotations related to this gene include cytokine activity. This gene belongs to the chemokine-like factor gene superfamily, a novel family that is similar to the chemokine and transmembrane 4 superfamilies. Master regulator of recycling and plasma membrane expression an immune inhibitory ligand critical for immune tolerance to self and anti-tumour immu-

nity.

ECT2

Epithelial Cell Transforming 2 is a Protein Coding gene. Diseases associated with *ECT2* include Breast Cancer. Among its related pathways are Signalling by Rho GTPases and p75 NTR receptor-mediated signalling. GO annotations related to this gene include protein homodimerisation activity and GTPase activator activity. The expression of this gene is elevated with the onset of DNA synthesis and remains elevated during G2 and M phases. Drive tumour cell proliferation and invasion. Also stimulates genotoxic stress-induced *RHOB* activity in breast cancer cells leading to their cell death.

FGF20

Fibroblast Growth Factor 20 is a Protein Coding gene. Diseases associated with *FGF20* include Renal Hypodysplasia/Aplasia 2 and Renal Agenesis, Bilateral. Among its related pathways are Gastric cancer and Negative regulation of FGFR3 signalling. GO annotations related to this gene include growth factor activity and fibroblast growth factor receptor binding. The protein encoded by this gene is a member of the fibroblast growth factor family. The fibroblast growth factors possess broad mitogenic and cell survival activities, and are involved in a variety of biological processes including embryonic development, cell growth, morphogenesis, tissue repair, tumour growth and invasion. This gene product is a secreted neurotrophic factor but lacks a typical signal peptide. It is expressed in normal brain, particularly the cerebellum, and may regulate central nervous system development and function. Homodimerisation of this protein was shown to regulate its receptor binding activity and concentration gradient in the extracellular matrix. Genetic variations of this gene have been associated with Parkinson disease susceptibility.

FZD1

Frizzled Class Receptor 1 is a Protein Coding gene. Diseases associated with *FZD1* include Exudative Vitreoretinopathy and Brachydactyly, Type B1. Among its related pathways are Gastric cancer and Association Between Physico-Chemical Features and Toxicity Associated Pathways. GO annotations related to this gene include GPCR activity and transmembrane signalling receptor activity. Members of the 'frizzled' gene family encode 7-transmembrane domain proteins that are receptors for Wnt signalling proteins. Functions in the canonical Wnt/beta-catenin signalling pathway.

GNAI1

G Protein Subunit Alpha I1 is a Protein Coding gene. Diseases associated with *GNAI1* include Pertussis and Cholera. Among its related pathways are Human cytomegalovirus infection and GPCR Pathway. GO annotations related to this gene include GTP binding and obsolete signal transducer activity. Guanine nucleotide-binding proteins function as transducers downstream of GPCRs in numerous signalling cascades. The alpha chain contains the guanine nucleotide binding site and alternates be-

tween an active, GTP-bound state and an inactive, GDP-bound state. Inhibits adenylate cyclase activity, leading to decreased intracellular Cyclic Adenosine Monophosphate (cAMP) levels (By similarity).

GPM6A

Glycoprotein M6A is a Protein Coding gene. GO annotations related to this gene include calcium channel activity. Involved in neuronal differentiation, including differentiation and migration of neuronal stem cells. Plays a role in neuronal plasticity and is involved in neurite and filopodia outgrowth, filopodia motility and probably synapse formation. GPM6A-induced filopodia formation involves Mitogen-Activated Protein Kinase (MAPK) and Src signalling pathways. May be involved in neuronal nerve growth factor-dependent Ca^{2+} influx. May be involved in regulation of endocytosis and intracellular trafficking of GPCRs; enhances internalization and recycling of μ-type opioid receptor.

GPR157

G Protein-Coupled Receptor 157 is a Protein Coding gene. Diseases associated with *GPR157* include Stromal Dystrophy. GO annotations related to this gene include GPCR activity and transmembrane signalling receptor activity. Orphan receptor that promotes neuronal differentiation of radial glial progenitors. The activity of this receptor is mediated by a G(q)-protein that activates a phosphatidylinositol-calcium second messenger.

GPR37L1

G Protein-Coupled Receptor 37 Like 1 is a Protein Coding gene. Among its related pathways are Peptide ligand-binding receptors and Neuroscience. GO annotations related to this gene include GPCR activity. Has been shown to bind the neuroprotective and glioprotective factor prosaposin, leading to endocytosis followed by a MAPK phosphorylation cascade, however, other studies have shown that prosaposin does not increase activity. Regulates baseline blood pressure in females and protects against cardiovascular stress in males (By similarity). Mediates inhibition of astrocyte glutamate transporters and reduction in neuronal N-methyl-D-aspartate receptor activity (By similarity).

GRB10

Growth Factor Receptor Bound Protein 10 is a Protein Coding gene. Diseases associated with *GRB10* include Silver-Russell Syndrome and Spastic Paraplegia 17, Autosomal Dominant. Among its related pathways are Beta-Adrenergic Signalling and Signalling events Regulated by RET Tyrosine Kinase. GO annotations related to this gene include SH3/SH2 adaptor activity and insulin receptor binding. This gene encodes a growth factor receptor-binding protein that interacts with insulin receptors and insulin-like growth-factor receptors. Over-expression of some isoforms of the encoded protein inhibits tyrosine kinase activity and results in growth suppression.

This gene is imprinted in a highly isoform- and tissue-specific manner, with expression observed from the paternal allele in the brain, and from the maternal allele in the placental trophoblasts.

HGF

Hepatocyte Growth Factor is a Protein Coding gene. Diseases associated with *HGF* include Deafness, Autosomal Recessive 39 and Autosomal Recessive Non-Syndromic Sensorineural Deafness Type Dfnb. Among its related pathways are Interleukin-7 signalling and RET signalling. GO annotations related to this gene include identical protein binding and serine-type endopeptidase activity. This protein also plays a role in angiogenesis, tumorogenesis, and tissue regeneration. Although the encoded protein is a member of the peptidase S1 family of serine proteases, it lacks peptidase activity. Mutations in this gene are associated with nonsyndromic hearing loss.

IDH3G

Isocitrate Dehydrogenase (NAD^+) 3 Gamma is a Protein Coding gene. Diseases associated with *IDH3G* include Periventricular Heterotopia. Among its related pathways are Pyruvate metabolism and Citric Acid (TCA) cycle and Citrate cycle (TCA cycle). GO annotations related to this gene include magnesium ion binding and oxidoreductase activity, acting on the CH-OH group of donors, NAD or NADP as acceptor. Isocitrate dehydrogenases catalyze the oxidative decarboxylation of isocitrate to 2-oxoglutarate. These enzymes belong to two distinct subclasses, one of which utilizes NAD^+ as the electron acceptor and the other $NADP^+$. Five isocitrate dehydrogenases have been reported: three NAD^+-dependent isocitrate dehydrogenases, which localize to the mitochondrial matrix, and two $NADP^+$-dependent isocitrate dehydrogenases, one of which is mitochondrial and the other predominantly cytosolic. NAD^+-dependent isocitrate dehydrogenases catalyze the allosterically regulated rate-limiting step of the tricarboxylic acid cycle.

IGSF8

Immunoglobulin Superfamily Member 8 is a Protein Coding gene. This gene encodes a member the EWI subfamily of the immunoglobulin protein superfamily. This protein interacts with the tetraspanins CD81 and CD9 and may regulate their role in certain cellular functions including cell migration and viral infection. The encoded protein may also function as a tumour suppressor by inhibiting the proliferation of certain cancers.

IPO9

IPO9 (Importin 9) is a Protein Coding gene. GO annotations related to this gene include binding and protein transporter activity. Functions in nuclear protein import as nuclear transport receptor. Serves as receptor for nuclear localization signals (NLS) in cargo substrates. Is thought to mediate docking of the importin/substrate complex to the nuclear pore complex (NPC) through binding to nucleoporin and the complex

is subsequently translocated through the pore by an energy requiring, Ran-dependent mechanism (PubMed:11823430).

IQSEC1

IQ Motif And Sec7 Domain 1 is a Protein Coding gene. Among its related pathways are Arf6 signalling events and EGF/EGFR Signalling Pathway. GO annotations related to this gene include lipid binding and ARF guanyl-nucleotide exchange factor activity. Guanine nucleotide exchange factor for ARF1 and ARF6. Guanine nucleotide exchange factor activity is enhanced by lipid binding. Accelerates GTP binding by ARFs of all three classes. Guanine nucleotide exchange protein for ARF6, mediating internalisation of beta-1 integrin.

IRF6

Interferon Regulatory Factor 6 is a Protein Coding gene. Diseases associated with *IRF6* include Popliteal Pterygium Syndrome and Van Der Woude Syndrome 1. Among its related pathways are Interferon gamma signalling and Innate Immune System. GO annotations related to this gene include DNA-binding transcription factor activity. This gene encodes a member of the interferon regulatory transcription factor (IRF) family. Family members share a highly-conserved N-terminal helix-turn-helix DNA-binding domain and a less conserved C-terminal protein-binding domain. The encoded protein may be a transcriptional activator. Mutations in this gene are also associated with non-syndromic orofacial cleft type 6.

ITGA1

Integrin Subunit Alpha 1 is a Protein Coding gene. Diseases associated with *ITGA1* include Intestine Carcinoma In Situ and Colon Carcinoma In Situ. Among its related pathways are Focal Adhesion and Dilated cardiomyopathy (DCM). GO annotations related to this gene include signalling receptor binding and collagen binding. This gene encodes the alpha 1 subunit of integrin receptors. This protein heterodimerizes with the beta 1 subunit to form a cell-surface receptor for collagen and laminin. The heterodimeric receptor is involved in cell-cell adhesion and may play a role in inflammation and fibrosis.

LAMC2

Laminin Subunit Gamma 2 is a Protein Coding gene. Diseases associated with *LAMC2* include Epidermolysis Bullosa, Junctional, Herlitz Type and Epidermolysis Bullosa, Junctional, Non-Herlitz Type. Among its related pathways are MET promotes cell motility and Integrin Pathway. GO annotations related to this gene include heparin binding. Laminins, a family of extracellular matrix glycoproteins, are the major noncollagenous constituent of basement membranes. They have been implicated in a wide variety of biological processes including cell adhesion, differentiation, migration, signalling, neurite outgrowth and metastasis.

LINS1

Lines Homolog 1 is a Protein Coding gene. Diseases associated with *LINS1* include Mental Retardation, Autosomal Recessive 27 and Autosomal Recessive Non-Syndromic Intellectual Disability. The Drosophila segment polarity gene lin encodes a protein, lines, which plays important roles in development of the epidermis and hindgut. This gene encodes a protein containing a lines-like domain.

MEGF10

Multiple EGF Like Domains 10 is a Protein Coding gene. Diseases associated with *MEGF10* include Myopathy, Areflexia, Respiratory Distress, And Dysphagia, Early-Onset and Dysphagia. GO annotations related to this gene include endopeptidase inhibitor activity. This gene encodes a member of the multiple epidermal growth factor-like domains protein family. Necessary for astrocyte-dependent apoptotic neuron clearance in the developing cerebellum (PubMed:27170117). Plays role in muscle cell proliferation, adhesion and motility. Controls the balance between skeletal muscle satellite cells proliferation and differentiation through regulation of the notch signalling pathway. May also function in the mosaic spacing of specific neuron subtypes in the retina through homotypic retinal neuron repulsion. Mosaics provide a mechanism to distribute each cell type evenly across the retina, ensuring that all parts of the visual field have access to a full set of processing elements.

NANP

N-Acetylneuraminic Acid Phosphatase is a Protein Coding gene. Diseases associated with *NANP* include Parasitic Protozoa Infectious Disease and Intracranial Abscess. Among its related pathways are Synthesis of substrates in N-glycan biosythesis and Transport to the Golgi and subsequent modification. GO annotations related to this gene include hydrolase activity and N-acylneuraminate-9-phosphatase activity.

NETO1

Neuropilin And Tolloid Like 1) is a Protein Coding gene. GO annotations related to this gene include ionotropic glutamate receptor binding. This gene encodes a transmembrane protein containing two extracellular CUB domains followed by a low-density lipoprotein class A (LDLa) domain. This protein is thought to play a critical role in spatial learning and memory by regulating the function of synaptic N-methyl-D-aspartic acid receptor complexes in the hippocampus.

NIPA1

NIPA Magnesium Transporter 1 is a Protein Coding gene. Diseases associated with *NIPA1* include Spastic Paraplegia 6, Autosomal Dominant and Spastic Paraplegia 6. Among its related pathways are Miscellaneous transport and binding events and Transport of glucose and other sugars, bile salts and organic acids, metal ions and amine compounds. GO annotations related to this gene include magnesium ion transmembrane transporter activity. This gene encodes a magnesium transporter that associates with early endosomes and the cell surface in a variety of neuronal and epithelial cells.

This protein may play a role in nervous system development and maintenance. Multiple transcript variants encoding different isoforms have been found for this gene. Mutations in this gene have been associated with autosomal dominant spastic paraplegia 6.

PCDHGC4

Protocadherin Gamma Subfamily C, 4 is a Protein Coding gene. GO annotations related to this gene include calcium ion binding. This gene is a member of the protocadherin gamma gene cluster. Potential calcium-dependent cell-adhesion protein, these neural cadherin-like cell adhesion proteins most likely play a critical role in the establishment and function of specific cell-cell connections in the brain.

PHYH

Phytanoyl-CoA 2-Hydroxylase is a Protein Coding gene. Diseases associated with *PHYH* include Refsum Disease, Classic and Retinitis Pigmentosa. Among its related pathways are Peroxisome and Metabolism. GO annotations related to this gene include electron transfer activity and cofactor binding. This gene is a member of the PhyH family and encodes a peroxisomal protein that is involved in the α-oxidation of 3-methyl branched fatty acids. Specifically, this protein converts phytanoyl-CoA to 2-hydroxyphytanoyl-CoA.

RAB32

RAB32, Member RAS Oncogene Family) is a Protein Coding gene. Among its related pathways are Vesicle-mediated transport and Sertoli-Sertoli Cell Junction Dynamics. GO annotations related to this gene include GTP binding. The protein encoded by this gene anchors the type II regulatory subunit of protein kinase A to the mitochondrion and aids in mitochondrial fission. The encoded protein also appears to be involved in autophagy and melanosome secretion.

RBP4

Retinol Binding Protein 4 is a Protein Coding gene. Diseases associated with *RBP4* include Retinal Dystrophy, Iris Coloboma, And Comedogenic Acne Syndrome and Microphthalmia, Isolated, With Coloboma 10. Among its related pathways are Metabolism of fat-soluble vitamins and the visual cycle I (vertebrates). GO annotations related to this gene include protein heterodimerisation activity and retinol binding. This protein belongs to the lipocalin family and is the specific carrier for retinol (vitamin A alcohol) in the blood. It delivers retinol from the liver stores to the peripheral tissues. In plasma, the RBP-retinol complex interacts with transthyretin which prevents its loss by filtration through the kidney glomeruli. A deficiency of vitamin A blocks secretion of the binding protein post-translationally and results in defective delivery and supply to the epidermal cells.

RUNX3

RUNX Family Transcription Factor 3 is a Protein Coding gene. Diseases associated

with *RUNX3* include Testicular Yolk Sac Tumour and Cleidocranial Dysplasia. Among its related pathways are Wnt / Hedgehog / Notch and Measles. GO annotations related to this gene include DNA-binding transcription factor activity and RNA polymerase II regulatory region sequence-specific DNA binding. This gene encodes a member of the runt domain-containing family of transcription factors. A heterodimer of this protein and a beta subunit forms a complex that binds to a number of enhancers and promoters, and can either activate or suppress transcription.

SCN4B

Sodium Voltage-Gated Channel Beta Subunit 4 is a Protein Coding gene. Diseases associated with *SCN4B* include Long Qt Syndrome 10 and Familial Atrial Fibrillation. Among its related pathways are Cardiac conduction and L1CAM interactions. GO annotations related to this gene include ion channel binding and voltage-gated sodium channel activity. The protein encoded by this gene is one of several sodium channel beta subunits. These subunits interact with voltage-gated alpha subunits to change sodium channel kinetics.

SCUBE3

Signal Peptide, CUB Domain And EGF Like Domain Containing 3 is a Protein Coding gene. Diseases associated with *SCUBE3* include Lung Cancer. GO annotations related to this gene include calcium ion binding. This gene encodes a member of the signal peptide, complement subcomponents C1r/C1s, Uegf, bone morphogenetic protein-1 and epidermal growth factor-like domain containing protein family.

SLC25A36

Solute Carrier Family 25 Member 36 is a Protein Coding gene. GO annotations related to this gene include pyrimidine nucleotide transmembrane transporter activity. Mitochondrial transporter that imports/exports pyrimidine nucleotides into and from mitochondria. Participates in mitochondrial genome maintenance, regulation of mitochondrial membrane potential and mitochondrial respiration.

SLC6A18

Solute Carrier Family 6 Member 18 is a Protein Coding gene. Diseases associated with *SLC6A18* include Iminoglycinuria and Hyperglycinuria. Among its related pathways are Amino acid transport across the plasma membrane and Transport of glucose and other sugars, bile salts and organic acids, metal ions and amine compounds. GO annotations related to this gene include neurotransmitter:sodium symporter activity. The SLC6 family of proteins, which includes SLC6A18, act as specific transporters for neurotransmitters, amino acids, and osmolytes like betaine, taurine, and creatine. SLC6 proteins are sodium co-transporters that derive the energy for solute transport from the electrochemical gradient for sodium ions.

TFAP4

Transcription Factor AP-4 is a Protein Coding gene. Diseases associated with *TFAP4*

include Spinocerebellar Ataxia 12. Among its related pathways are Proteoglycans in cancer. GO annotations related to this gene include protein homodimerisation activity and protein heterodimerisation activity. Transcription factors of the basic helix-loop-helix-zipper family contain a basic domain, which is used for DNA binding, and HLH and ZIP domains, which are used for oligomerization. Transcription factor AP4 activates both viral and cellular genes.

THRB

Thyroid Hormone Receptor Beta is a Protein Coding gene. Diseases associated with *THRB* include Thyroid Hormone Resistance, Selective Pituitary and Thyroid Hormone Resistance, Generalized, Autosomal Dominant. Among its related pathways are Neural Stem Cell Differentiation Pathways and Lineage-specific Markers and Thyroid hormone signalling pathway. GO annotations related to this gene include DNA-binding transcription factor activity and enzyme binding. The protein encoded by this gene is a nuclear hormone receptor for triiodothyronine. It is one of the several receptors for thyroid hormone, and has been shown to mediate the biological activities of thyroid hormone. Knockout studies in mice suggest that the different receptors, while having certain extent of redundancy, may mediate different functions of thyroid hormone.

TLX2

T Cell Leukemia Homeobox 2 is a Protein Coding gene. Diseases associated with *TLX2* include Intestinal Pseudo-Obstruction and Neuronal Intestinal Dysplasia. Among its related pathways are ALK2 signalling events and Cell Differentiation - Index. This gene is a member of an orphan homeobox-containing transcription factor family. Transcription activator that binds DNA elements via its homeobox. Required for normal cell death of enteric neurons in the gastrointestinal tract.

TNS3

Tensin 3 is a Protein Coding gene. Diseases associated with *TNS3* include Anisakiasis and Primary Syphilis. Among its related pathways are MET promotes Cell Motility and Signalling by GPCR. GO annotations related to this gene include phosphatase activity. May play a role in actin remodelling. Involved in the dissociation of the integrin-tensin-actin complex. Seems to be involved in mammary cell migration.

TSPAN32

Tetraspanin 32 is a Protein Coding gene. This gene, which is a member of the tetraspanin superfamily, is one of several tumour-suppressing subtransferable fragments located in the imprinted gene domain of chromosome 11p15.5, an important tumour-suppressor gene region. Alterations in this region have been associated with Beckwith-Wiedemann syndrome, Wilms tumor, rhabdomyosarcoma, adrenocortical carcinoma, and lung, ovarian and breast cancers.

ZNF273

Zinc Finger Protein 273 is a Protein Coding gene. Among its related pathways are

Herpes simplex virus 1 infection and Gene Expression. GO annotations related to this gene include nucleic acid binding. This nuclear protein is involved in transcriptional regulation.

mtDNA Copy Number

Primers and Probes

Table S8: *qPCR standard primer sequences and product size.*

Gene	Forward Sequence 5′-3′	Reverse Sequence 5′-3′	Product Size (bp)
B2M	CGCAATCTCCAGTGACAGAA	GCAGAATAGGCTGCTGTTCC	1092
MT-ND1	CAGCCGCTATTAAAGGTTCG	AGAGTGCGTCATATGTTGTTC	1040
MT-ND4	ATCGCTCACACCTCATATCC	TAGGTCTGTTTGTCGTAGGC	1072
MT-RNR2	CAGTGACACATGTTTAACGGC	GGAGGGGGGTTCATAGTAG	1026

Table S9: *qPCR primer sequences and product size.*

Gene	Forward Sequence 5′-3′	Reverse Sequence 5′-3′	Product Size (bp)
Original B2M	CACTGAAAAAGATGAGTATGCC	AACATTCCCTGACAATCCC	231
New B2M	GTGGAGCATTCAGACTTGTCTTTC	CCACTTAACTATCTTGGGCTGT	141
MT-ND1	ACGCCATAAAACTCTTCACCAAAG	GGGTTCATAGTAGAAGAGCGATGG	111
MT-ND4	ACCTTGGCTATCATCACCCGAT	AGTGCGATGAGTAGGGGAAGG	107
MT-RNR2	CCAACGGAACAAGTTACCCTAG	CGAACCTTTAATAGCGGCTGC	126

Table S10: *qPCR probe sequence, fluorophore and quencher.*

Gene	Fluorophore	Quencher	Sequence 5′-3′
B2M	FAM	BHQ_1	CCGTGTGAACCATGTGACTTTGTC
MT-ND1	HEX	BHQ_1	ACCCGCCACATCTACCATCACCCTC
MT-ND4	Cy5	BHQ_2	CAACCAGCCAGAACGCCTGAACGCA
MT-RNR2	HEX	BHQ_1	TACGACCTCGATGTTGGATCAGGACA

qPCR Measurements

Table S11: *T-Test values for change in Ct score between singleplex to duplex and triplex.*

Duplex/Triplexed	B2M	ND4	RNR2
B2M	-	0.013	0.458
ND4	0.276	-	0.015
RNR2	0.184	0.142	-
Triplex	0.057	0.071	0.012

Table S12: *T-Test values for change in Ct score between duplex and triplex.*

Duplex/Triplexed	B2M	ND4	RNR2
B2M	-	0.405	0.020
ND4	0.135	-	0.289
RNR2	0.171	0.289	-

Table S13: *Figure 3.12 graphs' linear models showing the equation of the model, adjusted R-squared value and the correlation between the* MT-ND1 *and* MT-RNR2 *copy number measurements.*

Graph	Formula	Adjusted R-squared	Correlation
A	y = 141.215x - 9279.769	0.993	0.821
B	y = 46.030x -2388.520	0.434	0.714
C	y = 3.498x - 271.098	0.902	0.857
D	y = 71.630x -7745.290	0.348	0.420
E	y= 0.354x + 657.989	-0.088	0.275

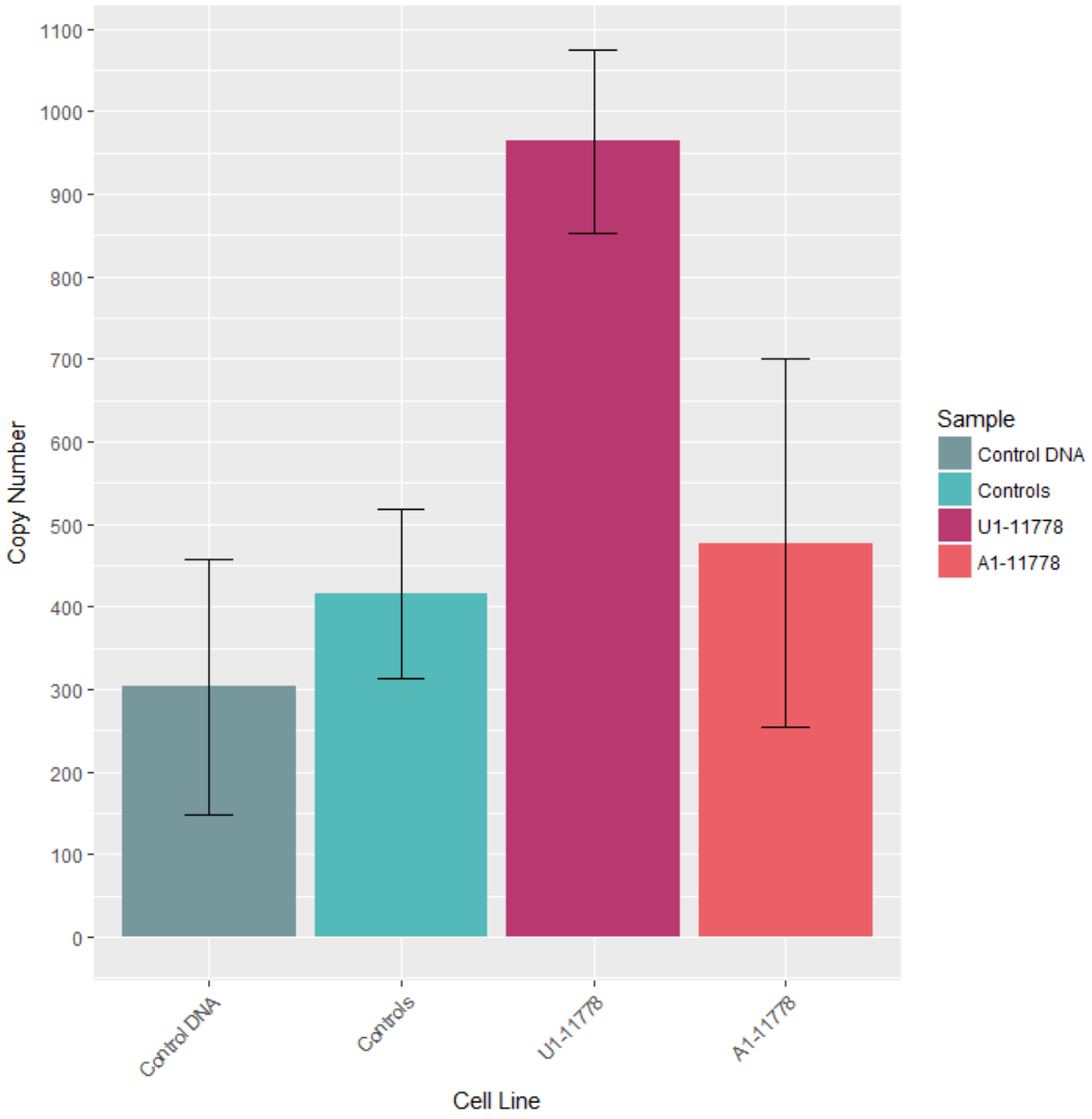

Figure S9: *Preliminary qPCR copy number measurements for control DNA sample, control fibroblast samples C1 and C2, unaffected sample U1-11778 and affected A1-11778. U1-11778 is the unaffected mother of sample A1-11778 with the same mitochondrial background. Two biological replicates of each sample were taken with three technical replicates and error bars indicate standard deviation.*

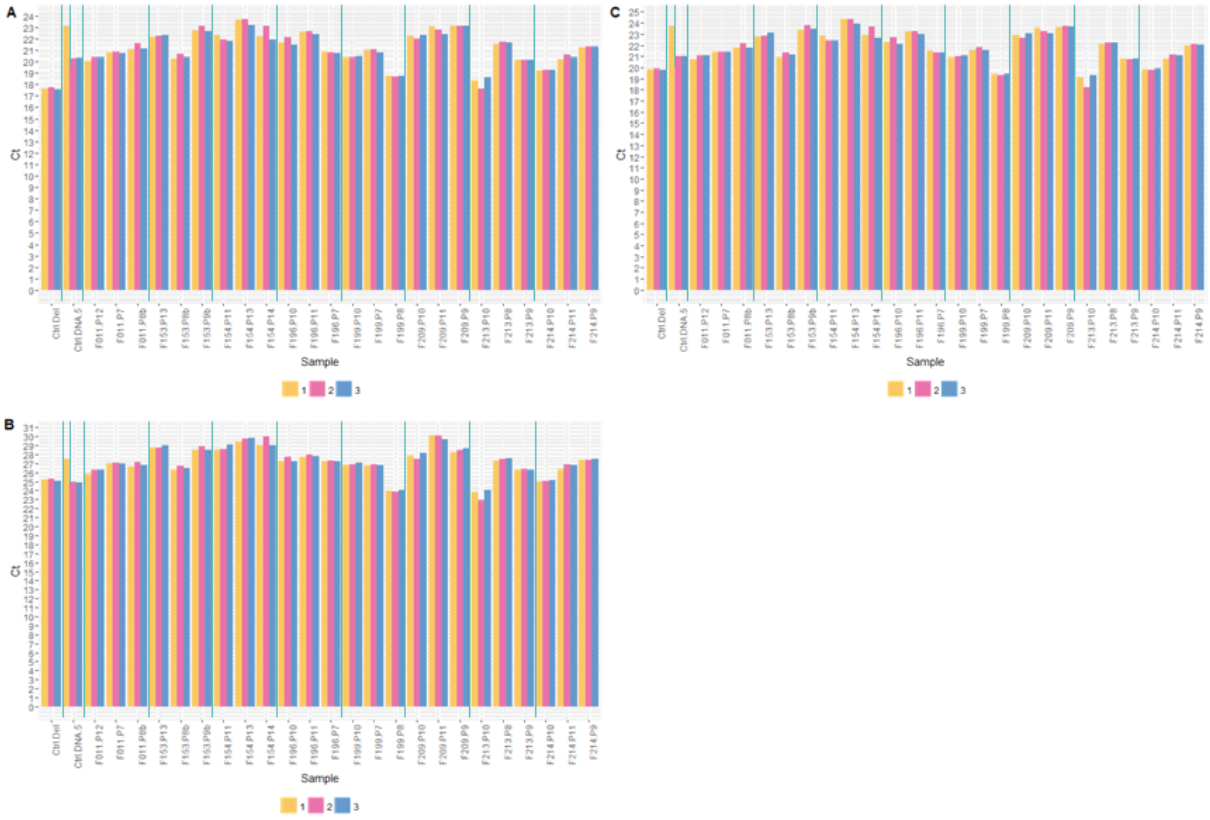

Figure S10: *qPCR Ct measurement, showing each biological replicate in* MT-RNR2 *(A),* B2M *(B) and* MT-ND4 *(C). A new dilution of Ctrl DNA 5 was prepared after the first replicate; demarcation indicates that replicate 2 and 3 used the new dilution.*

Table S14: *Welch two sample t-test significance of mtDNA copy number and percentage deletion.*

		Copy Number	**% Deletion**
Controls Grouped	A1-11778	0.061	0.990
	A2-14484	0.127	0.669
	A3-11778	0.701	0.307
	A4-11778	0.036	0.804
	A5-3460	0.086	0.589
Mutation Grouped	m.11778G>A	0.132	0.490
	m.14484T>C	0.127	0.669
	m.3460G>A	0.086	0.589
Disease Grouped	LHON	0.110	0.533

ATP Production During Metabolic Stress

Table S15: *Welch two sample t-test significance of ATP assay.*

		Glucose	Deoxyglucose	Glucose & Oligomycin A	Deoxyglucose & Oligomycin A
Control Grouped	A1-11778	0.377	0.271	0.908	0.353
	A2-14484	0.730	0.595	0.360	0.881
	A3-11778	0.231	0.996	0.452	0.815
	A4-11778	0.227	0.017	0.137	0.492
	A5-3460	0.342	0.328	0.466	0.913
Mutation Grouped	m.11778G>A	0.093	0.130	0.286	0.438
	m.14484T>C	0.730	0.595	0.360	0.881
	m.3460G>A	0.342	0.328	0.466	0.913
Disease Grouped	LHON	0.629	0.908	0.316	0.642

Cellular Oxygen Consumption

Table S16: *Welch two sample t-test significance of Seahorse measurements.*

		Basal Respiration	**ATP Production**	**Proton Leak**	**Maximal Respiration**	**Spare Respiratory Capacity**	**Non-Mitochondrial Respiration**
Controls Grouped	A1-11778	0.004	0.028	0.944	0.013	0.016	0.155
	A2-14484	0.183	0.179	0.460	0.227	0.244	0.875
	A3-11778	0.056	0.072	0.898	0.649	0.731	0.340
	A4-11778	0.001	1.19e-05	0.414	0.021	0.032	0.820
	A5-3460	0.002	0.001	0.737	0.009	0.012	0.049
Mutation Grouped	m.11778G>A	0.002	1.25e-04	0.743	0.066	0.091	0.873
	m.14484T>C	0.183	0.179	0.460	0.227	0.244	0.875
	m.3460G>A	0.002	0.001	0.737	0.009	0.012	0.049
Disease Grouped	LHON	0.003	2.74e-04	0.669	0.083	0.113	0.652

Table S17: *Two sample t-test significance of maximal calcium uptake.*

		Maximal Calcium Uptake
Controls Grouped	A1-11778	0.632
	A2-14484	0.415
	A3-11778	0.166
	A4-11778	0.580
	A5-3460	0.004
Mutation Grouped	m.11778G>A	0.573
	m.14484T>C	0.415
	m.3460G>A	0.004
Disease Grouped	LHON	0.673

Table S18: *Number of cells used to quantify maximal calcium uptake from each cell line.*

		Mutation	**n**
Controls	C1	-	13
	C2	-	12
	C3	-	14
LHON	A1-11778	m.11778G>A	13
	A2-14484	m.14484T>C	12
	A3-11778	m.11778G>A	9
	A4-11778	m.11778G>A	14
	A5-3460	m.3460G>A	16

Mitochondrial Membrane Potential

Table S19: *Two sample t-test significance of mitochondrial $\Delta\Psi m$.*

		Mitochondrial Membrane Potential
Controls Grouped	A1-11778	0.149
	A2-14484	0.160
	A3-11778	0.831
	A4-11778	0.396
	A5-3460	0.858
Mutation Grouped	m.11778G>A	0.222
	m.14484T>C	0.160
	m.3460G>A	0.858
Disease Grouped	LHON	0.183

Mitochondrial Network

Table S20: *Number of cells used to quantify mitochondrial network and ER:mitochondrial co-localisation from each cell line.*

		Mutation	**n**
Controls	C1	-	22
	C2	-	20
	C3	-	23
LHON	A1-11778	m.11778G>A	13
	A2-14484	m.14484T>C	21
	A3-11778	m.11778G>A	17
	A4-11778	m.11778G>A	20
	A5-3460	m.3460G>A	21

Table S21: *Welch two sample t-test significance of mitochondrial network measurements.*

		Average Length	**Maximum Length**	**Minimum Length**	**Total Length**	**Average Volume**	**Maximum Volume**	**Minimum Volume**	**Total Volume**	**Number of Fragments**
Controls Grouped	A1-11778	0.267	0.221	0.760	0.251	0.047	0.036	0.299	0.006	0.360
	A2-14484	0.464	0.524	0.847	0.060	0.710	0.939	0.851	0.890	0.058
	A3-11778	0.530	0.330	0.714	0.746	0.848	0.775	0.919	0.645	0.912
	A4-11778	0.466	0.403	0.696	0.471	0.013	0.036	0.571	0.285	0.760
	A5-3460	0.058	0.024	0.092	0.131	0.174	0.458	0.895	0.617	0.016
Mutation Grouped	m.11778G>A	0.308	0.748	0.794	0.865	0.097	0.221	0.576	0.310	0.947
	m.14484T>C	0.464	0.524	0.847	0.060	0.710	0.939	0.851	0.890	0.058
	m.3460G>A	0.058	0.024	0.092	0.131	0.174	0.458	0.895	0.617	0.016
Disease Grouped	LHON	0.637	0.237	0.600	0.377	0.773	0.673	0.748	0.635	0.203

ER-Mitochondrial Interactions

Table S22: *Welch two sample t-test significance of endoplasmic reticulum:mitochondrial co-localisation, number of cells per cell line previously indicated in Table S20.*

		Pearson Correlation	**M1**	**M2**
Controls Grouped	A1-11778	0.618	0.171	0.784
	A2-14484	0.001	0.273	3.36e-04
	A3-11778	0.175	0.272	0.197
	A4-11778	0.180	0.036	0.153
	A5-3460	0.081	0.416	0.082
Mutation Grouped	m.11778G>A	0.833	0.769	0.913
	m.14484T>C	0.001	0.273	3.36e-04
	m.3460G>A	0.081	0.416	0.082
Disease Grouped	LHON	0.060	0.735	0.025

MITOCHONDRIAL DISEASE MOUSE

Mitochondrial Heteroplasmy Level

PCR was used to amplify a 222 bp fragment spanning the m.5024 mutation site, using a biotinylated forward primer (5′-Biotin-TTCCACCCTAGCTATCATAAGC) and a non-biotinylated reverse primer (5′-GTAGGTTTAATTCCTGCCAATCT). PCR products were combined with dH_2O, PyroMark PCR Kit (979006; QIAGEN) and 1 µl Streptavidin Sepharose High Performance Beads (17-5113-01; GE Healthcare), and purified and denatured using a PyroMark Q24 Vacuum Workstation.

Sequencing was carried out with PyroMark Gold Q24 Reagents (970802; QIAGEN) according to manufacturer's directions, using the sequencing primer (5′-TGTAGGATGAAGTCTTACA).

Primers and Probes

Table S23: *Pyrosequencing primer sequences and product size.*

Gene	Forward Sequence 5′-3′	Reverse Sequence 5′-3′
PCR Primer	Biotin-TTCCACCCTAGCTATCATAAGC	CGTAGGTTTAATTCCTGCCAATCT
Sequencing Primer	TGTAGGATGAAGTCTTACA	

Immunofluorescence Microscopy

Table S24: *Welch two sample t-test significance of differences in the length of retinal layers.*

		PR	ONL	OPL	INL	IPL	RGC
Controls Grouped	M1	0.146	0.020	0.162	0.519	0.120	0.262
	M2	0.626	0.172	0.005	0.087	0.003	0.127
	M3	0.086	0.943	0.163	0.053	0.233	0.204
	M4	0.079	0.046	0.007	0.009	0.003	0.025
	M5	0.520	0.042	0.001	0.100	1.96e-04	0.008
Mutant Grouped		0.200	0.453	0.008	0.122	0.028	0.063

Table S25: *Welch two sample t-test significance of differences in the area (μm^2) of which a single cell occupies in ONL and INL retinal layers and differences in length (μm) per cell for the RGC layer spacing.*

		ONL	**INL**	**RGC**
Controls Grouped	M1	0.801	0.073	0.214
	M2	0.154	0.809	0.874
	M3	0.042	0.070	0.364
	M4	0.041	3.51e-06	0.120
	M5	0.025	0.015	0.316
Mutant Grouped		0.004	4.00e-04	0.320